POLISH SOCIETY OF THEORETICAL AND APPLIED MECHANICS

JOURNAL OF THEORETICAL AND APPLIED MECHANICS

No. 1 • Vol. 62

Quarterly

WARSAW, JANUARY 2024

JOURNAL OF THEORETICAL AND APPLIED MECHANICS
(until 1997 Mechanika Teoretyczna i Stosowana, ISSN 0079-3701)

Beginning with Vol. 45, No. 1, 2007, *Journal of Theoretical and Applied Mechanics* (JTAM) has been selected for coverage in Thomson Reuters products and custom information services. Now it is indexed and abstracted in the following:

- **Science Citation Index Expanded** (also known as SciSearch®)
- **Journal Citation Reports/Science Edition**

* * * * *

Editorial Office

Al. Armii Ludowej 16, room 650; 00-637 Warsaw, Poland
phone (+48) 664 099 345, e-mail: biuro@ptmts.org.pl

www.jtam.pl

* * * * *

Rozwój kwartalnika naukowego *Journal of Theoretical and Applied Mechanics*, ISSN 1429-2955, jest dofinansowany ze środków Ministra Edukacji i Nauki przyznanych z pomocy *de minimis* w ramach programu „Rozwój czasopism naukowych", umowa RCN/SN/0056/2021/1.

JOURNAL OF THEORETICAL AND APPLIED MECHANICS
62, 1, pp. 3-17, Warsaw 2024
https://doi.org/10.15632/jtam-pl/174698

BENDING OF A SANDWICH BEAM WITH AN INDIVIDUAL FUNCTIONALLY GRADED CORE

Krzysztof Magnucki
Łukasiewicz Research Network – Poznan Institute of Technology, Rail Vehicles Center, Poznan, Poland
e-mail: krzysztof.magnucki@pit.lukasiewicz.gov.pl

Krzysztof Sowiński
Poznan University of Technology, Institute of Applied Mechanics, Poznan, Poland
e-mail: krzysztof.sowinski@put.poznan.pl

This paper is devoted to a clamped sandwich beam with an individual functionally graded core under a uniformly distributed load. A non-linear shear deformation theory is developed with consideration of the classical shear stress formula for beams. Two differential equations of the equilibrium of the beam are obtained based on the principle of stationary total potential energy. The shear effect function and the relative deflection line of the beam are determined. Moreover, a numerical FEM model (Ansys system) of this beam is elaborated. Detailed calculations of exemplary beams are realised using two methods, analytical and numerical FEM.

Keywords: sandwich beam, functionally graded core, non-linear shear deformation theory

1. Introduction

Shear deformation theories of beams, plates and shells have been extensively refined in the twenty-first century. The demand for new, more accurate and generalised shear theories becomes more apparent with increasing interest in the application of composite structures in engineering. The significance of this topic can be proven by the number of articles and original theories developed over the last two decades.

Huang (2003) described various studies on stress-strain modelling of adhesively bonded sandwich beams and proposed his model of sandwich beams. Reddy (2004) presented a fundamental theory and analysis associated with the mechanics of laminated composite plates and shells. Zenkour (2006) modelled a static response for a rectangular plate supported with a functionally graded plate.

Berdichevsky (2010) derived a two-dimensional theory of sandwich plates by asymptotic analysis of three-dimensional linear elasticity. Carrera *et al.* (2011) discussed classical and modern approaches to the beam theory and paid particular attention to their typical applications. Meiche *et al.* (2011) developed an advanced hyperbolic shear deformation theory. Mantari *et al.* (2012) presented an original shear deformation theory for sandwich and composite plates, where the displacement field is parameterized. Thai and Vo (2013) proposed a sinusoidal shear deformation theory for bending, buckling and vibration of functionally graded plates. Sahoo and Singh (2013) discussed an original inverse trigonometric zigzag theory and implemented it for static analysis of laminated composite and sandwich panels.

Kolakowski and Mania (2015) investigated the dynamic interactive response of square FGM plates subjected to in-plane pulse loading using the modified classical laminate plate theory. Mahi *et al.* (2015) introduced a hyperbolic shear deformation theory with five degrees of freedom applicable to bending and free vibration analysis of isotropic, functionally graded sandwich and

laminated composite plates. Marczak and Jędrysiak (2015) studied free-vibration of periodic three-layered sandwich structures referring to Kirchoff's thin plate theory and the tolerance averaging technique. Domagalski and Jędrysiak (2016) presented a work on geometrically non--linear vibrations of beams with periodic structures.

Banat and Mania (2017) considered non-linear buckling and failure analysis of fibre metal laminate thin-walled structures under axial compression. Özütok and Madenci (2017) presented a higher-order shear deformation theory including a non-linear distribution of shear stress through the thickness of a laminated beam. Pei *et al.* (2018) established a variationally consistent higher--order theory for problems of functionally graded beams, referring to the principle of virtual work. Birman and Kardomateas (2018) discussed the current development and interest in mathematical modelling and the application of sandwich structures. Ghayesh (2018) focused on vibrations of axially functionally graded beams incorporating shear deformation and imperfection.

Kumar *et al.* (2019) developed a modern higher-order shear deformation theory for a functionally graded plate. Magnucki *et al.* (2020) referred to the Zhuravsky shear stress formula to develop a shear deformation theory. Żur *et al.* (2020) focused on buckling and free-vibration analyses of functionally graded nanoplates with magneto-electroelastic coupling. Dhuria *et al.* (2021) analysed the effect of porosity distribution on the static and buckling response of a simply supported plate with FGM.

Magnucki (2022) presented analytical models of homogeneous beams with bi-symmetrical cross sections, sandwich beams and beams with symmetrically varying mechanical properties. Magnucki *et al.* (2022) conducted a study on the axisymmetric bending problem of a generalised circular sandwich plate with varying mechanical properties along its thickness. Jędrysiak (2023) investigated slender, elastic, nonperiodic beams with a functionally graded structure on the macro-level and a nonperiodic structure on the micro-level referring to the tolerance modelling method.

The main objective of the study is to formulate a linear theory with the assumption of a non-linear shear deformation for a three-layer beam with an individual functionally graded core. The function of the variation of Young's modulus is generalised so that it can describe a beam with homogeneous mechanical properties, as well as a classic three-layer and five-layer beam with an optional ratio of stiffness between the layers.

According to the literature review, there are numerous papers investigating the problem of the shear effect in structures. Many of them refer to a numerical approach or analytical formulation with a predefined, usually parametric shear deformation function. In the present paper, the shear deformation function is obtained analytically in the exact manner with consideration of the classical shear stress formula. An analytical model of a beam is developed using the proposed non-linear shear deformation theory. The subject of the study is a clamped sandwich beam of length L, width b, and total depth h with an individual functionally graded core under a uniformly distributed load of intensity q (Fig. 1). The bending problem of this beam is studied, taking into account the shear effect. Its solution is compared with the results of numerical finite element method analysis in the Ansys system.

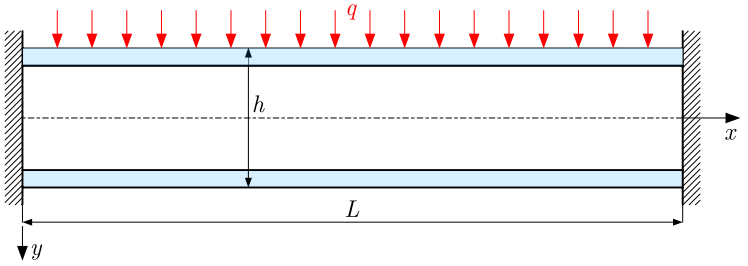

Fig. 1. A scheme of a clamped sandwich beam with an individual functionally graded core

2. Analytical model of the sandwich beam

The rectangular cross section and variation of Young's modulus in the depth direction of the beam are shown in Fig. 2.

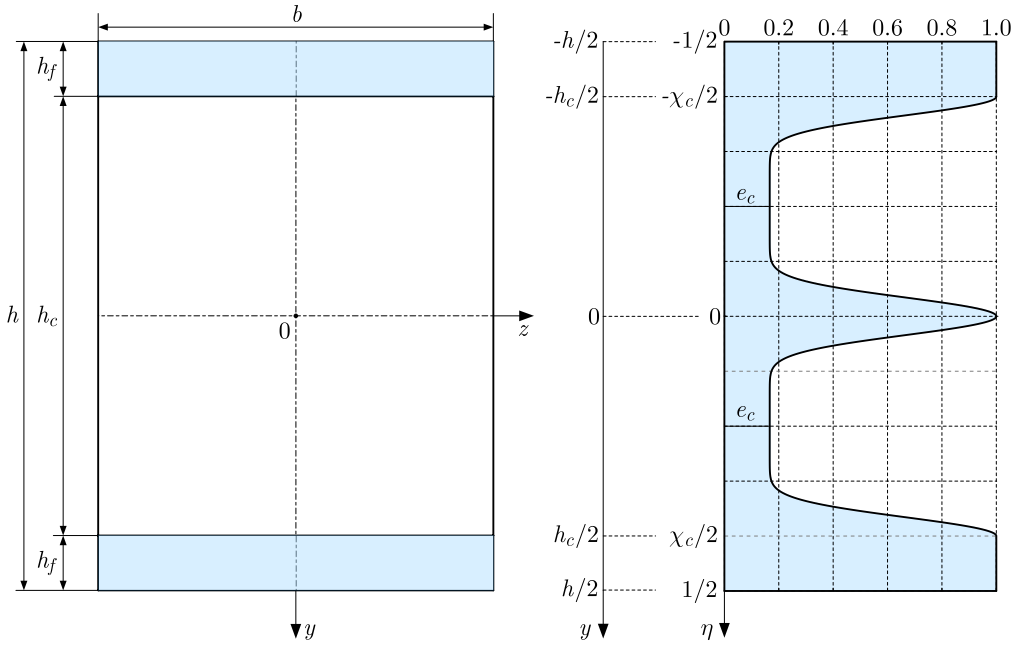

Fig. 2. Schemes of the rectangular cross section and variation of Young's modulus in the depth direction of the beam

The variation of Young's modulus in the depth direction takes the form

$$E_f(\eta) = E_f f_e(\eta) \tag{2.1}$$

where: E_f – Young's modulus of faces, also $f_e(\eta)$ – dimensionless function, which in successive layers is as follows:
— the upper face $(-1/2 \leqslant \eta \leqslant -\chi_c/2)$

$$f_e(\eta) = 1 \tag{2.2}$$

— the core $(-\chi_c/2 \leqslant \eta \leqslant \chi_c/2)$

$$f_e(\eta) = e_c + \frac{1-e_c}{2^n}\Big[1+\cos\Big(\frac{4}{\chi_c}\pi\eta\Big)\Big]^n \tag{2.3}$$

— the lower face $(\chi_c/2 \leqslant \eta \leqslant 1/2)$

$$f_e(\eta) = 1 \tag{2.4}$$

and dimensionless quantities: the coordinate $\eta = y/h$, coefficient of the core e_c, thickness of the core $\chi_c = h_c/h$, exponent n – natural number. The deformation of a planar cross section after bending of this beam is presented in Fig. 3. The longitudinal displacements according to this scheme (Fig. 3) in successive layers are as follows:
— the upper face $(-1/2 \leqslant \eta \leqslant -\chi_c/2)$

$$u^{(uf)}(x,\eta) = -h\Big[\eta\frac{dv}{dx} - f_d^{(uf)}(\eta)\psi_f(x)\Big] \tag{2.5}$$

— the core $(-\chi_c/2 \leqslant \eta \leqslant \chi_c/2)$

$$u^{(c)}(x,\eta) = -h\Big[\eta\frac{dv}{dx} - f_d^{(c)}(\eta)\psi_f(x)\Big] \tag{2.6}$$

— the lower face $(\chi_c/2 \leqslant \eta \leqslant 1/2)$

$$u^{(lf)}(x,\eta) = -h\Big[\eta\frac{dv}{dx} - f_d^{(lf)}(\eta)\psi_f(x)\Big] \tag{2.7}$$

where: $v(x)$ – deflection, $\psi_f(x) = u_f(x)/h$ – dimensionless longitudinal displacement on the outer surfaces of the beam-shear effect function, $f_d^{(uf)}(\eta)$, $f_d^{(c)}(\eta)$, $f_d^{(lf)}(\eta)$ – dimensionless deformation functions in these layers.

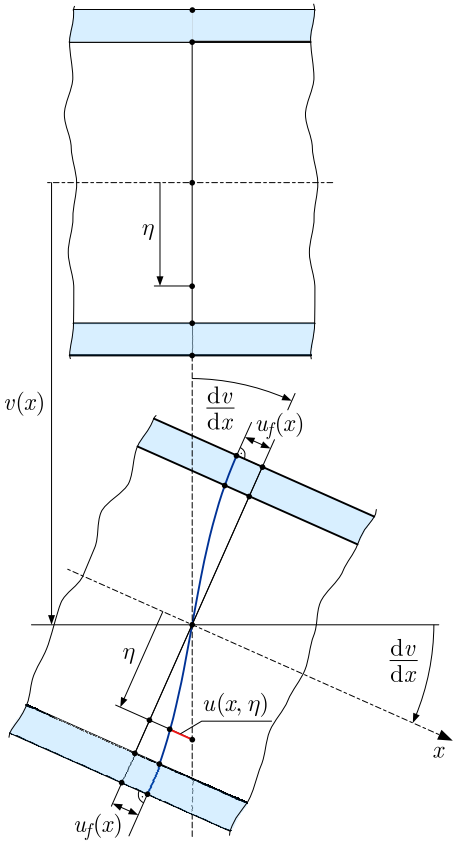

Fig. 3. Scheme of a planar cross-section deformation of the analysed beam

Consequently, the strains and stresses are as follows:
— the upper face $(-1/2 \leqslant \eta \leqslant -\chi_c/2)$

$$\begin{aligned}
\varepsilon_x^{(uf)}(x,\eta) &= \frac{\partial u}{\partial x} = -h\Big[\eta\frac{d^2v}{dx^2} - f_d^{(uf)}(\eta)\frac{d\psi_f}{dx}\Big] \\
\sigma_x^{(uf)}(x,\eta) &= -E_f h\Big[\eta\frac{d^2v}{dx^2} - f_d^{(uf)}(\eta)\frac{d\psi_f}{dx}\Big] \\
\gamma_{xy}^{(uf)}(x,\eta) &= \frac{dv}{dx} + \frac{\partial u}{h\partial\eta} = \frac{df_d^{(uf)}}{d\eta}\psi_f(x) \\
\tau_{xy}^{(uf)}(x,\eta) &= \frac{E_f}{2(1+\nu)}\frac{df_d^{(uf)}}{d\eta}\psi_f(x)
\end{aligned} \tag{2.8}$$

— the core $(-\chi_c/2 \leqslant \eta \leqslant \chi_c/2)$

$$\begin{aligned}
\varepsilon_x^{(c)}(x,\eta) &= \frac{\partial u}{\partial x} = -h\Big[\eta\frac{d^2v}{dx^2} - f_d^{(c)}(\eta)\frac{d\psi_f}{dx}\Big] \\
\gamma_{xy}^{(c)}(x,\eta) &= \frac{dv}{dx} + \frac{\partial u}{h\partial\eta} = \frac{df_d^{(c)}}{d\eta}\psi_f(x) \\
\sigma_x^{(c)}(x,\eta) &= -E_f h\Big[\eta\frac{d^2v}{dx^2} - f_d^{(c)}(\eta)\frac{d\psi_f}{dx}\Big]f_e^{(c)}(\eta) \\
\tau_{xy}^{(c)}(x,\eta) &= \frac{E_f}{2(1+\nu)}f_e^{(c)}(\eta)\frac{df_d^{(c)}}{d\eta}\psi_f(x)
\end{aligned} \tag{2.9}$$

— the lower face $(\chi_c/2 \leqslant \eta \leqslant 1/2)$

$$\begin{aligned}
\varepsilon_x^{(lf)}(x,\eta) &= \frac{\partial u}{\partial x} = -h\Big[\eta\frac{d^2v}{dx^2} - f_d^{(lf)}(\eta)\frac{d\psi_f}{dx}\Big] \\
\gamma_{xy}^{(lf)}(x,\eta) &= \frac{dv}{dx} + \frac{\partial u}{h\partial\eta} = \frac{df_d^{(lf)}}{d\eta}\psi_f(x) \\
\sigma_x^{(lf)}(x,\eta) &= -E_f h\Big[\eta\frac{d^2v}{dx^2} - f_d^{(lf)}(\eta)\frac{d\psi_f}{dx}\Big] \\
\tau_{xy}^{(lf)}(x,\eta) &= \frac{E_f}{2(1+\nu)}\frac{df_d^{(lf)}}{d\eta}\psi_f(x)
\end{aligned} \tag{2.10}$$

where ν – Poisson's ratio is constant for the structure. Taking into account the papers by Magnucki (2022) and Magnucki *et al.* (2022), the unknown dimensionless deformation functions $f_d^{(uf)}(\eta)$, $f_d^{(c)}(\eta)$, $f_d^{(lf)}(\eta)$ are determined with consideration of the classical shear stress formula for the rectangular cross section of the beam

$$\tau_{xy}^{(Cl)}(x,\eta) = \overline{Q}_z(\eta)\frac{T(x)}{J_z}h^2 \tag{2.11}$$

where: $T(x)$ – transverse-shear force, $\overline{Q}_z(\eta)$ – dimensionless first moment of the cross section area part, J_z – inertia moment of the cross section. Therefore, the dimensionless first moments of successive layers of this sandwich beam with the individual functionally graded core are of the form:

— the upper face $(-1/2 \leqslant \eta \leqslant -\chi_c/2)$

$$\overline{Q}_z^{(uf)}(\eta) = \frac{1}{8}(1-4\eta^2) \tag{2.12}$$

— the core $(-\chi_c/2 \leqslant \eta \leqslant \chi_c/2)$

$$\overline{Q}_z^{(c)}(\eta) = \frac{1}{8}[1-\chi_c^2 + e_c(\chi_c^2 - 4\eta^2) - 8J_c(\eta)] \tag{2.13}$$

where

$$J_c(\eta) = \frac{1-e_c}{2^n}\int\limits_{-\chi_c/2}^{\eta}\Big(1+\cos\frac{4\pi\eta_1}{\chi_c}\Big)^n\eta_1\,d\eta_1 \tag{2.14}$$

— the lower face $(\chi_c/2 \leqslant \eta \leqslant 1/2)$

$$\overline{Q}_z^{(lf)}(\eta) = \frac{1}{8}(1-4\eta^2) \tag{2.15}$$

Equating the shear stresses in Eqs. (2.8), (2.9) and (2.10) with classical shear stress formula (2.11) with consideration of the dimensionless first moments in Eqs. (2.12), (2.13) and (2.14), after simple transformations, the unknown dimensionless deformation functions for successive layers satisfying the continuity conditions between them are obtained in the following form:
— the upper face $(-1/2 \leqslant \eta \leqslant -\chi_c/2)$

$$f_d^{(uf)}(\eta) = -C_f + \frac{1}{24}(3 - 4\eta^2)\eta \tag{2.16}$$

— the core $(-\chi_c/2 \leqslant \eta \leqslant \chi_c/2)$

$$f_d^{(c)}(\eta) = \int \frac{\overline{Q}_z^{(c)}(\eta)}{f_e(\eta)}\, d\eta \tag{2.17}$$

— the lower face $(\chi_c/2 \leqslant \eta \leqslant 1/2)$

$$f_d^{(uf)}(\eta) = C_f + \frac{1}{24}(3 - 4\eta^2)\eta \tag{2.18}$$

where the dimensionless coefficient

$$C_f = -\frac{1}{48}(3 - \chi_c^2)\chi_c + \int_0^{\chi_c/2} \frac{\overline{Q}_z^{(c)}(\eta)}{f_e(\eta)}\, d\eta \tag{2.19}$$

The graph of dimensionless functions in Eqs. (2.2), (2.3) and (2.4) of the variation of Young's modulus and the shape of deformation of the planar cross section of an exemplary beam ($\chi_c = 4/5$, $e_c = 1/30$, $n = 7$), taking into account functions Eqs. (2.16), (2.17) and (2.8), is shown in Fig. 4.

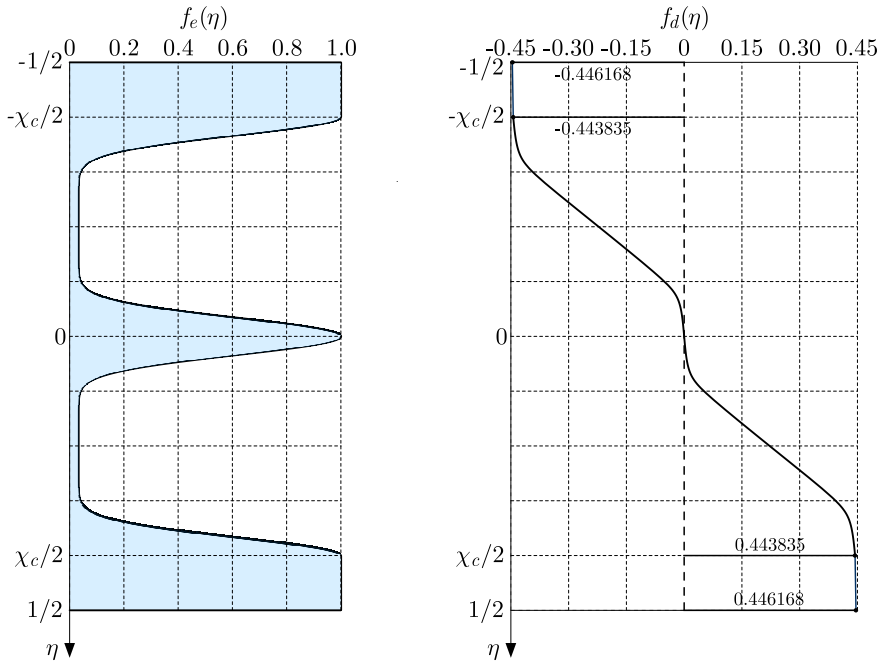

Fig. 4. The graph of dimensionless functions of Young's modulus variation and the shape of deformation of the planar cross section of the exemplary beam

3. Analytical bending study of the sandwich beam

The elastic strain energy is described as

$$U_e = \frac{1}{2}E_f bh \int_0^L \Big[\Phi_{\varepsilon,\gamma}^{(uf)}(x) + \Phi_{\varepsilon,\gamma}^{(c)}(x) + \Phi_{\varepsilon,\gamma}^{(lf)}(x)\Big]\, dx \tag{3.1}$$

where

$$\Phi_{\varepsilon,\gamma}^{(uf)}(x) = \int_{-1/2}^{-\chi_c/2} \Big\{ \big[\varepsilon_x^{(uf)}(x,\eta)\big]^2 + \frac{1}{2(1+\nu)}\big[\gamma_{xy}^{(uf)}(x,\eta)\big]^2 \Big\}\, d\eta$$

$$\Phi_{\varepsilon,\gamma}^{(c)}(x) = \int_{-\chi_c/2}^{\chi_c/2} \Big\{ \big[\varepsilon_x^{(c)}(x,\eta)\big]^2 + \frac{1}{2(1+\nu)}\big[\gamma_{xy}^{(c)}(x,\eta)\big]^2 \Big\} f_e(\eta)\, d\eta$$

$$\Phi_{\varepsilon,\gamma}^{(lf)}(x) = \int_{\chi_c/2}^{1/2} \Big\{ \big[\varepsilon_x^{(lf)}(x,\eta)\big]^2 + \frac{1}{2(1+\nu)}\big[\gamma_{xy}^{(lf)}(x,\eta)\big]^2 \Big\}\, d\eta$$

Substituting expressions in Eqs. $(2.8)_{1,3}$, $(2.9)_{1,2}$, $(2.10)_{1,2}$ for strains into Eq. (3.1), after integration, one obtains

$$U_e = \frac{1}{24}E_f bh^3 \int_0^L \Big[C_{vv}\Big(\frac{d^2v}{dx^2}\Big)^2 - 2C_{v\psi}\frac{d^2v}{dx^2}\frac{d\psi_f}{dx} + C_{\psi\psi}\Big(\frac{d\psi_f}{dx}\Big)^2 + C_\psi\frac{\psi_f(x)^2}{h^2}\Big]\, dx \tag{3.2}$$

where the dimensionless coefficients

$$C_{vv} = 1 - \chi_c^3 + 12J_{vv} \qquad C_{v\psi} = 3(1-\chi_c^2)C_f + \frac{1}{40}(4 - 5\chi_c^3 + \chi_c^5) + 12J_{v\psi}$$

$$C_{\psi\psi} = \frac{1}{672}\Big\{84[96(1-\chi_c)C_f + 5 - 6\chi_c^2 + \chi_c^4]C_f + \frac{1}{10}(68 - 105\chi_c^3 + 42\chi_c^5 - 5\chi_c^7)\Big\} + 12J_{\psi\psi}$$

$$C_\psi = \frac{1}{2(1+\nu)}\Big[\frac{1}{80}(8 - 15\chi_c + 10\chi_c^3 - 3\chi_c^5) + 12J_\psi\Big]$$

$$J_{vv} = \int_{-\chi_c/2}^{\chi_c/2} \eta^2 f_e(\eta)\, d\eta \qquad J_{v\psi} = \int_{-\chi_c/2}^{\chi_c/2} \eta f_d^{(c)}(\eta) f_e(\eta)\, d\eta$$

$$J_{\psi\psi} = \int_{-\chi_c/2}^{\chi_c/2} [f_d^{(c)}(\eta)]^2 f_e(\eta)\, d\eta \qquad J_\psi = \int_{-\chi_c/2}^{\chi_c/2} \Big(\frac{df_d^{(c)}}{d\eta}\Big)^2 f_e(\eta)\, d\eta$$

The work of the load is in the form

$$W = \int_0^L qv(x)\, dx \tag{3.3}$$

Based on the principle of stationary total potential energy $\delta(U_e - W) = 0$, the system of two differential equations of equilibrium of this sandwich beam is obtained in the following form

$$C_{vv}\frac{d^4v}{dx^4} - C_{v\psi}\frac{d^3\psi_f}{dx^3} = \frac{q}{E_f bh^3} \qquad C_{v\psi}\frac{d^3v}{dx^3} - C_{\psi\psi}\frac{d^2\psi_f}{dx^2} + C_\psi\frac{\psi_f(x)}{h^2} = 0 \tag{3.4}$$

The fourth-order expression, Eq. $(3.4)_1$, of this system is equivalent to the second-order equation of the form

$$C_{vv}\frac{d^2v}{dx^2} - C_{v\psi}\frac{d\psi_f}{dx} = -\frac{M_b(x)}{E_f b h^3} \tag{3.5}$$

where $M_b(x)$ is the bending moment. Thus, Eqs. (3.5) and $(3.4)_2$ are the governing equations of the sandwich beam. These two equations, after a simple transformation, are reduced to one equation in the form

$$\frac{d^2\psi_f}{d\xi^2} - (\alpha\lambda)^2\psi_f(\xi) = -\frac{C_{v\psi}}{C_{vv}C_{\psi\psi} - C_{v\psi}^2}\lambda^2\frac{T(\xi)}{E_f b h} \tag{3.6}$$

where: $\xi = x/L$ – dimensionless coordinate, $\lambda = L/h$ – relative length of the beam, and

$$\alpha = \sqrt{\frac{C_{vv}C_{\psi}}{C_{vv}C_{\psi\psi} - C_{v\psi}^2}}$$

is a dimensionless coefficient. The end part of this beam with a uniformly distributed load and reactions is shown in Fig. 5.

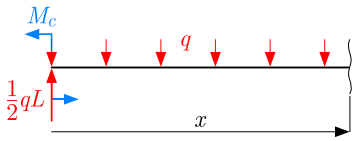

Fig. 5. Scheme of the beam end part with the load end reactions

The bending moment and the shear force according to this scheme, in the dimensionless coordinate ξ, are as follows

$$M_b(\xi) = \frac{1}{2}(\xi - \xi^2 - 2\overline{M}_c)qL^2 \qquad T(\xi) = \frac{1}{2}(1 - 2\xi)qL \tag{3.7}$$

where $\overline{M}_c = M_c/(qL^2)$ is the unknown dimensionless reactive moment. Therefore, Eq. (3.6), taking into account the transverse shear force in Eq. $(3.7)_2$, is of the form

$$\frac{d^2\psi_f}{d\xi^2} - (\alpha\lambda)^2\psi_f(\xi) = -6\frac{C_{v\psi}}{C_{vv}C_{\psi\psi} - C_{v\psi}^2}\lambda^3(1 - 2\xi^2)\frac{q}{E_f b} \tag{3.8}$$

The solution of this equation is as follows

$$\psi_f(\xi) = [C_1\sinh(\alpha\lambda\xi) + C_2\cosh(\alpha\lambda\xi) + C_0(1 - 2\xi)]\frac{q}{E_f b} \tag{3.9}$$

where C_1, C_2 are integration constants, and

$$C_0 = 6\frac{C_{v\psi}}{C_{vv}C_{\psi}}\lambda$$

Taking into account the two conditions: $\psi_f(0) = 0$ – clamped end, and $\psi_f(1/2) = 0$ – the symmetry plane of the beam, these constants are as follows $C_1 = C_0/\tanh(\alpha\lambda/2)$ and $C_2 = -C_0$. Consequently, the function in Eq. (3.9), that is, the shear effect function is in the following form

$$\psi_f(\xi) = \overline{\psi}_f(\xi)\frac{q}{E_f b} \tag{3.10}$$

where

$$\overline{\psi}_f(\xi) = 6\Big\{1 - 2\xi - \frac{\sinh[\alpha\lambda(1-2\xi)/2]}{\sinh(\alpha\lambda)/2}\Big\}\frac{C_{v\psi}}{C_{vv}C_{\psi}}\lambda \tag{3.11}$$

Equation (3.5) in the dimensionless coordinate, with consideration of the expressions in Eqs. (3.7) and (3.10), is as follows

$$\frac{d^2\overline{v}}{d\xi^2} = \Big[\frac{C_{v\psi}}{\lambda^3}\frac{d\overline{\psi}_f}{d\xi} - 6(\xi - \xi^2 - 2\overline{M}_c)\Big]\frac{\lambda^3}{C_{vv}}\frac{q}{E_f b} \tag{3.12}$$

where $\overline{v}(\xi) = v(\xi)/L$ is the relative deflection of the beam. Integrating this equation and taking into account the boundary condition $d\overline{v}/d\xi\big|_0 = 0$ – clamped end, and $d\overline{v}/d\xi\big|_{1/2} = 0$ – symmetry plane of the beam, one obtains

$$\frac{d\overline{v}}{d\xi} = \Big[\frac{C_{v\psi}}{\lambda^3}\overline{\psi}_f(\xi) - 6\Big(\frac{1}{2}\xi^2 - \frac{1}{3}\xi^3 - 2\overline{M}_c\xi\Big)\Big]\frac{\lambda^3}{C_{vv}}\frac{q}{E_f b} \tag{3.13}$$

where: $\overline{M}_c = 1/12$. Thus, integrating this equation and taking into account the boundary condition $\overline{v}(0) = 0$ and the function in Eq. (3.11), one obtains the relative deflection-bending line of the beam

$$\overline{v}(\xi) = \overline{v}(\xi)\frac{q}{E_f b} \tag{3.14}$$

where

$$\begin{aligned}\overline{v}(\xi) &= \Big[6f_{\psi}(\xi)\frac{C_{v\psi}^2}{C_{vv}C_{\psi}}\frac{1}{\lambda^2} - \frac{1}{2}(2\xi - \xi^2 - 1)\xi^2\Big]\frac{\lambda^3}{C_{vv}}\\ f_{\psi}(\xi) &= \xi - \xi^2 - \frac{\cosh(\alpha\lambda/2) - \cosh[(\alpha\lambda(1-2\xi)/2]}{\alpha\lambda\sinh(\alpha\lambda/2)}\end{aligned} \tag{3.15}$$

Consequently, the relative maximum deflection

$$\overline{v}_{max} = \overline{v}\Big(\frac{1}{2}\Big) = \overline{v}_{max}\frac{q}{E_f b} \tag{3.16}$$

where the dimensionless maximum deflection

$$\overline{v}_{max} = \overline{v}\Big(\frac{1}{2}\Big) = (1 + C_{se})\frac{\lambda}{32C_{vv}} \tag{3.17}$$

and the shear coefficient

$$C_{se} = 48\Big[1 - 4\frac{\cosh(\alpha\lambda/2)}{\alpha\lambda\sinh(\alpha\lambda/2)}\Big]\frac{C_{v\psi}^2}{C_{vv}C_{\psi}}\frac{1}{\lambda^2} \tag{3.18}$$

The shear stresses described by Eqs. (2.8), (2.9) and (2.10), with consideration of Eqs. (2.16), (2.17) and (2.18), in successive layers, are as follows:
— the upper face $(-1/2 \leqslant \eta \leqslant -\chi_c/2)$

$$\tau_{xy}^{(uf)}(x,\eta) = \overline{\tau}_{xy}^{(uf)}(x,\eta)\frac{q}{b} \tag{3.19}$$

where, the dimensionless stress

$$\overline{\tau}_{xy}^{(uf)}(x,\eta) = \frac{1}{2(1+\nu)}\overline{Q}_z^{(uf)}\overline{\psi}_f(x) \tag{3.20}$$

— the core $(-\chi_c/2 \leqslant \eta \leqslant \chi_c/2)$

$$\overline{\tau}_{xy}^{(c)}(x,\eta) = \frac{1}{2(1+\nu)}\overline{Q}_z^{(c)}\overline{\psi}_f(x) \tag{3.21}$$

— the lower face $(\chi_c/2 \leqslant \eta \leqslant 1/2)$

$$\overline{\tau}_{xy}^{(lf)}(x,\eta) = \frac{1}{2(1+\nu)}\overline{Q}_z^{(lf)}\overline{\psi}_f(x) \tag{3.22}$$

Exemplary calculations are carried out for a beam family of the following selected dimensionless sizes and material constants: $\lambda = 30$, $\chi_c = 4/5$, $e_c = 1/30$, $\nu = 0.3$, as well as the exponent – natural number $n = 0, 2, 7, 14, 25, \to \infty$. The graphs of the dimensionless functions given in Eqs. (2.2), (2.3) and (2.4) of Young's modulus variation and the dimensionless shear stresses in Eqs. (3.20), (3.21) and (3.22) in the beam cross section for $\xi = 0.1$, and the exponent value $n = 7, \to \infty$ are shown in Figs. 6a and 6b. The maximum shear stress $\overline{\tau}_{max}(\xi) = \overline{\tau}_{xy}^{(c)}(\xi, 0)$ occurs at the neutral surface $(\eta = 0)$ in the core.

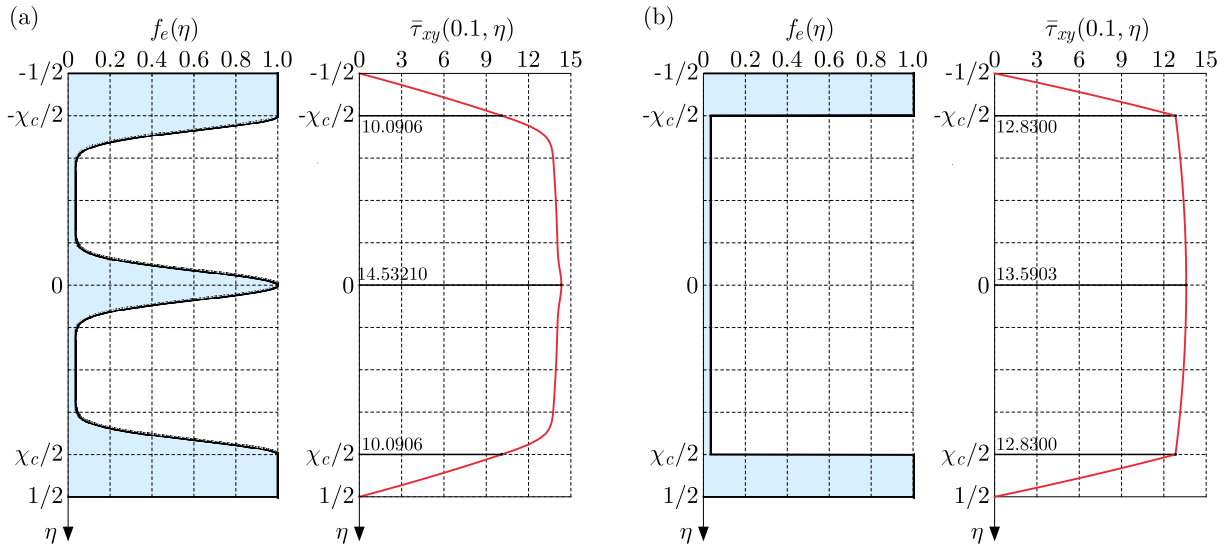

Fig. 6. The graph of dimensionless functions of Young's modulus variation and the dimensionless shear stress: (a) for $n = 7$ and (b) classical sandwich beam for $n \to \infty$

The results of analytical calculations of the dimensionless coefficient C_{vv}, maximum dimensionless shear stresses, shear coefficient C_{se}, Eq. (3.18), and dimensionless maximum deflection $\overline{v}_{max}$, Eq. (3.17), are specified in Table 1.

Table 1. The value of coefficients, shear stresses and maximum deflections – analytical calculations

	n					
	0	2	7	14	25	∞
C_{vv}	1.0	0.73063	0.64218	0.60630	0.58281	0.505067
$\overline{\tau}_{max}$	18.0000	15.1103	14.3210	14.0761	13.9253	13.5903
C_{se}	0.01376	0.09186	0.13953	0.15146	0.15996	0.17078
$\overline{v}_{max}$	855.4	1260.9	1497.2	1604.8	1679.4	1955.9

Moreover, the graphs of maximum dimensionless shear stresses $\overline{\tau}_{max}$ and maximum deflections $\overline{v}_{max}$ are shown in Figs. 7a and 7b.

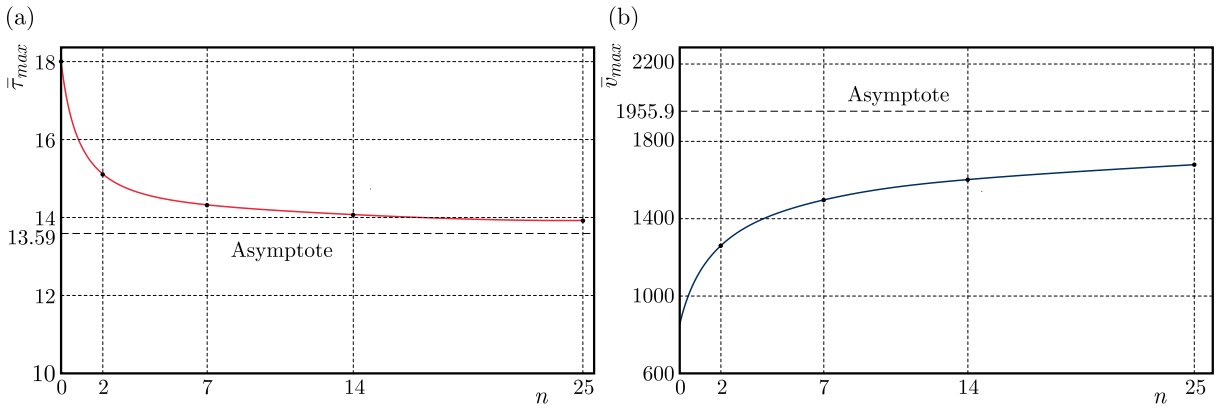

Fig. 7. The graph of (a) the maximum dimensionless shear stresses $\overline{\tau}_{max}$ and (b) the maximum dimensionless deflections $\overline{v}_{max}$

4. Numerical FEM bending study of the sandwich beam

The numerical model of the family of selected beams with the same parameters as in the analytical study is developed in the Ansys 2021 R2 system and is examinef in linear static structural analysis. The following parameters are applied in the study: $E_f = 70\,\text{GPa}$, $b = 50\,\text{mm}$, $h = 50\,\text{mm}$, thus $L = 1500\,\text{mm}$ ($\lambda = 1/30$).

Due to symmetry of the geometry, load and mechanical parameters, only a quarter of the beam is considered. The symmetric boundary conditions are applied by restricting the normal displacements at the selected faces shown in Fig. 8a. The clamped boundary condition is imposed on the face of the free end of the beam in the following manner. Displacements along the y-axis are blocked referring to the remote point located in the centre of the coordinate system ($v = 0$). In addition, the translations towards the x-axis are restrained globally ($u = 0$) on the same face. Such a boundary condition is consistent with analytical study and also allows deformations of the face at the end of the beam in the y and z directions, which ensures no stress concentration phenomenon. The force $F_y = 1\,\text{kN}$ is applied to the top of the quarter of the model, which corresponds to the uniformly distributed load (Fig. 1) of $q = 8/3\,\text{N/mm}$.

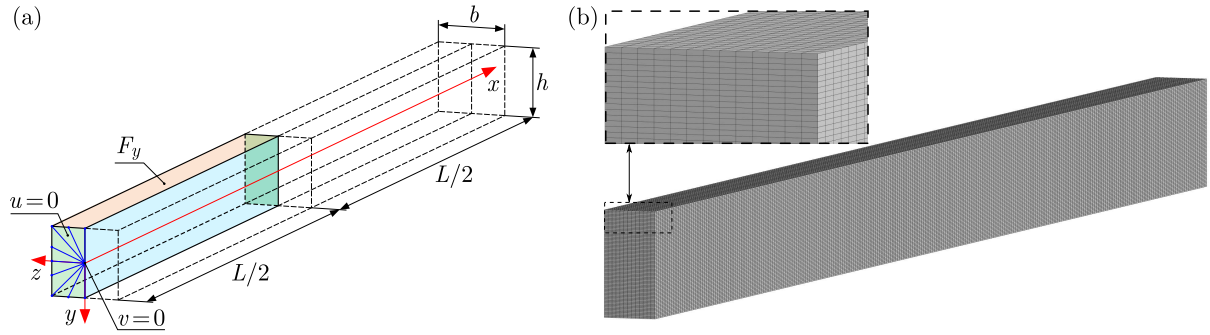

Fig. 8. (a) Geometry and boundary conditions in finite element analysis. (b) Numerical FEM model of the sandwich beam

The geometry is divided into uniform second-order hexahedral SOLID186 finite elements with twenty nodes and three degrees of freedom at each node (Fig. 8b). A sufficient number of finite elements is found through mesh convergence study with the accuracy criterion imposed on the maximum deflection, shear stress, and elastic strain energy. Such an analysis is carried out assuming the greatest gradient of Young's modulus except for $n \to \infty$, that is, for $n = 25$. The finite element model consists of over 1.3 million nodes and 312 thousand elements, assuming there are 300, 80 and 13 elements along x, y and z directions (Fig. 8a), respectively. The ratio

of the number of elements to the model size is highest along the depth of the beam (y-axis) due to the variable mechanical property towards this direction.

The mechanical properties of the material are coherent with analytical study, i.e. isotropic, perfectly elastic, where Young's modulus is described by the function in Eqs. (2.1) and (2.3). At any point of the geometry, the calculated values of Young's modulus are mapped to the centres of hexahedral finite elements. An exemplary distribution of Young's modulus for $n = 2$ is shown in Fig. 9.

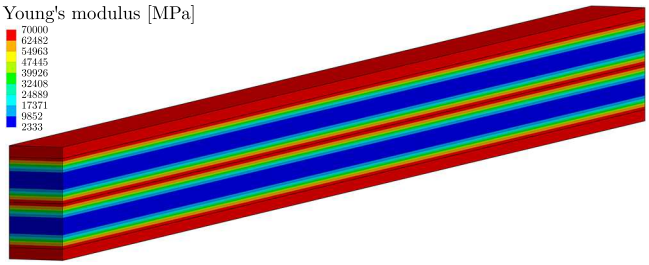

Fig. 9. Young's modulus E distribution for $n = 2$

The deflections v obtained for this case, i.e. displacements toward the y-axis, are shown in Fig. 10a. Following the analytical study, the shear stress is studied for $\xi = x/L = 0.1$. In that case, the surface at $x = 150\,\text{mm}$ parallel to the yz plane is considered as presented in Fig. 10b.

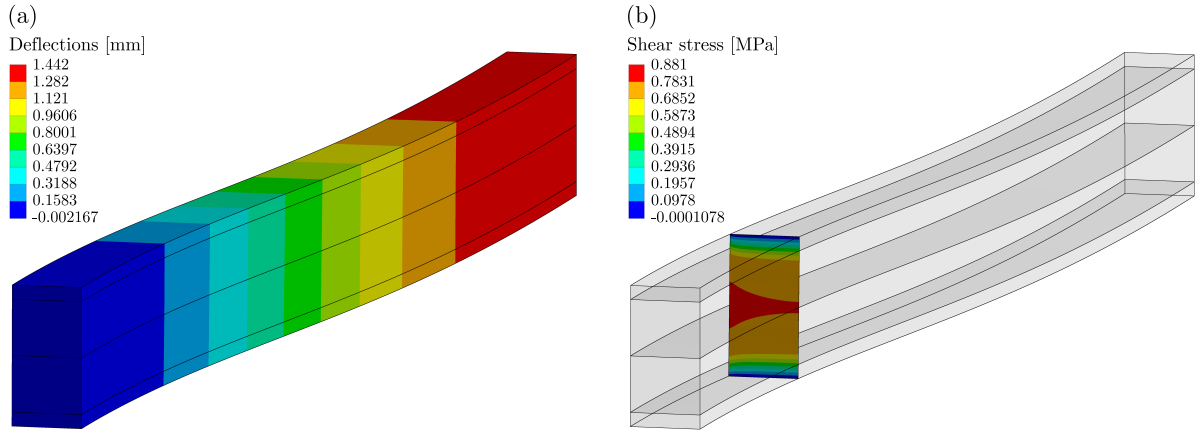

Fig. 10. (a) Deflections $v(x)$ for $n = 2$. (b) Shear stress τ_{xy} in the surface parallel to yz plane at $x = 150\,mm$ ($\xi = x/L = 0.1$) for $n = 2$

The results of the numerical study are further compared with the analytical solutions. It should be noted that in the case of a three-dimensional finite element model, the shear stress τ_{xy} varies along the width of the beam (Fig. 10b). To study the results, the mean of that function along width is considered. The maximum deflection v_{max} in FEM analyses are taken from the neutral surface for $z = 0$. To maintain consistency with the analytical study, the obtained results are further considered in a dimensionless form, that is

$$\overline{v}_{max} = \frac{E_f b}{qL} v_{max} \qquad \overline{\tau}_{max} = \frac{b}{q} \tau_{max} \tag{4.1}$$

Exemplary distributions of shear stress along the depth of the beam described by the dimensionless parameter η and corresponding dimensionless functions of Young's modulus are presented in Figs. 11a and 11b. These show a near-perfect agreement with the analytical outcomes shown in Figs. 6a and 5b.

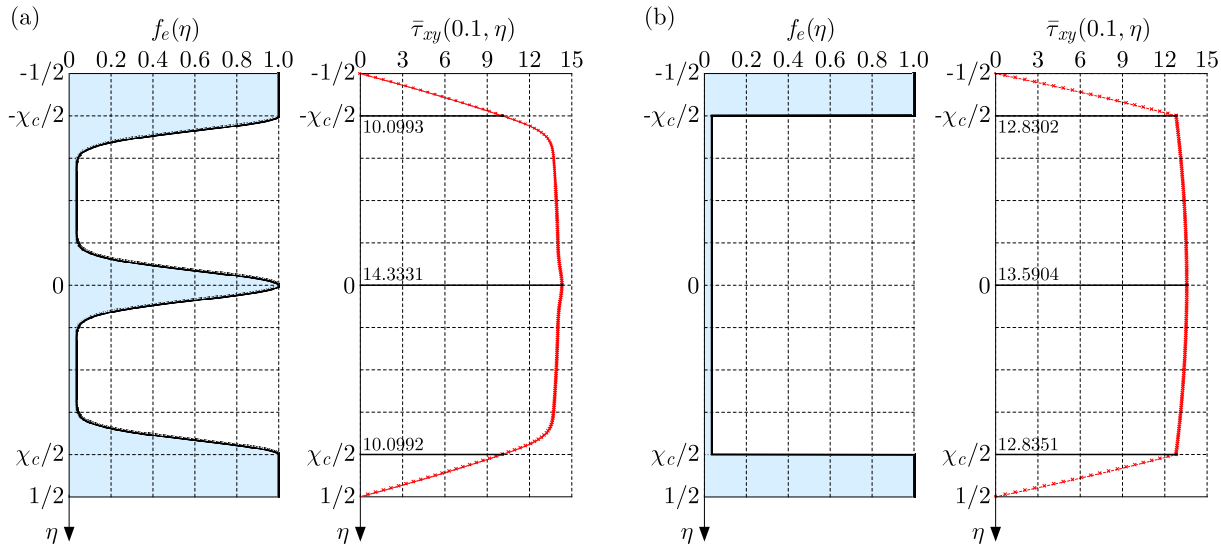

Fig. 11. The graph of dimensionless functions of Young's modulus variation and dimensionless shear stress (a) for $n = 7$ and (b) for $n \to \infty$ from the numerical study

The numerically obtained maxima of shear stress $\overline{\tau}_{max}$ and deflections $\overline{v}_{max}$ for all the values considered of the parameter n are summarised in Table 2 in a dimensionless form. When comparing the dimensionless maximum shear stresses and deflections calculated analytically and numerically (Tables 1 and 2), it is easy to notice that the differences between them are insignificant, less than 0.1%.

Table 2. The maximum shear stresses and deflections – numerical FEM analysis

	n					
	0	2	7	14	25	∞
$\overline{\tau}_{max}$	18.0023	15.1169	14.3331	14.0808	13.9379	13.5904
$\overline{v}_{max}$	854.9	1261.0	1497.7	1605.6	1680.4	1956.9

5. Conclusions

Most of the papers investigating the problem of the shear effect in beams refer to numerical methods or analytical studies, whereas the deformation function is assumed in advance within the number of theories mentioned in the literature review. The choice of the deformation function can have a direct effect on the accuracy of the solution. In the present paper, a linear theory with the assumption of nonlinear shear deformation is developed and applied taking into account the classical shear stress formula for beams. Unlike the number of theories and papers, the shear deformation function is the result of an analytical solution, which leads to an exceptionally coherent solution compared to the FEM study.

The generalised form of the function that describes Young's modulus allowed us to analyse beams with various mechanical properties, including homogeneous and layered beams within the proposed theory. Using the principle of stationary potential energy, two differential equations of equilibrium were derived and then solved. Relative deflections and shear stresses were calculated for exemplary beams with different variations in Young's modulus.

To verify the accuracy of the developed theory, the outcome of the analytical study was compared with the results of numerical FEM analysis in the Ansys system. The beam was

modelled as a three-layered structure, while its core had a variable Young's modulus along its depth.

Following the results in Figs. 6 and 12, both analytical and numerical analyses yielded consistent shear stress distributions for all exemplary structures. Comparison of the maximum relative deflection and maximum relative shear stress shown in Tables 1 and 2 shows a nearly identical result from both methods. The relative differences between these are less than 0.1%, proving that the theory developed is accurate. Having in mind the fact that it is suitable for beams with different Young's modulus distributions, i.e. homogenous and nonhomogeneous, it can be applied to numerous practical analyses of composite structures.

Acknowledgement

The paper is developed based on the scientific activity of the Łukasiewicz Research Network – Poznan Institute of Technology, Rail Vehicles Center, and the statutory activity of the Poznan University of Technology, funded by the Ministry of Science and Higher Education in Poland (grant No. 0612/SBAD/3605).

References

1. Banat D., Mania R.J., 2017, Failure assessment of thin-walled FML profiles during buckling and postbuckling response, *Composites Part B: Engineering*, **112**, 278-289
2. Berdichevsky V.L., 2010, An asymptotic theory of sandwich plates, *International Journal of Engineering Science*, **48**, 3, 383-404
3. Birman V., Kardomateas G.A., 2018, Review of current trends in research and applications of sandwich structures, *Composites Part B: Engineering*, **142**, 221-240
4. Carrera E., Giunta G., Petrolo M., 2011, *Beam Structures, Classical and Advanced Theories*, John Wiley & Sons
5. Dhuria M., Grover N., Goyal K., 2021, Influence of porosity distribution on static and buckling responses of porous functionally graded plates, *Structures*, **34**, 1458-1474
6. Domagalski Ł., Jędrysiak J., 2016, Geometrically nonlinear vibrations of slender meso-periodic beams. The tolerance modeling approach, *Composite Structures*, **136**, 270-277
7. Ghayesh M.H., 2018, Vibration analysis of shear-deformable AFG imperfect beams, *Composite Structures*, **200**, 910-920
8. Huang S.J., 2003, An analytical method for calculating the stress and strain in adhesive layers in sandwich beams, *Composite Structures*, **60**, 1, 105-114
9. Jędrysiak J., 2023, Theoretical tolerance modelling of dynamics and stability for axially functionally graded (AFG) beams, *Materials*, **16**, 5, 2096
10. Kolakowski Z., Mania R.J., 2015, Dynamic response of thin FG plates with a static unsymmetrical stable postbuckling path, *Thin-Walled Structures*, **86**, 10-17
11. Kumar R., Lal A., Singh B.N., Singh J., 2019, New transverse shear deformation theory for bending analysis of FGM plate under patch load, *Composite Structures*, **208**, 91-100
12. Magnucki K., 2022, An individual shear deformation theory of beams with consideration of the Zhuravsky shear stress formula, *Current Perspectives and New Directions in Mechanics, Modelling and Design of Structural Systems*, 682-689
13. Magnucki K., Lewinski J., Magnucka-Blandzi E., 2020, A shear deformation theory of beams of bisymmetrical cross sections based on the Zhuravsky shear stress formula, *Engineering Transactions*, **68**, 4, 353-370
14. Magnucki K., Magnucka-Blandzi E., Wittenbeck L., 2022, Bending of a generalized circular sandwich plate under a concentrated force with consideration of a nonlinear shear deformation theory, *Archives of Mechanics*, **74**, 267-282

15. Mahi A., Adda Bedia E.A., Tounsi A., 2015, A new hyperbolic shear deformation theory for bending and free vibration analysis of isotropic, functionally graded, sandwich and laminated composite plates, *Applied Mathematical Modelling*, **39**, 9, 2489-2508

16. Mantari J.L., Oktem A.S., Guedes Soares C., 2012, A new higher order shear deformation theory for sandwich and composite laminated plates, *Composites Part B: Engineering*, **43**, 3, 1489-1499

17. Marczak J., Jędrysiak J., 2015, Tolerance modelling of vibrations of periodic three-layered plates with inert core, *Composite Structures*, **134**, 854-861

18. Meiche N.E., Tounsi A., Ziane N., Mechab I., Adda Bedia E.A., 2011, A new hyperbolic shear deformation theory for buckling and vibration of functionally graded sandwich plate, *International Journal of Mechanical Sciences*, **53**, 4, 237-247

19. Özütok A., Madenci E., 2017, Static analysis of laminated composite beams based on higher-order shear deformation theory by using mixed-type finite element method, *International Journal of Mechanical Sciences*, **130**, 234-243

20. Pei Y.L., Geng P.S., Li L.X., 2018, A modified higher-order theory for FG beams, *European Journal of Mechanics – A/Solids*, **72**, 186-197

21. Reddy J.N., 2004, *Mechanics of Laminated Composite Plates and Shells: Theory and Analysis*, CRC Press

22. Sahoo R., Singh B.N., 2013, A new shear deformation theory for the static analysis of laminated composite and sandwich plates, *International Journal of Mechanical Sciences*, **75**, 324-336

23. Thai H.-T., Vo T.P., 2013, A new sinusoidal shear deformation theory for bending, buckling, and vibration of functionally graded plates, *Applied Mathematical Modelling*, **37**, 5, 3269-3281

24. Zenkour A.M., 2006, Generalized shear deformation theory for bending analysis of functionally graded plates, *Applied Mathematical Modelling*, **30**, 1, 67-84

25. Żur K.M., Arefi M., Kim J., Reddy J.N., 2020, Free vibration and buckling analyses of magneto-electro-elastic FGM nanoplates based on nonlocal modified higher-order sinusoidal shear deformation theory, *Composites Part B: Engineering*, **182**, 107601

Manuscript received August 3, 2023; accepted for print September 12, 2023

JOURNAL OF THEORETICAL AND APPLIED MECHANICS
62, 1, pp. 19-30, Warsaw 2024
https://doi.org/10.15632/jtam-pl/174870

ULTRAHIGH FREQUENCY VIBRATION CONTROL IN A PIEZOELECTRIC PHONONIC CRYSTAL BEAM AT THE NANOSCALE CONSIDERING SURFACE EFFECTS

Zexin Zhang, Denghui Qian

School of Naval Architecture and Ocean Engineering, Jiangsu University of Science and Technology, Zhenjiang, China

corresponding author Denghui Qian: e-mail: dhqian@just.edu.cn

Long Ren, Qi Wang

China Nanhu Academy of Electronics and Information Technology, Jiaxing, China

In this paper, a piezoelectric phononic crystal beam at the nanoscale has been mechanically modeled by using the surface piezoelectric theory. The band gap has been calculated by the plane wave expansion method and the band gap structure picture has been analyzed. The influence of electromechanical coupling effects, surface effects and geometry on the band gap properties are discussed separately. This study contributes positively to the design and active control of nanoelectromechanical systems.

Keywords: phononic crystal, nanobeam, surface effects, electromechanical coupling effects

1. Introduction

In 1992, M.M. Sigalas and E.N. Economou first confirmed theoretically that the three--dimensional periodic lattice structure formed by filling a certain matrix material in a spherical scatterer has characteristics of an elastic wave/acoustic wave band gap. Compared with the electromagnetic wave band gap of a photonic crystal, they defined a concept of an elastic wave/acoustic wave band gap phononic crystal (Sigalas and Economou, 1992). Due to its band gap, defect state and other characteristics, scholars have carried out extensive research on phononic crystals in the fields of ship and ocean, aerospace engineering and construction (Yin *et al.*, 2022), such as low-frequency vibration isolation/sound insulation/absorption (Chu *et al.*, 2023; Zou *et al.*, 2023; Zuo *et al.*, 2022), subwavelength acoustic focusing (Yang *et al.*, 2022; Yao *et al.*, 2021), acoustic/elastic wave cloak design (Ghoreshi and Bahrami, 2022), ultrahigh frequency resonators (Yao *et al.*, 2021), wave filters (Lee *et al.*, 2023), etc.

In recent years, scholars have done a lot of research between phononic crystal band gap regulation and metamaterial design, such as introducing other physical fields (magnetic field, electric field, temperature, etc.) to regulate the nature of the phononic band gap, which can realize dynamic control of acoustic waves, such as piezomagnetic phononic crystals, piezoelectric phononic crystals, magneto-electroelastic phononic crystals and so on (Qian *et al.*, 2022). Among them, piezoelectric materials as functional materials, such as piezoelectric ceramics, piezoelectric crystals and piezoelectric polymers, have characteristics of a fast response, more flexible and intelligent, and its principle is mutual conversion between mechanical energy and electrical energy, which can be used to actively regulate the band gap by an electric field, and it is widely used in the fabrication of electromechanical transducers and acoustic devices with acoustic-electric effects. The main types of piezoelectric phononic crystals are single, embedded piezoelectric/elastic composite, and externally attached piezoelectric film/elastic structure composite type.

The above phononic crystals are all studied under the macroscopic scale size, with continuous development of nano-preparation technology. The study of the structure of materials with nanoscale size tends to be popular, and a number of works on the study of the structure of nano-phononic crystals emerged (Chen *et al.*, 2017; Huang and Yu, 2006; Yan and Jiang, 2011; Zhen *et al.*, 2012). The band gap of phononic crystals has also been shifted from hertz (Hz), megahertz (MHz) to gigahertz (GHz), and terahertz (THz).

Nanomaterials exhibit several unique effects due to their small size and specific properties. These effects include the surface effect, small size effect, quantum size effect, and macro quantum tunneling effect (Du *et al.*, 2000). The classical continuum theory in the macro scale mechanical model falls short in accurate describing the behavior of nanomaterials due to size-dependent effects observed in them.

However, many scholars have modified the classical mechanics theory and proposed higher-order theories, such as: micropolar theory (Surana *et al.*, 2017), nonlocal elastic continuum theory (Eringen and Edelen, 1972), surface elasticity theory (Gurtin *et al.*, 1998), strain gradient theory (Aifantis, 1999), and modified coupled stress theory (Yang *et al.*, 2002). The surface/interface of nanostructured scatterers has different elastic characteristics from the internal bulk material. Gurtin and Murdoch (1975) established a surface/interface elastic model which abstracts the surface/interface into a thickness-independent elastic film that is intimately bound to the internal material and does not slip. The theoretical model can be used to analyze the surface/interface effect of nanostructured scatterers.

For piezoelectric nanomaterials, the traditional surface elastic model has some limitations. Piezoelectric nanomaterials exhibit surface piezoelectric and dielectric effects, which are key factors overlooked by traditional surface elastic models. To address these limitations, Huang and Yu (2006) proposed a surface piezoelectric model that incorporates the effects of surface piezoelectricity, elasticity, and dielectricity. Their approach to this model allowed for an examination of the stress and charge response pertaining to the surface piezoelectric effect in piezoelectric rings. Notably, the outcomes of their investigation unveiled the substantial influence of surface piezoelectricity on electromechanical characteristics of piezoelectric nanostructures.

Moreover, vibration and buckling characteristics of piezoelectric nanobeams were explored by Yan and Jiang (2011), taking into account the influence of surface effects. Their research underscored the paramount role of surface residual stress and surface piezoelectricity, which revealed a substantial influence over the resonant frequency and critical buckling potential. In comparison, the impact of surface elasticity was comparatively less significant. This implies that the surface piezoelectric effect and surface residual stress should be carefully considered in the design and analysis of nanoscale piezoelectric structures.

Overall, these studies provide a valuable theoretical support for the application of nanoscale piezoelectric materials. By considering the surface piezoelectric, surface elastic, and surface dielectric effects, researchers can gain a more comprehensive understanding of the electromechanical behavior of piezoelectric nanomaterials and optimize their performance in various applications.

In recent years, researchers have made a significant progress in the development of calculation methods to analyze the band gap structure of phononic crystals. At present, the commonly used methods are: plane wave expansion method (PWE) (Zuo *et al.*, 2022), lumped mass method (Kong *et al.*, 2023), finite difference time domain (FDTD) method (Cao *et al.*, 2004), finite element method (FEM) (Lu *et al.*, 2022). As a mature method for numerical simulation of mechanical systems, the finite element method has a worked well with periodic structures and has also been successfully applied to the calculation of one-, two- and three-dimensional structures. However, it produces a large number of node degrees of freedom, which increases the computation amount and requires huge cost. The calculation amount of PWE is much smaller than that of FEM, and its calculation results have also been verified to be consistent with FEM (Qian and

Shi, 2017). The PWE method transforms the band structure calculation into the solution of a generalized eigenvalue problem by expanding the material and displacement field of the periodic structure into Fourier series and combining the Bloch theorem.

In this paper, a mechanical model of a circular cross-section piezoelectric phononic crystal nanobeam is proposed by considering the surface effect. Through a combination of PWE, Euler-Bernoulli beam theory and surface elasticity theory, the control equation for a circular cross section phononic crystal nanobeam is obtained. It proposes a computational approach to study the band gap structure, and explores the effects of mechanical-electrical coupling, surface effect, and geometric size on the first two orders of the band gap in phononic crystals through band gap calculations and analysis of the band structure diagram.

2. Model and method

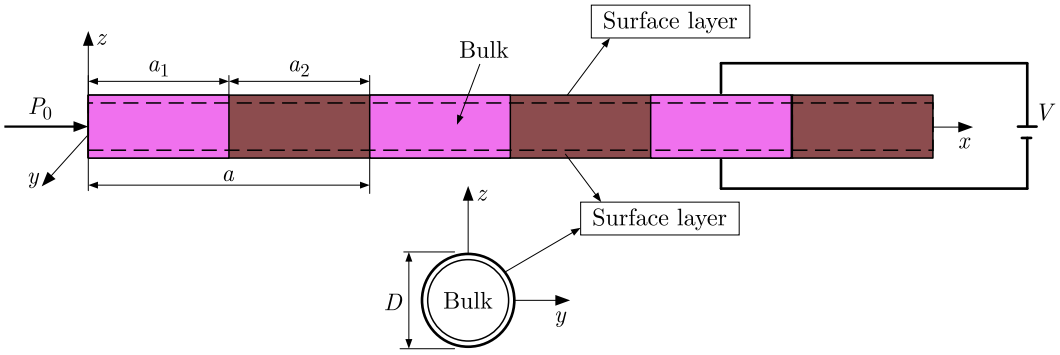

Fig. 1. A model of a piezoelectric phononic crystal nanobeam with surface effects

This paper discusses the investigation of a circular piezoelectric nanophononic crystal beam. The beam structure is composed of alternating cycles of a piezoelectric material, specifically PZT-5H, and an elastic material known as an epoxy resin. The primary focus of this study is to analyze the properties and behavior of this unique crystal beam configuration. A Cartesian coordinate system is shown in Fig. 1. The x-axis represents the axial direction, the y-axis represents the width direction, and the z-axis represents the height direction. In the crystal beam structure, an electric field V is applied to the epoxy resin. In addition, an applied axial force P_0 is considered. These external inputs introduce mechanical-electrical coupling effects into the system. The lattice parameter a has the following definition

$$a = a_1 + a_2 \tag{2.1}$$

where a_1, a_2 are sizes of the piezoelectric material PZT-5H and the elastic material epoxy resin in a cell.

In the proposed analysis, the circular cross section of the piezoelectric nano-phononic crystal beam has a diameter of D. In this particular study, material interface effects are neglected, but the surface effects are still considered and assumed to exist on the surface of the beam. To reflect these surface effects, the beam structure is divided into a surface layer and a block layer. However, the thickness of the surface layer is usually ignored, so the beam cross-section is circular.

From the Euler-Bernoulli beam theory, the axial strain ε_x and deflection $w(x,t)$ at any point in the beam are defined as

$$\varepsilon_x = -z\frac{\partial^2 w(x,t)}{\partial x^2} \tag{2.2}$$

The electric field strength E_z in the direction z is represented by the potential Φ as

$$E_z = -\frac{\partial \Phi}{\partial z} \tag{2.3}$$

The block eigenstructure equation of PZT-5H is expressed as

$$\sigma_x = c_{11}\varepsilon_x - e_{31}E_z \qquad D_z = e_{31}\varepsilon_x + \kappa_{33}E_z \tag{2.4}$$

where σ_x denotes the axial stress and D_z denotes the surface potential shift in the z-direction. c_{11}, e_{31} and κ_{33} denote the modulus of elasticity, piezoelectricity constant, and dielectric constant, respectively.

According to the potential shift boundary condition in electromagnetic theory, the normal potential shifts can be equal. In the Gurtin-Murdoch surface theory model, the surface layer potential shifts and the interface potential shifts are the same, so the PZT-5H surface layer constitutive equation can be derived:

$$\sigma_x^s = \sigma_x^0 + c_{11}^s\varepsilon_x^s - e_{31}^s E_z^s \qquad D_z^s = D_z^0 \tag{2.5}$$

where σ_x^s and σ_x^0 denote the axial surface stress and residual surface stress, respectively. D_z^s and D_z^0 denote the surface potential shift and residual surface potential shift, respectively. E_z^s denotes the surface electric field strength in the z-direction, so $E_z^s = E_z$ due to equality of the electric field strengths of the surface layer and the bulk layer. ε_x^s denotes the surface strain. c_{11}^s and e_{31}^s denote the surface Young's elastic modulus and the surface piezoelectric constant.

Disregarding the free charge, it follows from Gauss' theorem

$$\frac{\partial D_z}{\partial z} = 0 \tag{2.6}$$

Substituting Eqs. (2.2) and (2.3) into $(2.4)_2$ and (2.6)

$$\Phi = -\frac{1}{2}z^2\frac{e_{31}}{\kappa_{33}}\frac{\partial^2 w(x,t)}{\partial x^2} + zf_1(x,y) + f_2(x,y) \tag{2.7}$$

Considering the electric field boundary conditions $\Phi(-D/2) = 0$ and $\Phi(D/2) = V$, the electric potential is obtained as

$$\Phi = -\frac{e_{31}}{2\kappa_{33}}\frac{\partial^2 w(x,t)}{\partial x^2}\Big(z^2 - \frac{D^2}{4}\Big) + \frac{V}{D}z + \frac{V}{2} \tag{2.8}$$

Substituting Eq. (2.8) into (2.3), the electric field strength E_z can be expressed as

$$E_z = z\frac{e_{31}}{\kappa_{33}}\frac{\partial^2 w(x,t)}{\partial x^2} - \frac{V}{D} \tag{2.9}$$

Substituting Eqs. (2.8) and (2.9) into $(2.4)_1$ and $(2.5)_1$, the axial stresses in the PZT-5H block and surface layer can be expressed as

$$\begin{aligned} \sigma_x &= e_{31}\frac{V}{D} - \Big(c_{11} + \frac{e_{31}^2}{\kappa_{33}}\Big)z\frac{\partial^2 w(x,t)}{\partial x^2} \\ \sigma_x^s &= \sigma_x^0 + e_{31}^s\frac{V}{D} - \Big(c_{11}^s + \frac{e_{31}^s e_{31}}{\kappa_{33}}\Big)z\frac{\partial^2 w(x,t)}{\partial x^2} \end{aligned} \tag{2.10}$$

For the block part of the epoxy, the eigenstructure equation can be described as

$$\sigma_x = E\varepsilon_x \tag{2.11}$$

where E denotes the elastic modulus.

The epoxy surface layer portion of the epoxy resin, whose intrinsic formula is expressed as

$$\sigma_x^s = \sigma_x^0 + E^s \varepsilon_x^s \tag{2.12}$$

where E^S denotes the surface elastic modulus.

Substituting Eq. (2.2) into (2.11) and (2.12), the axial stress of the epoxy can be defined by bending deflection as

$$\sigma_x = -Ez\frac{\partial^2 w(x,t)}{\partial x^2} \qquad \sigma_x^s = \sigma_X^0 - E^s z\frac{\partial^2 w(x,t)}{\partial x^2} \tag{2.13}$$

All surface layer and block parameters have a certain correspondence

$$p_s \leftrightarrow l_s p_b \tag{2.14}$$

where p_s, p_b are the respective surface layer and block parameters, and l_s are the material internal parameters.

Derived from the generalized Young-Laplace equation and the corresponding formula (Yan and Jiang, 2011), the vibration control equation of the nanobeam considering surface effect can be expressed as

$$\frac{\partial^2 M}{\partial x^2} - P\frac{\partial^2 w(x,t)}{\partial x^2} - \frac{\partial}{\partial x}\int\limits_C T_x z \, dC - \int\limits_C T_z \, dC = -\rho S\frac{\partial^2 w(x,t)}{\partial t^2} \tag{2.15}$$

The corresponding parameters are shown as follows:

$$M = -\int\limits_S \sigma_x z \, dS \qquad P = P_0 + \int\limits_S \sigma_x \, dS \qquad T_x = \frac{\partial \sigma_x^s}{\partial x} \qquad T_z = \frac{\sigma_x^s}{R_c} \tag{2.16}$$

where M is the bending moment, P is the axial force, T_x and T_z are the traction jumps caused by surface stress, T_z only acts on the top and bottom of the beam. C and S represent the circumference and area of the interface, ρ is density of the material, and R_c is curvature.

For the z-direction surface tension T_z of the top and bottom surfaces of the beam, in the calculation of the circular section (Qian, 2018), it is regarded as a square section with an equal area. In this paper, it is improved: the z-axis is taken as the central axis, the left and right sweeps 45°, and the formed area is regarded as the upper and lower surface (as shown in Fig. 2). To obtain surface tension in the z-direction, integration along this boundary is performed.

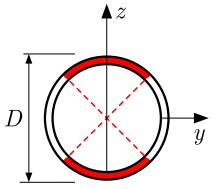

Fig. 2. Surface tension T_z integral region (red)

Substituting the above equations, the vibration control equations for piezoelectric and elastic nanobeams considering surface effects can therefore be uniformly expressed as

$$\frac{\partial^2}{\partial x^2}\left(m(x)\frac{\partial^2 w(x)}{\partial x^2}\right) - n(x)\frac{\partial^2 w(x)}{\partial x^2} = \omega^2 p(x) w(x) \tag{2.17}$$

where $m(x) = (m_1(x), m_2(x))$, $n(x) = (n_1(x), n_1(x))$, $p(x) = (p_1(x), p_2(x))$

$$\begin{aligned} &m_1(x) = \frac{\pi D^4}{64}\overline{c} + \frac{\pi D^3}{8}\overline{c}^s \qquad m_2(x) = \frac{\pi D^4}{64}E + \frac{\pi D^3}{8}E^s \\ &n_1(x) = \frac{\pi D}{4}\left(\sigma_x^0 + e_{31}^s\frac{V}{D} + 2e_{31}V\right) + P_0 \qquad n_2(x) = \frac{\pi D}{4}\sigma_x^0 + P_0 \\ &p_1(x) = \rho_1 A \qquad p_2(x) = \rho_2 A \end{aligned} \tag{2.18}$$

where $\overline{c} = c_{11} + e_{31}^2/\kappa_{33}$, $\overline{c}^s = c_{11}^s + e_{31}^s e_{31}/\kappa_{33}$, ρ_1, ρ_2 represent density of the PZT-5H and epoxy resin.

Due to the axial periodicity of the structural material, $M(x)$, $N(x)$ and $P(x)$ are all periodic functions in the x-direction, and can therefore be expanded into a Fourier series. Here, three functions can be expressed uniformly by $g(x)$

$$g(x) = \sum_G g(G) \mathrm{e}^{\mathrm{i}Gx} \tag{2.19}$$

where G is the reciprocal lattice vector and $g(G)$ is the Fourier expansion coefficient which can be defined as

$$g(G) = \begin{cases} g_A f + g_B(1-f) & \text{fox} \quad G = 0 \\ (g_A - g_B)\Upsilon(G) & \text{fox} \quad G \neq 0 \end{cases} \tag{2.20}$$

where g_A, g_B are the corresponding coefficients of the material, respectively, and $f = a_2/a$ denotes the filling ratio of the epoxy resin to the whole protocell and, in addition, $\Upsilon(G) = f \sin(Ga_2/2)/(Ga_2/2)$ is a structural function, and is only related to the shape of the scatterer epoxy resin.

Due to the periodicity of the structure and Bloch's theorem, the displacement field $w(x)$ can be decomposed as follows

$$w(x) = w_k(x) \mathrm{e}^{\mathrm{i}(kx - \omega t)} \tag{2.21}$$

where k is the Bloch wave vector confined to the first Brillouin zone. The function w_k has the same periodicity as the material parameters and can be expressed as a Fourier series

$$w_k(x) = \sum_{G'} \mathrm{e}^{\mathrm{i}G'x} w_k(G') \tag{2.22}$$

Substituting it into Eq. (2.21), w_k can be defined as

$$w(x) = \mathrm{e}^{-\mathrm{i}\omega t} \sum_{G'} \mathrm{e}^{\mathrm{i}(G'+k)x} w_k(G') \tag{2.23}$$

Substituting Eqs. (2.19) and (2.23) into (2.17) and selecting N inverted lattice vectors for calculation, we can obtain the following equation

$$(\boldsymbol{MG} + \boldsymbol{NG} - \omega^2 \mathbf{PG}) \times \mathbf{w}(\mathbf{G}) = \mathbf{0} \tag{2.24}$$

where

$$\begin{aligned} &[\boldsymbol{MG}]_{ij} = (\mathbf{k} + \mathbf{G}_i)^2 m(\mathbf{G}_i - \mathbf{G}_j)(\mathbf{k} + \mathbf{G}_j)^2 \\ &[\mathbf{NG}]_{ij} = n(\mathbf{G}_i - \mathbf{G}_j)(\mathbf{k} + \mathbf{G}_j)^2 \qquad [\mathbf{PG}]_{ij} = p(\mathbf{G}_i - \mathbf{G}_j) \end{aligned} \tag{2.25}$$

Equation (2.24) is a linear equation for solving the generalized eigenvalues of ω^2. For a given Bloch wave vector $\mathbf{k}$ in the first Brillouin zone, a series of eigenvalues ω_{kn} $(n = 1, 2, \ldots)$ can be obtained. The energy band structure of this piezoelectric nanophononic crystal beam can be obtained when $\mathbf{k}$ varies over $[-\pi/2, \pi/2]$.

3. Numerical results and analyses

3.1. Band structures of PC nanobeams with circular cross sections

The band gap structure of piezoelectric nanophononic crystal beams with a circular cross--section was determined based on the parameters provided in Table 1. The results of energy

Table 1. Bulk material parameters of PZT-5H and epoxy (Yan and Jiang, 2011)

Material	ρ [kg/m^3]	E [GPa]	c_{11} [GPa]	e_{31} [C/m2]	κ_{33} [C/(Vm)]
PZT-5H	7500	–	126	−6.5	$1.3 \cdot 10^{-8}$
Epoxy	1180	76	–	–	–

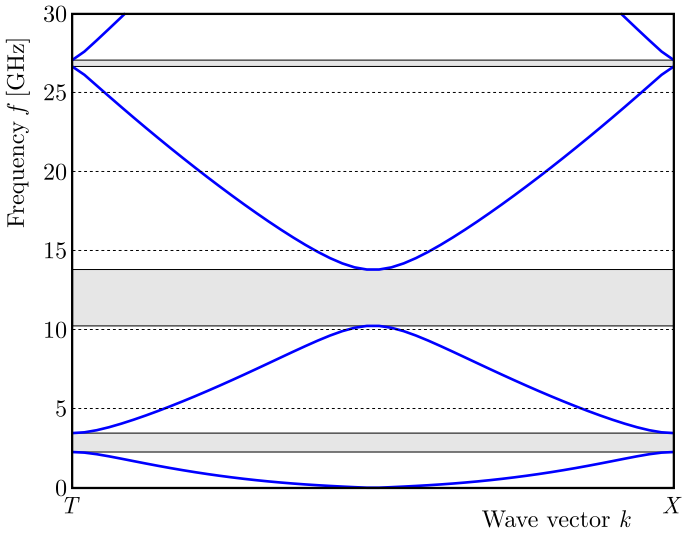

Fig. 3. Band structure of piezoelectric nanophononic crystal beams with a circular cross-section considering surface effects

band structure calculations are illustrated in Fig. 3. The geometric parameters used for the calculations were: $a_1 = a_2 = 50\,\text{nm}$, and $D = 10\,\text{nm}$. The parameters for the surface layer were as follows: $\sigma_x^0 = 1\,\text{N/m}$ and $l_s = 1\,\text{nm}$. The applied voltage was $V = 0.2\,\text{V}$, and the applied axial force was $P_0 = 110^{-8}\,\text{N}$.

As depicted in Fig. 3, there are three fully open band gaps below 30 GHz. In this paper, the characteristics of the first two orders of the band gap are investigated. Specifically, the first-order band gap ranges from 2.2762 Hz to 3.4735 GHz, with a band gap width of 1.913 GHz. The second-order band gap spans from 10.2557 GHz to 13.8244 GHz, with a band gap width of 3.5687 GHz.

3.2. Influence of electromechanical coupling effects on band gap characteristics

As shown in Fig. 4, it illustrates the influence of voltage on the vibration band gap of piezoelectric nanophononic crystal beams with surface effects. The calculation parameters for this analysis are provided in Table 1. From the figure, it can be observed that as the voltage varies from $-50\,\text{V}$ to $20\,\text{V}$, the starting frequency of the first-order and the second-order band gap decreases continuously and tends to 0. This indicates that the band gap shifts towards lower frequencies as the voltage increases. The width of the first-order and the second-order band gap exhibits non-monotonic behavior. The former initially decreases, then increases, and finally decreases again, ultimately approaching 0. The later shows a gradual increase, reaching a peak, and then decreases until it tends to 0.

As shown in Fig. 5, it illustrates the impact of the applied axial force P_0 on the band gap of piezoelectric nanophononic crystal beams. In Fig. 5, as the axial force varies from $-40 \cdot 10^{-8}\,\text{N}$ to $10 \cdot 10^{-8}\,\text{N}$, the starting frequency of the first two orders of the band gap increases continuously from 0. This indicates that the band gap shifts towards higher frequencies as the axial force increases. Furthermore, the width of the band gap initially increases, then decreases, and finally increases again.

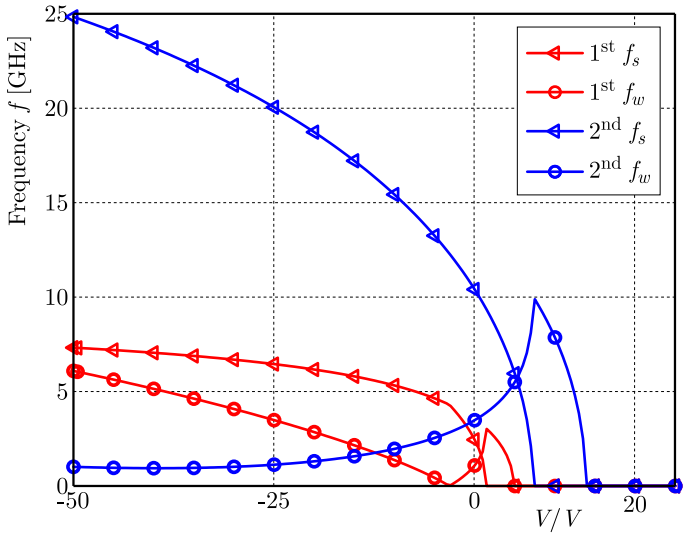

Fig. 4. The influence of voltage V on the band gap

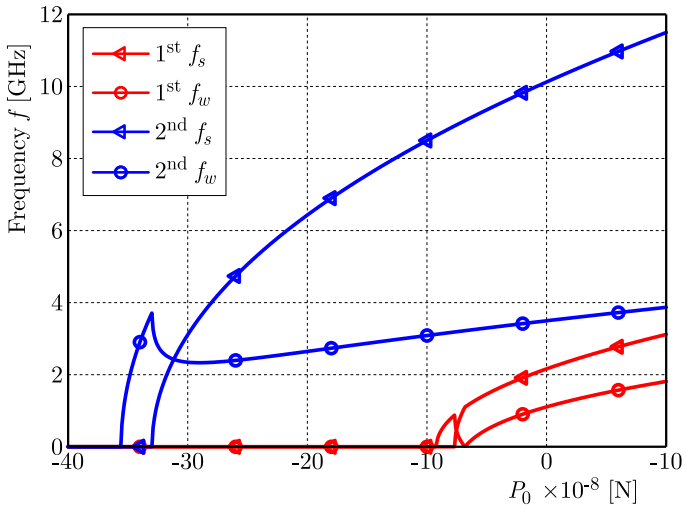

Fig. 5. The influence of the applied axial force P_0 on the band gap

3.3. Influence of surface effects on band gap characteristics

Figure 6 demonstrates the influence of the material characterization length l_s on the band gap of the system. The range of l_s values considered is from 0 nm to 1 nm. From the figure, it is evident that the characterization length l_s exhibits an increasing trend on both the onset frequency and band gap width of the first-order. As the value of l_s increases, the onset frequency of the first-order band gap shifts towards higher frequencies, and the width of the band gap also increases. Similarly, the onset frequency and band gap width of the second-order also show a similar increasing trend with the characterization length l_s. As the value of l_s increases, the onset frequency of the second-order band gap shifts towards higher frequencies, and the width of the band gap also increases.

As shown in Fig. 7, it illustrates the impact of surface residual stress σ_x^0 on the band gap of the system. The range of σ_x^0 values considered is from 0 N/m to 1 N/m. According to the figure, it is evident that the surface residual stress σ_x^0 has a weak increasing trend on both the onset frequency and width of the first-order and the second-order band gap. However, the trend can be approximated as remaining relatively constant within the range of values considered. This indicates that as the surface residual stress σ_x^0 increases within the given range, there is a slight

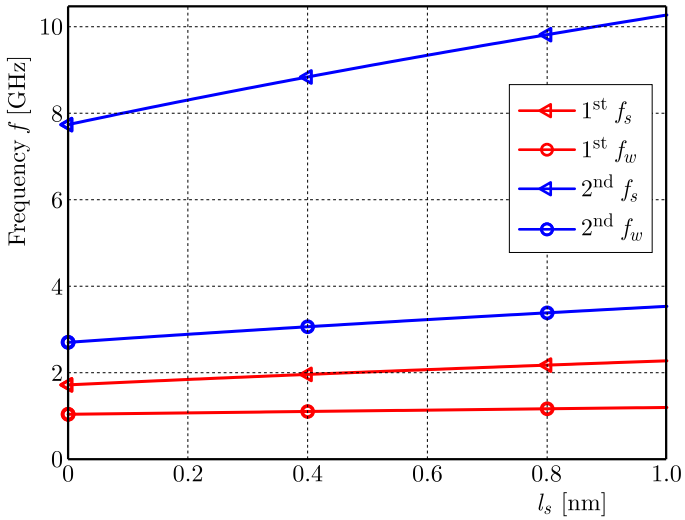

Fig. 6. The influence of the material characterization length l_s on the band gap

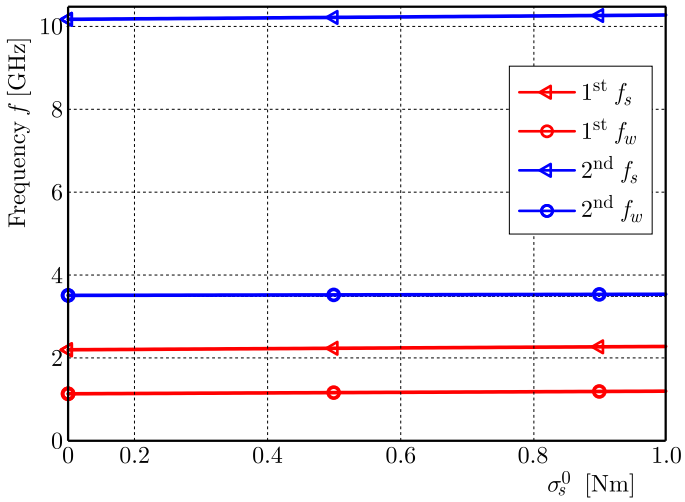

Fig. 7. The influence of the surface residual stress σ_x^0 on the band gap

overall effect on the band gap characteristics. The onset frequency and width of both the first--order and the second-order band gap may experience minimal changes, potentially exhibiting a gradual increase. However, these changes are generally small compared to the range of values considered, and the trend can be approximated as remaining constant.

3.4. Influence of geometric parameters on band gap characteristics

As shown in Fig. 8, it demonstrates the impact of the circular cross-section diameter D of a piezoelectric nanophononic crystal beam on the first-order starting frequency, band gap width, and the second-order starting frequency, band gap width. In this analysis, the diameter D is varied from 0 nm to 25 nm, while other parameters remain consistent with Table 1. From the figure, it can be observed that as the diameter D increases, there is a consistent trend in changes of the first-order and the second-order starting frequencies as well as the band gap widths. Specifically, the values initially decrease and then increase.

Figure 9 depicts the influence of the length ratio a_1/a_2 between the PZT-5H and epoxy resin on the onset frequency and band gap width of the first two orders of the band gap. As the length ratio a_1/a_2 increases, the onset frequency of both the first-order and the second-order band gap

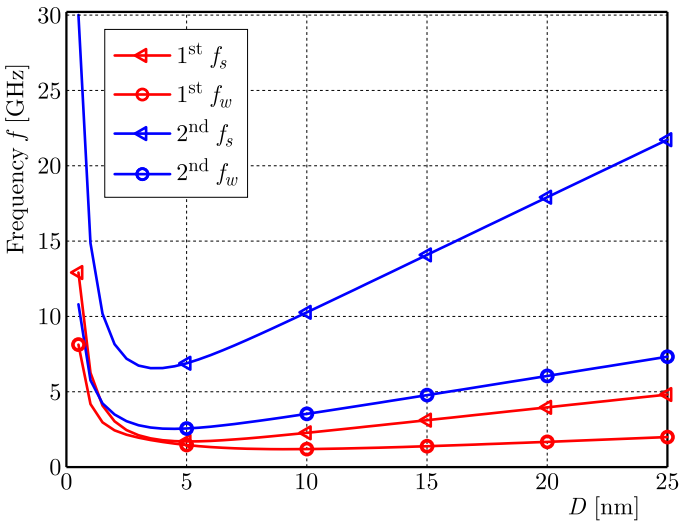

Fig. 8. The influence of the cross-sectional diameter D on the band gap

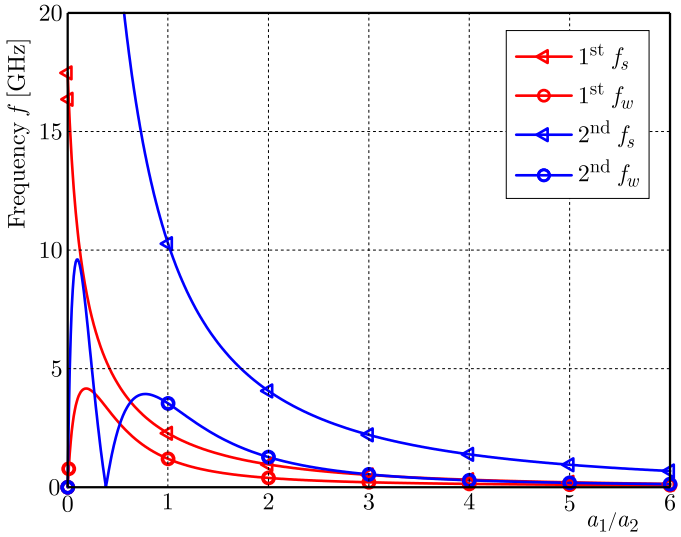

Fig. 9. The influence of a_1/a_2 on the band gap

decreases and tends towards 0. This suggests that a higher length ratio corresponds to lower starting frequencies of the band gaps. Concerning the band gap width, the trend observed for both the first-order and the second-order band gap can be roughly approximated as initially increasing up to a peak, and then decreasing towards 0. This implies that there is an optimal length ratio that maximizes the band gap width for each order of the band gap. It is important to avoid excessive length ratios if a wide band gap width is desired in engineering applications. Instead, designing the length ratio near the peak value can help maximize the band gap width.

4. Conclusions

In this paper, the band gap characteristics of piezoelectric nanophononic crystal beams with circular cross-sections are analyzed and explored in terms of the electromechanical coupling effect, surface effect, and geometry, respectively, and the following conclusions are drawn:

- With an increase of voltage V, the first two orders of the band gap move towards the lower frequency. The first order band gap shows a minus increase and tends to 0, the second

order band gap increases first and then decreases and tends to 0. With an increase of the applied axial force P_0, the first two orders of the band gap move in the lower frequency direction, and the width of the band gap shows the tendency of an increase and decrease.

- The increase of the material characterization length l_s makes the starting frequency of the band gap move in the high frequency direction, and the bandwidth increases. The increase in the surface residual stress σ_x^0 has a smaller effect on the band gap characteristics and can be approximated as remaining relatively stable.
- As the diameter D of the circular cross-section increases, the onset frequency and width of the band gap of the first two orders both decrease and then increase. The increase of the length ratio a_1/a_2 makes the onset frequency of the first two orders of the band gap decrease and tend to zero, which means that a higher length ratio corresponds to a lower onset frequency of the band gap, and the width of the first two orders of the band gap exhibits an increase and then decreases and tends to zero.

Acknowledgments

This research was supported by the National Natural Science Foundation of China (No. 52301373), the Young Elite Scientists Sponsorship Program by CAST (2022QNRC001) and the Natural Science Foundation of Jiangsu Higher Education Institutions of China (No. 22KJB580005).

References

1. Aifantis E.C., 1999, Strain gradient interpretation of size effects, *International Journal of Fracture*, **95**, 299-314
2. Cao Y., Hou Z., Liu Y., 2004, Finite difference time domain method for band-structure calculations of two-dimensional phononic crystals, *Solid State Communications*, **132**, 8, 539-543
3. Chen A.-L., Tian L.-Z., Wang Y.-S., 2017, Band structure properties of elastic waves propagating in the nanoscaled nearly periodic layered phononic crystals, *Acta Mechanica Solida Sinica*, **30**, 2, 113-122
4. Chu J., Zhou G., Liang X., Liang H., Yang Z., Chen T., 2023, A metamaterial for low--frequency vibration damping, *Materials Today Communications*, **36**, 106464
5. Du S., Shi D., Deng H., 2000, Special effects and applications of nanostructured materials, *Nature Magazine*, **22**, 2, 101-106
6. Eringen A.C., Edelen D.G.B., 1972, On nonlocal elasticity, *International Journal of Engineering Science*, **10**, 3, 233-248
7. Ghoreshi M., Bahrami A., 2022, Acoustic invisibility cloak based on two-dimensional solid-fluid phononic crystals, *Solid State Communications*, **342**, 114646
8. Gurtin M.E., Weissmüller J., Larché F., 1998, A general theory of curved deformable interfaces in solids at equilibrium, *Philosophical Magazine A*, **78**, 5, 1093-1109
9. Gurtin M.E., Murdoch I.A., 1975, A continuum theory of elastic material surfaces, *Archive for Rational Mechanics and Analysis*, **57**, 4, 291-323
10. Huang G.-Y., Yu S.-W., 2006, Effect of surface piezoelectricity on the electromechanical behaviour of a piezoelectric ring, *Physica Status Solidi (B)*, **243**, 4, R22-R24
11. Kong D., Wang N., Wang G., Sheng Z., Zhang Y., 2023, Analytical model of vibro-acoustic coupling between the membrane loaded with concentrated masses and the acoustic cavity, *Thin--Walled Structures*, **182**, 110317
12. Lee D., Youn B.D., Jo S.-H., 2023. Deep-learning-based framework for inverse design of a defective phononic crystal for narrowband filtering, *International Journal of Mechanical Sciences*, **255**, 108474

13. Lu J.-F., Cheng J., Feng Q.-S., 2022, Plane wave finite element model for the 2-D phononic crystal under force loadings, *European Journal of Mechanics – A/Solids*, **91**, 104426

14. Qian D., 2018, Bandgap properties of a piezoelectric phononic crystal nanobeam with surface effect, *Journal of Applied Physics*, **124**, 5, 055101

15. Qian D., Shi Z., 2017, Using PWE/FE method to calculate the band structures of the semi-infinite beam-like PCs: Periodic in z-direction and finite in x-y plane, *Physics Letters A*, **381**, 17, 1516-1524

16. Qian D., Zou P., Zhang J., Chen M., 2022, Tunability of resonator with pre-compressed springs on thermo-magneto-mechanical coupling band gaps of locally resonant phononic crystal nanobeam with surface effects, *Mechanical Systems and Signal Processing*, **176**, 109184

17. Sigalas M.M., Economou E.N., 1992, Elastic and acoustic wave band structure, *Journal of Sound and Vibration*, **158**, 2, 377-382

18. Surana K.S., Joy A.D., Reddy J.N., 2017, Non-classical continuum theory for solids incorporating internal rotations and rotations of Cosserat theories, *Continuum Mechanics and Thermodynamics*, **29**, 2, 665-698

19. Yan Z., Jiang L.Y., 2011, The vibrational and buckling behaviors of piezoelectric nanobeams with surface effects, *Nanotechnology*, **22**, 24, 245703

20. Yang F., Chong A.C.M., Lam D.C.C., Tong P., 2002, Couple stress based strain gradient theory for elasticity, *International Journal of Solids and Structures*, **39**, 10, 2731-2743

21. Yang T., Xiao B., Feng Y., Pei D., Liu Y., Chen M., Jiang H., Zheng Z., Wang Y., 2022, Acoustic edge mode in spiral-based metamaterials at subwavelength scale, *Results in Physics*, **42**, 106008

22. Yao L., Zhang D., Xu K., Dong L., Chen X., 2021, Topological phononic crystal plates with locally resonant elastic wave systems, *Applied Acoustics*, **177**, 107931

23. Yin J., Cai L., Fang X., Xiao Y., Yang H., Zhang H., Zhong J., Zhao H., Yu D., Wen J., 2022, Review on research progress of mechanical metamaterials and their applications in vibration and noise control, *Advances in Mechanics*, **52**, 3, 508-586

24. Zhen N., Wang Y.-S., Zhang C., 2012, Surface/interface effect on band structures of nanosized phononic crystals, *Mechanics Research Communications*, **46**, 81-89

25. Zou Y., Wang Z., Adjei P., Zhao X., 2023, The sound insulation performance of light wood frame construction floor structure based on phononic crystal theory, *Journal of Building Engineering*, **75**, 107039

26. Zuo S., Liu P., Wu X., Zhang Q., Kong Y., Zhou D., 2022, Study on broad flexural wave bandgaps of piezoelectric phononic crystal plates for the vibration and noise attenuation, *Thin-Walled Structures*, **178**, 109481

Manuscript received August 8, 2023; accepted for print September 27, 2023

JOURNAL OF THEORETICAL AND APPLIED MECHANICS
62, 1, pp. 31-45, Warsaw 2024
https://doi.org/10.15632/jtam-pl/174960

UNSTEADY BODY FORCE MODEL FOR ROTATING STALL IN AXIAL COMPRESSOR WITH VARIOUS INLET CONDITIONS

Jin Guo

COMAC Shanghai Aircraft Design and Research Institute, Shanghai, China, and
College of Energy and Power Engineering, Nanjing University of Aeronautics and Astronautics, Nanjing, Jiangsu, China
e-mail: guojin_nj@126.com

To analyze the dynamic stall of multistage axial compressors, a three-dimensional unsteady numerical model is established based on the body force model. For a two-stage axial compressor with a clean inlet, the calculated maximum steady static pressure rise coefficient is only 0.1% different compared with the experimental data. The characteristic frequency of the dynamic stall evolution basically agrees with the experimental results, which proves the effectiveness of the model. For the compressor with a combined radial-circumferential total pressure inlet distortion, the predictions preliminarily verify the ability of the model for qualitative description of the flow instability process with the complex inlet distortion.

Keywords: unsteady body force model, rotating stall. complex inlet distortion, axial compressor

1. Introduction

Aerodynamic instability characteristics of areoengine compressors due to the inverse pressure gradient of the internal viscous gas directly affect the operational reliability of engines (Day, 2016). The pursuit for a design of a highly loaded compressor has heightened the problem of flow stability. Meanwhile, with gradual application of new concepts such as boundary layer ingesting (BLI) jet engines (Uranga *et al.*, 2014) in future aero propulsion systems, the compressor must continuously operate with a complex inlet distortion, which has a significant effect on the compressor stability. It is imperative to establish efficient and re-liable models to predict compressor instability in various inlet conditions.

The aerodynamic instability of the compressor is mainly manifested in two unsteady phenomena: rotating stall and surge (Day, 2016). Compared with surge, which is an axial oscillating unsteady flow pattern caused by the interaction between the compressor and downstream components with the cavity effect, rotating stall features more three-dimensionality. In the research area of axial compressors, the rotating stall has been the focus of attention.

One of the most direct approaches for predicting the dynamic stall process of the axial compressor is the three-dimensional unsteady Reynolds-averaged Navier-Stokes (URANS) method, which treats the flow stability as an initial boundary value problem and simulates the whole dynamic stall process (Huang *et al.*, 2019a,b; Wang *et al.*, 2020; Zhang and Vahdati, 2020). It is undeniable that the URANS simulation can effectively describe the multi-scale flow interaction in turbomachinery and play a positive role in the understanding of the instability mechanism. The method and other higher-order computational fluid dynamics (CFD) methods will be central to the forecasting technique of the flow stability of the compressor in the future. However, as for the current computing level, the full-annulus unsteady CFD simulation of multistage compressors is time-consuming, which leads makes it difficult to be popularized as a conventional technology in engineering practice. Therefore, the development of an efficient stability analysis

model is still of great practical significance to improve the fidelity of the existing compressor design system.

An alternative approach of the flow stability analysis is to focus on the modeling of the main scale flow in the compressor within the framework of the time marching technology of CFD. Central to the modeling is to describe the blade effect in reasonable reduction of dimensionality to lower the computational cost. According to the ideology, the actuator disk model (Hu *et al.*, 1999) and body force model (Gong *et al.*, 1999; Longley, 2007; Righi *et al.*, 2018) have been established. In the actuator disk model, the blade row is treated as a discontinuity and the flow process inside the blade passage is not solved. While in the body force model, the boundary effect of the blade is modeled as a distributed force source terms to effectively simulate main flow characteristics in the blade passage. Gong *et al.* (1999) developed a three-dimensional incompressible model for analyzing the dynamic stall process of multistage axial compressors based on the body force model. Longley (2007) investigated the modeling method for the blade force in the reverse-flow condition and established a three-dimensional unsteady compressible model to analyze the rotating stall and surge of a multistage axial compressor. Righi *et al.* (2018) proposed a highly robust three-dimensional unsteady throughflow model for the rotating stall and surge in an axial compressor based on the improved Gong's blade force model. Recently, Rosa Taddei (2021) developed a meanline body force approach to simulate the two-dimensional flow behavior during the rotating stall in a transonic compressor.

The aforementioned models focus on simulation of the stall dynamic process of a compressor within uniform inflow. Numerous numerical studies (Cao *et al.*, 2017; Guo and Hu, 2018; Mao and Dang, 2020) have examined the effectiveness of the body force model for simulating steady transfer characteristics of a circumferential large-scale distortion in the axial compressor. There are rare comprehensive investigations on the simulation of the dynamic stall process for multistage compressors with an inlet distortion through the body force approach. The construction method of the blade force plays a significant role in this kind of model, especially, a comprehensive and effective correlation between blade force source terms and local aerodynamic and geometric parameters under inlet distortions remains to be addressed elaborately.

This study aims to develop a three-dimensional unsteady numerical model to analyze the dynamic stall process of a multistage axial compressor in various inlet conditions. The distributed blade force source terms are established by concepts of the deviation angle and loss coefficient in through flow theory, which can be suitable for stability evaluation of the compressor in the throughflow design stage. The model is implemented by an in-house program and capability to quantitatively describe the dynamic stall process of a compressor with a clean inlet is evaluated on a two-stage axial compressor at Nanjing University of Aeronautics and Astronautics (NUAA). Besides, the potential of the model for efficient simulation of dynamic stall processes with complex inlet distortions is demonstrated in detail.

2. Theoretical methods

The flow in the compressor is governed by a three-dimensional unsteady compressible equation in the absolute cylindrical coordinate system. The boundary effect of blades is modeled by distributed force source terms and a blockage coefficient of the blade profile, instead of a traditional body-fitted mesh approach. The main governing equation of the model is as follows

$$\frac{\partial b\mathbf{U}}{\partial t}+\frac{\partial b(\mathbf{E}-\mathbf{E}_v)}{\partial z}+\frac{\partial b(\mathbf{F}-\mathbf{F}_v)}{r\partial\theta}+\frac{\partial rb(\mathbf{G}-\mathbf{G}_v)}{r\partial r}=b\mathbf{S}+\mathbf{S}_b+b\mathbf{S}_F \tag{2.1}$$

In the non-bladed region, the blade blockage coefficient b is equal to 1, and the bladed terms $\mathbf{S}_b$ and $\mathbf{S}_F$ are equal to 0. $\mathbf{U}$ is speed, $\mathbf{E},\mathbf{F},\mathbf{G}$ – inviscid fluxes, $\mathbf{E}_v,\mathbf{F}_v,\mathbf{G}_v$ – viscid fluxes. The remaining terms are defined as

$$\begin{aligned}
&\mathbf{U} = [\rho, \rho u, \rho v, \rho w, \rho e^*]^{\mathrm{T}} \qquad \mathbf{E} = [\rho u, \rho u^2 + p, \rho vu, \rho wu, \rho u h^*]^{\mathrm{T}} \\
&\mathbf{F} = [\rho v, \rho uv, \rho v^2 + p, \rho wv, \rho v h^*]^{\mathrm{T}} \qquad \mathbf{G} = [\rho w, \rho uw, \rho vw, \rho w^2 + p, \rho w h^*]^{\mathrm{T}} \\
&\mathbf{E}_v = [0, \tau_{zz}, \tau_{z\theta}, \tau_{zr}, \boldsymbol{\tau}_z \mathbf{u} - q_z]^{\mathrm{T}} \qquad \mathbf{F}_v = [0, \tau_{\theta z}, \tau_{\theta\theta}, \tau_{\theta r}, \boldsymbol{\tau}_\theta \mathbf{u} - q_\theta]^{\mathrm{T}} \\
&\mathbf{G}_v = [0, \tau_{rz}, \tau_{r\theta}, \tau_{rr}, \boldsymbol{\tau}_r \mathbf{u} - q_r]^{\mathrm{T}} \qquad \mathbf{S} = \left[0, 0, \frac{-\rho vw + \tau_{r\theta}}{r}, \frac{\rho v^2 + p - \tau_{\theta\theta}}{r}, 0\right]^{\mathrm{T}}
\end{aligned} \tag{2.2}$$

The term e^* and h^* denotes the total energy and the total enthalpy per unit mass of the gas, respectively. The term τ is the turbulent Reynolds stress and q is the turbulent heat flux. The specific expressions are as follows

$$\begin{aligned}
&e^* = \frac{p}{\rho(\gamma - 1)} + \frac{1}{2}(u^2 + v^2 + w^2) \qquad h^* = e^* + \frac{p}{\rho} \\
&\boldsymbol{\tau}_z = [\tau_{zz}, \tau_{z\theta}, \tau_{zr}] \qquad \boldsymbol{\tau}_\theta = [\tau_{\theta z}, \tau_{\theta\theta}, \tau_{\theta r}] \qquad \boldsymbol{\tau}_r = [\tau_{rz}, \tau_{r\theta}, \tau_{rr}] \\
&\mathbf{u} = [u, v, w] \qquad \boldsymbol{\tau} = \mu_t[\nabla \mathbf{u} + (\nabla \mathbf{u})^{\mathrm{T}}] - \left(\frac{2}{3}\mu_t \nabla \mathbf{u}\right)\mathbf{I} \\
&\mathbf{q} = [q_z, q_\theta, q_r] = -k_t \nabla T = -\frac{c_p \mu_t}{\mathrm{Pr}_t} \nabla T
\end{aligned} \tag{2.3}$$

The assumption of a calorically perfect gas is employed for the model, and the ideal gas law $p = \rho R_g T$ is satisfied. The value of c_p and γ are assumed to be constant. The calculation methods for the eddy viscosity coefficient μ_t and the turbulent heat conductivity coefficient k_t are presented in Section 2.2.

In the bladed region, the terms b, S_b and S_F are expressed as

$$b = N|\theta_p - \theta_s|\frac{1}{2\pi} \qquad \mathbf{S}_b = \left[0, p\frac{\partial b}{\partial z}, 0, p\frac{\partial b}{\partial r}, 0\right]^{\mathrm{T}} \qquad \mathbf{S}_F = [0, F_z, F_\theta, F_r, F_\theta \Omega r]^{\mathrm{T}} \tag{2.4}$$

where N is the number of blades. The terms θ_p and θ_s are the circumferential coordinates of the pressure and suction sides of the blades, respectively. The term F represents the instantaneous blade force per unit volume of the flow and Ω is the angular velocity of the rotor, as shown in Fig. 1.

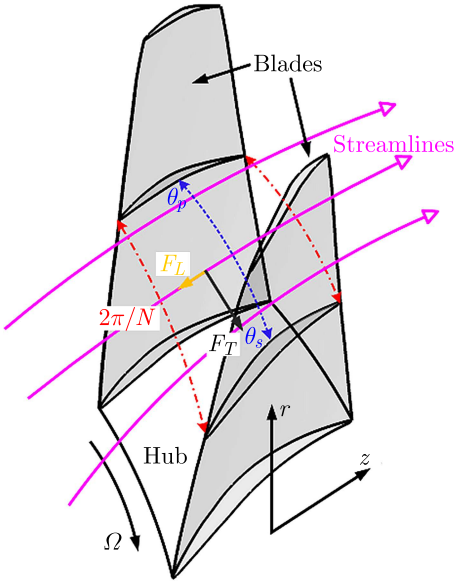

Fig. 1. Schematic of aerodynamic and geometric parameters in the bladed region

According to the circumferentially averaged theory of the local flowpath, the value of F_v is 0 in the bladed region. Then the circumferential inviscid flux vector $\mathbf{F}$ is transformed into

$$\mathbf{F} = \Omega r[\rho, \rho u, \rho v, \rho w, \rho e^*]^{\mathrm{T}} \tag{2.5}$$

2.1. Unsteady blade force model

The modeling of the unsteady blade force $\mathbf{F}$ plays a central role in the developed model. A method of the blade force construction with a clear physical meaning is employed in the present work. A quasi-steady blade force is constructed directly from the equation of steady circumferential momentum. Subsequently, an instantaneous blade force is modeled by a first--order lagging response function. This provides an effective approach to consider the effect of the radial flow. Meanwhile, the robustness of the model is enhanced because there is no need to introduce the artificial iteration coefficient.

To begin this process, the blade force is decomposed into two parts: the turning force $\mathbf{F}_T$ perpendicular to the relative velocity $\mathbf{u}_{rel}$ and the loss force $\mathbf{F}_L$ parallel but opposite to $\mathbf{u}_{rel}$ by referring to Marble (1964), as shown as

$$\mathbf{F}_T\mathbf{u}_{rel} = 0 \qquad \mathbf{F}_L = -\frac{F_L}{u_{rel}}\mathbf{u}_{rel} \tag{2.6}$$

where $\mathbf{u}_{rel} = [u, v - \Omega r, w]$, $\mathbf{F}_T = [F_{T,z}, F_{T,\theta}, F_{T,r}]$ and $\mathbf{F}_L = [F_L, z, F_L, \theta, F_L, r]$.

The value of F_L is determined by the local loss coefficient

$$F_L = \rho T\frac{u_m}{u_{rel}}\frac{\Delta s}{\Delta m} = -\frac{\rho RT}{\Delta m}\frac{u_m}{u_{rel}}\ln\left[1 - \varpi\left(1 - \left(1 + \frac{\gamma - 1}{2}\mathrm{Ma}_1^2\right)^{-\frac{\gamma}{\gamma-1}}\right)\frac{1}{(T_2^*/T_1^*)^{\frac{\gamma}{\gamma-1}}}\right] \tag{2.7}$$

where $u_m = \sqrt{u^2 + w^2}$ is the instantaneous meridional velocity and u_{rel} is the magnitude of relative velocity. The term Δs denotes the entropy increase from the inlet to the outlet of the blade passage and Δm represents the meridional length of the blade passage. For the rotor passage, the terms Ma and T^* are the relative Mach number and the relative total temperature, respectively. For the stator passage, the two terms signify the absolute values. Subscripts 1 and 2 indicate the inlet and outlet of the blade passage, respectively.

The total circumferential force F_θ is obtained by the steady circumferential momentum equation

$$F_\theta = F_{T,\theta} + F_{L,\theta} = \frac{1}{b}\frac{\partial b(\rho u v^* - \tau_{z\theta})}{\partial z} + \frac{1}{br}\frac{\partial rb(\rho w v^* - \tau_{r\theta})}{\partial r} - \left(\frac{-\rho w v^*}{r} + \frac{\tau_{r\theta}}{r}\right) \tag{2.8}$$

The imposed circumferential velocity v^* in the bladed region is determined as follows

$$v^* = \begin{cases} \Omega r - u_m\tan(\kappa + \delta) & \text{rotor} \\ u_m\tan(\kappa + \delta) & \text{stator} \end{cases} \tag{2.9}$$

where κ is the blade metal angle and δ is the deviation between the actual flow direction and blade metal angle due to the flow viscous effect and the centrifugal force of the curved blade passage.

The radial turning force $F_{T,r}$ is correlated to the three-dimensional blade mean camber surface. Hence, the end bend effect is reflected in this model to a certain extent, as shown in the equation

$$F_{T,r} = F_{T,\theta}\frac{n_r}{n_\theta} \tag{2.10}$$

where n_r and n_θ are the radial and circumferential components of the normal vector of the blade mean camber surface.

Up to now, every component of the quasi-steady blade force can be determined when the local loss coefficient ϖ and the deviation angle δ are obtained. When the gas moves forward normally, according to the deviation angle and loss model in the through flow theory of the

compressor (Johnsen and Bullock, 1965; Creveling and Carmody, 1968), the local deviation angle and the loss coefficient are calculated by the incidence, Mach number, and typical blade geometry at different circumferential and radial positions. To modify and broaden the incidence characteristics of different elementary cascades, numerical blowing experiments can be employed by the three-dimensional RANS method.

When the compressor is throttled to a low mass flow rate near stall, the axial velocity in the flowpath may be negative. However, it should be noted that under the local circumferentially averaged theory, the reverse flow is not necessarily presented. In the reversed flow region, similar to the analysis of Longley (2007) and Righi *et al.* (2018), the loss force is no longer calculated. The turning force is limited to be perpendicular to the local mean camber surface of the blade instead of the relative flow direction. The benefit of this is that the robustness is guaranteed and the high loss is naturally introduced by adjusting the gas flow direction. The outlet flow angle should be specified at the blade inlet in the reverse flow. In the current numerical study, it can be found that the dynamic stall process obtained by the model basically agrees with the experimental data when the outlet direction of the flow is consistent with the blade stagger angle.

More importantly, in the dynamic stall process of the compressor, it suffers a delayed dynamic response of the local blade force to the upstream aerodynamic disturbance. To effectively describe the formation of the rotating stall, this dynamic effect should be quantified in the model.

Because the circumferential turning force is dominant, this term is modified with the unsteady response by a first-order lagging response function, as shown in the equation

$$\lambda\Big(\frac{\partial F_{T,\theta}}{\partial t} + \Omega\frac{\partial F_{T,\theta}}{\partial \theta}\Big) = F^{ss}_{T,\theta} - F_{T,\theta} \tag{2.11}$$

where $F^{ss}_{T,\theta}$ is the quasi-steady circumferential turning force, and $\lambda = c_m/u_m$ represents the lagging response time. The term c_m denotes the meridional blade chord length.

2.2. Numerical solution

A cell-centered finite-volume method is utilized to discretize Eq. (2.1). The time terms are solved using an explicit four-stage Runge-Kutta scheme. In the unsteady calculation, the global minimum time step according to the CFL number is selected as a unified time step of the computational domain. The inviscid flux of the space term is calculated by the low-diffusion flux-splitting scheme (LDFSS(2)) proposed by Edwards (1997).

The discretization of the viscous flux in Eq. (2.1) is much easier due to its elliptic characteristic compared with that of the inviscid flux. As can be found in Eqs. (2.3), the viscous flux at the interface can be determined only by obtaining the eddy viscosity coefficient μ_t, the turbulent heat conductivity coefficient k_t, and the partial derivatives of the velocity and static temperature. The model focuses on the energy exchange between different streamlines caused by the turbulent diffusion in the main flow instead of the small-scale viscous flow near the wall. The aerodynamic loss in the flow field is mainly loaded through the loss force term. Hence, the eddy viscosity coefficient μ_t is calculated by a simple semi-empirical method proposed by Gallimore and Cumpsty (1986). Namely, the criterion number $\mu_t/(\rho u L_{ref})$ is determined in advance in the global flow field. Subsequently, the local μ_t is carried out according to the local instantaneous flow field. The parameter L_{ref} is the compressor characteristic length. The turbulent Prandtl number in the global flow field is given as 0.9 and combined with the μ_t to calculate k_t.

2.3. Boundary conditions

To ensure the robustness of the model, the inlet and outlet boundaries of the computational domain are treated as open boundaries. Thus, the gas is allowed to flow in and out freely. When

the gas normally flows into the computational domain, the total pressure, total temperature, and flow direction distribution are given at the domain inlet. The total pressure specified at the inlet would be treated as the static pressure where the flow exits the domain inlet. The outlet pressure is calculated by the classical throttling model based on the quadratic parabolic analytic function, as shown in

$$\frac{p_e - p_0^*}{0.5\rho_0 U_m^2} = K_t \phi^2 \tag{2.12}$$

where p_e is the static pressure at the domain outlet. The parameters p_0^* and ρ_0 are the average total pressure and density of the inflow, respectively. The term U_m is the rim speed at the midspan of the compressor inlet and K_t is the throttle coefficient. The term $\phi = u_e/U_m$ denotes the flow coefficient at the compressor outlet. If the reverse flow is present at the outlet, p_e will be regarded as the total pressure.

In the condition of the clean inlet, some circumferential non-uniform artificial initial small disturbances are introduced to induce the stall initiation process. Working at the steady condition, a small disturbance will disappear quickly without any influence on the compressor flow field. While the compressor is throttled to the stall point, the small disturbance will expand nonlinearly and eventually evolve into the mature rotating stall cell. In this model, a sinusoidal total pressure distortion of amplitude 0.1% is applied at the inlet boundary. The disturbance is canceled after 0.1 of rotor revolutions.

3. Numerical results and discussion

In this Section, a two-stage axial compressor at the laboratory located in NUAA is employed to quantitatively evaluate the ability of the model to effectively simulate the dynamic process of the rotating stall in a multistage compressor. A steady and dynamic experiment has been performed on the compressor within the clean inlet to collect abundant data to validate the developed model. Meanwhile, to further demonstrate the potential of the model for efficiently simulating the dynamic stall process with a complex inlet distortion, the model is applied to predict the stall flow behavior of the two-stage axial compressor with the combined radial-circumferential total pressure inlet distortion.

Typical aerodynamic and geometric parameters of the compressor are listed in Table 1.

Table 1. Design parameters of NUAA two-stage compressor

Parameter	Value
Number of blades (R1/S1/R2/S2)	19/22/18/20
Shroud diameter [mm]	900
Hub-to-shroud ratio	0.6
Design speed [rpm]	1500
Mass flow [kg/s]	25.0
Total pressure ratio	1.035

3.1. Model validation for dynamic stall process under clean inlet

The dynamic stall process of the compressor has been measured at 800 rpm. Figure 2 presents a schematic of the test rig. The steady pressure parameters of the compressor inlet are measured by four static pressure taps on the casing wall and six six-hole total pressure combs (Fig. 2, plane I and plane II). The steady pressure parameters of the compressor outlet are measured by

16 static pressure taps on the casing and hub and eight total pressure combs (Fig. 2, plane III and plane IV). To investigate the dynamic process of the compressor from the steady-state to rotating stall, six single-point differential-pressure probes are distributed along the circumference of plane II to monitor the perturbation of the total pressure at 85% span of the compressor inlet. The pressure-sensing holes of the probes are facing the flow direction. High-frequency response Kulite sensors are selected as the pressure sensor.

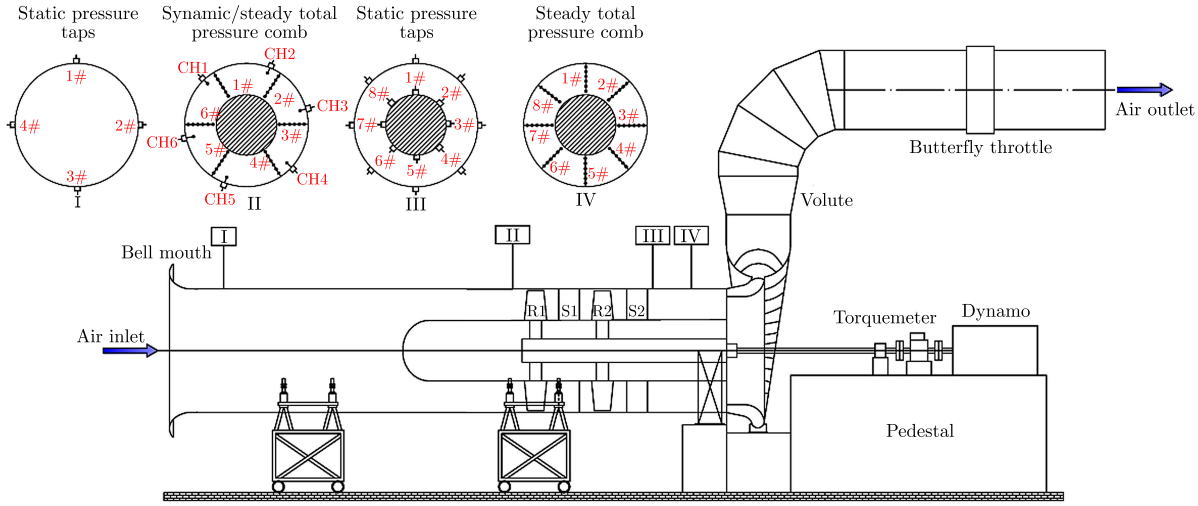

Fig. 2. Schematic of the test rig and measurement arrangement

The dimensionless process is carried out for the collected dynamic total pressure by

$$\widetilde{p}^* = \frac{p^*(t) - \overline{p}^*}{\overline{p}^*} \tag{3.1}$$

where $\overline{p}^*$ represents the average value of the sampling period. To focus on the main low-order frequency signals in the dynamic stall, low-pass filtering is utilized to eliminate the interference of high-order frequency signals in the flow field of the compressor.

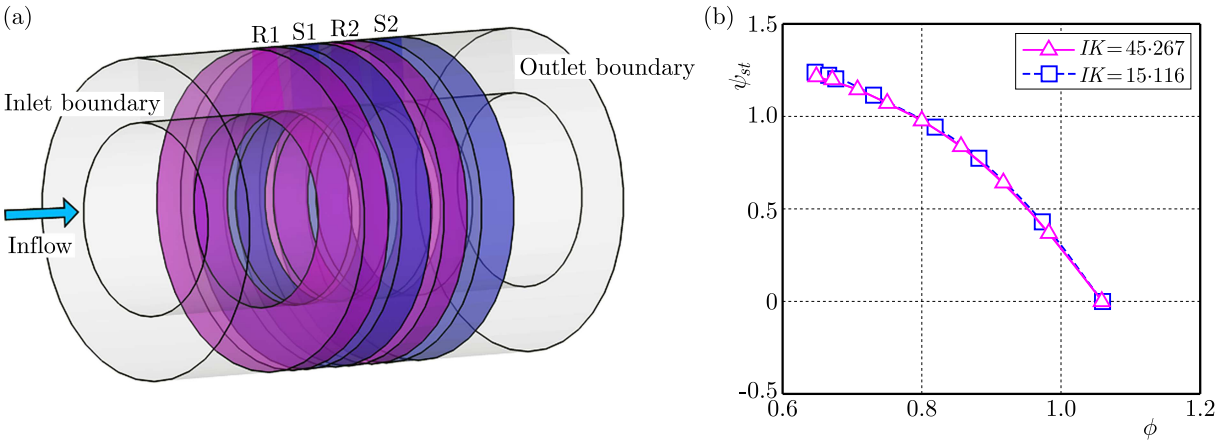

Fig. 3. (a) Schematic of the computational domain for the compressor in the model. (b) Meridional mesh independency study

Figure 3a displays the computational domain of the two-stage compressor in the unsteady body force model. The dependency of the solution for the developed model on the mesh density has been assessed based on the steady performance of the compressor. The cell number along the radial, circumferential, and streamwise directions are expressed as I, J and K, respectively.

It should be noted that the model is based on the circumferentially averaged theory of the local flowpath and the governing equation is solved in the cylindrical coordinate system. Therefore, the solution is theoretically not sensitive to quantity of the circumferential mesh. This has also been proved by Mao and Dang (2020). Particularly, in calculating the steady performance of the compressor with the clean inlet, simply one grid is set in the circumferential direction. Figure 3b plots the computed characteristic curves of the steady static pressure rise coefficient based on two sets of meridional grids. The static pressure rise coefficient ψ_{st} is defined as

$$\psi_{st} = \frac{p_2 - p_0^*}{0.5\rho_0 U_m^2} \tag{3.2}$$

where p_2 represents the average static pressure at the last-stage stator outlet of the compressor. It can be found that characteristics obtained by two different sets of grids are nearly the same. The coarse mesh is selected for the later full-annulus unsteady computation to further shorten the time cost of simulating the dynamic stall process. The detailed computational mesh is shown in Fig. 4.

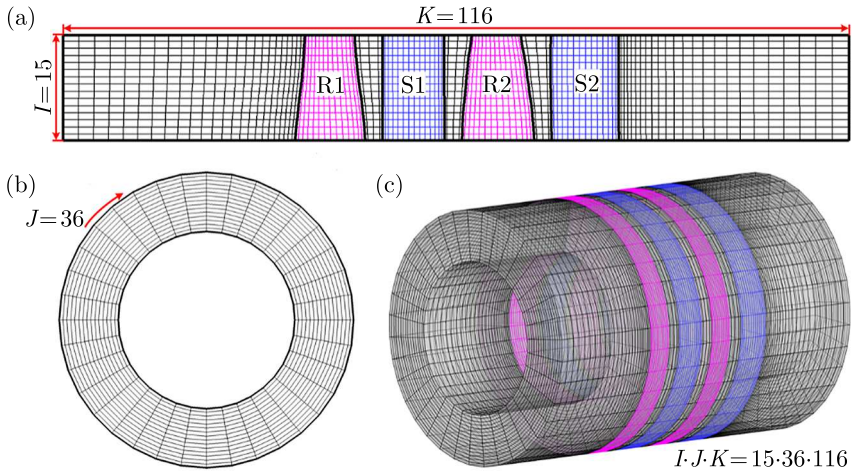

Fig. 4. Three-dimensional computational mesh of the compressor in the model

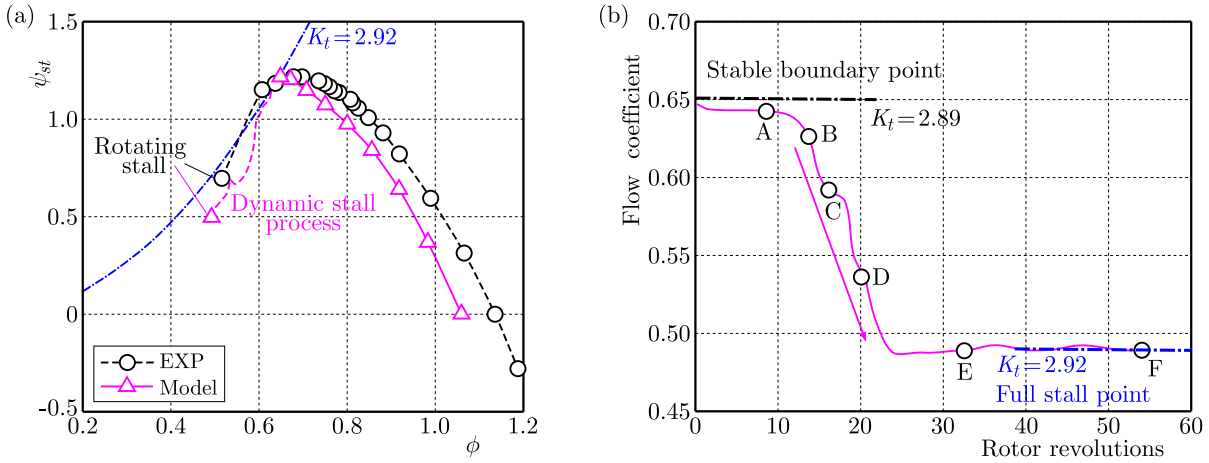

Fig. 5. (a) Compressor pressure rise coefficient at different throttle openings. (b) Time history of the flow coefficient during the stall

The compressor is throttled by adjusting the throttle coefficient until the rotating stall occurs. Figure 5a gives a comparison between the calculated and experimental results of the pressure rise characteristics of the compressor at different throttle openings. It can be seen that

the overall characteristics obtained by the model are in line with the experimental results. The comparison shows only about a 0.1% difference in the maximum static pressure rise coefficient between the calculated and experimental results.

Figure 5b further illustrates the time history of the flow coefficient during the compressor stall obtained by the model. As can be found in Fig. 5b, the throttle coefficient increases from 2.89 to 2.92 near the stall point and the dynamic stall process begins. After about 30 rotor revolutions, a fully developed rotating stall is formed. Subsequently, the average overall characteristic point of the compressor remains constant.

To further reveal formation of the stall cell, axial velocity contours at the midspan of the compressor in different rotor revolutions are displayed in Fig. 6. A slight closing of the downstream valve at the stable boundary point has a great influence on the development of internal flow. The generation of the stall cell is at the second-stage stator and it gradually expands to the whole compressor inlet. A stable single cell, about a third of the circumferential length of the compressor, is finally formed.

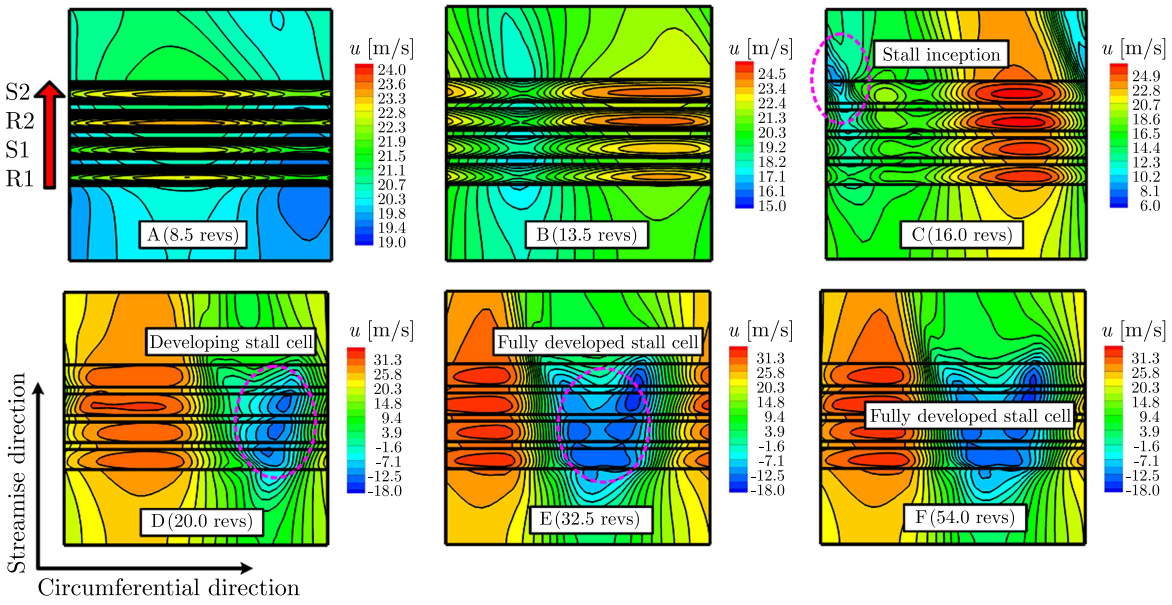

Fig. 6. Formation process of the stall cell in the compressor obtained by the model

Figure 7 shows the total pressure traces at different circumferential locations at the 85% span of the compressor inlet during the stall obtained by the experiment and calculation. As can be observed, the main characteristics of the dynamic stall evolution obtained by calculation basically agree with the experimental results. The stall precursor of the compressor is a typical large-scale modal wave disturbance. The experimental results show that the propagation frequency of the final stall cell is 42% of the rotor speed (5.6 Hz). While the prediction of the propagation frequency is 38% of the rotor speed (5.1 Hz). Overall, the characteristic frequency of the dynamic stall evolution obtained by the model is similar to that from the experimental data.

3.2. Numerical prediction of dynamic stall process for complex distortion

To exhibit the potential of the model for quantitative description of the dynamic stall process with a complex inlet distortion, the dynamic stall process of the compressor with a combined radial-circumferential total pressure inlet distortion is simulated by the developed model. Its capability to describe the aerodynamic instability process of the multistage compressor with the distorted inlet is temporarily investigated by numerical simulations at this stage. Besides, the rationality of calculation results is discussed based on the previous qualitative consensus.

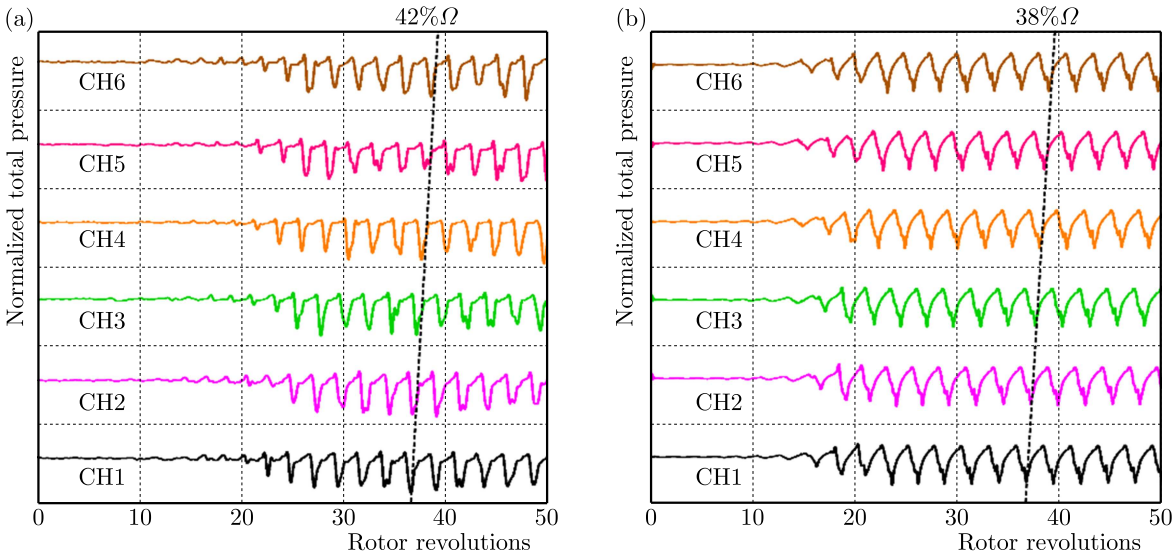

Fig. 7. Total pressure traces at 85% span of the compressor inlet at different circumferential locations during stall: (a) experimental result, (b) numerical results

Figure 8 plots the contour of the total pressure distortion at the computational domain inlet. The low-pressure distorted region occupies a 50% span near the tip in the radial direction and 120° in the circumferential direction. The absolute total pressure in the distorted region decreases by 0.5%.

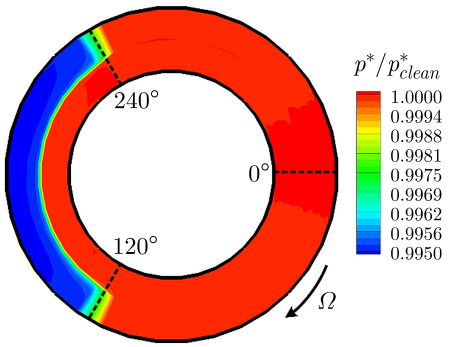

Fig. 8. Distribution of total pressure at the inlet

A large-scale circumferential nonuniform disturbance exists at the compressor inlet with the distorted inflow, so the artificial small disturbance is no longer introduced in the model. Figure 9 provides the calculated time-averaged pressure rise coefficient of the compressor with the inlet distortion. It can be found that the distortion results in a significant decrease of the peak pressure rise coefficient and makes the stall condition in advance. The partially enlarged drawing near the stall stage is further displayed in Fig. 9b. As can be seen, the calculation results show that the compressor gradually transits from the full stable state (point A) to the small--scale oscillation state (points C, D, E) during the throttling process with the inlet distortion. Point B is the critical stable state when the compressor enters the small-scale oscillation region. In this region, the average pressure rise of the compressor no longer increases with the decrease of the flow coefficient and reaches the peak near the critical point B. With further throttling, the oscillation amplitude of the flow parameter increases gradually until the full deep stall (point F) appears.

The transfer characteristics of the combined radial-circumferential distortion in the two-stage compressor are analyzed by taking the full stable state (point A) as an example. Figure 10 plots

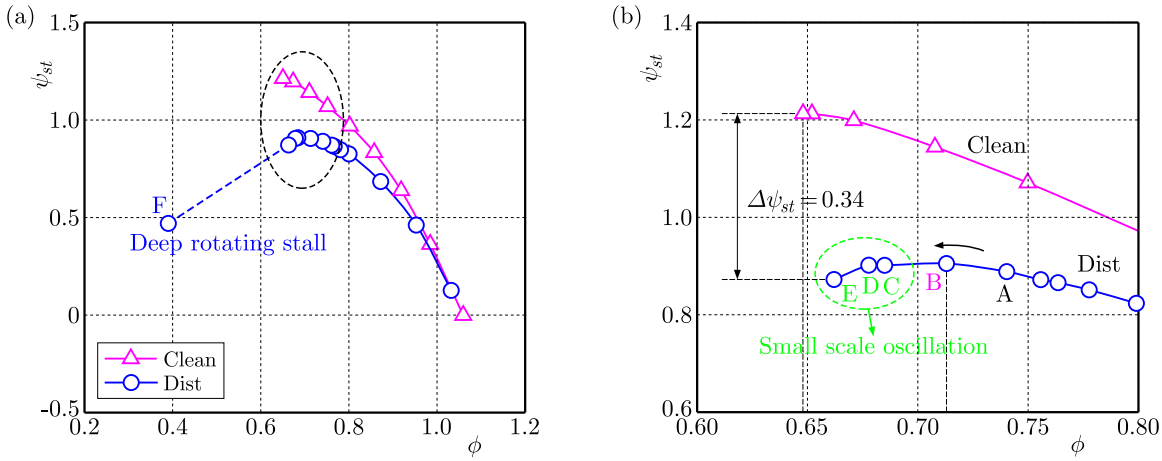

Fig. 9. Comparison of the pressure rise coefficient between the clean inlet and inlet distortion: (a) time-averaged pressure rise coefficient of the compressor, (b) partially enlarged drawing

the dimensionless axial velocity distribution at the rotor inlet of each stage. Figure 11 presents the total pressure distribution at the stator outlet of each stage. Due to the low-pressure distorted region at the tip, the axial velocity near the side of the rotor away from the distorted region (240°) is smaller than that at other circumferential positions of the same blade height while the corresponding incidence is larger and the blade aerodynamic load increases. Therefore, the maximum total pressure is obtained at the root of the stator outlet. Correspondingly, the axial velocity near the rotor entering the distorted region (120°) is larger, the corresponding incidence is smaller, and the blade aerodynamic load decreases. The minimum total pressure is at the tip of the stator outlet. Moreover, as the distorted region transfers downstream, the extreme regions of flow parameters are significantly shifted along the rotating direction due to rotor rotation.

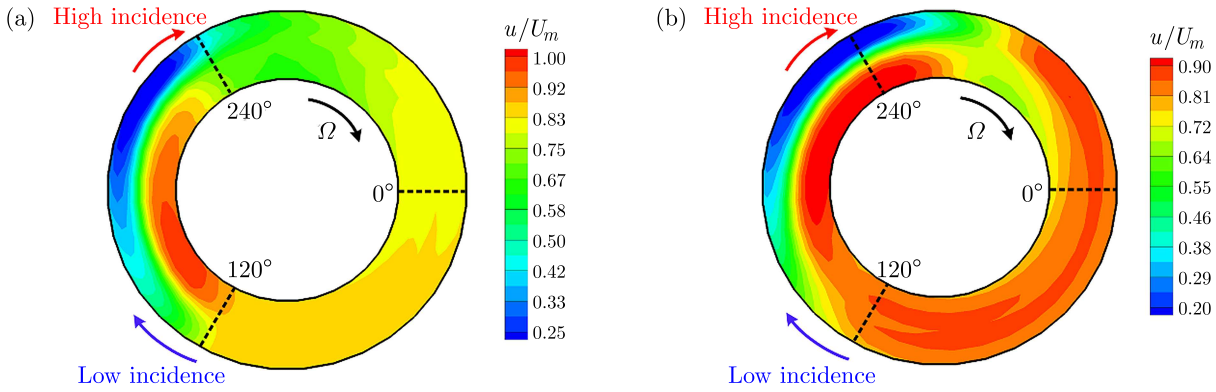

Fig. 10. Distribution of axial velocity at the rotor inlet of each stage at point A: (a) at the R_1 inlet, (b) at the R_2 inlet

The evolution of the internal disturbance in the compressor under a small-scale oscillation is analyzed taking point E as an example. Figure 12 displays the mass flux traces at different circumferential locations near the tip of each stage outlet.

Before the deep stall, some local flow disturbances are generated in the region with the large incidence on the side of the rotor leaving the distorted region. The flow disturbances are suppressed and even disappeared in the region with the small incidence on the side of the rotor entering the distorted region. Therefore, the circumferential propagation of the local flow disturbance presents great periodicity due to the circumferential inlet distortion. The stability of the whole compressor depends on the balance between the disturbance decay in the

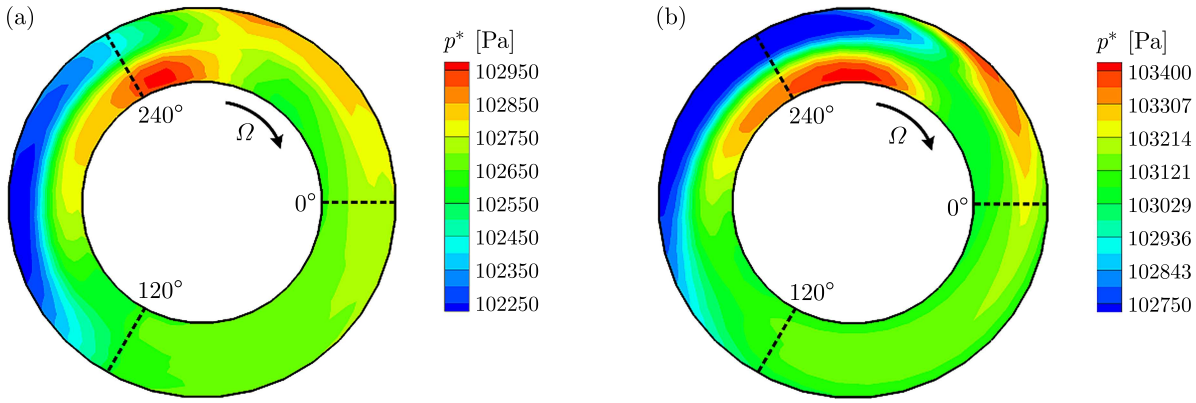

Fig. 11. Distribution of total pressure at each stage outlet at point A: (a) at the S_1 outlet, (b) at the S_2 outlet

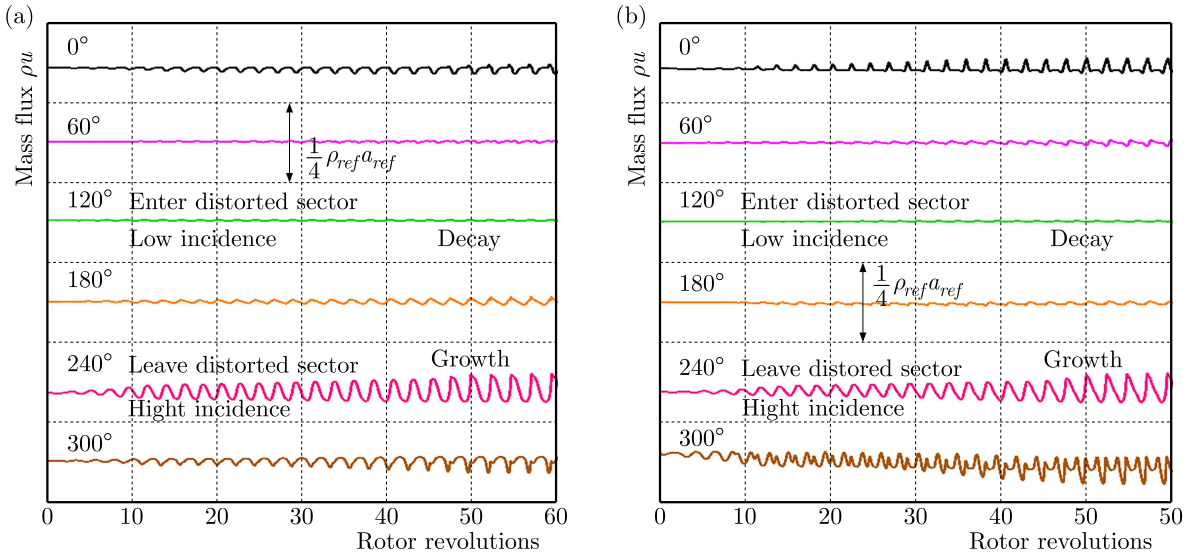

Fig. 12. Mass flux traces at different circumferential locations near the tip of each stage outlet: (a) at the S_1 outlet, (b) at the S_2 outlet

non-distorted region and the disturbance growth in the distorted region. The above phenomenon has also been confirmed in the experimental research on the aerodynamic stability of a five-stage high-pressure compressor by Jahnen *et al.* (1999) and a BLI fan by Perovic *et al.* (2019). This supports the reliability of the model to predict the stall inception of the compressor with the complex inlet distortion.

Figure 13 displays the total pressure traces near the tip of the compressor inlet at different circumferential locations during the stall. Figure 14 shows the time-frequency characteristics of the total pressure near the tip in the non-distorted region (0°) and distorted region (180°). The amplitude-frequency characteristic of the dynamic pressure signal is calculated by the fast Fourier transform (FFT). It is found that the frequency of the stall cell predicted by the model with the combined distortion is 4.7 Hz (35% of the rotor speed), which is close to the value (38% of the rotor speed) with the clean inlet. This phenomenon suggests that the frequency of the final stall cell is not significantly influenced by the distorted inlet. Its frequency is mainly determined by the inherent parameters of the compression system. The conclusion is also supported by the early experimental results of Fortin and Moffatt (1990). Besides, it can be seen in Fig. 14 that the amplitude of the stall cell in the distorted region is stronger than that in the undistorted region.

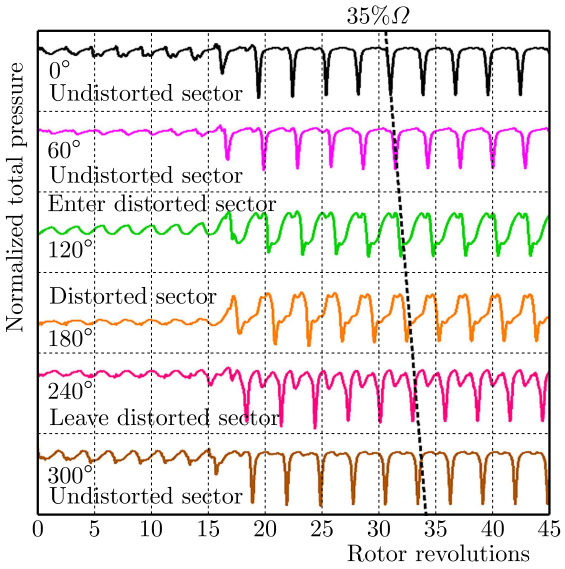

Fig. 13. Total pressure traces near the tip of the compressor inlet at different circumferential locations during the stall

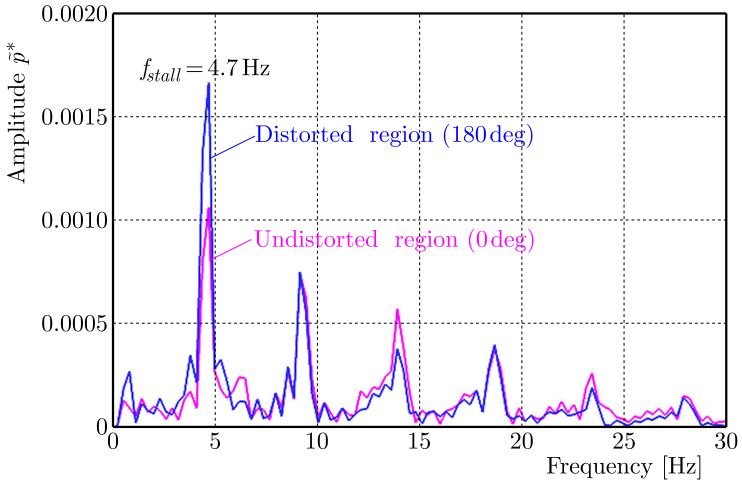

Fig. 14. Amplitude-frequency characteristics of total pressure near the tip of the compressor inlet

Despite the lack of experimental data, the predicted results are consistent with the basic understanding of the early classical experimental research, and the ability of the model to quantitatively describe the flow instability process with the complex inlet distortion can be preliminarily verified.

4. Conclusions

This study develops a three-dimensional unsteady numerical model based on the body force model to analyze the dynamic stall process of a multistage axial compressor in various inlet conditions. The boundary effect of blades is transformed into distributed force source terms in the model. A quasi-steady blade force is constructed directly from the steady circumferential momentum equation combined with the deviation angle and the loss model in the through flow theory. Subsequently, an instantaneous blade force is modeled by a first-order lagging response function to quantify the dynamic response of the blade force to the upstream disturbance during the dynamic stall of the compressor.

According to the abundant experimental data of a two-stage axial compressor with a clean inlet, the capability of the developed model to quantitatively describe the dynamic stall process in a multistage compressor is evaluated. The calculated main performances and characteristic frequency of the dynamic stall evolution are in line with the experimental results, which proves the model has great effectiveness in predicting the compressor performance and the dynamic stall process with a low computational cost.

The dynamic stall process of the compressor with a combined radial-circumferential total pressure inlet distortion is also simulated by the developed model, which reveals that the model has potential for describing the dynamic stall process with the complex inlet distortion. The calculation shows a large non-uniformity of the rotor inlet incidence due to the inlet distortion in the critical stall condition, which has a considerable influence on the development of the local flow disturbance before the stall. The flow disturbance formed in the region of the high incidence decays sharply in the region of the low incidence. Once the balance between the disturbance decay in the non-distorted region and the disturbance growth in the distorted region is disturbed, a full rotating stall occurs. Besides, the frequency of the stall cell predicted by the model with the combined distortion is close to that with the clean inlet. The above-predicted results are consistent with the basic understanding of the early classical experimental research. The ability of the model for qualitative description of the flow instability process with the complex inlet distortion can be preliminarily verified.

Further experimental investigation on the inlet distortion will be promoted to improve simulation of the model. Besides, the time marching scheme for unsteady simulations can be improved by introducing acceleration techniques when the model is used for compressors with more stages and computational grids. Meanwhile, the proposed model focuses on the compressor with the long-scale modal wave stall initiation. The description of the short-scale disturbance stall initiation process of the high-speed compressor is not involved and remains to be further improved in the future work.

Funding

The research was funded by the National Science and Technology Major Project of China (grant No. 2017-II-0004-0017).

References

1. Cao T., Hield P., Tucker P.G., 2017, Hierarchical immersed boundary method with smeared geometry, *Journal of Propulsion and Power*, **33**, 5, 1151-1163
2. Creveling H.F., Carmody R.H., 1968, Axial-flow compressor computer program for calculating off design performance, *NASA CR*, **72472**
3. Day J., 2016, Stall, surge, and 75 years of research, *Journal of Turbomachinery*, **138**, 1, 011001
4. Edwards J.R., 1997, A low-diffusion flux-splitting scheme for Navier-Stokes calculations, *Computers and Fluids*, **26**, 6, 635-659
5. Fortin J., Moffatt W.C., 1990, Inlet flow distortion effects on rotating stall, *ASME International Gas Turbine and Aeroengine Congress and Exposition*, **90-GT-215**
6. Gallimore S.J., 1986, Spanwise mixing in multistage axial flow compressors: Part II – Throughflow calculations including mixing, *Journal of Turbomachinery*, **108**, 1, 10-16
7. Gallimore S.J., Cumpsty N.A., 1986, Spanwise mixing in multistage axial flow compressors: Part I – Experimental investigation, *Journal of Turbomachinery*, **108**, 1, 2-9
8. Gong Y., Tan C.S., Gordon K.A., Greitzer E.M., 1999, A computational model for short--wavelength stall inception and development in multistage compressors, *Journal of Turbomachinery*, **121**, 4, 726-734

9. Guo J., Hu J., 2018, A three-dimensional computational model for inlet distortion in fan and compressor, *Proceedings of the Institution of Mechanical Engineers, Part A: Journal of Power and Energy*, **232**, 2, 144-156

10. Hu J., Peters T., Fottner L., 1999, Numerical simulation of flow instabilities in high speed multistage compressors, *Journal of Thermal Science*, **8**, 1, 23-31

11. Huang Q., Zhang M., Zheng X., 2019a, Compressor surge based on a 1D-3D coupled method – Part 1: Method establishment, *Aerospace Science and Technology*, **90**, 342-356

12. Huang Q., Zhang M., Zheng X., 2019b, Compressor surge based on a 1D-3D coupled method – Part 2: Surge investigation, *Aerospace Science and Technology*, **90**, 289-298

13. Jahnen W., Peters T., Fottner L., 1999, Stall inception in a 5-stage HP-compressor with increased load due to inlet distortion, *ASME International Gas Turbine and Aeroengine Congress and Exhibition*, **99-GT-440**

14. Johnsen I.A., Bullock R.O., 1965, Aerodynamic design of axial-flow compressors, *NASA SP-36*

15. Longley J.P., 2007, Calculating stall and surge transients, *ASME Turbo Expo*, Montreal, 125-136

16. Mao Y., Dang T., 2020, A three-dimensional body-force model for nacelle-fan systems under inlet distortions, *Aerospace Science and Technology*, **106**, 106085

17. Marble F.E., 1964, Three-dimensional flow in turbomachines, [In:] *Aerodynamics of Turbines and Compressors. (HSA-1)*, Vol. 1, William R. Hawthorne (Edit.), Princeton: Princeton University Press

18. Perovic D., Hall C.A., Gunn E.J., 2019, Stall inception in a boundary layer ingesting fan, *Journal of Turbomachinery*, **141**, 9, 091007

19. Righi M., Pachidis V., Könözsy L., Pawsey L., 2018, Three-dimensional through-flow modelling of axial flow compressor rotating stall and surge, *Aerospace Science and Technology*, **78**, 271-279

20. Rosa Taddei S., 2021, A novel blade force approach to two-dimensional meanline simulation of transonic compressor rotating stall, *Aerospace Science and Technology*, **111**, 106509

21. Uranga A., Drela M., Greitzer E.M., Titchener N.A., Lieu M.K., Siu N.M., Huang A.C., Gatlin G.M., Hannon J.A., 2014, Preliminary experimental assessment of the boundary layer ingestion benefit for the D8 aircraft, *52nd Aerospace Sciences Meeting*, **AIAA 2014-0906**

22. Wang M., Sun H., Wang Z., Wang Y., Magagnato F., Luan Y., 2020, Numerical investigation of the effects of system volume and average mass flow on the surge characteristics of an axial compressor, *Aerospace Science and Technology*, **106**, 106172

23. Zhang W., Vahdati M., 2020, Stall and recovery process of a transonic fan with and without inlet distortion, *Journal of Turbomachinery*, **142**, 1, 011003

Manuscript received January 19, 2023; accepted for print September 2, 2023

JOURNAL OF THEORETICAL AND APPLIED MECHANICS
62, 1, pp. 47-60, Warsaw 2024
https://doi.org/10.15632/jtam-pl/175127

LABORATORY STUDY OF DYNAMIC FRACTURE IN PRE-DRILLED BOREHOLES AND ASSOCIATED HOST ROCK BEHAVIOUR

Cheng Guo Zhang
College of Energy and Mining Engineering, Shandong University of Science and Technology, Qingdao, China, and State Key Laboratory of Mining Disaster Prevention and Control Co-founded by Shandong Province and the Ministry of Science and Technology, Shandong University of Science and Technology, Qingdao, China

Xuebin Gu
College of Energy and Mining Engineering, Shandong University of Science and Technology, Qingdao, China

Weiyao Guo
College of Energy and Mining Engineering, Shandong University of Science and Technology, Qingdao, China, and State Key Laboratory of Mining Disaster Prevention and Control Co-founded by Shandong Province and the Ministry of Science and Technology, Shandong University of Science and Technology, Qingdao, China, and Graduate School of Engineering, Nagasaki University, Nagasaki, Japan
corresponding authors Weiyao Guo, e-mail: 363216782@qq.com

Xufei Gong
College of Energy and Mining Engineering, Shandong University of Science and Technology, Qingdao, China, and State Key Laboratory of Mining Disaster Prevention and Control Co-founded by Shandong Province and the Ministry of Science and Technology, Shandong University of Science and Technology, Qingdao, China

Hengyu Fang
College of Energy and Mining Engineering, Shandong University of Science and Technology, Qingdao, China

He Huang
Nantun Coal Mine, Yankuang Energy Group Co., Ltd., Jining, China

To better understand the influence of the openings and their relationship with the host rock, laboratory tests were conducted on a range of sandstone specimens with different proportions of D/H (hole diameter/specimen height) ratio. Acoustic emission (AE) and video monitoring were used to capture the rock specimen responses. The results showed that if the D/H ratio was less than 0.3, the fracture mode occurred in the hole, indicating that this was an appropriate ratio. In addition, the "short quiet period" of AE energy can be used as a precursor for determining the burst in the opening.

Keywords: rock burst, pre-drilled hole, size ratio, acoustic emission

1. Introduction

The rock burst is one of the most challenging topics in underground excavation projects, particularly under high stress. It often occurs suddenly and is accompanied by violent rock ejection, which seriously threatens safety and productivity (Zhao *et al.*, 2021; Chen *et al.*, 2022; Zhang *et al.*, 2022). To study the mechanism of rock burst, many extensive researches were conducted in the literature previously, using methodologies including numerical simulation (Baranowski *et al.*, 2022), analytical analysis (Kucewicz *et al.*, 2023) and laboratory tests (Farhadian, 2021). Among them, laboratory testing on rock specimens in various conditions are a common method to establish the first understanding of rock behaviour under different types of loading.

In the rock burst related laboratory testing, uniaxial, biaxial and triaxial are common loading types used to specimens (Huang *et al.*, 2022; Liu *et al.*, 2021). In particular, the relationship between rock failure and acoustic emission characteristics are studied for identifying fracture and energy release mechanisms (Dong *et al.*, 2021; Chen *et al.*, 2023). For example, there are studies on the rock unit near the excavation opening to examine the relationship between the stress gradient, loading rate and temperature and the deformation (Su *et al.*, 2017, 2019). Faradonbeh *et al.* (2020) established a comprehensive database of true-triaxial unloading tests on rocks with a wide range of properties. He *et al.* (2012) adopted a self-developed triaxial loading system to study the role of confinement to rock burst initiation in different types of rock.

Another group of tests is focused on the borehole behaviour in a rock block under different types of loading, simulating the rock burst condition in the holes. In those tests, the excavations and nearby rock were mainly simplified into small-sized specimens to study failure laws of the opening during the loading process. The effect of the opening shape have also been studied in the literature. For example, in non-circular cavity research, Wu *et al.* (2019) studied failure characteristics of U-shaped cavities under a uniaxial loading. Luo *et al.* (2019) studied failure characteristics of the D-shaped cavity under the true triaxial loading. In research on circular openings, Hu *et al.* (2019) and Liang *et al.* (2019) studied the biaxial loading of circular caverns, mainly discussing the laws of the acoustic emission and rock burst. Zhang *et al.* (2016) explored the impact of lateral stress on rock bursts in circular caverns under a biaxial loading. Si *et al.* (2018) and Gong *et al.* (2017) studied the rock burst process and failure characteristics of circular caverns under the true triaxial loading.

Apart from the shape of excavations, in small-scale laboratory experimental research, the size effect is a critical factor. For example, Martin (1997) found that as the borehole size increases, the tangential stress at failure approaches the unconfined compressive strength of the material but a significant strength-scale effect is observed for boreholes less than 75 mm in diameter. The ratio of the hole diameter to the specimens size (i.e. size ratio) is closely related to the test results, and it is not fully studied in the previous studies. Therefore, uniaxial loading tests were performed on sandstone specimens with different scales of D/H, while AE and video monitoring were used to capture the response of the rock specimens. The findings of this study are expected to provide a reference for determining the extent of failure of underground openings.

2. Specimen preparation and test setup

2.1. Specimen preparation

Green sandstone samples with uniform texture were selected from a mine site in Shandong Province in China for tests. The material was processed into five specimens with circular holes (30 mm in diameter) according to ISRM's requirements, as shown in Fig. 1 and Table 1. Measuring mechanical parameters, the uniaxial compressive strength was equal to 82 MPa, the elastic modulus has reached 12.8 GPa. The scanning electron microscope (SEM) results show that sandstone has a dense cementation structure with fewer intergranular pores and fissures, indicating that the sandstone has good homogeneity, as shown in Fig. 1c. The five specimens are classified A-E according to the D/H ratio (i.e. hole diameter/height), as shown in Table 1.

2.2. Test system setup

The experimental system, shown in Fig. 2a, consists of the following three parts: loading equipment (RLJW-2000 servo rock-testing machine), an acoustic emission instrument (AMSY-6 acoustic emission detection system produced by Vallen, Germany), and a visual observation system (EOS C100 camera). During the test, two acoustic emission sensors were arranged on

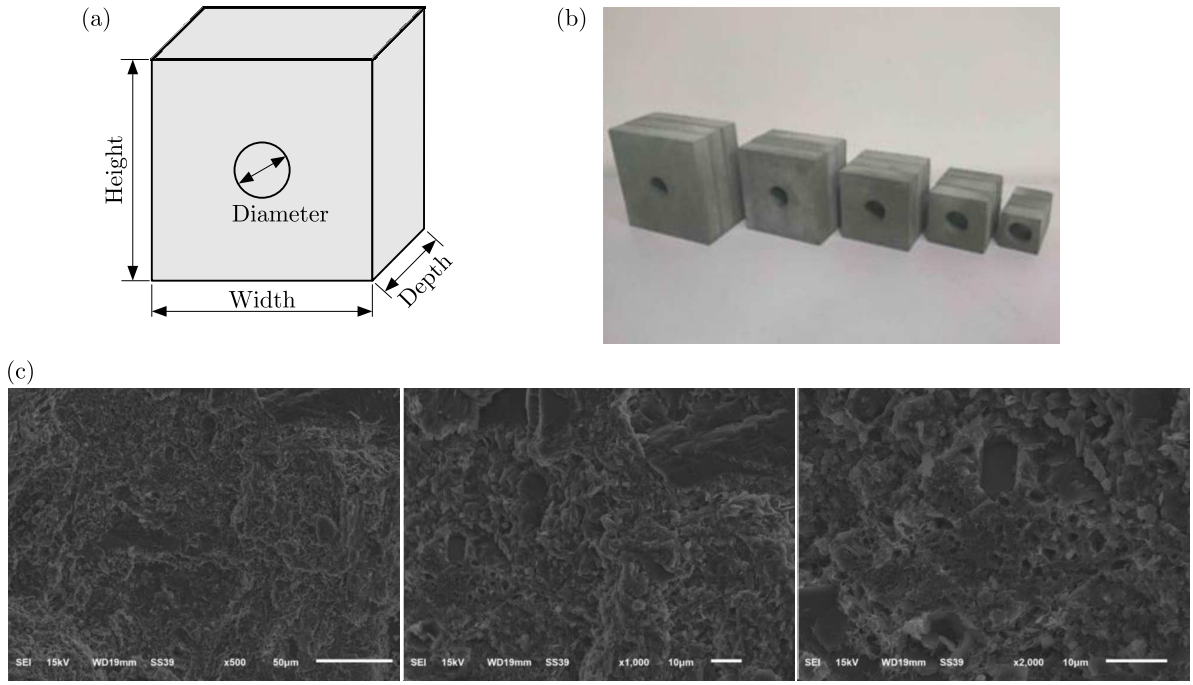

Fig. 1. (a) Geometrical features of the specimen, (b) manufactured specimens and (c) microscopic feature

Table 1. Dimensions of specimens

Type	Height H [mm]	Depth [mm]	Diameter D [mm]	D/H
A	50	30	30	0.6
B	75	30	30	0.4
C	100	30	30	0.3
D	125	30	30	0.24
E	150	30	30	0.2

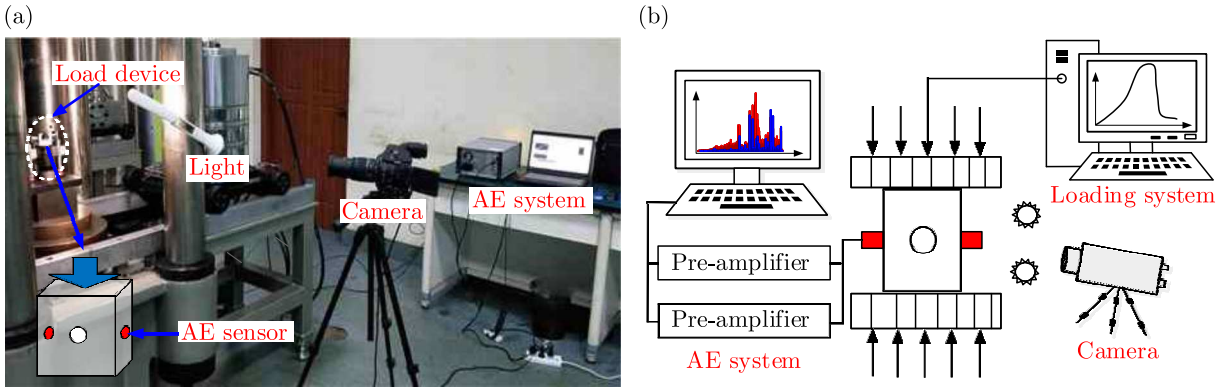

Fig. 2. Experimental system: (a) test system layout, (b) schematic diagram

two non-loading surfaces on the left and right sides of the sample. The sensor layout and loading methods are shown in Fig. 2b. Images of the excavation hole destruction process were obtained by the visual observation system, and the entire test process was recorded.

A displacement control method was used in the uniaxial test. Axial pressure was applied at a loading rate of 0.25 mm/min up to specimen fracture while recording data and images by means of acoustic emission. The acoustic emission threshold equaled 40 dB and the sampling frequency was 10 MHz.

3. Results and analysis

3.1. Variation of mechanical parameters

The stress-strain curves of the specimens under five different D/H ratios are shown in Fig. 3a. The peak stress for each specimen size increased as the D/H ratio decreased from 0.6 to 0.24. The opposite was observed when D/H was equal to 0.2. When the D/H ratio decreased to a certain value, the peak stress no longer significantly changed. When the D/H ratio was 0.6, the peak stress was 19.3 MPa. When the D/H ratio was reduced to 0.3, the peak stress increased to 67.2 MPa. When the D/H ratio was 0.24 or 0.2, the peak stress was 81.2 MPa or 79.1 MPa, as shown in Fig. 3b. The aforementioned data demonstrates that when the D/H ratio reaches 0.24, compared to the uniaxial compressive strength of the complete green sandstone, the difference is within 4% and the peak stress is stable; however, owing to the existence of holes, the overall strength was reduced.

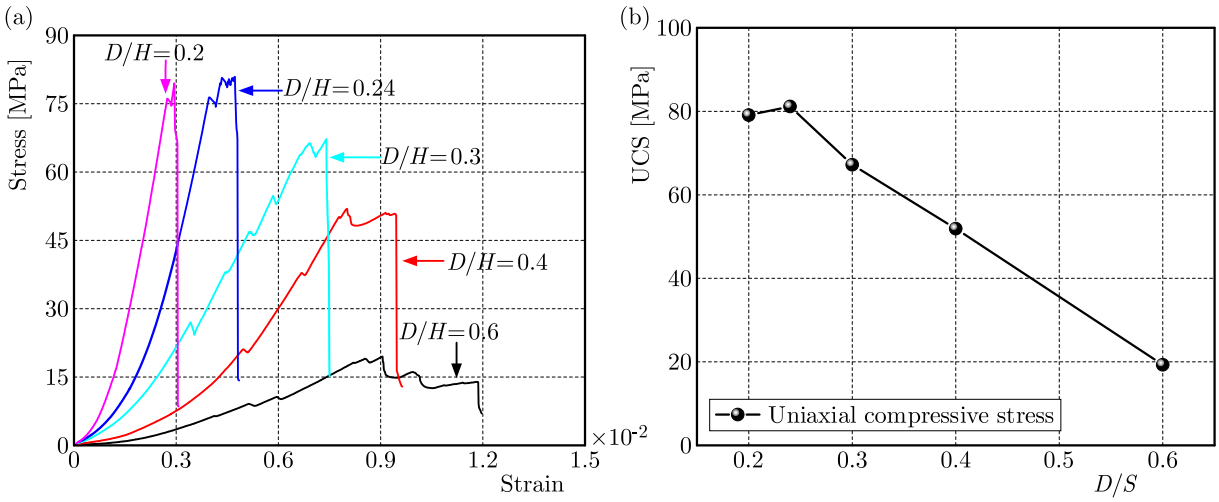

Fig. 3. Stress-strain curve and the UCS of different D/H ratios: (a) stress-strain curve, (b) uniaxial compressive stress

In addition, there were apparent differences in the stress-strain curves for the five D/H ratios. As the D/H ratio decreases, the number of times the stress decreases is gradually reduced, and the stress growth rate gradually increases. For the stress curve before the peak, the D/H value is equal to 0.3 as the threshold value. When the D/H ratio is 0.6 and 0.4, the stress decreases on three occasions in the stress curve, and on five occasions when the D/H value is 0.3. This indicates that when the D/H value is greater than or equal to 0.3, the stress decreases several times and the distribution becomes more uniform. However, when the D/H value is less than 0.3, the number of times the stress decreases is lower and only distributed near the peak. The curves of the D/H ratios of 0.2 and 0.24 both demonstrated a decrease several times near the peak, which is clearly different from the other D/H ratios.

When failure first occurs near a hole, V-shaped breakouts are formed on both sides owing to the stress concentration; however, the specimen remains to have a load-bearing capacity as a whole, and there is no decrease in stress observed in the axial direction. This behaviour is consistent with the findings from previous literature (Si *et al.*, 2018; Gong *et al.*, 2017). Therefore, the main reason for the numerous aforementioned times the stress decreases is the overall rupture of the specimen. When the D/H value is greater than or equal to 0.3, a destruction of the specimen occurs during the stress-loading stage before the peak, and its level is relatively large. When the D/H ratio is 0.24 or 0.2, the loading process was stable in the early stage and there was no main fracture.

3.2. Fracture process of the borehole

Table 2 and Fig. 3 present the relationship between the stress and loading time as well as the corresponding images of the failure process of the five ratio size samples. As shown in Table 2, the number of times the stress decreases is reduced with a decrease in the D/H ratio, and the time of hole failure gradually approaches the time of the stress decrease with a decrease in the D/H ratio. Meanwhile, the degree of hole failure became evident as the D/H ratio decreased.

Table 2. Statistics of hole failure characteristics

D/H	Pre-peak stress drop times	First decrease in stress value	First fracture time of hole	Hole fracture form
0.6	3	161.9	None	Not obvious
0.4	3	218.1	None	Not obvious
0.3	5	198.9	400.5	Slight V-pit
0.24	1	288.8	288.4	Obvious V-pit
0.2	1	254.6	254	Obvious V-pit

As shown in Table 2, when the D/H ratio is greater than or equal to 0.3, stress drop occurs several times in the pre-peak stress curve, but no significant fractures occur in the hole. However, when the D/H ratio is less than or equal to 0.24, the time to fracture and stress decrease are nearly the same.

The following Section provides an analysis based on the data presented in Fig. 4. As shown in Fig. 4a, 4b and 4c, when $D/H = 0.6$, the stress decreases three times in the stress-time curve before the peak. There is no evident change in the hole in the corresponding image record. As shown in Fig. 4a, the extent of cracks above the hole gradually increases. It can be inferred here that the decrease in stress is not related to damage of the hole, but to overall damage of the specimen. When the same D/H value is 0.4, the stress-time curve presents three apparent times of the stress decrease, and then the stress decreases to a lower value; however, the hole does not change during the corresponding time. When the D/H ratio is 0.3, the hole begins to fail. The first decrease in stress and the hole failure occur at 198.9 s and 400.5 s, respectively. The stress decreases five times in the stress curve; however, the hole completely fails only at the fifth decrease in stress. The aforementioned data demonstrates that when the D/H ratio is less than or equal to 0.3, the specimen appears to be integrally damaged, causing a decrease in the stress; the holes are not apparently damaged at this size ratio.

As shown in Fig. 4d and 4e, when the D/H ratio is 0.24 or 0.2, the entire pre-peak stress-time curve is relatively complete, there are no small decreases in the stress, and the fracture form of the hole is more apparent. Combined with the data in Table 2, it was found that when the decrease in stress occurred close to the time of hole failure, the hole damage gradually became more severe as the stress increased until the rock burst.

3.3. Acoustic emission characteristics

3.3.1. Analysis of AE event counts

Figure 5 presents the stress-time and acoustic emission ringing count curves with five ratios. The ringing count is the number of oscillations in the signal that crosses the threshold. It is a parameter that reflects the intensity and frequency of the acoustic emission activity and can be used to reflect the rupture law inside the sample.

As shown in Fig. 5, the acoustic emission pattern of different specimens is similar to that of the stress-strain curve, indicating that the time of stress reduction corresponds to the peak time of ringing counts. There are also several peaks in the ringing counts in regions where there

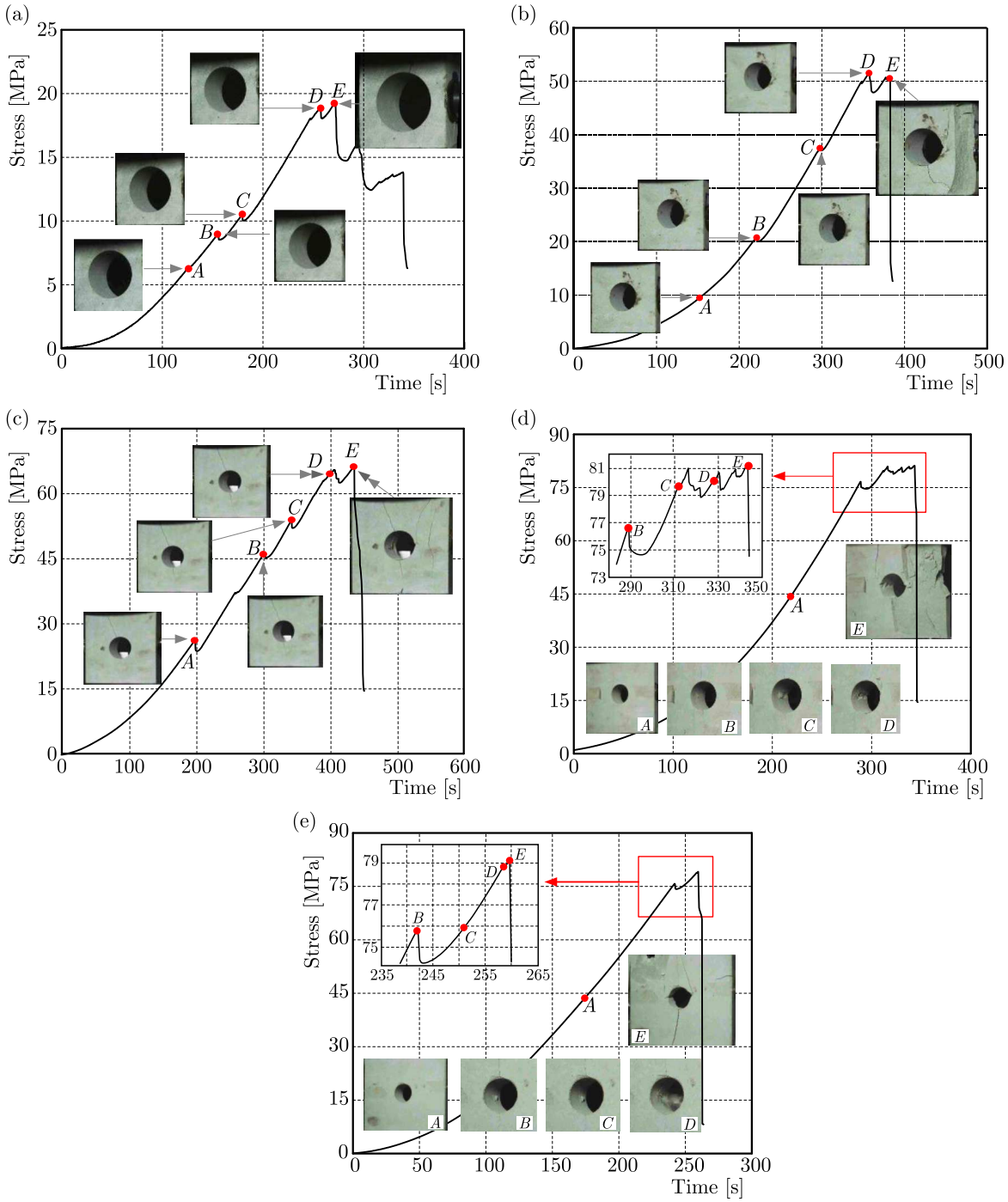

Fig. 4. Failure process of specimens with different D/H ratios: (a) $D/H = 0.6$, (b) $D/H = 0.4$, (c) $D/H = 0.3$, (d) $D/H = 0.24$, (e) $D/H = 0.2$

is no significant stress drop, indicating that the AE is more sensitive to specimen fracture than stress. For example, when the D/H ratio is 0.6, the curve has three distinct stress drop times before it peaks, with distinct ringing counts occurring at the corresponding times.

By combining the data in Figs. 4 and 5, it was found that the rule of hole failure was also consistent with the rule of ringing technology. When the D/H ratio was greater than or equal to 0.3, the ringing count increased several times during the pre-peak period. Based on the decreases in the stress curve and the damage indicated by the image of the hole, it was found

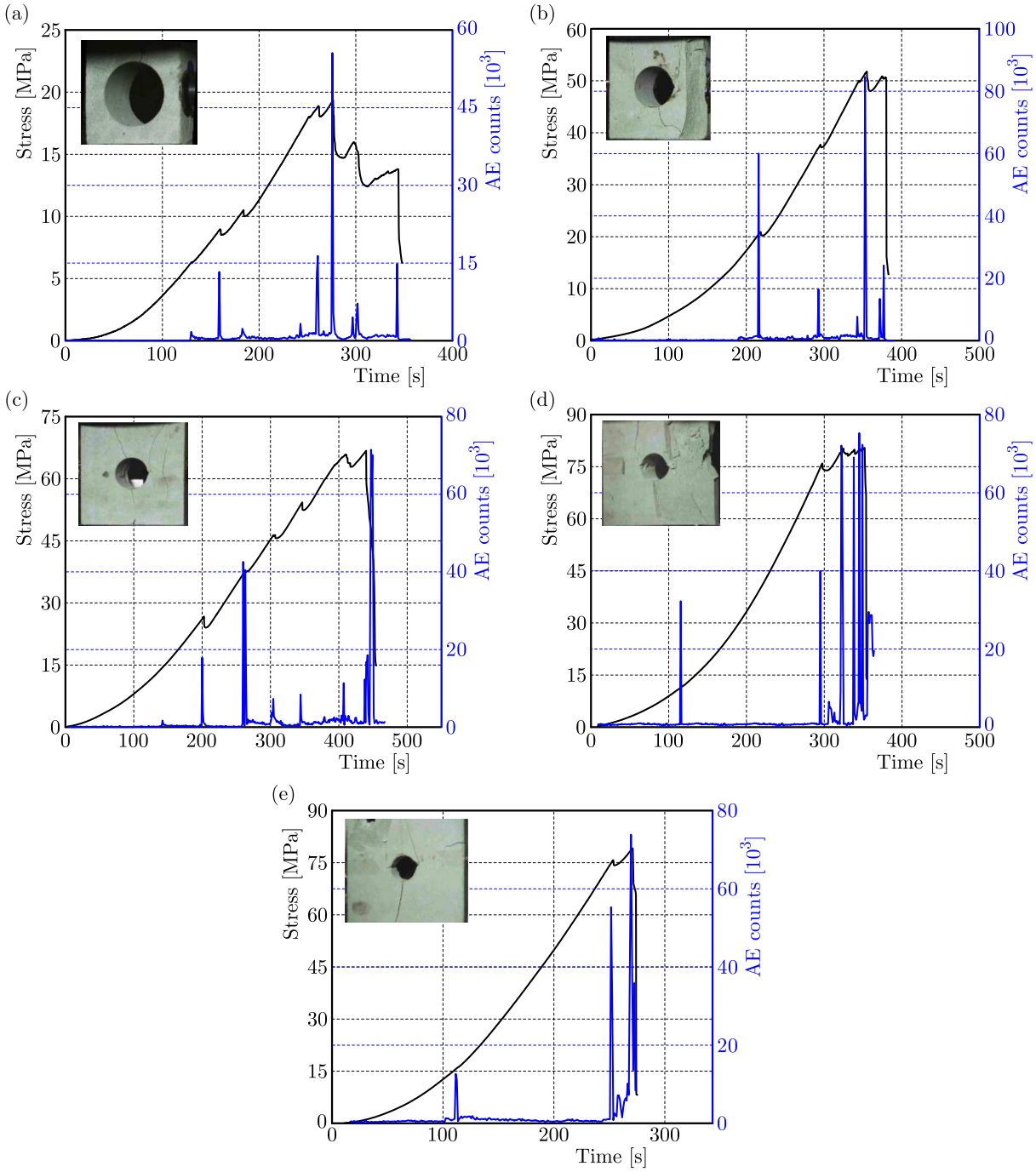

Fig. 5. Stress-time and acoustic emission ringing count curves: (a) $D/H = 0.6$, (b) $D/H = 0.4$, (c) $D/H = 0.3$, (d) $D/H = 0.24$, (e) $D/H = 0.2$

that the peak of the ringing count was mainly owing to the overall damage of the sample, and the hole damage in the entire process was not apparent.

When the D/H ratio was 0.24 and 0.2, the peak of the acoustic emission ringing count was mainly concentrated at the time the first decrease occurred, sufficiently corresponding to the hole failure time, which was manifested as a peak of the ringing count when the hole ruptured. At the same time, these two ratios are different from the hole failure law, and there is a count peak in the two ratios before loading. However, the stress curve and hole do not change.

3.3.2. Analysis of AE energy

The stress-time and acoustic emission energy curves under five sizes of ratios are shown in Fig. 6. They were calculated as the area under the detection envelope of the event signal, including the count rate and total count. The acoustic emission energy rate represents the amount of energy released per unit time during the test, and the cumulative energy is the sum of the released energies. According to the change law of acoustic emission energy, the destruction process can be divided into the three following periods: quiet, development, and outbreak or explosion.

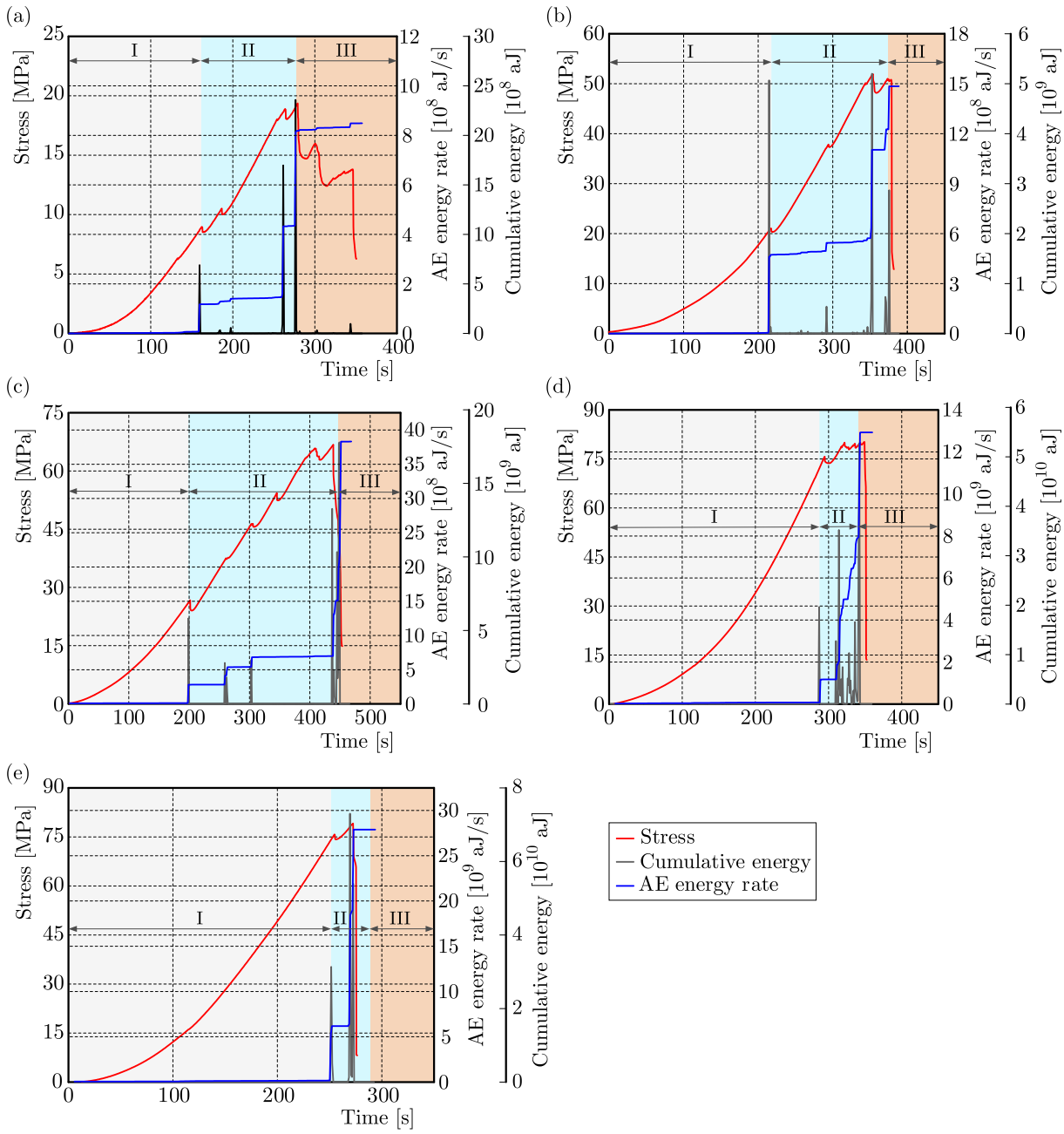

Fig. 6. Stress-time and acoustic emission energy curves: (a) $D/H = 0.6$, (b) $D/H = 0.4$, (c) $D/H = 0.3$, (d) $D/H = 0.24$, (e) $D/H = 0.2$

(1) Quiet period: When the D/H ratio was 0.6, 0.4, or 0.3, the quiet period accounted for approximately 50% of the loading time, and no apparent changes were observed in the hole ground conditions, the entire sample, and the acoustic emission energy rate. The cumulative energy steadily increased, indicating that no energy was released during this period, which was the energy accumulation period. When the D/H ratio was 0.24 or 0.2, the proportion of quiet periods increased to approximately 80%, and the holes and specimens remained unchanged.

(2) Development period: When the D/H ratio was 0.6, 0.4, or 0.3, the specimen demonstrated large cracks, stress drops occurred where the hole damage was not apparent, the acoustic emission energy rate demonstrated a large sudden increase, and the accumulated energy demonstrated a step growth, which indicated the release of energy owing to the overall destruction of the sample. When the D/H ratio was 0.24 or 0.2, the holes were gradually destroyed, the acoustic emission energy rate increased, and the accumulated energy gradually increased in steps, indicating that the hole destruction process was accompanied by an energy release. A low level appeared after the energy rate suddenly increased with the energy rate and the step-like cumulative energy indicating that there was a "short quiet period" of acoustic emission energy.

(3) Explosion period: The specimen had the greatest degree of damage in this period; the stress reached its peak, the acoustic emission energy rate sharply increased, and the cumulative energy increased approximately linearly and reached a maximum. When the D/H ratio was 0.6 or 0.4, macroscopic cracks appeared on the surface of the specimen, but the hole did not show significant V-pit damage. When the D/H ratio was 0.3, 0.24, or 0.2, the specimen was severely destroyed at the hole and, eventually, the whole specimen was destroyed.

The aforementioned analysis demonstrates that with a decrease in the D/H ratio, the time of the sudden increase in the acoustic emission energy rate gradually shifts back, indicating that the specimen transfers from overall damage to the hole damage. A similar test by Liu and Li (2010) found that the acoustic emission energy was basically unchanged before the hole was destroyed, and the acoustic emission energy rate suddenly increased when the hole began to break. In this study, the same rule was found for samples with D/H ratios of 0.24 and 0.2. At the same time, from the beginning of the hole destruction to the occurrence of rock bursting, there was a short quiet period of acoustic emission energy; after several conversions of the "energy peak-short quiet period", rock bursting occurred in the sample. This indicates that the "short quiet period" of acoustic emission energy in the development period can be used as a precursor for bursts in the opening.

4. Discussion

4.1. Failure characteristics in different hole tests and the damage mechanism

Table 3 lists the data of the hole fracture form under different D/H ratios. As the D/H ratio decreases from 0.5 to 0.21, the specimens show significant V-shaped pit damage, i.e., red sandstone and granite ($D/H = 5$). V-shaped pits were formed on both sides of the opening wall and it extended along the axial direction of the hole, which is consistent with field observations (Zhang *et al.*, 2012). In this paper, no significant V-shaped pit was exhibited when D/H was greater than 0.3, which may be related to stress conditions. The hole test can be considered as a planar strain problem, ignoring deformation in the axial direction of the hole. When the specimen is under biaxial stress, the horizontal stress increases the overall stability of the specimen, leading to destruction of the hole wall under the maximum tangential stress. Under a uniaxial loading, a specimen with a large D/H ratio corresponds to a larger strain, which can easily lead to an overall splitting damage of the specimen.

Table 3. Comparison of the hole test with different D/H ratios

D/H	0.5	0.5	0.39
Rock type	Red sandstone	Granite	Granite
Loading method	True triaxial (Gong *et al.*, 2017)	True triaxial (Si *et al.*, 2018)	Biaxial (Hu *et al.*, 2019)
Size	100 × 100 × 100 mm	100 × 100 × 100 mm	200 × 20 × 200 mm
Hole failure form			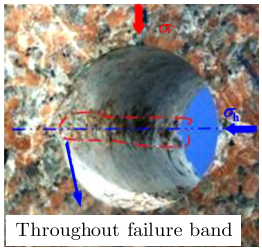
D/H	0.35	0.3	0.21
Rock type	Marble	Granite	Granite
Loading method	Uniaxial (Liu and Li, 2010)	Biaxial (Liang *et al.*, 2019)	Biaxial (Zhang *et al.*, 2016)
Size	100 × 100 × 100 mm	150 × 150 × 150 mm	150 × 150 × 75 mm
Hole failure form	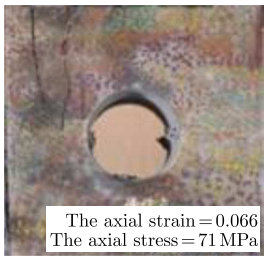	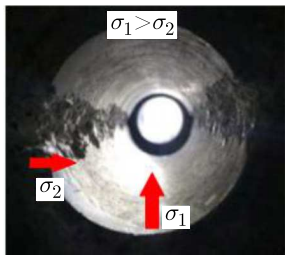	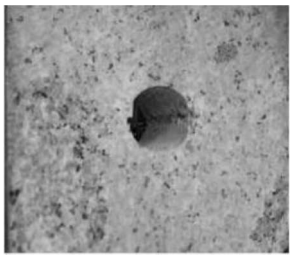

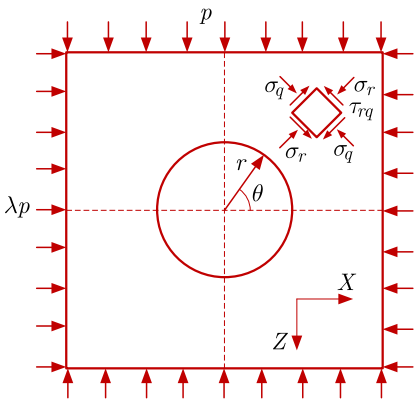

Fig. 7. Tunnel stress calculation model

It is assumed that the rock mass is in a three-way stress state before tunnel excavation, where X and Y are the horizontal, and Z the vertical stress directions. Assuming that the tunnel axial direction is arranged along the Y-direction, the surrounding rock can be regarded as a homogeneous, continuous and isotropic elastomer before damage, and no deformation occurs along the axial direction of the tunnel. Therefore, the problem can be regarded as a planar strain problem and the tunnel stress calculation model can be established as shown in Fig. 7.

By elastic mechanics, the stress in the tunnel rock is

$$\begin{aligned}
\sigma_r &= \frac{p}{2}\Big[(1+\lambda)\Big(1-\frac{R^2}{r^2}\Big)-(1-\lambda)\Big(1-4\frac{R^2}{r^2}+3\frac{R^4}{r^4}\Big)\cos(2\theta)\\
\sigma_\theta &= \frac{p}{2}\Big[(1+\lambda)\Big(1+\frac{R^2}{r^2}\Big)+(1-\lambda)\Big(1+3\frac{R^4}{r^4}\Big)\cos(2\theta)\\
\tau_{r\theta} &= -\frac{p}{2}\Big[(1-\lambda)\Big(1+2\frac{R^2}{r^2}-3\frac{R^4}{r^4}\Big)\sin(2\theta)
\end{aligned} \tag{4.1}$$

where p is the vertical stress, λ is the lateral pressure coefficient, σ_r, σ_θ and $\tau_{r\theta}$ are the radial, tangential and shear stresses of the surrounding rock in polar coordinates, respectively, R is the radius of the tunnel excavation, r is the distance from the rock unit to the center of the tunnel and θ is the angle between the rock unit and the horizontal direction.

From Eqs. (4.1), when $r = R$, only tangential stress exists at the tunnel wall, and the maximum tangential stress is located at the midpoint of the two tunnel gangs ($\theta = 0^\circ$). The maximum tangential stress is

$$\sigma_{\theta_{\max}} = (3-\lambda)p \tag{4.2}$$

When the maximum tangential stress in the tunnel wall exceeds the uniaxial strength of the rock material, the tunnel wall breaks. In the tests in this paper, when D/H was greater than 0.3, the hole wall suffered V-shaped pit damage, indicating that the maximum tangential stress on both sides of the hole exceeded its material strength, leading to failure on both sides of the hole.

4.2. The guiding significance of borehole behaviour

The estimation of the extent of damage is an important aspect in the assessment of underground tunnel and/or roadway stability and its support. Martin *et al.* (1999) calculated the damage range of a circular cavern, and the ratio of the damage range to the radius of the cavern was 1.0-1.5, indicating that the destruction area of the cavern was 1.5 times the excavation radius. The stress in the radial direction of the cavern was distributed in a gradient; the position distant from the cavern gradually reached the original rock stress level, and the surrounding rock gradually reached an undamaged state. There was a transition between the undamaged and damaged areas, called the affected area of damage. This area provides damage energy for the damaged area.

A similar rule was observed in the test in this study, and a certain range was required when a specimen with a fixed hole diameter (30 mm in diameter) failed. Combined with the analysis of the test data in this study, when the D/H ratio was greater than or equal to 0.3, the loading stress curve fluctuated. Visual observations of the hole fracture process confirmed that the integrity of the sample was damaged, and the integrity of the sample damaged the acoustic emission data. Irregular fluctuations occurred when the multiple AE activity peaks occurred during the pre-peak period. When the D/H ratio was less than 0.3, the loading curve stabilized. The video image recordings proved that the first rockburst occurred after the hole fracture, accompanied by acoustic emission activity, indicating that significant hole fracture occurred in the specimen when the D/H ratio was less than 0.3. For a specimen with a fixed hole diameter, the decrease in the D/H ratio was due to an increase in the rock area around the cavern. When the surrounding rock area was small, the hole damage area and the affected area were also small, energy for the hole damage could not be supplied, and stress failure occurred in the entire specimen. When the surrounding rock area was consistent, hole failure required sufficient energy, and the hole first destroyed the specimen and subsequently failed. At the same time, under this test material, the appropriate D/H ratio is 0.4 or 0.2.

5. Conclusions

This study conducted a series of laboratory tests to investigate the failure characteristics of pre-driven openings in rock specimens to better understand the impact of the size factor on the failure process. The main findings are summarized as follows:

- The D/H ratio has a controlling effect on the stress curve, and the overall strength of the specimen decreases with increasing D/H ratios. When the D/H ratio is greater than or equal to 0.3, the stress curve is unstable, and the stress decreases multiple times. When the D/H ratio is less than 0.3, the stress curve is stable without several points of stress reduction.
- The D/H ratio affects the failure pattern of the hole specimen. When the D/H ratio is greater than or equal to 0.3, the hole fracture is not apparent, and the reduction in stress causes the integral fracture of the specimen. When the D/H ratio is less than 0.3, V-shaped pit occurs in the hole, and the hole degradation precedes the overall failure of the specimen.
- The AE evolution characteristics of the hole specimen with different D/H ratios can be categorized into three stages: quiet, development, and explosive. When the D/H ratio is 0.24 or 0.2, the "short quiet period" of AE energy can be used as a precursor for rock bursts.

The results of this study can provide a reference for determining the extent of failure of underground openings. Future studies should consider different loading environments and variations in the specimen size.

Acknowledgements

The research described in this paper was financially supported by Taishan Scholar Engineering Construction Fund of Shandong Province of China (No. tsqn201812071), National Natural Science Foundation of China (No. 52274086), the Major Program of Shandong Provincial Natural Science Foundation (No. ZR2019ZD13), and Education System government-sponsored study-abroad program of Shandong Province.

References

1. Baranowski P., Kucewicz M., Pytlik M., Małachowski J., 2022, Shock-induced fracture of dolomite rock in small-scale blast tests, *Journal of Rock Mechanics and Geotechnical Engineering*, **14**, 6, 1823-1835

2. Chen L.X., Guo W.Y., Jiang Y.J., Tan Y., Zhang Y.Y., Lu D., Han F., 2023, Experimental study on influence of lithology on directional propagation law of type-I cracks, *Journal of Central South University*, DOI: 10.1007/s11771-023-5371-z

3. Chen L.X., Guo W.Y., Zhang D.X., Zhao T.B., 2022, Experimental study on the influence of prefabricated fissure size on the directional propagation law of rock type-I crack, *International Journal of Rock Mechanics and Mining Sciences*, **160**, 105274

4. Dong L., Chen Y., Sun D., Zhang Y., 2021, Implications for rock instability precursors and principal stress direction from rock acoustic experiments, *International Journal of Mining Science and Technology*, **31**, 5, 789-798

5. Faradonbeh R.S., Taheri A., Ribeiro E.S., Karakus M., 2020, Rockburst assessment in deep geotechnical conditions using true-triaxial tests and data-driven approaches, *International Journal of Rock Mechanics and Mining Sciences*, **128**, 104279

6. Farhadian H., 2021, A new empirical chart for rockburst analysis in tunnelling: Tunnel rockburst classification (TRC), *International Journal of Mining Science and Technology*, **31**, 4, 603-610
7. Gong F.Q., Luo Y., Si X.F., Li X.B., 2017, Experimental modelling on rock burst in deep hard rock circular tunnels, *Chinese Journal of Rock Mechanics and Engineering*, **36**, 7, 1634-1648
8. He M.C., Jia X., Coli M., Livi E., Sousa L., 2012, Experimental study of rockbursts in underground quarrying of Carrara marble, *International Journal of Rock Mechanics and Mining Sciences*, **52**, 1-8
9. Hu X., Su G., Chen G., Mei S., Feng X., Mei G., Huang X., 2019, Experiment on rockbursts process of borehole and its acoustic emission characteristics, *Rock Mechanics and Rock Engineering*, **52**, 3, 783-802
10. Huang L., Si X., Li X., Gong F., Luo Y., 2022, Influence of maximum principal stress direction on the failure process and characteristics of D-shaped tunnels, *International Journal of Mining Science and Technology*, **32**, 5, 1125-1143
11. Kucewicz M., Baranowski P., Mazurkiewicz Ł., Małachowski J., 2023, Comparison of selected blasting constitutive models for reproducing the dynamic fragmentation of rock, *International Journal of Impact Engineering*, **173**, 104484
12. Liang P., Zhang Y.B., Tian B.Z, Yao X.L., Sun L., Liu X.X., 2019, Experimental study on energy evolution characteristics in the process of tunnel rock burst, *Chinese Journal of Rock Mechanics and Engineering*, **38**, 4, 736-746
13. Liu D., Ling K., Li D., He M., Li J.,Han Z., Zhang S., 2021, Evolution of anisotropy during sandstone rockburst process under double-faces unloading, *Journal of Central South University*, **28**, 8, 2472-2484
14. Liu Z.W., Li Y.H., 2010, Experimental investigation on the deformation and crack behavior of rock specimen with a hole undergoing uniaxial compressive load, *Engineering Mechanics*, **27**, 8, 133-139
15. Luo Y., Gong F., Liu D., Wang S., Si X., 2019, Experimental simulation analysis of the process and failure characteristics of spalling in D-shaped tunnels under true-triaxial loading conditions, *Tunnelling and Underground Space Technology Incorporating Trenchless Technology Research*, **90**, 42-61
16. Martin C.D., 1997, Seventeenth Canadian Geotechnical Colloquium: The effect of cohesion loss and stress path on brittle rock strength, *Canadian Geotechnical Journal*, **34**, 5, 698-725
17. Martin C.D., Kaiser P.K., McCreath D.R., 1999, Hoek-Brown parameters for predicting the depth of brittle failure around tunnels, *Canadian Geotechnical Journal*, **36**, 1, 136-151
18. Si X.F., Gong F.Q., Luo Y., Li X., 2018, Experimental simulation on rockburst process of deep three-dimensional circular cavern, *Rock and Soil Mechanics*, **39**, 2, 621-634
19. Su G., Jiang J., Feng X., Jiang Q., Chen Z., Mo J., 2019, Influence of loading rate on strainburst: an experimental study, *Bulletin of Engineering Geology and the Environment*, **78**, 5, 3559-3573
20. Su G., Zhai S., Jiang J., Zhang G., Yan L., 2017, Influence of radial stress gradient on strainbursts: An experimental study, *Rock Mechanics and Rock Engineering*, **50**, 10, 2659-2676
21. Wu H., Kulatilake P., Zhao G., Liang W., Wang E., 2019, A comprehensive study of fracture evolution of brittle rock containing an inverted U-shaped cavity under uniaxial compression, *Computers and Geotechnics*, **116**, 1-16
22. Zhang C., Feng X.T., Zhou H., Qiu S., Wu W., 2012, Case histories of four extremely intense rockbursts in deep tunnels, *Rock Mechanics and Rock Engineering*, **45**, 3, 275-288
23. Zhang W., Guo W., Wang Z., 2022, Influence of lateral pressure on mechanical behavior of different rock types under biaxial compression, *Journal of Central South University*, **29**, 11, 3695-3705

24. Zhang Y.B., Li J., Liu X.X., Tian B., 2016, Experimental study of influence of lateral pressure on the characteristics of acoustic emission and damage during the rock burst of tunnel, *Chinese Journal of Underground Space and Engineering*, **12**, 5, 1192-1197

25. Zhao T.B., Xing M.L., Guo W.Y., Wang C.W., Wang B., 2021, Anchoring effect and energy--absorbing support mechanism of large deformation bolt, *Journal of Central South University*, **28**, 2, 572-581

Manuscript received April 10, 2023; accepted for print September 6, 2023

JOURNAL OF THEORETICAL AND APPLIED MECHANICS
62, 1, pp. 61-73, Warsaw 2024
https://doi.org/10.15632/jtam-pl/175498

RESEARCH ON VIBRATION CHARACTERISTICS OF MOTORIZED SPINDLE AT HIGH SPEED BASED ON POWER FLOW

Yudong Bao, Zhentao Zhou, Linkai Wu, Ye Dai

Key Laboratory of Advanced Processing Technology and Intelligent Manufacturing (Heilongjiang Province), Harbin University of Science and Technology, Harbin, China, and
School of Mechanical and Power Engineering, Harbin University of Science and Technology, Harbin, China
corresponding author Yudong Bao, e-mail: baoyudong@hrbust.edu.cn

To show dynamic properties of a motorized spindle at high speed, C01 type motorized spindle bearing-rotor system is used as a study object, and the dynamic model of the bearing-rotor system is established. The method to analyze vibration characteristics of motorized spindles by power flow is proposed, and it is found that the vibration energy is not necessarily considerable at the position where the vibration displacement response is significant. Finally, the system vibration energy distribution under different bearing stiffness is analyzed. The power flow method can analyze the dynamic characteristics of the bearing-rotor system in terms of energy distribution.

Keywords: harmonic response, motorized spindle, natural frequency, power flow, vibration characteristics

1. Introduction

As the core component of CNC machine center processing, the working performance of the motorized spindle will affect quality of processed parts. With the development of motorized spindles towards higher speed and higher precision, higher requirements are also placed on the dynamics of such systems. When the frequency of the external excitation reaches the natural frequency of the motorized spindle, the spindle system will resonate. Especially in high-speed and high-precision machining, the impact of the bearing-rotor system vibration characteristics on dynamic performance of motorized spindles cannot be neglected. For this reason, many scholars have conducted numerous researches on vibration characteristics of the bearing-rotor system.

Cao and Altintas (2007) put forward a general gauge model of the spindle system, which can simulate and analyze bearing performance, dynamic and static characteristics of the spindle. Shi *et al.* (2019) used MATLAB to obtain the natural frequency and critical speed of the motorized spindle, and analyzed the vibration response of the motorized spindle under the influence of unbalanced factors. Bai *et al.* (2018) established a vibration dynamics model of the broach--spindle-bearing dual rotor system under the condition of a high-speed cutting force on the spindle end, and carried out finite element analysis on the natural frequency and mode shape of the motorized spindle. Huang *et al.* (2016) established dynamics of the motorized spindle based on the finite element beam theory model, and obtained the vibration response of the motorized spindle under different rotational speeds, bearing clearance and initial eccentricity. Wang and Peng (2013) obtained the 1st to 5th order natural frequencies and mode shapes of the spindle with vibration modal analysis of the ceramic electro-spindle. Although the motorized spindle bearing-rotor system has a certain research foundation in terms of vibration characteristics, the vibration analysis of the system has not been thoroughly studied from the energy viewpoint.

The vibrating energy information from the shaft system can be reflected by the power flow analysis, and then the motorized spindle vibration characteristics can be described more accurately. Chen *et al.* (2013) established a high-speed motorized spindle power flow model based on the law of energy conservation, and simulated and analyzed the temperature rise of each part of the motorized spindle. Xiao (2021) used the power flow method to study the actual vibration state of the rolling mill. According to the analysis results, vibration suppression measures were taken, and a good vibration suppression effect was achieved. Rejab *et al.* (2014) studied the vibration power flow of the paddy power-train bracket of a passenger car, and obtained the main noise transmission path and resonance frequency. Qiao *et al.* (2016) used the power flow method combined with vibration energy to evaluate active vibration isolation performance of rotating machinery, and proposed an indirect measurement method related to power flow and vibration energy.

By analyzing the literature, it can be seen that the power flow method can be combined with data visualization means to visually describe the vibration energy distribution pattern and vibration transmission path in mechanical structures, which can be used as a reference for analyzing system characteristics or vibration isolation and suppression capability. The displacement response is usually a localized indicator of the structure, while the power flow response can provide global information. The power flow is very sensitive to changes in structural parameters and damage relative to the displacement response. By analyzing the path and distribution of the power flow, the load transfer mechanisms and energy flow paths within the structure can be better understood, and the energy of the vibration source entering the end of the spindle through different transfer paths can be reduced to increase the machining accuracy. Thus, it has great application and research space in analyzing system structural characteristics and fault and damage diagnosis.

Therefore, this paper introduces power flow in the study of motorized spindle vibration characteristics, takes C01 type motorized spindle bearing-rotor system as the research object. Then the first six-order natural frequencies and mode shapes of the motorized spindle are obtained by simulation, and the modal analysis test bench is set up to confirm correctness of the simulating results.

2. Mathematical model

2.1. Structural analysis of the motorized spindle

Motorized spindles primarily consist of bearings, motor, spindle, cooling system, tool changing system, sealing structure, etc. The motor, spindle and bearings are the core processing components of the motorized spindle. To analyze dynamic characteristics of the motorized spindle, the corresponding dynamic model needs to be established first (Gao *et al.*, 2020). Combined with the structure of the motorized spindle, the rotor of the motor is fixed on the main shaft to form the rotor part, and the two ends of the rotor are supported by bearings, which are a typical rotor support system. Therefore, the rotor dynamics theory is used to model the motorized spindle system.

The cross-sectional view and node division of C01 type motorized spindle is shown in Fig. 1. The part circled by the red frame in the figure is the rotating body of the motorized spindle, and it is also the bearing-rotor system simulated in this paper. The bearing-rotor system obtained after node division is divided into 23 nodes and 22 shaft elements. The properties of each beam element are defined based on length, diameter and material properties of the corresponding shaft elements, then rigid disc elements are superimposed at appropriate positions to represent the concentrated mass.

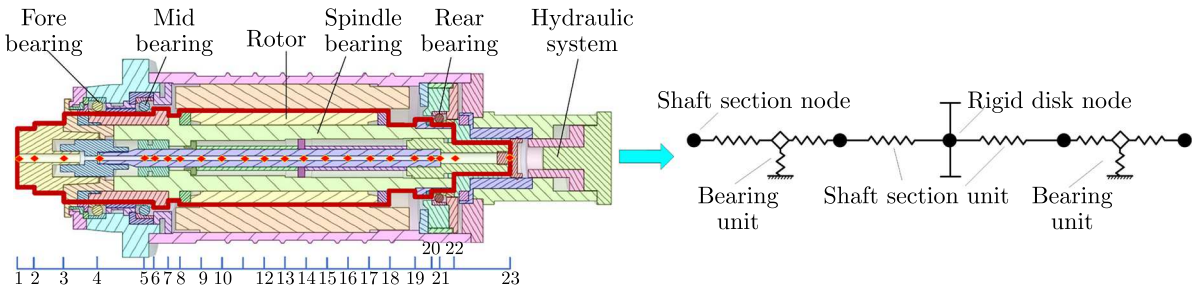

Fig. 1. Motorized spindle rotor system and the simplified model

2.2. Quasi-static model of the angular contact ball bearing

After the bearing is externally loaded, the relative position of the center of the rolling element and the curvature center of the inner and outer rings will change, as shown in Fig. 2.

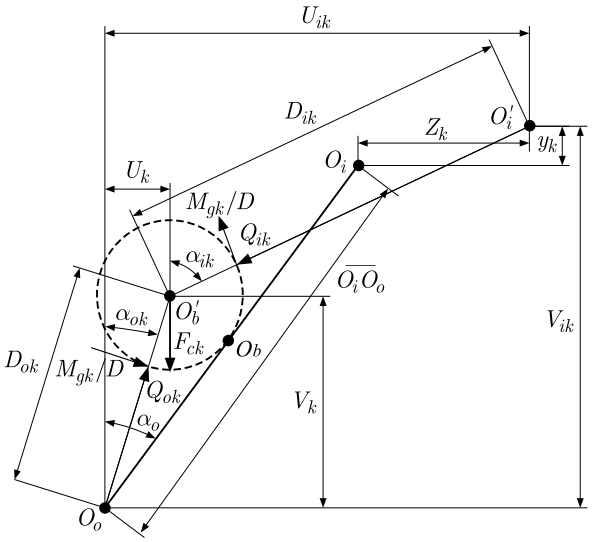

Fig. 2. Bearing inner ring curvature center change and the force diagram

The forces and torques exerted on the bearing ring (Yang *et al.*, 2022) are

$$F_{xi} = \sum_{k=1}^{N}\left(Q_{ik}\sin\alpha_{ik} + \frac{M_{gk}}{D}\cos\alpha_{ik}\right) \qquad F_{xo} = \sum_{k=1}^{N}\left(Q_{ok}\sin\alpha_{ok} + \frac{M_{gk}}{D}\cos\alpha_{ok}\right)$$

$$F_{yi} = \sum_{k=1}^{N}\left(Q_{ik}\cos\alpha_{ik} - \frac{M_{gk}}{D}\sin\alpha_{ik}\right)\cos\varphi_k$$

$$F_{yo} = \sum_{k=1}^{N}\left(-Q_{ok}\cos\alpha_{ok} - \frac{M_{gk}}{D}\sin\alpha_{ok}\right)\sin\varphi_k$$

$$F_{zi} = \sum_{k=1}^{N}\left(Q_{ik}\cos\alpha_{ik} - \frac{M_{gk}}{D}\sin\alpha_{ik}\right)\sin\varphi_k$$

$$F_{zo} = \sum_{k=1}^{N}\left(-Q_{ok}\cos\alpha_{ok} - \frac{M_{gk}}{D}\sin\alpha_{ok}\right)\sin\varphi_k \tag{2.1}$$

$$M_{yi} = \sum_{k=1}^{N}\left[r_{ic}\left(Q_{ik}\sin\alpha_{ik} + \frac{M_{gk}}{D}\cos\alpha_{ik}\right) - f_i M_{gk}\right]\sin\varphi_k$$

$$M_{yo} = \sum_{k=1}^{N}\Big[r_{oc}\Big(Q_{ok}\sin\alpha_{ok} + \frac{M_{gk}}{D}\cos\alpha_{ok}\Big) - f_o M_{gk}\Big]\sin\varphi_k$$

$$M_{zi} = -\sum_{k=1}^{N}\Big[r_{ic}\Big(Q_{ik}\sin\alpha_{ik} + \frac{M_{gk}}{D}\cos\alpha_{ik}\Big) - f_i M_{gk}\Big]\cos\varphi_k$$

$$M_{zo} = \sum_{k=1}^{N}\Big[r_{oc}\Big(Q_{ok}\sin\alpha_{ok} + \frac{M_{gk}}{D}\cos\alpha_{ok}\Big) - f_o M_{gk}\Big]\cos\varphi_k$$

where O_i, O_o and O_b represent the initial center of curvature of the inner and outer raceways of the bearing and the center of the rolling element, and refer to the center of the rolling element and the center of curvature of the inner ring raceway after the bearing is deformed by the force. U_{ik} and V_{ik} are the distance between the centers of curvature of the inner and outer ring raceways after loading, U_k and V_k represent the distance between the center of the rolling element and the curvature centers of the inner and outer ring raceways after loading, and the subscript k represents the k-th rolling element. α_0 is the initial contact angle of the bearing, α_{ik} and α_{ok} represent the contact angle of the inner and outer raceways after deformation under the load. The contact deformation n of the inner and outer ring is set as δ_{ik} and δ_{ok}, and rolling body diameter is expressed as D. Q_{ik} is the action force applied to the rolling element by the inner ring, and Q_{ok} is the force exerted on the rolling element by the outer ring. M_{gk} is the torque acting on the rolling element, and F_{ck} is the centrifugal force of the rolling element.

According to the geometric relationship, α_{ik} and α_{ok} can be represented by U_k and V_k

$$\begin{aligned} \sin\alpha_{ok} &= \frac{U_k}{(f_o-0.5)D+\delta_{ok}} & \cos\alpha_{ok} &= \frac{V_k}{(f_o-0.5)D+\delta_{ok}} \\ \sin\alpha_{ik} &= \frac{U_{ik}-U_k}{(f_i-0.5)D+\delta_{ik}} & \cos\alpha_{ik} &= \frac{V_{ik}-V_k}{(f_i-0.5)D+\delta_{ik}} \end{aligned} \tag{2.2}$$

The relationship between bearing the deformation and applied force can be expressed as

$$\mathbf{F} = \mathbf{K}\boldsymbol{\delta} \tag{2.3}$$

The stiffness matrix can be obtained by taking partial derivative of Eq. (2.3) with respect to the deformation $\boldsymbol{\delta} = [\delta_x, \delta_y, \delta_z, \gamma_y, \gamma_z]$

$$\mathbf{K} = \begin{bmatrix} \dfrac{\partial F_x}{\partial \delta_x} & \dfrac{\partial F_x}{\partial \delta_y} & \dfrac{\partial F_x}{\partial \delta_z} & \dfrac{\partial F_x}{\partial \gamma_y} & \dfrac{\partial F_x}{\partial \gamma_z} \\ \dfrac{\partial F_y}{\partial \delta_x} & \dfrac{\partial F_y}{\partial \delta_y} & \dfrac{\partial F_y}{\partial \delta_z} & \dfrac{\partial F_y}{\partial \gamma_y} & \dfrac{\partial F_y}{\partial \gamma_z} \\ \dfrac{\partial F_z}{\partial \delta_x} & \dfrac{\partial F_z}{\partial \delta_y} & \dfrac{\partial F_z}{\partial \delta_z} & \dfrac{\partial F_z}{\partial \gamma_y} & \dfrac{\partial F_z}{\partial \gamma_z} \\ \dfrac{\partial M_y}{\partial \delta_x} & \dfrac{\partial M_y}{\partial \delta_y} & \dfrac{\partial M_y}{\partial \delta_z} & \dfrac{\partial M_y}{\partial \gamma_y} & \dfrac{\partial M_y}{\partial \gamma_z} \\ \dfrac{\partial M_z}{\partial \delta_x} & \dfrac{\partial M_z}{\partial \delta_y} & \dfrac{\partial M_z}{\partial \delta_z} & \dfrac{\partial M_z}{\partial \gamma_y} & \dfrac{\partial M_z}{\partial \gamma_z} \end{bmatrix} \tag{2.4}$$

2.3. Kinematic model of the rigid disc element

The motorized spindle shaft system is simplified to a single-disc rotor system as shown in Fig. 3. $OXYZ$ is a fixed coordinate system, o is the center of the disc, Ω and is the shaft speed. The shaft AB bends in the rotating state, and the deformed axis is represented by $A'B'$. P is any point on the disc, its position angle is denoted by φ, and the distance from the center of the disc is r.

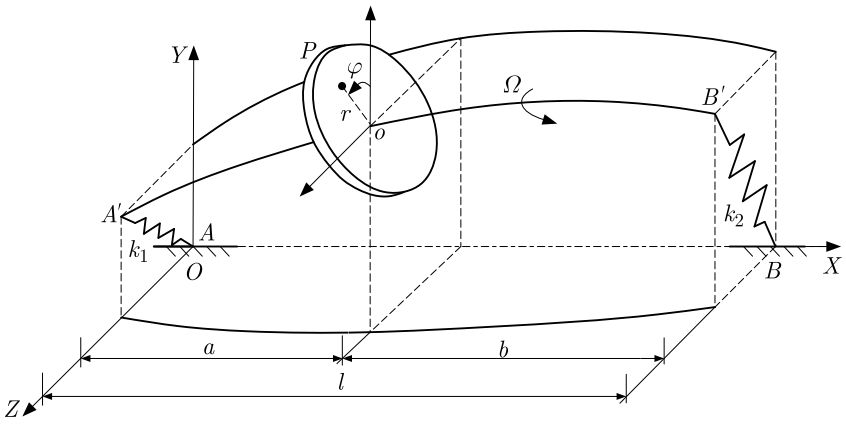

Fig. 3. Motorized spindle shaft system

The velocity of point P can be obtained by derivation

$$\begin{aligned}
\dot{x} &= \dot{u} + \Omega r\theta_z \sin\varphi + \Omega r\theta_y \cos\varphi - r\dot{\theta}_z \cos\varphi + r\dot{\theta}_y \sin\varphi \\
\dot{y} &= \dot{v} - \Omega r \sin\varphi - r\theta_z\dot{\theta}_z \cos\varphi \\
\dot{z} &= \dot{w} + \Omega r \cos\varphi - r\theta_y\dot{\theta}_y \sin\varphi
\end{aligned} \tag{2.5}$$

The total kinetic energy of the disc can be expressed as

$$T = \frac{1}{2}\int_b^a \int_0^{2\pi} l_d \rho r(x^2 + y^2 + z^2)\, dr\, d\varphi \tag{2.6}$$

where l_d is width of the disc, ρ is density, b is inner diameter of the disc, and a is the outer diameter.

Ignoring the effect of damping, the differential equation of motion for a rigid disc is

$$\mathbf{M}^d\ddot{\mathbf{q}} - \Omega\mathbf{G}^d\dot{\mathbf{q}} = \mathbf{F}^d \tag{2.7}$$

where $\mathbf{M}^d$ is the mass matrix of the disc, $\mathbf{G}^d$ is the gyro matrix, $\mathbf{F}^d$ is the external force vector, $\mathbf{q}$ is the displacement vector.

2.4. Elastic shaft element motion model

The Timoshenko beam element and its deformed structure are shown in Fig. 4 (Du and Liu, 2014). Each beam element has two left and right nodes A and B, and the node displacement is set as $\mathbf{q} = [u, v, w, \theta_y, \theta_z]^{\mathrm{T}}$.

The expression for kinetic energy of the beam element of length L is

$$T = \int_0^L \frac{1}{2} J\rho\Omega^2\, dz + \int_0^L \frac{1}{2}\rho A(\dot{u}^2 + \dot{v}^2 + \dot{w}^2)\, dz + \int_0^L \frac{1}{2} I\rho(\dot{\theta}_y^2 + \dot{\theta}_z^2)\, dx + \int_0^L \frac{1}{2}\Omega J\rho(\dot{\theta}_y\theta_z - \theta_y\dot{\theta}_z)\, dx \tag{2.8}$$

where I is radial moment of inertia, J is polar moment of inertia, and R is radius of the beam element section.

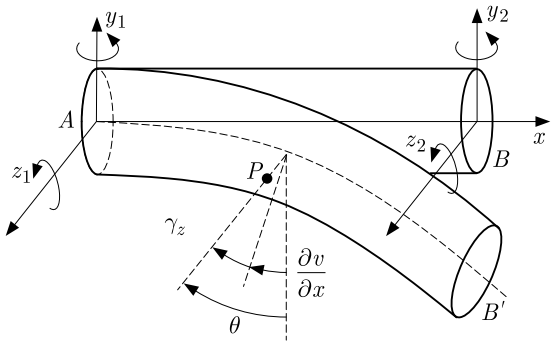

Fig. 4. Timoshenko beam and its deformation

The potential energy of the beam element is

$$\begin{aligned} V = &\int_0^L \frac{1}{2} EA\Big(\frac{\partial u}{\partial x}\Big)^2 \, dx + \int_0^L \frac{1}{2} EI\Big[\Big(\frac{\partial \theta_y}{\partial x}\Big)^2 + \Big(\frac{\partial \theta_z}{\partial x}\Big)^2\Big] \, dx \\ &+ \int_0^L \frac{1}{2} k_s AG\Big[\Big(\theta_y + \frac{\partial w}{\partial x}\Big)^2 + \Big(\theta_z - \frac{\partial v}{\partial x}\Big)^2\Big] \, dx \\ &+ \int_0^L \frac{1}{2} EA\left[\left(\frac{1}{2}\Big(\frac{\partial v}{\partial x}\Big)^2\right)^2 + \left(\frac{1}{2}\Big(\frac{\partial w}{\partial x}\Big)^2\right)^2\right] dx \end{aligned} \tag{2.9}$$

The work done by the external force is

$$W = \int_0^L (q_x u + q_y v + q_z w + m_y \theta_y + m_z \theta_z) \, dx + \int_0^L \frac{1}{2} \Omega^2 v^2 \rho A \, dx + \int_0^L \frac{1}{2} \Omega^2 w^2 \rho A \, dx \tag{2.10}$$

Combined with the generalized Hamilton principle

$$\delta I = \delta \int_{t_1}^{t_2} (T - V + W) \, dt = 0 \tag{2.11}$$

The differential equation of beam motion in matrix form is

$$\mathbf{F}^b = \mathbf{M}^b \ddot{\mathbf{q}} - \Omega \mathbf{G}^b \dot{\mathbf{q}} + (\mathbf{K}^b - \Omega^2 \mathbf{M}_C^b)\mathbf{q} \tag{2.12}$$

where $\mathbf{M}^b$ is the mass matrix of the beam, $\mathbf{M}_C^b$ is the mass matrix used to calculate the centrifugal force, $\mathbf{G}^b$ is the gyro matrix considering the gyro effect, $\mathbf{K}^b$ is the stiffness matrix, and $\mathbf{F}^b$ is the force vector.

Combining the differential equations of motion of the bearing model, rigid disc and beam elements, the differential equation of motion of the bearing-rotor system can be expressed as

$$\mathbf{M}_{sys} \ddot{\mathbf{q}} - \mathbf{D}_{sysy} \dot{\mathbf{q}} + \mathbf{K}_{sys} \mathbf{q} = \mathbf{F}_{ext} \tag{2.13}$$

where $\mathbf{M}_{sys}$ is the mass matrix of the system, $\mathbf{D}_{sys}$ is the system damping matrix (including the gyro matrix), $\mathbf{K}_{sys}$ is the system stiffness matrix, $\mathbf{q}$ and $\mathbf{F}_{ext}$ is the displacement vector and the external excitation force, respectively.

2.5. Power flow theory of the bearing-rotor system

The propagation of vibration in the mechanical structure is actually the propagation of vibration energy. The theoretical idea of the vibration power flow is to use the energy angle to describe the vibration propagation in the system. By introducing the power flow concept, both the magnitude for the force and speed and their phase relationship are considered, which avoids some problems caused by simply using the effective value of speed or acceleration to express the difference in the vibration level (Liu *et al.*, 2010; Li and Wu, 2015).

Assume $F(t)$ is the force acting on a node of the structure at a certain time, and $V(t)$ is the node velocity due to excitation. The time-domain expression of the vibration power flow is

$$P(t) = F(t)V(t) \tag{2.14}$$

Because the power flow at each node varies over time, the average power flow over a while is calculated in the frequency domain. Then, the corresponding power flow calculation expression is as follows

$$P = \frac{1}{T} \lim_{T\to\infty} \int_0^T F(t)V(t)\, dt \tag{2.15}$$

For a simple harmonic excitation $F = |F|\cos(\omega t)$, the system will produce a simple harmonic motion with the same frequency as the excitation force but lagged by a phase angle φ. The response of the system is superimposed by the instantaneous response and the steady-state response. The former will disappear owing to the damping loss within a period of time. The steady-state power flow can be expressed as

$$\begin{aligned} P &= \frac{1}{T}\int_0^T FV\, dt = -\frac{1}{T}\int_0^T |F|\cos(\omega t)\omega|X|\sin(\omega t+\varphi)\, dt \\ &= -\frac{\omega}{2}|F|\,|X|\sin\varphi = -\pi f|F|\,|Xt|\sin\varphi \end{aligned} \tag{2.16}$$

where ω is the angular velocity, t is time, φ is the phase angle, and $|X|$ is the nodal displacement.

The power flow in complex representation is as follows

$$P = \frac{1}{T}\int_0^T \mathrm{Re}\,(\widetilde{F}\mathrm{e}^{\mathrm{i}\omega t})\,\mathrm{Re}\,(\widetilde{V}\mathrm{e}^{\mathrm{i}\omega t})\, dt = \frac{1}{2}\mathrm{Re}\,(FV^*) \tag{2.17}$$

where $\widetilde{F}$, $\widetilde{V}$ are all complex numbers, $(\cdot)^*$ means the conjugate, Re means the real part.

3. Results and discussion

3.1. Numerical simulation and experimental validation

The design rated speed of C01 motorized spindle is 20000 r/min, the material of the spindle is Copper Alloy, the material of the motor rotor is 20CrMnTi, and the material of the stator is Ni3H4. Table 1 shows the specific material parameters. The bearing preload settings of C01 motorized spindle are shown in Table 2.

The eigenvalues and eigenvectors of the system can be obtained numerically by solving Eq. (2.13). The eigenvalues correspond to natural frequencies, and the eigenvectors correspond to principal vibration patterns of the spindle bearing-rotor system, as shown in Fig. 5 and Table 3.

Table 1. Specific material properties

Material name	Density [kg/m^3]	Young's modulus [GPa]	Poisson's ratio
Copper alloy	8300	110	0.34
20CrMnTi	7800	207	0.25
Ni3H4	3440	304	0.24

Table 2. Prestressing force of each bearing specific material properties

Bearing	Front bearing	Middle bearing	Rear bearing
Preload [N]	1400	800	600

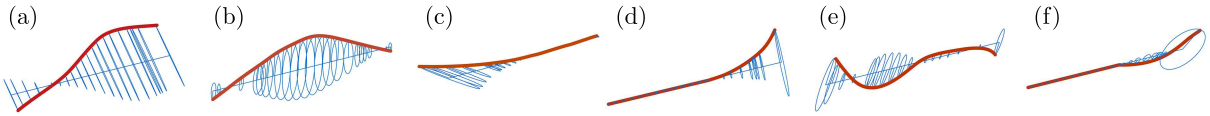

Fig. 5. Natural vibration mode of the rotor: (a) first order, (b) second order, (c) third order, (d) fourth order, (e) fifth order, (f) sixth order

Table 3. First six orders of the natural frequency [Hz] and vibration modes of spindle

Order	1	2	3	4	5	6
Frequency [Hz]	428.32	498.59	1621.6	2382.1	3697.3	5354.4
Mode shape	bending	bending	swing	swing	bending	swing

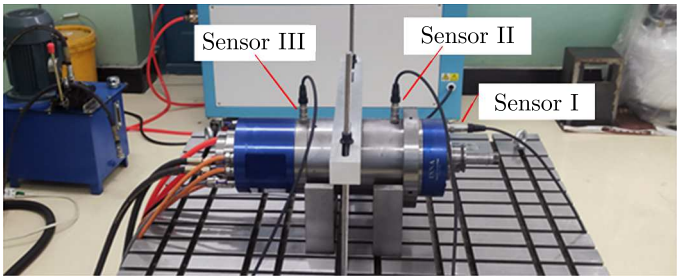

Fig. 6. Actual installation of vibration sensor

In order to obtain the natural frequency of C01 type motorized spindle, a modal experiment for the motorized spindle is designed. The basic principle of the modal experiment is: the motorized spindle placed on the V-shaped block is tapped with an impact hammer to excite the whole structure and make it vibrate, and the vibration response of different measuring points is collected by the acceleration sensor set on the outer shell of the motorized spindle. After the collected signal is sent to the dynamic signal analyzer for fast Fourier transform and other related analyses, the natural frequency of each order can be obtained.

As shown in Fig. 6, the three sensors are used for data acquisition in the modal experiment. Sensor I is arranged on the front bearing housing end face of the motorized spindle, and is used to measure axial vibration of the system. Sensors II and III are arranged at the front and rear ends of the outer housing corresponding to the bearing positions, and are used to measure radial vibration transmitted to the outer case through the bearings.

The frequency responding profiles of the three vibration measuring spots finally collected in the experiment are shown in Fig. 7. The first three natural frequencies of the modal experiment can be obtained as 115 Hz, 426 Hz, and 492 Hz, respectively. 426 Hz and 492 Hz correspond to the first two natural frequencies of 428.32 Hz and 498.59 Hz calculated from the simulation results. The mode shape of the smallest natural frequency measured in the experiment is axial torsion

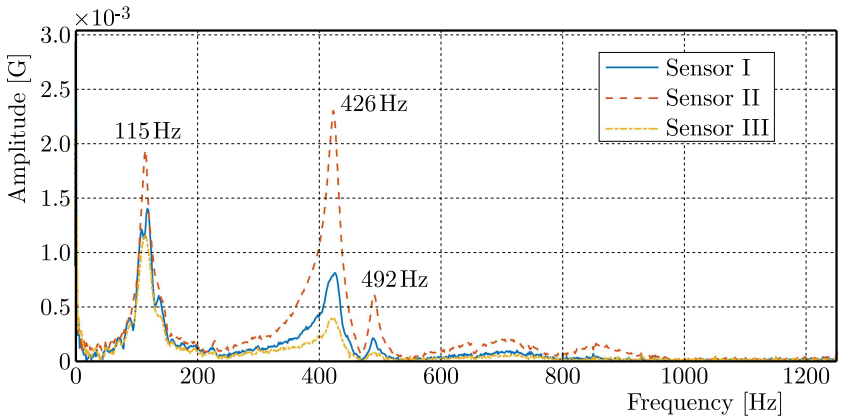

Fig. 7. Modal test results

(Chen *et al.*, 2014; Guo and Wu, 2006). Due to simplification of the model, the system stiffness becomes larger during superposition of the stiffness matrix, resulting in suppression of this frequency experimentally determined in the numerical simulation. The difference between the experimentally measured natural frequency and the simulated natural frequency is tiny, and the maximum error does not exceed 1.34%, which validates the accuracy of the theoretical modeling.

3.2. Comparison of the harmonic response power flow analysis under a mass unbalance excitation

The centrifugal force induced by mass eccentricity is one of the primary excitation sources. Through analysis of the harmonic response under the unbalanced excitation, the amplitude of the shaft system under eccentric mass action can be known, so as to judge whether the design of the spindle structure is satisfying for processing requirements.

Assuming that there is an eccentric mass on a disc, the resulting centrifugal force is

$$F = me\omega \tag{3.1}$$

where m is eccentric mass, e is the eccentricity radius, and ω is the rotation speed. F can be decomposed into two mutually perpendicular harmonic forces on the y and z axes

$$F_y = me\omega^2 \cos(\omega t) \qquad F_z = me\omega^2 \sin(\omega t) \tag{3.2}$$

Combined with the bearing-rotor dynamical model, the unbalanced mass point is set at the turntable, the offset distance is set to $0.1 \cdot 10^{-4}$ m, the analysis frequency range is 100-3000 Hz, and the damping of 0.008 Ns/mm is applied at the spring of the simulated bearing. The harmonic response analysis is performed and the displacement responses of each node of motorized spindle bearing-rotor system are displayed in Fig. 8.

Under the unbalanced excitation, the response peaks appear at each order natural frequency. The resonance amplitude of the second-order natural frequency is relatively small, indicating that the motorized spindle is not very sensitive to this order natural frequency under the unbalanced excitation. The response amplitude before the first-order natural frequency has been rising, indicating that the rigidity of the motorized spindle gradually decreases in this stage. The stiffness performance of the front end of the spindle is better than that of the middle and rear sections below 1500 Hz. After 1500 Hz, the front-to-back performance of the spindle is almost identical without a resonance, and the spindle back-end response value is smaller in the case of the resonance.

Figure 9 shows the power flow variation at each node of the rotor system with the frequency under the unbalanced excitation. The power flow response of the bearing-rotor system also

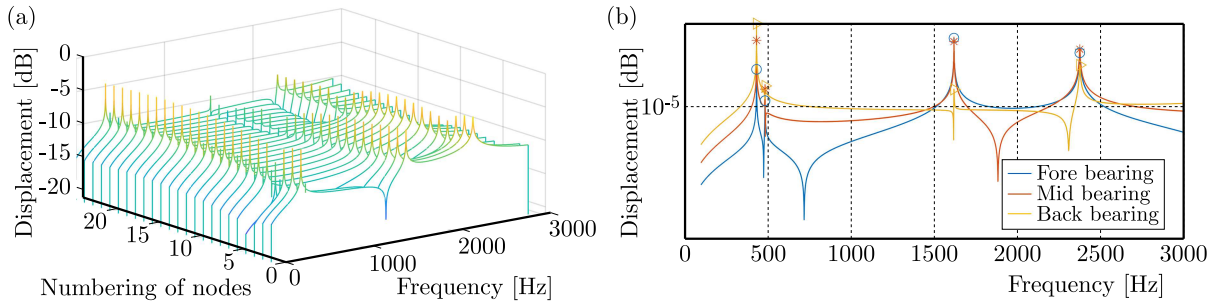

Fig. 8. Displacement response under the unbalanced mass excitation: (a) full node, (b) bearing nodes

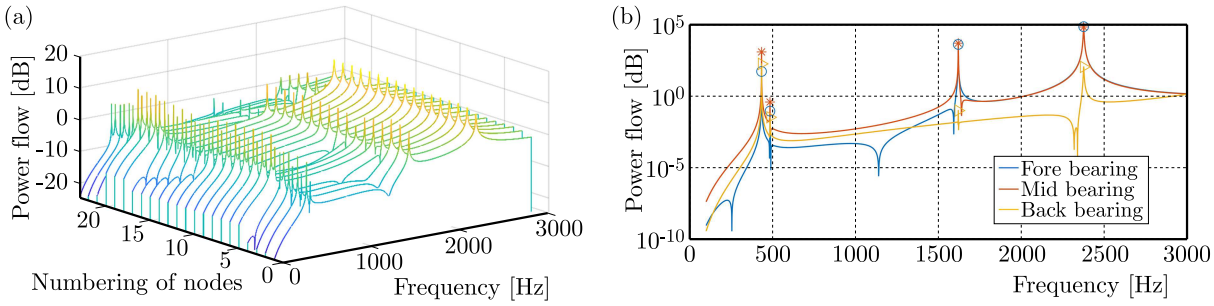

Fig. 9. Power flow of the rotor system: (a) full node, (b) bearing nodes

has resonance peaks at various natural frequencies. This is because the system will vibrate substantially under the resonance condition, and the vibration energy at this time should also have a maximum value. On the whole, the power flow response curve and the displacement response curve have similar fluctuation trends, which shows that the power flow method can analyze the dynamic impact of the bearing-rotor system from the perspective of energy. By comparing the power flow of the three bearing positions, it can be seen that under the unbalanced excitation, the power flow response of the front bearing in the frequency range of 100-1600 Hz is relatively low, and the power flow response of the front bearing is basically the same as that of the middle bearing after the third order natural frequency. Combined with the displacement response under the unbalanced excitation, at the first two orders of natural frequency, the displacement response of the rear bearing is the largest, but the power flow response is close to or less than that at the front and middle bearings. On the whole, the power flow response curves of the front and intermediate bearings are closer to the displacement response. These phenomena show that in terms of power flow, the energy at the rear bearing is relatively small, and the energy distribution of the front and middle bearings is close due to their close positions, which reflects the difference between power flow analysis and harmonic response analysis.

3.3. Effect of bearing stiffness on the system power flow

The power flow analysis method is very sensitive to structural or parameter changes of the system, so different bearing stiffnesses are set, and the corresponding power flow response curves are calculated to analyze the effect that bearing support rigidity has over the system dynamic characteristics.

For the spindle bearing support structure, only one bearing support stiffness is changed at a time. In order to make the simulation results optimal and not distorted, the bearing stiffness change amplitude is set to 0.3 K, and the radial stiffness of the front, middle and rear bearings are $3.5 \cdot 10^8$ N/mm (K_1), $2.6 \cdot 10^8$ N/mm (K_2) and $1.9 \cdot 10^8$ N/mm (K_3). Under working condition 1, only the stiffness of the front bearing K_1 is changed, under case 2, only the stiffness of the front bearing is changed K_2, and so on, totaling 9 different support conditions. The power flow

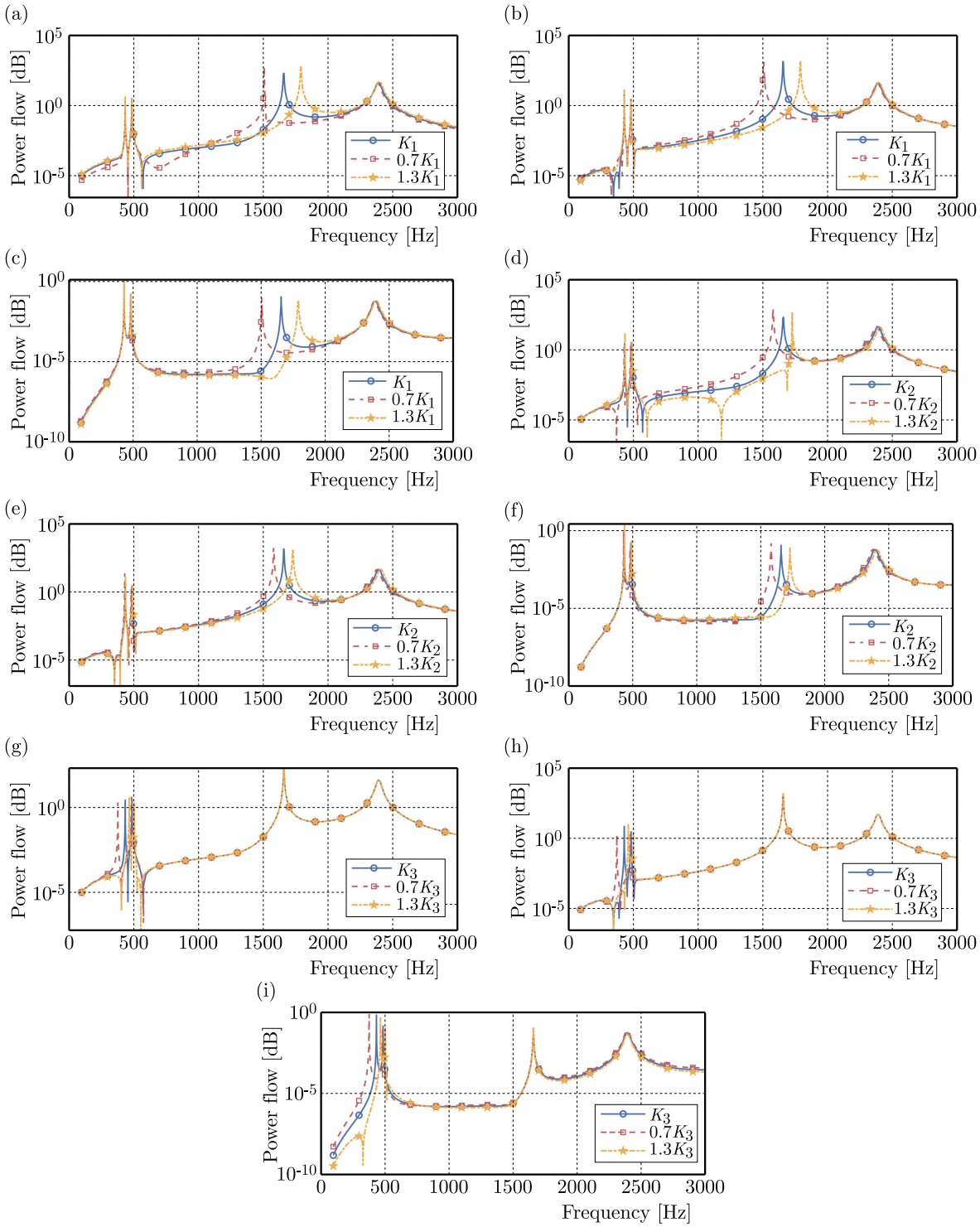

Fig. 10. Power flow response of each bearing position under different working conditions

curves under each working condition are given in Fig. 10. Changing the front bearing support stiffness has the greatest effect on the 3rd order natural frequency, which shows that the 3rd order natural frequency decreases when the front bearing support stiffness decreases, and the other order natural frequencies remain approximately the same. Increasing the mid-bearing support stiffness causes a large increase in the 3rd-order natural frequency and a small increase in the 4th-order natural frequency. Raising the rigidity of the intermediate bearing has almost no impact on the power flow at the middle bearing position, but causes a large increase in the

power flow at the front bearing position within 500 Hz to 1600 Hz. Changing the rear bearing stiffness mainly affects the 1st and 2nd order natural frequencies, and has basically no effect on the region above 1000 Hz. An increase in the rear bearing stiffness enlarges the 1st and 2nd order natural frequencies, making the 1st and 2nd order resonance peak distances smaller, which helps the system to quickly jump over the resonance region.

In summary, the power flow analysis can further analyze dynamic characteristics of motorized spindles from the energy point of view. The changes in the system structure or parameters are reflected in the power flow response, indicating that power flow analysis methods can be applied to analyze structure changes and guide structural optimization or fault detection work.

4. Conclusion

In this paper, the harmonic response and power flow of the bearing-rotor system are studied by establishing the bearing-rotor dynamic model of the motorized spindle, and the displacement response and energy distribution of the system nodes are obtained and compared. The main conclusions are as follows:

- The first six natural frequencies of the bearing-rotor system are acquired through finite element simulation, and the first three natural frequencies have large fluctuations, which are 428.32 Hz, 498.59 Hz, and 1621.6 Hz, respectively. Despite the failure to obtain the natural frequency at low rotational speeds, the largest error between simulation results and high-speed range experimental results does not exceed 1.34%.
- The method of analyzing the vibration characteristics of the motorized spindle bearing--rotor system at high speeds by the power flow is proposed. The displacement response at the rear bearing is the largest at the first two orders of natural frequency, but its power flow response is close to or smaller than the power flow response at the front and middle bearings.
- The bearing stiffness change has a greater influence on the first 3 orders of natural frequency of the system, and stiffness changes of the front and middle bearings mainly affect the position of the vibration power flow peak at the 3rd order of natural frequency. The rear bearing stiffness changes mainly affect the position of the peak of the vibration power flow at the 1st and 2nd order natural frequency.

Acknowledgments

This work has been supported by Opening Project of the Key Laboratory of Advanced Processing Technology and Intelligent Manufacturing (Heilongjiang Province), Harbin University of Science and Technology (KFKT202205), and National Natural Science Foundation of China (51875142), China.

References

1. Bai X.J., Li J.Y., Gou W.D., 2018, Vibration analysis and research of high speed motorized spindle under the influence of cutting force, *Journal of Qinghai University*, **36**, 1, 61-69+74
2. Cao Y.Z., Altintas Y., 2007, Modeling of spindle-bearing and machine tool systems for virtual simulation of milling operations, *International Journal of Machine Tools and Manufacture*, **47**, 9, 1342-1350
3. Chen X.A., Zhang P., He Y., 2013, Power flow model of high-speed motorized spindles and its thermal characteristics, *Transactions of the Chinese Society for Agricultural Machinery*, **44**, 9, 250-254
4. Chen X.A., Zhang P., He Y., 2014, Axial vibration of high-speed motorized spindles, *Journal of Vibration and Shock*, **33**, 20, 70-74+90

5. Du L.H., Liu F.K., 2014, Analysis of beam deflection based on euler and Timoshenko theory, *Journal of Lanzhou Institute of Technology*, **21**, 2, 41-44
6. Gao F., Cheng M.K., Li Y., 2020, Analysis of coupled vibration characteristics of PMS grinding motorized spindle, *Journal of Mechanical Science and Technology*, **34**, 9, 3497-3515
7. Guo D.Q., Wu Y.H., 2006, The model analysis of the ceramic bearing electric spindle, *Development and Innovation of Machinery and Electrical Products*, **19**, 1, 7-8
8. Huang W.D., Gan C.B., Yang S.X., 2016, Dynamic modeling and vibration response analysis of high speed motorized spindle, *Journal of Zhejiang University (Engineering Science)*, **50**, 11, 2198-2206
9. Li G., Wu W.W., 2015, Vibration and sound radiation research based on power flow method, *Journal of Ship Mechanics*, **19**, 5, 609-618
10. Liu C.F., Zhang C., Zhang G.X., 2010, Dynamic stiffness analysis of DVG850 high-speed vertical machining center headstock, *Coal Mine Machinery*, **31**, 12, 88-90
11. Qiao B., Zhao T., Chen X., Liu J., 2016, The assessment of active vibration isolation performance of rotating machinery using power flow and vibrational energy: experimental investigation, *Proceedings of the Institution of Mechanical Engineers, Part C: Journal of Mechanical Engineering Science*, **230**, 2, 159-173
12. Rejab M.N.A., Rahman R.A., Hamzah R.I.R., 2014, Measurement of vibration power flow through elastomeric powertrain mounts in passenger car, *Applied Mechanics and Materials*, **471**, 30-34
13. Shi H.T., Zhao J.Z., Zhang Y., 2019, Dynamic modeling and vibration response analysis of 170SD30 ceramic motorized spindle, *Modular Machine Tool and Automatic Manufacturing Technique*, **542**, 4, 32-36+40
14. Wang W.K., Peng Y.Y., 2013, Ceramic motorized spindle vibration modal analysis based on ANSYS, *Electron Test*, **8**, 136-138
15. Xiao B., 2021, *Research on Vibration Energy of Hot Tandem Mill Based on Power Flow*, Dissertation. University of Science and Technology Beijing
16. Yang J.F., Shi Z., He Z.K., 2022, Theoretical model and simulation of the dynamic stiffness of angular contact ball bearing based on the analytical matrix method, *China Measurement and Test*, **48**, z1, 129-134

Manuscript received June 19, 2023; accepted for print August 28, 2023

JOURNAL OF THEORETICAL AND APPLIED MECHANICS
62, 1, pp. 75-88, Warsaw 2024
https://doi.org/10.15632/jtam-pl/174905

NONLINEAR DYNAMIC MODEL OF A TURBINE BLADE CONSIDERING VIBRATION AND CRACK COUPLING

Yujiang Wang, Deyi Luo, Yuanxing Huang, Yue Peng, Xudong Wang, Xingwang Yan

School of Mechanical and Automotive Engineering, Guangxi University of Science and Technology, Liuzhou, China
corresponding author Yuanxing Huang, e-mail: 260013935@qq.com

Hongming Xiao, Zhongling Huang

Wuling New Energy Automobile Co., Ltd., Liuzhou, China

In order to further investigate dynamic characteristics of turbine runner blades under the coupling effect of vibration and crack, in this article, a runner blade with a crack was taken as the research object. The coupling effect of vibration and crack was analyzed, a nonlinear dynamic model considering the coupling of the runner blade was developed, and the vibration and fatigue characteristics were investigated. First, based on the contact characteristics of the breathing crack surfaces in the runner blade under hydraulic excitation, a breathing crack surface contact model was established. Subsequently, a nonlinear dynamic model considering the coupling effect of vibration and crack was obtained. The crack surface contact force and crack stiffness matrix were established and the vibration and fatigue characteristics were analyzed. Finally, the feasibility of the dynamic model was verified by a case study, and the dynamic and vibration fatigue characteristics under the coupling effect of vibration and crack were revealed. The research results show that with propagation of the crack, the crack surface contact force increases and the dynamic stress amplitude at the crack tip increases as well. When the sum of the frequency of the hydraulic excitation and the crack surface contact force acting on the runner blade is close to the natural frequency of the runner blade, a combined resonance will occur. When the coupling effect of vibration and crack is taken into consideration, the vibration fatigue crack propagation model is more accurate and can provide a basis for fatigue strength and life prediction of runner blades.

Keywords: runner blade, vibration and crack coupling effect, dynamic model, nonlinear, vibration fatigue

1. Introduction

Runner blades are the main force bearing and transmitting components of hydraulic turbine generator units. Under the action of long-term hydraulic excitation, runner blades often experience complex vibration phenomena, and long-term vibration can lead to generation of fatigue cracks in different degrees and different ways. The generation of fatigue cracks can further aggravate the vibration of runner blades, causing a significant decline in the dynamic performance of the unit, and even affect its safety. In order to assess the operation efficiency and reliability of hydraulic turbines, it is necessary to develop a dynamic model of runner blade with cracks.

Currently, the available research on dynamic models of runner blades with cracks has mainly considered the effect of fluid-solid coupled as well as the effects of hydraulic parameters, structural parameters, and crack parameters and has developed dynamic models of runner blades through simulation and theoretical analysis. For instance, Yang *et al.* (2014)

used a singular element of the Ansys software to simulate the tip effect of cracks. A two--dimensional finite element analysis model of the crack was developed, and then, a dynamic model of a blade with crack was constructed. In another study, Fernandes *et al.* (2016) constructed a finite element model of a crack by using mixed-type finite elements, and developed a dynamic model of a cracked blade with different crack angles. However, under hydraulic excitation, the runner blade crack can expand changing the stiffness and resulting in a change of the dynamic response and the crack propagation rate. The dynamic response and crack propagation rate affect each other. This phenomenon is called the coupling effect between vibration and crack propagation. This coupling relationship can affect vibration characteristics and lead to crack arrest and instability propagation of the runner blade. In order to better reveal the vibration and fatigue characteristics of the runner blades, it is necessary to take the coupling relationship between vibration and fatigue cracks propagation into consideration.

At present, the research on the coupling of vibration and crack has been mainly focused on two aspects: crack stiffness and crack surface contact force. In terms of crack stiffness, scholars have considered changes in the stiffness during crack opening and closing, and have developed breathing crack models. For example, Chondros *et al.* (2001) used a nonlinear model to simulate crack stiffness and investigate vibration characteristics of a cracked beam. Liu and Chen (2010) studied the coupling problem between vibration and fatigue crack propagation of cracked beams using a single degree-of-freedom spring vibrator model and a nonlinear breathing crack stiffness model. Nevertheless, the study ignored the opening-closing phenomenon of the breathing crack, which is local contact behavior. Andreaus and Baragatti (2011) developed a contact finite element model to investigate forced vibration of structures containing cracks. The contact finite element breathing crack model considered elastic deformation when simulating the opening and closing of cracks, increasing the accuracy of the simulated stiffness changes. However, during the opening and closing process of the breathing crack, contact forces are generated on the crack surface, thus, it is necessary to study the contact forces on the crack surface in depth. For instance, Kucher *et al.* (2007) considered the contact on a blade breathing crack surface as a friction-free contact problem, introduced nonlinear contact stiffness at the crack as a penalty factor, and obtained an approximate expression of the contact force on the crack surface. To solve the convergence problem, Duan and Singh (2007) introduced a tangent smooth function into the Kucher equation, combining the Lagrange multiplier and penalty function methods in a contact problem. Bednarz (2017) considered the effect of crack parameters such as the crack gap on the crack surface contact force of a blade structure, and established an expression for the crack surface contact force using the penalty stiffness method. Although the crack stiffness and surface contact force models constructed in the above research included structural material parameters and crack parameters, the effect of vibration characteristics on the crack stiffness and surface contact force was not taken into consideration. The vibration characteristics affect the crack opening-closing cycle as well as the gap size of the crack during each cycle, which in turn affect the crack stiffness and contact force characteristics on the crack surface. Therefore, it is necessary to take into account the effect of vibration characteristics and develop a mathematical model able to reflect the internal relationship between crack stiffness and crack surface contact force characteristics.

Taking a turbine runner blade with cracks as the research object, this paper constructs a breathing crack contact model of a runner blade, develops a crack stiffness model including structural parameters, material parameters, crack parameters and vibration characteristics, formulates an analytical equation of the crack surface contact force, and obtains a nonlinear dynamic model which couples the vibration and crack propagation characteristics of the runner blade. The dynamic characteristics are obtained by decoupling the dynamic model, and then, the fatigue crack propagation model of the runner blade is obtained.

2. Breathing crack contact model

The blade can be considered as a shell structure. In order to develop an analytical model for the surface contact of breathing cracks in the blade excited by hydraulic excitation, the following assumptions need to be introduced:

(1) It is assumed that the surface contact behavior of the breathing crack is based on a gradual opening and closing process, the change trend of which is linear.
(2) When the crack surfaces contact with each other, the effect of axial displacement is relatively small and can be ignored, and only the effect of the radial displacement along the contact surfaces of the crack on the contact force is taken into consideration.
(3) According to the opening closing behavior characteristics of breathing cracks, the contact between corresponding point pairs on the crack surfaces can be used to simulate this behavior.

Based on the above assumptions, a breathing crack surface contact model of a runner blade was developed, as shown in Fig. 1. According to the third assumption of the breathing crack contact model, two groups of corresponding crack contact point-pairs were: point a to point b (upper surface), and point a' to point b' (lower surface). During the actual movement of the runner blade, two forms of contact behavior on the crack surface of the runner blade can occur. The first form is displayed in Fig 1 (II) and the second in Fig. 1 (III).

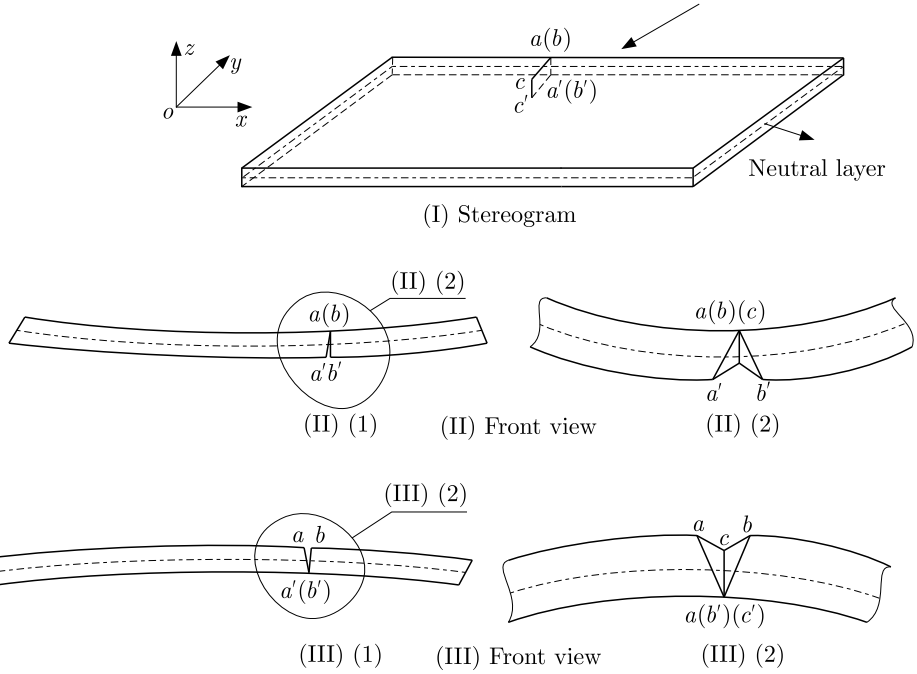

Fig. 1. The breathing crack surfaces contact model of the turbine runner blade

3. Coupling effect of vibration and crack

3.1. Crack surface contact force

Based on the shell-like mechanical model of the breathing crack surface of the blade shown in Fig. 1. When the crack opens, the surface contact force of the breathing crack in the local coordinate system can be expressed as (Luo *et al.*, 2019)

$$f'_a = -K^*(\overline{u}_a - \overline{u}_b - b_c)\delta(\overline{u}_a - \overline{u}_b - b_c) \qquad f'_b = -f'_a \tag{3.1}$$

and

$$f'_{a'} = -K^*(\overline{u}_{a'} - \overline{u}_{b'} - b_c)\delta(\overline{u}_{a'} - \overline{u}_{b'} - b_c) \qquad f'_{b'} = -f'_{a'} \tag{3.2}$$

Equation (3.1) is the crack surface contact force in the first contact form, f'_a and f'_b, represent the crack surface contact force acting on points a and b, respectively. Similarly, Eqs. (3.2) is the crack surface contact force in the second contact form, $f_{a'}$ and $f_{b'}$ represent the crack surface contact force acting on points a' and b', respectively. In addition, $\delta(\overline{u}_a - \overline{u}_b - b_c)$ is the unit step function, which expressed as

$$\delta(\overline{u}_a - \overline{u}_b - b_c) = \begin{cases} 1 & \text{for} \quad \overline{u}_a - \overline{u}_b - b_c \geqslant 0 \\ 0 & \text{for} \quad \overline{u}_a - \overline{u}_b - b_c < 0 \end{cases}$$

Moreover, $\overline{u}_a$ and $\overline{u}_b$ represent the radial displacement of points a and b, respectively, along the x-axis in the local coordinate system, $\overline{u}_{a'}$ and $\overline{u}_{b'}$ represent the radial displacement of points a' and b', respectively, along the x-axis in the local coordinate system, b_c is the crack gap width, and K^* is the contact stiffness of the shell element, also called penalty stiffness, which can be expressed as

$$K^* = \frac{EA_c^2}{3(1-2\nu)V} \tag{3.3}$$

where V is the volume of the crack contact area of a plane shell element, A_c is the crack contact area of a plane shell element, ν is Poisson's ratio of the runner blade material, and E is its elastic modulus.

Subsequently, $\overline{u}_a$ and $\overline{u}_b$ in Eqs. (3.1) and $\overline{u}_{a'}$, $\overline{u}_{b'}$ in Eqs. (3.2), can be calculated based on the neutral surface of the crack, and the distance between the contact-point pair can be transformed into the displacement of the corresponding points A and A' on the neutral surface. When the first contact form is expressed in the local coordinate system of the crack in Fig. 1 (II), $\overline{u}_a$ and $\overline{u}_b$ in Eqs. (3.1) can be expressed as follows

$$\overline{u}_a = \overline{u}_A + \frac{h}{2}\overline{\theta}_{yA} \qquad \overline{u}_b = \overline{u}_{A'} + \frac{h}{2}\overline{\theta}_{yA'} \tag{3.4}$$

where $\overline{u}_A$ and $\overline{u}_{A'}$ represent the lateral displacement of points A and A' along the x-axis, $\overline{\theta}_{yA}$ and $\overline{\theta}_{yA'}$ represent the angular displacement of points A and A' around the y-axis, and h denotes the thickness of the shell element.

When the second contact form is expressed in the local coordinate system of the crack in Fig. 1 (III), $\overline{u}_{a'}$ and $\overline{u}_{b'}$ in Eqs. (3.2) can be expressed as follows

$$\overline{u}_{a'} = \overline{u}_A - \frac{h}{2}\overline{\theta}_{yA} \qquad \overline{u}_{b'} = \overline{u}_{A'} - \frac{h}{2}\overline{\theta}_{yA'} \tag{3.5}$$

For the first contact form, the contact force acting on the crack surface of points a and b can be obtained by substituting Eq. (3.4) into Eqs. (3.1)

$$\begin{aligned} f'_a &= -K^*\Big[\overline{u}_A - \overline{u}_{A'} + \frac{h}{2}(\overline{\theta}_{yA} - \overline{\theta}_{yA'}) - b_c\Big]\delta\Big[\overline{u}_A - \overline{u}_{A'} + \frac{h}{2}(\overline{\theta}_{yA} - \overline{\theta}_{yA'}) - b_c\Big] \\ f'_b &= -f'_a \end{aligned} \tag{3.6}$$

For the second contact form, the contact force acting on the crack surface of points a' and b' can be obtained by substituting Eqs. (3.5) into Eqs. (3.2)

$$\begin{aligned} f'_{a'} &= -K^*\Big[\overline{u}_A - \overline{u}_{A'} - \frac{h}{2}(\overline{\theta}_{yA} - \overline{\theta}_{yA'}) - b_c\Big]\delta\Big[\overline{u}_A - \overline{u}_{A'} - \frac{h}{2}(\overline{\theta}_{yA} - \overline{\theta}_{yA'}) - b_c\Big] \\ f'_{b'} &= -f'_{a'} \end{aligned} \tag{3.7}$$

The radial and angular displacement of points A and A' in the local coordinate system of the crack in Eqs. (3.6) and (3.7) can be expressed by a displacement interpolation function. Therefore, the contact force acting on the crack surface of points a and b in the first type of contact can be expressed as

$$f'_a = -K^*(\boldsymbol{\psi}_1\mathbf{Pu} - b_c)\delta(\boldsymbol{\psi}_1\mathbf{Pu} - b_c) \qquad f'_b = -f'_a \tag{3.8}$$

where $\boldsymbol{\psi}_1$ is 1×20 row vector, and $(\boldsymbol{\psi}_1)_1 = b_c/(2a)$, $(\boldsymbol{\psi}_1)_3 = [3h/(8a^3)](2l_cb_c + b_c^2)$, $(\boldsymbol{\psi}_1)_5 = (2ab_ch - 3b_c^2h - 6b_cl_ch)/(8a^2)$, $(\boldsymbol{\psi}_1)_{16} = -b_c/(2a)$, $(\boldsymbol{\psi}_1)_{18} = -[3h/(8a^3)](2l_cb_c + b_c^2)$, $(\boldsymbol{\psi}_1)_{20} = -(-2ab_ch - 3b_c^2h - 6b_cl_ch)/(8a^2)$, and the rest are zero, which is related to the structural parameters and crack parameters of the shell element. In addition, l_c is the length of the crack from the left end of the plane shell element.

Similarly, the crack surface contact force in the second type of contact can be expressed as

$$f'_{a'} = -K^*(\boldsymbol{\psi}_2\mathbf{Pu} - b_c)\delta(\boldsymbol{\psi}_2\mathbf{Pu} - b_c) \qquad f'_{b'} = -f'_{a'} \tag{3.9}$$

where $\boldsymbol{\psi}_2$ is 1×20 row vector, and $(\boldsymbol{\psi}_2)_1 = b_c/(2a)$, $(\boldsymbol{\psi}_2)_3 = -[3h/(8a^3)](2l_cb_c + b_c^2)$, $(\boldsymbol{\psi}_2)_5 = -(2ab_ch - 3b_c^2h - 6b_cl_ch)/(8a^2)$, $(\boldsymbol{\psi}_2)_{16} = -b_c/(2a)$, $(\boldsymbol{\psi}_2)_{18} = [3h/(8a^3)](2l_cb_c + b_c^2)$, $(\boldsymbol{\psi}_2)_{20} = (-2ab_ch - 3b_c^2h - 6b_cl_ch)/(8a^2)$, and the other elements are zero, which is related to the structural parameters and crack parameters of the shell element.

According to Eqs. (3.8) and (3.9), the contact force on the crack surface is affected by vibration characteristics, which are related to material parameters, such as the elastic modulus and Poisson's ratio, structural parameters such as length and thickness of the shell element, crack parameters such as crack length, gap width, crack angle, contact area and contact area volume, vibration characteristics including radial displacement along x-axis and the angular displacement around the y-axis.

According to Eqs. (3.8) and (3.9), the crack surface contact force of a shell element includes two step functions, $(\boldsymbol{\psi}_1\mathbf{Pu} - b_c)\delta(\boldsymbol{\psi}_1\mathbf{Pu} - b_c)$ and $(\boldsymbol{\psi}_2\mathbf{Pu} - b_c)\delta(\boldsymbol{\psi}_2\mathbf{Pu} - b_c)$, which are nonlinear terms, thus, the crack surface contact force is a nonlinear force.

3.2. Crack stiffness matrix

According to deformation characteristics of plane shell elements with cracks under the action of crack propagation, strain energy is released. In addition, according to the stress characteristics of runner blades with cracks, considering only the strain energy released by type I (open type) and type II (sliding type) cracks, the strain energy P_c released due to crack propagation can be expressed as

$$P_c = \frac{1}{E}\int_{A_c}(K_{\mathrm{I}}^2 + K_{\mathrm{II}}^2)\, dA_c \tag{3.10}$$

where K_{I} and K_{II} correspond to mode I and II stress intensity factors at different crack inclination angles, which can be expressed as follows

$$K_{\mathrm{I}} = F_{\mathrm{I}}(\alpha)\sigma_\alpha\lambda_{\mathrm{I}}(l)\sqrt{\pi l} \qquad K_{\mathrm{II}} = F_{\mathrm{II}}(\alpha)\tau_\alpha\lambda_{\mathrm{II}}(l)\sqrt{\pi l} \tag{3.11}$$

where α is the crack propagation angle, σ_α is the normal stress along the crack propagation angle direction at any time, τ_α is the shear stress along the crack propagation angle direction at any time. $F_{\mathrm{I}}(\alpha)$ and $F_{\mathrm{II}}(\alpha)$ are the propagation angle correction coefficients of mode I and II cracks, respectively, which can be determined based on the crack propagation angle α, $\lambda_{\mathrm{I}}(l)$ and $\lambda_{\mathrm{II}}(l)$ represent the stress intensity factor correction functions of mode I and II cracks, respectively, which can be determined based on relative length of the crack.

Considering large geometric deformation of the runner blade and ignoring the effect of bending deformation of the y-axis, the displacement-strain relationship for the crack section of the plane shell element can be expressed as

$$\begin{aligned} \varepsilon_{l_x} &= \frac{\partial u}{\partial x} + z\frac{\partial^2 w}{\partial x^2} + \frac{1}{2}\Big(\frac{\partial w}{\partial x}\Big)^2 \qquad \varepsilon_y = 0 \\ \gamma_{l_x y} &= \frac{\partial u}{\partial y} + \frac{\partial v}{\partial x} + 2z\frac{\partial^2 w}{\partial x \partial y} + \frac{\partial w}{\partial x}\frac{\partial w}{\partial y} \end{aligned} \tag{3.12}$$

Equation (3.12) can be transformed into a matrix form as follows

$$\boldsymbol{\varepsilon}_c = \widetilde{\mathbf{S}}_0\mathbf{u} + \frac{1}{2}\sum_{j=1}^{3}\mathbf{k}_j\mathbf{u}^{\mathrm{T}}\widetilde{\mathbf{S}}_j\mathbf{u} \tag{3.13}$$

where

$$\boldsymbol{\varepsilon}_c = \begin{bmatrix} \varepsilon_{l_x} \\ 0 \\ \gamma_{l_x y} \end{bmatrix} \qquad \widetilde{\mathbf{S}}_0 = \begin{bmatrix} \frac{\partial}{\partial x} & 0 & z\frac{\partial^2}{\partial x^2} \\ 0 & 0 & 0 \\ \frac{\partial}{\partial y} & \frac{\partial}{\partial x} & 2z\frac{\partial^2}{\partial x \partial y} \end{bmatrix}\mathbf{N}$$

$\mathbf{N} =$

$$\begin{bmatrix} N_{u1} & 0 & 0 & 0 & 0 & N_{u2} & 0 & 0 & 0 & 0 & N_{u3} & 0 & 0 & 0 & 0 & N_{u4} & 0 & 0 & 0 & 0 \\ 0 & N_{v1} & 0 & 0 & 0 & 0 & N_{v2} & 0 & 0 & 0 & 0 & N_{v3} & 0 & 0 & 0 & 0 & N_{v4} & 0 & 0 & 0 \\ 0 & 0 & N_{w1} & N_{\theta_x 1} & N_{\theta_y 1} & 0 & 0 & N_{w2} & N_{\theta_x 2} & N_{\theta_y 2} & 0 & 0 & N_{w3} & N_{\theta_x 3} & N_{\theta_y 3} & 0 & 0 & N_{w4} & N_{\theta_x 4} & N_{\theta_y 4} \end{bmatrix}$$

and N_{ui}, N_{vi}, N_{wi}, $N_{\theta_x i}$, $N_{\theta_y i}$ $(i = 1, 2, 3, 4)$ are form functions, $\mathbf{k}_j$ $(j = 1, 2, 3)$, where $\mathbf{k}_1 = [1, 0, 0]^{\mathrm{T}}$, , $\mathbf{k}_2 = [0, 1, 0]^{\mathrm{T}}$, $\mathbf{k}_3 = [0, 0, 1]^{\mathrm{T}}$, $\widetilde{\mathbf{S}}_j$ $(j = 1, 2, 3)$ is 20×20 matrix, where

$$\widetilde{\mathbf{S}}_1 = \begin{bmatrix} \frac{\partial \mathbf{N}_3^{\mathrm{T}}}{\partial x} & \mathbf{O}_{20\times 1} & \mathbf{O}_{20\times 1} \end{bmatrix}\begin{bmatrix} \frac{\partial \mathbf{N}_3}{\partial x} \\ \mathbf{O}_{1\times 20} \\ \mathbf{O}_{1\times 20} \end{bmatrix} \qquad \widetilde{\mathbf{S}}_2 = \begin{bmatrix} \mathbf{O}_{20\times 1} & \mathbf{O}_{20\times 1} & \mathbf{O}_{20\times 1} \end{bmatrix}\begin{bmatrix} \frac{\partial \mathbf{N}_3}{\partial x} \\ \mathbf{O}_{1\times 20} \\ \mathbf{O}_{1\times 20} \end{bmatrix}$$

$$\widetilde{\mathbf{S}}_3 = \begin{bmatrix} \frac{\partial \mathbf{N}_3^{\mathrm{T}}}{\partial y} & \frac{\partial \mathbf{N}_3^{\mathrm{T}}}{\partial x} & \mathbf{O}_{20\times 1} \end{bmatrix}\begin{bmatrix} \frac{\partial \mathbf{N}_3}{\partial x} \\ \mathbf{O}_{1\times 20} \\ \mathbf{O}_{1\times 20} \end{bmatrix}$$

and

$$\mathbf{N}_3 = [0, 0, N_{w1}, N_{\theta_x 1}, N_{\theta_y 1}, 0, 0, N_{w2}, N_{\theta_x 2}, N_{\theta_y 2}, 0, 0, N_{w3}, N_{\theta_x 3}, N_{\theta_y 3}, 0, 0, N_{w4}, N_{\theta_x 4}, N_{\theta_y 4}]$$

The relationship between stress and strain is

$$\boldsymbol{\sigma}_c = \mathbf{D}\boldsymbol{\varepsilon}_c \tag{3.14}$$

where $\boldsymbol{\sigma}_c = [\sigma_{l_x}, 0, \tau_{l_x y}]^{\mathrm{T}}$, $\mathbf{D}$ is the elastic matrix of the shell element, which can be expressed as

$$\mathbf{D} = \frac{E}{1-\nu^2}\begin{bmatrix} 1 & \nu & 0 \\ \nu & 1 & 0 \\ 0 & 0 & \frac{1-\nu}{2} \end{bmatrix} \tag{3.15}$$

By substituting Equations $(3.11)_1$ to (3.14) into Eq. (3.10), the following expression can be obtained

$$\begin{aligned} P_c = {} & \frac{1}{2}\mathbf{u}^{\mathrm{T}}\mathbf{k}_c\mathbf{u} + \frac{\pi l}{4E}\int_{A_c}\sum_{j=1}^{3}\sum_{k=1}^{3}\mathbf{u}^{\mathrm{T}}\mathbf{k}_j^{\mathrm{T}}\mathbf{u}\widetilde{\mathbf{h}}_{jk}\mathbf{u}^{\mathrm{T}}\mathbf{k}_k\mathbf{u}\,dA_c \\ & + \frac{\pi l}{2E}\int_{A_c}\sum_{j=1}^{3}(\mathbf{u}^{\mathrm{T}}\widetilde{\mathbf{g}}_j\mathbf{u}^{\mathrm{T}}\mathbf{k}_j\mathbf{u} + \mathbf{u}^{\mathrm{T}}\mathbf{k}_j^{\mathrm{T}}\mathbf{u}\widetilde{\mathbf{g}}_j^{\mathrm{T}}\mathbf{u})\,dA_c \end{aligned} \tag{3.16}$$

where

$$\widetilde{\mathbf{g}}_j = \widetilde{\mathbf{S}}_0^{\mathrm{T}}\mathbf{D}^{\mathrm{T}}\boldsymbol{\lambda}\widetilde{\mathbf{S}}_j \qquad \widetilde{\mathbf{h}}_{jk} = \widetilde{\mathbf{S}}_j^{\mathrm{T}}\mathbf{D}^{\mathrm{T}}\boldsymbol{\lambda}\mathbf{D}\widetilde{\mathbf{S}}_k \qquad \boldsymbol{\lambda} = \begin{bmatrix} F_{\mathrm{I}}^2(\alpha)\lambda_{\mathrm{I}}^2 & 0 & 0 \\ 0 & 0 & 0 \\ 0 & 0 & F_{\mathrm{II}}^2(\alpha)\lambda_{\mathrm{II}}^2 \end{bmatrix}$$

Subsequently, the shell element stiffness matrix $\mathbf{k}_c$ caused by crack propagation can be obtained

$$\mathbf{k}_c = \frac{2\pi l}{E}\int\limits_{A_c} \widetilde{\mathbf{S}}_0^{\mathrm{T}}\mathbf{D}^{\mathrm{T}}\boldsymbol{\lambda}\mathbf{D}\widetilde{\mathbf{S}}_0\, dA_c \tag{3.17}$$

According to Eq. (3.17), the crack-stiffness-matrix is affected by the vibration characteristics, which are related to material parameters, such as the elastic modulus and Poisson's ratio, structural parameters such as length and thickness of the shell element, crack parameters such as crack length, crack propagation angle, crack contact area and contact area volume, and vibration characteristics such as normal and shear stress amplitudes.

4. Dynamic coupling model of vibration and crack

The relationship between the generalized coordinate vector $\mathbf{i}$ of element $\mathbf{u}_i$ and the generalized coordinate vector $\mathbf{U}$ of the shell structure in the global coordinate system can be expressed as

$$\mathbf{u}_i = \mathbf{R}_i\mathbf{B}_i\mathbf{U} \tag{4.1}$$

where $\mathbf{B}_i$ is the coordinate matrix between the unit number and system number, and $\mathbf{R}_i$ is the conversion matrix between the coordinates unit $\mathbf{i}$ and the global coordinates.

For large geometric deformation and the crack surface contact force, the dynamic equation of a runner blade with a crack can be written as follows

$$\begin{aligned}
&(\mathbf{M}_t + \mathbf{M}_p)\ddot{\mathbf{U}} + \mathbf{C}\dot{\mathbf{U}} + (\mathbf{K} - \mathbf{K}_c)\mathbf{U} = \mathbf{F} + \mathbf{F}' - \mathbf{M}_d\ddot{\mathbf{U}}_d \\
&\quad + \frac{3}{2}\sum_{i=1}^{n}\sum_{j=1}^{3}\int\limits_V (\mathbf{G}_{ji}\mathbf{U}^{\mathrm{T}}\mathbf{k}_j\mathbf{U} + 2\mathbf{U}^{\mathrm{T}}\mathbf{G}_{ji}\mathbf{k}_j\mathbf{U})\, dV \\
&\quad - \sum_{i=1}^{n}\int\limits_{A_{ci}} \frac{3\pi l_i}{2E}\sum_{j=1}^{3}(\widetilde{\mathbf{G}}_{ji}\mathbf{U}^{\mathrm{T}}\mathbf{k}_j\mathbf{U} + 2\mathbf{U}^{\mathrm{T}}\widetilde{\mathbf{G}}_{ji}\mathbf{k}_j\mathbf{U})\, dA_{ci} \\
&\quad - \sum_{i=1}^{n}\frac{\pi l_i}{E}\int\limits_{A_{ci}}\sum_{j=1}^{3}\sum_{k=1}^{3}\mathbf{k}_j^{\mathrm{T}}\mathbf{U}\widetilde{\mathbf{H}}_{jki}\mathbf{U}^{\mathrm{T}}\mathbf{k}_k\mathbf{U}\, dA_{ci} + \frac{1}{2}\sum_{i=1}^{n}\sum_{j=1}^{3}\sum_{k=1}^{3}\int\limits_V \mathbf{k}_j^{\mathrm{T}}\mathbf{U}\mathbf{H}_{jki}\mathbf{U}^{\mathrm{T}}\mathbf{k}_k\mathbf{U}\, dV
\end{aligned} \tag{4.2}$$

where $\mathbf{G}_{ji} = \mathbf{B}_i^{\mathrm{T}}\mathbf{R}_i^{\mathrm{T}}\mathbf{g}_{ji}$, $\widetilde{\mathbf{G}}_{ji} = \mathbf{B}_i^{\mathrm{T}}\mathbf{R}_i^{\mathrm{T}}\widetilde{\mathbf{g}}_{ji}$, $\mathbf{H}_{jki} = \mathbf{B}_i^{\mathrm{T}}\mathbf{R}_i^{\mathrm{T}}\mathbf{h}_{jki}\mathbf{R}_i\mathbf{B}_i$, $\widetilde{\mathbf{H}}_{jki} = \mathbf{B}_i^{\mathrm{T}}\mathbf{R}_i^{\mathrm{T}}\widetilde{\mathbf{h}}_{jki}\mathbf{R}_i\mathbf{B}_i$. In addition, $\mathbf{U}$, $\dot{\mathbf{U}}$ and $\ddot{\mathbf{U}}$ correspond to the generalized coordinate vector, velocity vector, and acceleration vector in the global coordinate system of the blade with crack, $\ddot{\mathbf{U}}_d$ is the rigid body acceleration vector, $\mathbf{M}_d\ddot{\mathbf{U}}_d$ is the self-excited inertial force of the system, $\mathbf{M}_t$ and $\mathbf{M}_p$ are the mass matrix and additional mass matrix, respectively, $\mathbf{C}$ is the damping matrix, $\mathbf{K}$ is the stiffness matrix, $\mathbf{F}$ and $\mathbf{F}'$ are the hydraulic excitation and crack surface contact force, respectively.

According to Eq. (4.2), the dynamic equation of the blade with the crack includes the nonlinear crack surface contact force, a nonlinear term representing the large geometric deformation of the blade $\sum_{i=1}^{n}\sum_{j=1}^{3}\int_V(\mathbf{G}_{ji}\mathbf{U}^{\mathrm{T}}\mathbf{k}_j\mathbf{U} + 2\mathbf{U}^{\mathrm{T}}\mathbf{G}_{ji}\mathbf{k}_j\mathbf{U})\, dV$, and a nonlinear term representing the crack strain energy of the blade $-\sum_{i=1}^{n}\int_{A_{ci}}[\pi l_i/(2E)]\sum_{j=1}^{3}(\widetilde{\mathbf{G}}_{ji}\mathbf{U}^{\mathrm{T}}\mathbf{k}_j\mathbf{U} + 2\mathbf{U}^{\mathrm{T}}\widetilde{\mathbf{G}}_{ji}\mathbf{k}_j\mathbf{U})\, dA_{ci}$,

therefore the dynamic equation of the blade with the crack is a nonlinear equation. In the dynamic equation of the blade, the $\mathbf{F}'$ (nonlinear crack surface contact force) and $\mathbf{K}_c\mathbf{U}$ (elastic restoring force) terms caused by the crack as well as the nonlinear terms generated by crack strain energy of the blade include not only crack parameters, but also vibration parameters. Consequently, this is a coupling relationship between vibration and the crack.

5. Vibration and fatigue characteristics of runner blades

5.1. Dynamic characteristics of runner blades

By solving Eq. (4.2) using the multi-scale method, the dynamic response of the blade with the crack can be obtained

$$\mathbf{U} = \boldsymbol{\varphi}\boldsymbol{\eta} \qquad \dot{\mathbf{U}} = \boldsymbol{\varphi}\dot{\boldsymbol{\eta}} \qquad \ddot{\mathbf{U}} = \boldsymbol{\varphi}\ddot{\boldsymbol{\eta}} \tag{5.1}$$

where $\boldsymbol{\varphi}$ is the regular modal matrix and $\boldsymbol{\eta}$ is the corresponding modal coordinate array of the blade. Subsequently, the approximate solution of the displacement response $\mathbf{U}$ of the blade with the crack can be expressed as

$$\mathbf{U} = \sum_{r=1}^{n} \boldsymbol{\eta}_r \boldsymbol{\varphi}^{(r)} \tag{5.2}$$

Based on the developed finite element model of the blade, the relationship between displacement and strain is as follows

$$\boldsymbol{\varepsilon} = \mathbf{S}_0\mathbf{u} + \frac{1}{2}\sum_{j=1}^{3} \mathbf{S}_j\mathbf{u}^{\mathrm{T}}\mathbf{k}_j\mathbf{u} \tag{5.3}$$

where $\boldsymbol{\varepsilon} = [\varepsilon_x, \varepsilon_y, \gamma_{xy}]^{\mathrm{T}}$, can be expressed as

$$\begin{aligned} &\varepsilon_x(x,t) = \frac{\partial u}{\partial x} + z\frac{\partial^2 w}{\partial x^2} + \frac{1}{2}\Big(\frac{\partial w}{\partial x}\Big)^2 \qquad \varepsilon_y(x,t) = \frac{\partial v}{\partial y} + z\frac{\partial^2 w}{\partial y^2} + \frac{1}{2}\Big(\frac{\partial w}{\partial y}\Big)^2 \\ &\gamma_{xy}(x,t) = \frac{\partial u}{\partial y} + \frac{\partial v}{\partial x} + 2z\frac{\partial^2 w}{\partial x \partial y} + \frac{\partial w}{\partial x}\frac{\partial w}{\partial y} \end{aligned} \tag{5.4}$$

where $\mathbf{S}_j$ $(j = 1, 2, 3)$ is 20×20 matrix, and

$$\mathbf{S}_1 = \begin{bmatrix} \frac{\partial \mathbf{N}_3^{\mathrm{T}}}{\partial x} & \mathbf{O}_{20\times 1} & \mathbf{O}_{20\times 1} \end{bmatrix} \begin{bmatrix} \frac{\partial \mathbf{N}_3}{\partial x} \\ \frac{\partial \mathbf{N}_3}{\partial y} \\ \mathbf{O}_{1\times 20} \end{bmatrix} \qquad \mathbf{S}_2 = \begin{bmatrix} \mathbf{O}_{20\times 1} & \frac{\partial \mathbf{N}_3^{\mathrm{T}}}{\partial y} & \mathbf{O}_{20\times 1} \end{bmatrix} \begin{bmatrix} \frac{\partial \mathbf{N}_3}{\partial \overline{x}} \\ \frac{\partial \mathbf{N}_3}{\partial \overline{y}} \\ \mathbf{O}_{1\times 20} \end{bmatrix}$$

$$\mathbf{S}_3 = \begin{bmatrix} \frac{\partial \mathbf{N}_3^{\mathrm{T}}}{\partial y} & \frac{\partial \mathbf{N}_3^{\mathrm{T}}}{\partial x} & \mathbf{O}_{20\times 1} \end{bmatrix} \begin{bmatrix} \frac{\partial \mathbf{N}_3}{\partial x} \\ \frac{\partial \mathbf{N}_3}{\partial y} \\ \mathbf{O}_{1\times 20} \end{bmatrix}$$

The relationship between stress and strain is

$$\boldsymbol{\sigma} = \mathbf{D}\boldsymbol{\varepsilon} \tag{5.5}$$

Refer to Eq. (3.15) for the $\mathbf{D}$ matrix above. By combining Eqs. (4.1), (5.3) and (5.5), the dynamic stress at any position of the blade with the crack can be obtained as follows

$$\boldsymbol{\sigma} = \mathbf{D}\mathbf{S}_0\mathbf{R}_i\mathbf{B}_i\mathbf{U} + \frac{1}{2}\sum_{j=1}^{3} \mathbf{D}\mathbf{k}_j\mathbf{U}^{\mathrm{T}}\mathbf{B}_i^{\mathrm{T}}\mathbf{R}_i^{\mathrm{T}}\mathbf{S}_j\mathbf{R}_i\mathbf{B}_i\mathbf{U} \tag{5.6}$$

5.2. Vibration fatigue characteristics of blades with cracks

According to the Pairs fatigue crack propagation model, the fatigue crack propagation rate of a runner blade with a crack can be expressed as

$$\frac{dl}{dN} = C_0(\Delta K)^m \tag{5.7}$$

where l is the crack length of the member with the crack, N is the number of cycles of dynamic stress, m and C_0 are material constants of the members with the crack, and ΔK is the stress intensity factor amplitude. Considering the contact and vibration characteristics of the crack surface, the amplitude of the stress intensity factor can be expressed as

$$\Delta K = \frac{1}{2}\cos\frac{\alpha}{2}[\Delta K_{\mathrm{I}}(1+\cos\alpha) - 3\Delta K_{\mathrm{II}}\sin\alpha] + F(l)\frac{\Delta f(\mathbf{U})}{\sqrt{\pi l}} \tag{5.8}$$

where $F(l)$ is the crack shape correction factor, which is related to the crack size and which can be obtained from the stress intensity factor manual, ΔK_{I} and ΔK_{II} are the amplitudes of K_{I} and K_{II}, respectively, and $\Delta f(\mathbf{U})$ is the amplitude of the contact force acting on the crack surface, which can be determined by combining Equations (3.8), (3.9) and (5.2).

By substituting Eq. (5.8) into Eq. (5.7), the crack propagation rate model of the runner blade with the crack can be expressed as

$$\frac{dl}{dN} = C_0\Big(\frac{1}{2}\cos\frac{\alpha}{2}[\Delta K_{\mathrm{I}}(1+\cos\alpha) - 3\Delta K_{\mathrm{II}}\sin\alpha] + F(l)\frac{\Delta f(\mathbf{U})}{\sqrt{\pi l}}\Big)^m \tag{5.9}$$

According to Equations (5.6) and (5.9), due to the coupling effect between vibration and the crack, the contact force on the crack surface and the crack stiffness change continuously with propagation of the crack, resulting in a continuous change of the dynamic stress characteristics. Consequently, the crack propagation model of the runner blade is related not only to the amplitude of dynamic stress, but also to the amplitude of the contact force on the crack surface.

6. Case study

In this Section, a large Francis turbine in Guangxi is taken as an example. The main parameters of the runner are as follows: rated speed of 75 RPM, rated head of 59.4 m, rated flow of $Q_0 = 580\,\mathrm{m}^3/\mathrm{s}$, rated working condition of 302.5 MW, maximum runner diameter of 8.33 m, height of 5.19 m, upper crown and lower ring mass of $101.4 \cdot 10^3$ kg and $68 \cdot 10^3$ kg, respectively, and upper crown and lower ring moment of inertia of $8.52 \cdot 10^5\,\mathrm{kg{\cdot}m}^2$ and $1.15 \cdot 10^6\,\mathrm{kg{\cdot}m}^2$, respectively. In total, 13 blades are evenly distributed in the runner. A single blade has mass of $7.7 \cdot 10^3$ kg, width of 1.65 m, thickness of 0.62 m, elastic modulus of $E = 210$ GPa, material density of $7.85 \cdot 10^3\,\mathrm{kg/m}^3$, and Poisson's ratio of $\nu = 0.3$.

In actual operation, due to the thin water outlet edge of the blade and the stress concentration phenomenon at the "T-shaped" connection between the blade and upper crown, penetrating cracks often appear at the water outlet edge of the blade. Table 1 lists the statistical values of through cracks found on the outlet edge of the blade of a hydropower station. The runner blade material is ZG0Cr13Ni5Mo, the material constant is $m = 3.65$, $C_0 = 3.46 \cdot 10^{-10}$ and its allowable stress is $\sigma = 43.27 \cdot 10^7$ Pa.

In order to verify the correctness of the developed model, No. 3 blade under rated working conditions was taken as the research object. Based on the characteristics of hydraulic excitation acting on the blade, a crack 100 mm away from the upper crown was analyzed. It was assumed that the blade contained only a single crack. Two different crack lengths of 100 mm and 150 mm

Table 1. Statistical table of through cracks on the water outlet edge of blades of a hydropower station

Blade number	Crack location	Crack type	Crack size
3	100 mm from upper crown	Through crack	150 mm
8	20 mm from lower ring	Through crack	90 mm
9	30 mm from upper crown	Through crack	140 mm
11	50 mm from lower ring	Through crack	130 mm

Table 2. Each node direction displacement representation symbols of the crack blade

Displacement in each node direction	Representation symbol
Lateral displacement along X-axis	U_1, U_6, U_{11}, U_{16}, U_{21}, U_{26}, U_{31}, U_{36}, U_{41}, U_{46}, U_{51}, U_{56}
Lateral displacement along Y-axis	U_2, U_7, U_{12}, U_{17}, U_{22}, U_{27}, U_{32}, U_{37}, U_{42}, U_{47},? U_{52}, U_{57}
Lateral displacement along Z-axis	U_3, U_8, U_{13}, U_{18}, U_{23}, U_{28}, U_{33}, U_{38}, U_{43}, U_{48}, U_{53}, U_{58}
Angular displacement around Z-axis	U_4, U_9, U_{14}, U_{19}, U_{24}, U_{29}, U_{34}, U_{39}, U_{44}, U_{49}, U_{54}, U_{59}
Angular displacement around Y-axis	U_5, U_{10}, U_{15}, U_{20}, U_{25}, U_{30}, U_{35}, U_{40}, U_{45}, U_{50}, U_{55}, U_{60}

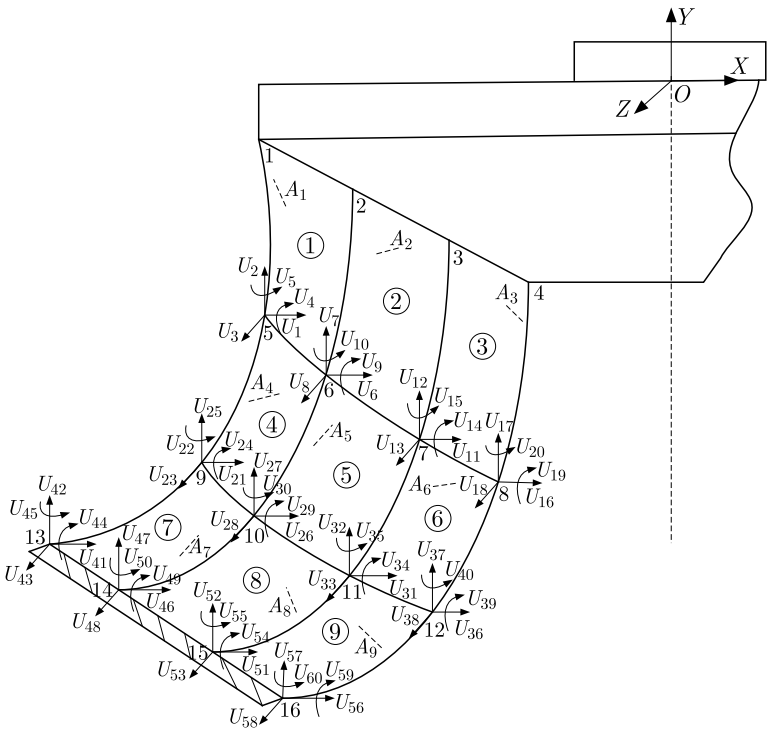

Fig. 2. Finite element model of the runner blade with cracks

and crack gap widths of 1.6 mm and 2 mm were investigated. In order to simplify the simulation model, the runner blade was divided into 9 rectangular elements, each blade had 60 degrees-of--freedom, the element number was represented by ①, ②, A_1, A_2,..., indicated the crack number, the node numbers were represented by $1, 2, \ldots$ (Table 2). The finite element model of the blade with the crack is illustrated in Fig. 2.

Time-domain simulation diagrams of the contact force on the crack surface and dynamic stress at the crack tip were obtained according to Eqs. (3.8), (3.9) and (5.6), for a crack length of 100 mm and crack gap width of 1.6 mm. The results are shown in Figs. 3a and 3b, respectively. For a crack length of 150 mm and crack gap width of 2 mm, the results are shown in Figs. 4a and 4b, respectively.

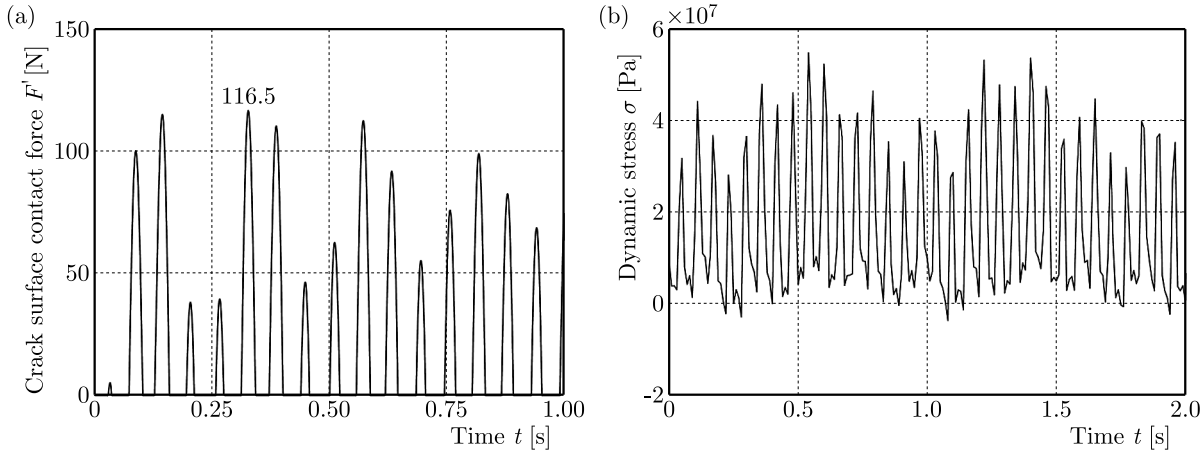

Fig. 3. (a) Simulation curve of the crack surfaces contact force and (b) time domain simulation curve crack-tip dynamic stress when the crack length was 100 mm and the crack gap width was 1.6 mm

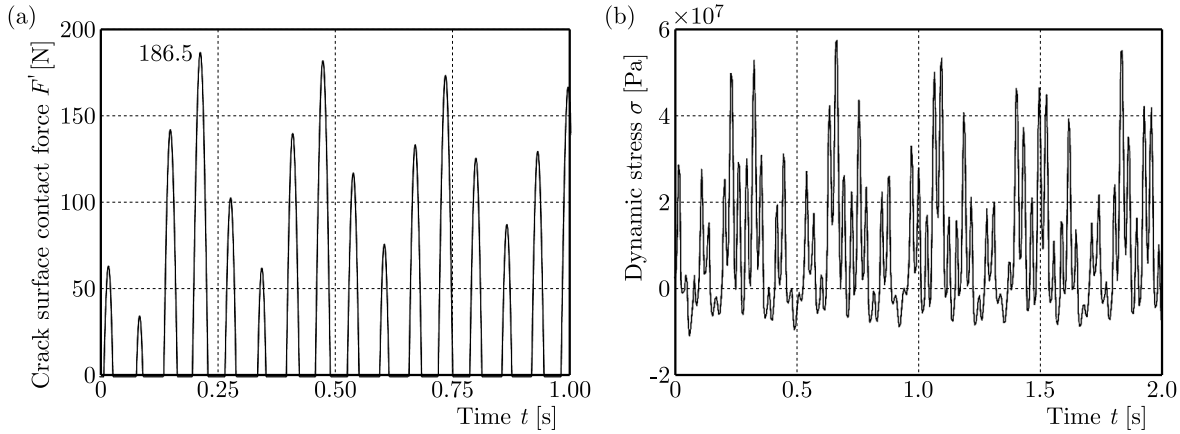

Fig. 4. (a) Simulation curve of the crack surfaces contact force and (b) time domain simulation curve crack-tip dynamic stress when the crack length was 150 mm and the crack gap width was 2 mm

According to Figs. 3a and 4a, the contact force on the crack surface increases with propagation of the crack. In addition, as the crack gap width increases, the period of the contact force on the crack surface increases as well. According to Figs. 3b and 4b, the dynamic stress amplitude at the crack tip increases with propagation of the crack.

As shown in Figs. 5a and 5b, the correctness of the developed model is verified. The fracture module in Ansys workbench was used to establish the crack, the surface unit surface body was inserted at the crack location and the grid was divided, dynamic load was applied and transient dynamic analysis was carried out. The results show that the closer the crack position is, the greater is the dynamic stress. Among them, the dynamic stress at the crack is 32.7 MPa and the mean dynamic stress in Fig. 3b is 30.1 MPa, the error is 2.6 MPa, and the error rate is 7.9%.

According to Eq. (3.17), the crack stiffness increases due to propagation of the crack, which leads to a continuous reduction of the natural frequency of the runner blade with the crack. Moreover, width of the crack gap increases due to propagation of the crack, and the period

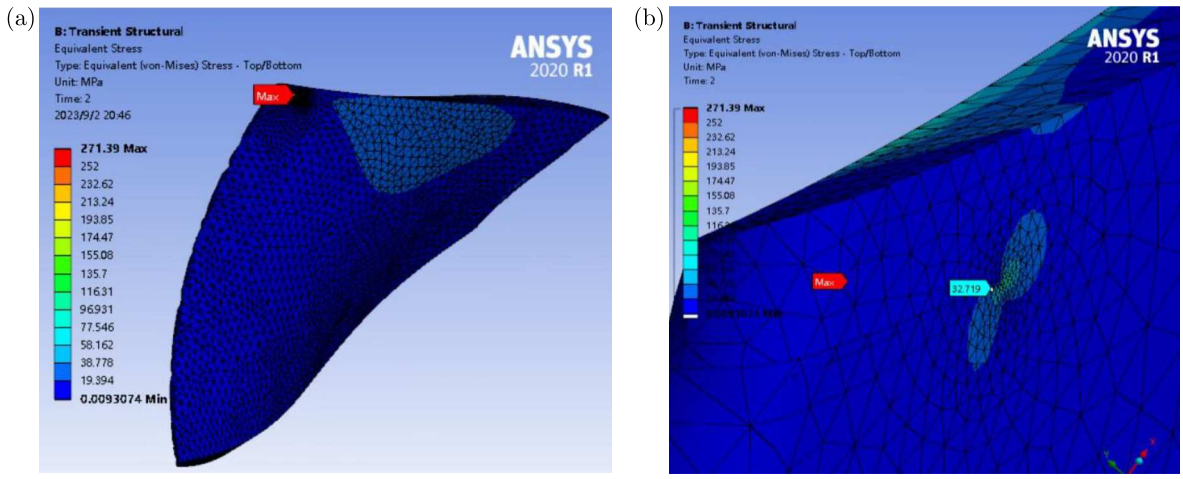

Fig. 5. (a) Blade crack model, (b) crack position force diagram

of the contact force on the crack surface increases as well. When the sum of the frequency of hydraulic excitation and the crack surface contact force acting on the blade is close to the natural frequency of the blade, a combined resonance of the runner blade will be caused. Based on the characteristics of hydraulic excitation acting on the blade, when the crack extends to 132 mm, the combined resonance will occur. By comparing Figs. 3b and 4b, it can be observed that when the crack length is 150 mm, the dynamic stress at the crack tip was more irregular than that when the crack length was 100 mm, which also provides a theoretical basis for unstable propagation of the crack under resonance.

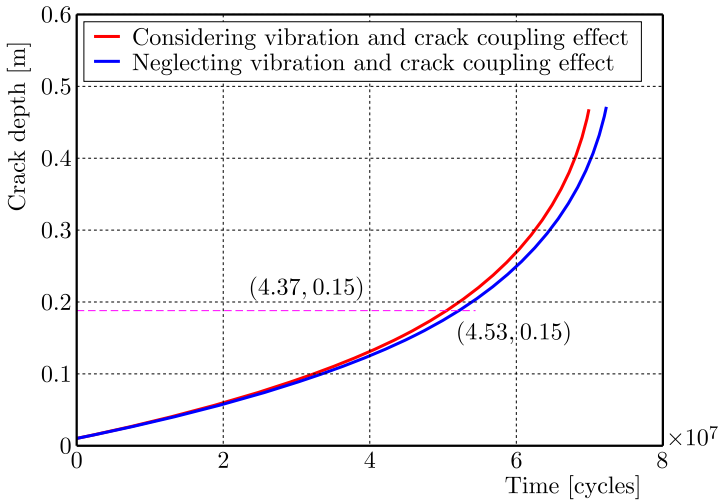

Fig. 6. Simulation curve of fatigue crack propagation

In Fig. 6, when only dynamic stress is considered without considering the coupling effect of vibration and crack, the crack propagation life curve is the blue line; and when the contact force and dynamic stress on the crack surface are considered, taking the coupling effect of vibration and crack into consideration, the crack propagation life curve is the one red. It can be observed that when the working condition was only the rated load, the crack expanded to the length of 150 mm after $4.53 \cdot 10^7$ s (524.3 days). When the coupling effect of vibration and crack was taken into consideration, the crack propagation to 150 mm took $4.42 \cdot 10^7$ s (511.6 days). According to (Yang *et al.*, 2014)], the turbine blades are mainly operated near the rated working conditions and are stopped for inspection every $4.25 \cdot 10^7$ s (491.7 days). When considering the coupling

effect of vibration and crack, the error between the simulation and test results is 4.04%, while, without considering the coupling effect of vibration and crack, the error is 6.63%. This indicates that the vibration fatigue crack propagation model considering the coupling effect of vibration and crack is more accurate, and provides a basis for fatigue strength and life prediction of blades.

7. Conclusions

- With propagation of the crack, the contact force on the crack surface increases, its period increases, and the dynamic stress amplitude at the crack tip increases as well.
- The propagation of the crack increases the crack stiffness, which leads to a continuous reduction in the natural frequency of the blade. When the sum of the frequency of hydraulic excitation and the crack surface contact force acting on the blade is close to the natural frequency of the blade, amd a combined resonance occurs, which also provides a theoretical basis for unstable propagation of cracks under the resonance.
- When the coupling effect of vibration and crack is taken into consideration, the developed vibration fatigue crack propagation model is more accurate, and can provide a basis for prediction of the fatigue strength and life of the blades.

Acknowledgments

The research was supported by a doctoral start-up fund of Guangxi University of Science and Technology (No. 03210126) as well as National Natural Science Foundation of China under grants No. 22262005. The supports are gratefully acknowledged.

References

1. Andreaus U., Baragatti P., 2011, Cracked beam identification by numerically analysing the nonlinear behaviour of the harmonically forced response, *Journal of Sound and Vibration*, **330**, 4, 721-742
2. Arvin H., Bakhtiari-Nejad F., 2011, Non-linear modal analysis of a rotating beam, *International Journal of Non-Linear Mechanics*, **46**, 6, 877-897
3. Bednarz J., 2017, Operational modal analysis for crack detection in rotating blades, *Archives of Acoustics*, **42**, 1, 105-112
4. Chondros T.G., Dimarogonas A.D., Yao J., 2001, Vibration of a beam with a breathing crack, *Journal of Sound and Vibration*, **239**, 1, 57-67
5. Cui W., Wang J., 2014, Coupling analysis of vibration and crack propagation for a cracked beam at resonant state (in Chinese), *Journal of Propulsion Technology*, **10**, 1404-1411
6. Duan C., Singh R., 2007, Dynamic analysis of preload nonlinearity in a mechanical oscillator, *Journal of Sound and Vibration*, **301**, 3, 963-978
7. Fernandes R., El-Borgi S., Ahmed K., *et al.*, 2016, Static fracture and modal analysis simulation of a gas turbine compressor blade and bladed disk system, *Advanced Modeling and Simulation in Engineering Sciences*, **3**, 1, 1-23
8. Guangxi Electric Power Experimental Research Institute, Guangxi University, Datang Yantan Hydropower Plant. Dynamic stress test and crack cause analysis report of runner blade of No. 3 unit in Yantan power plant, Nanning: Guangxi Electric Power Experimental Research Institute, 1998
9. He Q., Peng H., Zhai P., Zhen Y., 2016, The effects of unbalance orientation angle on the stability of the lateral torsion coupling vibration of an accelerated rotor with a transverse breathing crack, *Mechanical Systems and Signal Processing*, **75**, 330-344

10. Kang J.W., Zhang J.F., Liu B.C., Huang T., 2008, Improved thermal stress analysis for castings, *International Journal of Cast Metals Research*, **21**, 1-4, 324-329

11. Khorrami H., Rakheja S., Sedaghati R., 2017, Vibration behavior of a two-crack shaft in a rotor disc-bearing system, *Mechanism and Machine Theory*, **113**, 67-84

12. Kucher O., Kharyton V., Laine J.P., *et al.*, 2007, Harmonic balance method implementation for crack breathing process simulation, *Aerospace Technique and Technology*, **44**, 8, 150-156

13. Li Z.J., Wang Y.J., Li T.H., Ma X., Ji J., 2019, Effect of crack surface contact forces on vibration fatigue characteristics of beam structure, *Journal of the Brazilian Society of Mechanical Sciences and Engineering*, **41**, 12, 560

14. Li Z.J., Wang Y.J., Liu F.X., *et al.*, 2020, The hydrodynamic pressure characters acting on a turbine runner blade under the vortex rope in draft tube (in Chinese), *Journal of Guangxi University (Natural Science Edition)*, **45**, 6, 1351-1358

15. Liu W.G., Barkey M.E., 2018, The effects of breathing behaviour on crack growth of a vibrating beam, *Shock and Vibration*, **3**, 2579419.1-12

16. Liu W.G., Chen G.P., 2010, Coupling analysis of vibration fatigue crack propagation for breathing cracked beam (in Chinese), *China Mechanical Engineering*, **21**, 23, 2798-2802

17. Luo Y., Presas A., Wang Z., Xiao Y., Wang H., Jiang X., 2019, Operating conditions leading to crack propagation in turbine blades of tidal barrages. Influence of head and operating mode, *Engineering Failure Analysis*, 104254

18. Paris P., Erdogan F., 1963, A critical analysis of crack propagation laws, *Journal of Basic Engineering*, **85**, 4, 528-534

19. Saito A., Castanier M.P., Pierre c., Poudou O., 2009, Efficient nonlinear vibration analysis of the forced response of rotating cracked blades, *Journal of Computational and Nonlinear Dynamics*, **4**, 1, 53-63

20. Wang Y.J., Li Z.J., Li T.H., Liu F., Fu A., 2021, A mathematical model of the hydrodynamic pressure acting on a turbine runner blade under the rotor-stator interaction based on the quasi--three dimensional finite element method, *Mathematical Problems in Engineering*, **2021**, 3, 1-11

21. Yang L.F., Xu H., She Z.P., *et al.*, 2014, Stress intensity factor for mixed mode cracks by Williams element (in Chinese), *Journal of Ship Mechanics*, **18**, 1, 115-124

22. Yang X.F., Swamidas A.S.J., Seshadri R., 2001, Crack identification in vibrating beams using the energy method, *Journal of Sound and Vibration*, **244**, 2, 339-357

23. Zhao J.S., 2003, *Fracture Mechanics and Fracture Physics* (in Chinese), Wuhan, Huazhong University of Science and Technology Press

24. Zhu D., Tao R., Xiao R.F.A., Pan L., 2020, Solving the runner blade crack problem for a Francis hydro-turbine operating under condition-complexity, *Renewable Energy*, **149**, 298-320

Manuscript received June 21, 2023; accepted for print October 13, 2023

JOURNAL OF THEORETICAL AND APPLIED MECHANICS
62, 1, pp. 89-101, Warsaw 2024
https://doi.org/10.15632/jtam-pl/174709

ESTIMATION OF STRESS INTENSITY FACTOR FOR SURFACE CRACKS IN THE FIRTREE GROOVE STRUCTURE OF A TURBINE DISK USING POOL-BASED ACTIVE LEARNING WITH GAUSSIAN PROCESS REGRESSION

Kaimin Guo
Research Institute of Aero-Engine, Beihang University, Beijing, China

Hongzhuo Liu, Han Yan, Ziyuan Song, Shengming Zhang
School of Energy and Power Engineering, Beihang University, Beijing, China

Dawei Huang
School of Energy and Power Engineering, Beihang University, Beijing, China, and
Beijing Key Laboratory of Aero-Engine Structure and Strength, Beijing, China
e-mail: huangdawei@buaa.edu.cn

Xiaojun Yan
School of Energy and Power Engineering, Beihang University, Beijing, China, and
Beijing Key Laboratory of Aero-Engine Structure and Strength, Beijing, China, and
National Key Laboratory of Science and Technology on Aero-Engine Aero-thermodynamics, Beijing, China
e-mail: yanxiaojun@buaa.edu.cn

Calculation of the stress intensity factor K is a crucial and difficult task in linear elastic fracture mechanics. With the capacity to solve complex input-output problems of an underlying system, machine learning is especially useful in the calculation of K. However, when faced with complex systems, such as the firtree groove structure of a turbine disk, the data-consuming issue has always been a thorny problem in K-solutions combined with machine learning studies for a long time. In this paper, a novel K-solution method called PA-GPR (Pool-based Active learning with Gaussian Process Regression) for the calculation of the stress intensity factor for surface cracks in the firtree groove structure of a turbine disk is proposed. Using the pool-based active learning strategy, the proposed K-solution method could make the GPR model have a great regression performance with a few samples required. In the pool-based active learning strategy analysis, the learning function based on greedy sampling is proposed to select samples with a high contribution to the training of the GPR model. The calculation of K for a semi-elliptical surface crack in the firtree groove structure is evaluated to verify the accuracy and effectiveness of the proposed method. The results show that this novel method is accurate, time-saving and effective.

Keywords: damage tolerance, stress intensity factor solutions, machine learning, active learning

1. Introduction

Probabilistic damage tolerance analysis is essential for the assessment of integrity and reliability in practical engineering applications such as high-temperature components in aero engines (Basista and Węglewski, 2006; Huang *et al.*, 2018, 2019; P. Li *et al.*, 2018; Y. Li *et al.*, 2019; Rinaldi *et al.*, 2006), high-speed railway components, etc. In the probabilistic damage tolerance assessment of a turbine disk, it is necessary to carry out crack growth calculations in locally complex structures (such as the firtree groove structure, etc.) many times (up to 10^6) under

the assumption of the existence of an initial defect or crack, the convergence failure risk can be obtained by a statistical method.

The firtree groove structure is one of the most critical and complicated regions of a turbine disk (Yuan *et al.*, 2021). In the aspect of structure, the firtree groove structure is composed of many pairs of tenons with complex geometric characters. Meanwhile, the firtree groove structure bears many complicated loads, such as the centrifugal force of the blade, aerodynamic bending moment, thermal load and vibration load (Yang *et al.*, 2017). The complexity of geometry and load makes the firtree groove structure one of the most vulnerable parts of the turbine disk.

Consequently, due to the complexity of geometry and load of the firtree groove structure, it is difficult to evaluate the crack growth, especially the stress intensity factor K for (Cui and Wang, 2011; Witek, 2012).

Up to now, lots of K-solution methods have been developed for cracks in the firtree groove structure of a turbine disk, such as the finite element method (FEM) (Boulenouar *et al.*, 2014; Huang *et al.*, 2021; Moustabchir *et al.*, 2015, 2017; Shlyannikov *et al.*, 2016) and machine learning (ML). The finite element method usually becomes a reliable method to generate accurate K solutions. However, the accuracy of the finite element method is greatly influenced by the number of mesh elements of the model. When faced with a complex structure like the firtree groove structure, this number must be large. That means, consequently, a high computational cost of the finite element method.

Recently, K-solutions combined with ML have become a topic of growing interest (Keprate *et al.*, 2017; Liu *et al.*, 2020; Muñoz-Abella *et al.*, 2015; Xu *et al.*, 2021). With the capacity to solve complex input-output problems of an underlying system, ML is especially useful in the calculation of K. These solutions proceed in three steps (in this paper, the method that follows these steps is called the traditional ML method): (1) calculating the limit number of K data as the training data set; (2) training an ML model using training the data set and (3) predicting values of K using the trained ML model.

However, the data-consuming issue has always been a thorny problem in the K-solutions combined with ML studies for a long time. For regression problems, the generalization ability of a ML model is always related to a sample size of the training data set. A large quantity of data is usually required to get accurate results in the calculation of K. This problem is particularly acute in the face of complex structures, such as turbine disk grooves, etc. In some studies, the sample size of the training data set has even reached 10^6.

The active learning strategy is an efficient solution to this data-consuming problem. This strategy first uses the initial training data set T to train the regression ML model. Then the initial training data set T is enriched by adding new sample points based on the defined learning function. And finally, a new surrogate model is retained using the updated T, then the above-mentioned steps are repeated till the convergence criterion is satisfied.

This study presents a novel K-solution method called PA-GPR (Pool-based Active learning with Gaussian Process Regression) for the calculation of the stress intensity factor for surface cracks in the firtree groove structure of a turbine disk. The paper is organized as follows. Firstly, some problems of K-calculation for surface cracks in the firtree groove structure will be described. Then, details and principles of the proposed PA-GPR are elaborated, including the learning function and the convergence criterion. To demonstrate the accuracy and effectiveness of the proposed method, a calculation of K case is presented, i.e., calculation of K for a semi-elliptical surface crack in the firtree groove structure of a turbine disk. Furthermore, the mechanism of the learning function of active learning is discussed.

2. Problem description

The firtree groove structure is one of the most critical and complicated regions of turbine disks. As shown in Fig. 1, the geometry features include the number of firtree teeth n, flank length l, contact angle α, flank angles β and γ, outer radius R_0 and inner radius R_1 (Meguid *et al.*, 2000). Moreover, different kinds of loads including the centrifugal force, the thermal load, vibration load are applied to the firtree groove structure. The intricate structure and load conditions make the stress and fracture analysis a hard task. Figure 2 shows a typical stress distribution of the firtree groove structure.

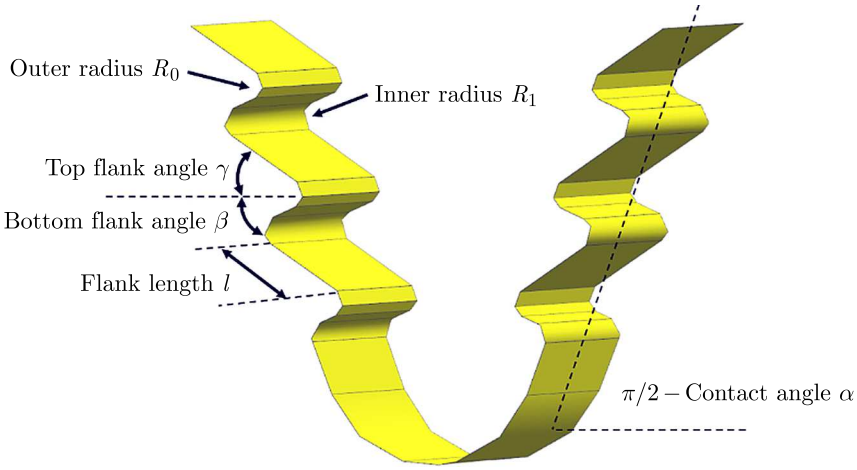

Fig. 1. Schematic of the firtree groove structure

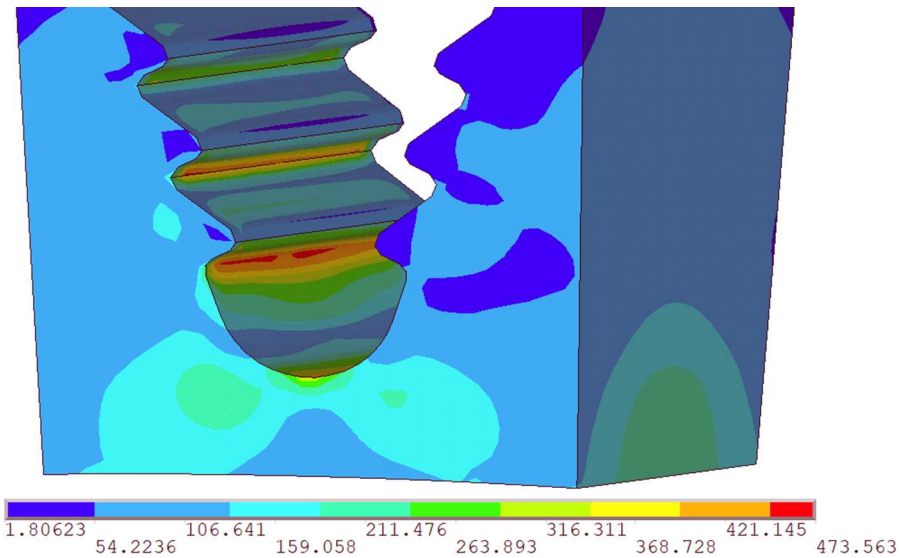

Fig. 2. An example of von Mises stress distribution of the firtree groove structure (the values on the scale are von Mises stress values, unit: MPa)

Cracks may occur at the firtree groove structure (especially at the bottom) due to cyclic loading or initial defects. Considering the requirement of the turbine disk failure risk, it is necessary to develop an efficient and rapid method for calculation of the K for a large number of repeated crack growth evaluations.

The effective K-solution method proposed in this paper focuses on the calculation of the stress intensity factor for surface cracks in the firtree groove structure. As shown in Fig. 3,

a semi-elliptical surface crack is located at the transition arc between the fifth teeth and the bottom of the groove. It is assumed that the leading edge of the crack keeps an elliptical shape during the propagation process. Key dimensional parameters of the crack are $\{a, c, \xi\}$, where a and c mean the depth and half-length of the surface crack, respectively. The ξ denotes the position of point P on the edge of the crack, $\xi = |AC|/|AB|$, as shown in Fig. 4.

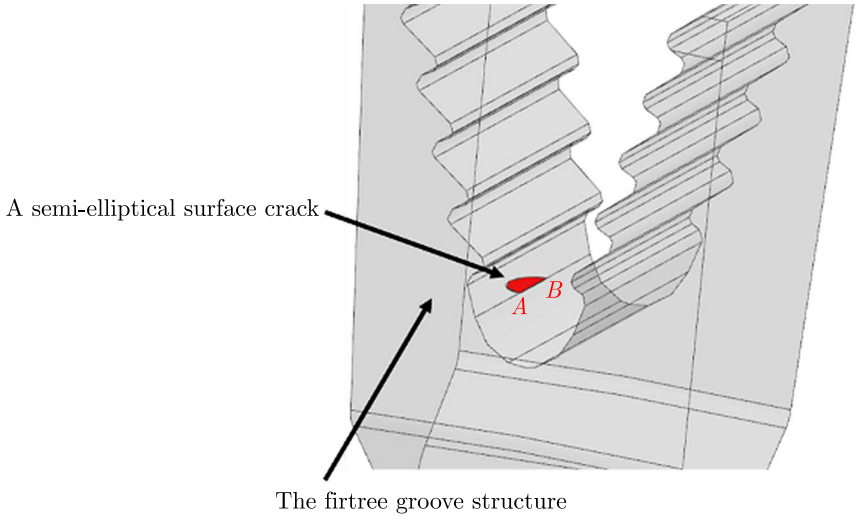

Fig. 3. A semi-elliptical surface crack in the firtree groove structure of a turbine disk

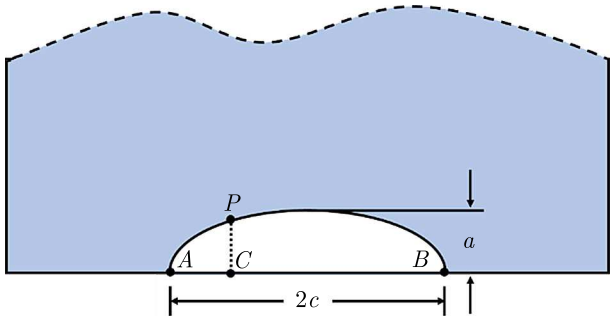

Fig. 4. The geometry configuration of a semi-elliptical surface crack in the firtree groove structure of a turbine disk

For a particular type of the firtree groove structure, the stress distribution and shape of the crack are certain, but the initial crack size is random. That means the dimensional parameters $\{a, c\}$ are random variables. Meanwhile, in order to accurately evaluate the value of K, it is necessary to calculate K at any point (point P as shown in Fig. 4) along the crack front, i.e., $0 \leqslant \xi \leqslant 1$.

3. Pool-based Active learning with Gaussian Process Regression (PA-GPR)

The proposed PA-GPR method includes two critical parts, the GPR algorithm and the pool--based active learning strategy. The GPR algorithm is adopted for the prediction of K. The pool--based active learning strategy is used in the training progress of the GPR model, making the trained GPR model have a great generalization ability with only a few training samples required.

3.1. PA-GPR for calculation of K

The Gaussian process regression, belonging to supervised learning, is a non-parametric model for regression analysis of data using Gaussian processes (Rasmussen, 2003). It can be written as

$$f \sim GP(m(x), k(x, x')) \tag{3.1}$$

where $m(x)$ and $k(x, x')$ represent the mean and covariance function, respectively. Equation (3.1) means the function f is distributed as a Gaussian process with the mean function m and covariance function k. More details could be seen in the literature (Rasmussen, 2003).

The flow diagram of the proposed PA-GPR method is shown in Fig. 5, and it is based on the following steps:

(1) Generate a candidate sample pool $\mathbf{S}$ including N_S samples. In the calculation process of K, the input variables are parameters that affect the stress intensity factor results, such as crack depth and dimensions of the cracked structure. The candidate sample pool $\mathbf{S}$ is generated by random sampling based on the distribution or range of the input variables.
(2) $\mathbf{S} = \mathbf{L} \cup \mathbf{U}$, $\mathbf{L} \cap \mathbf{U} = \emptyset$. $\mathbf{L}$ denotes the labeled data set and $\mathbf{U}$ is the unlabeled data set. The labeled data set $\mathbf{L}$ consists of N samples picked from $\mathbf{S}$. $\mathbf{L} = \{\mathbf{X}_1, \mathbf{X}_2, \ldots, \mathbf{X}_N\}$. Compared with the sample size of $\mathbf{S}$, N is typically several orders of magnitude smaller.
(3) After definition of the labeled data set $\mathbf{L}$, the corresponding response $\mathbf{Y}$ should be computed, i.e., $\mathbf{Y} = \{K_1, K_2, \ldots, K_N\}$. Then a training data set $\mathbf{T}$ should be defined, $\mathbf{T} = \{\mathbf{L}, \mathbf{Y}\}$.
(4) Train the GPR model using $\mathbf{T}$.
(5) If the convergence criterion (mentioned in Section 3.3) is not satisfied, the training data set $\mathbf{T}$ should be enriched by the learning function (mentioned in Section 3.2). In detail, the new sample $\mathbf{X}_{new}$ could be selected from the unlabeled data set $\mathbf{U}$ using the learning function. And the corresponding response K_{new} should be calculated. Then the training data set $\mathbf{T}$ becomes the new training data set $\mathbf{T}_{new}$ by adding a new sample, i.e., $\mathbf{T}_{new} = \mathbf{T} \cup \{\mathbf{X}_{new}, K_{new}\}$.
(6) Retrain the GPR model using $\mathbf{T}_{new}$. Repeat steps (4) to (5) until the convergence criterion is satisfied.

3.2. Learning function

Different sample points in the same sample pool have different degrees of contribution to training of the GPR model. In the traditional machine learning method for regression, there are often spatial overlaps or approximate overlaps among the sample points in the training data set, which makes these samples a poor contribution to training of the GPR model. On the contrary, if the selected samples can avoid spatial overlaps or approximate overlaps situations, these samples will make a high contribution to training of the GPR model. A more detailed explanation could be seen in Section 5. Consequently, the GPR model could have a great generalization ability with only a few samples required, as long as samples with great contributions are selected by the proposed learning function from the unlabeled data set $\mathbf{U}$.

Inspired by the greedy sampling (GS) strategy, this paper proposes a GS-based learning function to pick key samples with great contributions to training of the GPR model (Wu *et al.*, 2019; Yu and Kim, 2010). In different application situations, two different learning functions, i.e., GS on the inputs and GS on the outputs are proposed.

3.2.1. GS on the inputs

To achieve diversity in the input space, GS on the inputs could be elaborated as follows.

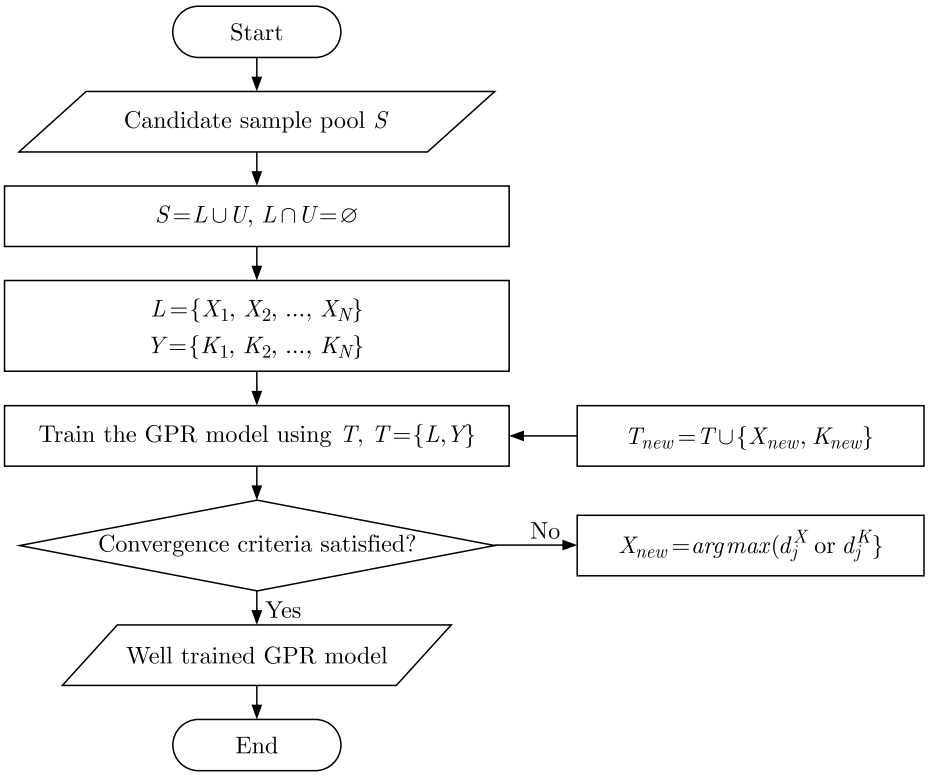

Fig. 5. Flowchart of the proposed PA-GPR

It is assumed that the labeled data set $\mathbf{L}$ consists of N samples $\mathbf{X}_i$ $(i = 1, 2, \ldots, N)$ picked from $\mathbf{S}$. For each of the remaining $N_S - N$ samples $\mathbf{X}_j$ $(j = N+1, N+2, \ldots, N_S)$, its distance to each of the labeled data set $\mathbf{L}$ could be calculated as

$$d_{ij}^X = \|X_i - X_j\|_2 \tag{3.2}$$

where $i = 1, 2, \ldots, N$, $j = N+1, N+2, \ldots, N_S$. Then the shortest distance from the j-th sample $\mathbf{X}_j$ to N labeled samples, $\mathbf{d}_j$ could be written as

$$d_j^X = \min(d_{ij}^X) \tag{3.3}$$

where $j = N+1, N+2, \ldots, N_S$.

The learning function based on GS on the inputs is proposed as

$$X_{new} = \arg\max(d_j^X) \tag{3.4}$$

the new sample point ($\mathbf{X}_{new}$, to be added in $\mathbf{T}$) could be chosen from $\mathbf{U}$ by this learning function.

3.2.2. GS on the outputs

In some application situations, the learning function based on GS on the outputs is more effective than GS on the inputs. Similar to the learning function based on GS on the inputs, details of the learning function based on GS on the outputs could be explained as follows.

Similarly, it is assumed that the training data set $\mathbf{T}$ consists of N samples $\{\mathbf{X}_i, K_i\}$ $(i = 1, 2, \ldots, N)$. The trained GPR model could predict the value of the corresponding response for each of the remaining $N_S - N$ samples as

$$\widehat{K_j} = f(X_j) \tag{3.5}$$

where $j = N+1, N+2, \ldots, N_S$.

Then the distance on the outputs from each of the remaining $N_S - N$ samples $\mathbf{X}_j$ $(j = N+1, N+2, \ldots, N_S)$ to each of the labeled data set $\mathbf{L}$ could be calculated by

$$d_{ij}^K = \|K_i - \widehat{K}_j\|_2 \tag{3.6}$$

where $i = 1, 2, \ldots, N$, $j = N+1, N+2, \ldots, N_S$. Then, the shortest distance on the outputs from the j-th sample X_j to N labeled samples, $\mathbf{d}_j$, could be written as

$$d_j^K = \min(d_{ij}^K) \tag{3.7}$$

where $j = N+1, N+2, \ldots, N_S$.

The learning function based on GS on the outputs is proposed as

$$X_{new} = \arg\max(d_j^K) \tag{3.8}$$

the new sample point ($\mathbf{X}_{new}$, to be added in $\mathbf{T}$) could be chosen from $\mathbf{U}$ by this learning function.

For GS on the inputs or outputs, it is difficult to determine which method is more effective. For validation cases in this research, two learning functions are both applied to find the learning function with better performance.

3.3. Convergence criterion

In this study, N_V labeled data (not belonging to the labeled data set $\mathbf{L}$) are randomly selected to make up the validation set. The GPR model has a good generalization ability when the mean relative validation error reaches convergence, which could be written as

$$\frac{1}{N_V}\sum_{p=1}^{N_V}\frac{|\widehat{K}_p - K_p|}{K_p} \leqslant \varepsilon \tag{3.9}$$

where ε means the convergence threshold.

4. K-solution using PA-GPR

In this Section, the PA-GPR method is applied to the calculation of K for a semi-elliptical surface crack in a turbine disk firtree groove structure. The prediction accuracy of the PA-GPR is firstly discussed. Then, two different K-solution methods, PA-GPR and the traditional ML method are compared in order to evaluate which one requires fewer samples. Here, the traditional ML model is also GPR, where the training data set is generated by random sampling from the candidate sample pool $\mathbf{S}$.

According to the surface crack in the firtree groove structure described in Section 2, the input variables are $\mathbf{X} = (a, c, \xi)$, and the output variable is the stress intensity factor K. Each of the input variable is defined as

$$c, a \in [0.1\,\text{mm}, 5\,\text{mm}] \qquad \frac{a}{c} \in [0.1, 1] \qquad \xi \in [0, 1] \tag{4.1}$$

$10^5 K$ samples for surface cracks in the firtree groove structure subjected to the centrifugal force and temperature are calculated using the professional fracture analysis software FRANC3D to make up the candidate sample pool $\mathbf{S}$. The FEM crack mesh generated by FRANC3D is shown in Fig. 6. In addition, $N_V = 200$, $\varepsilon = 1.62\%$. The mean relative validation error of this ML model is 1.62%. So, the convergence threshold ε value is set to 1.62%, to evaluate the effectiveness of the PA-GPR by comparing the sample size with the identical mean relative validation error. The initial labeled data set consists of 100 samples. After the application of two learning functions

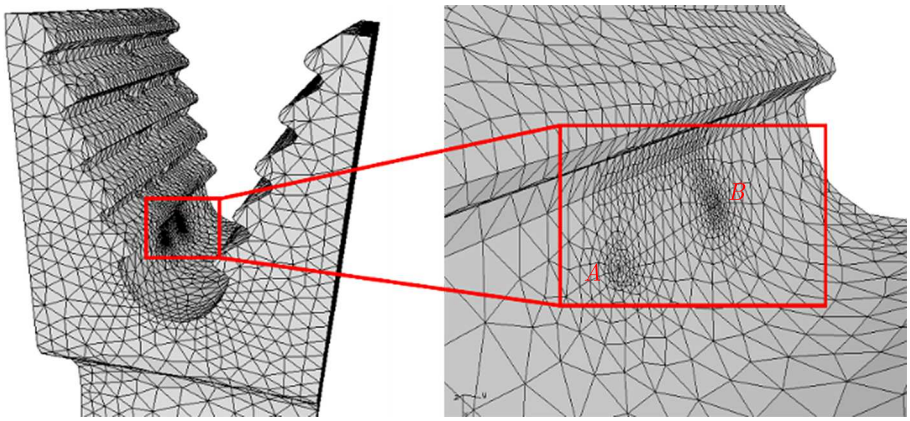

Fig. 6. The FEM crack mesh generated by FRANC3D

(GS on the outputs or inputs) in this validation case, it is found that the sample size is smaller when using the learning function based on GS on the inputs. Consequently, the learning function based on GS on the inputs is adopted.

The plot of the predicted K using PA-GPR vs. true K calculated by FRANC3D is shown in Fig. 7. It is shown that the 200 observation points are sited around the perfect prediction line. The K results with different dimensional parameters calculated by the proposed PA-GPR are compared with those calculated by FRANC3D (as shown in Fig. 8). It can be observed that the K result driven by PA-GPR is very close to the result calculated by FRANC3D.

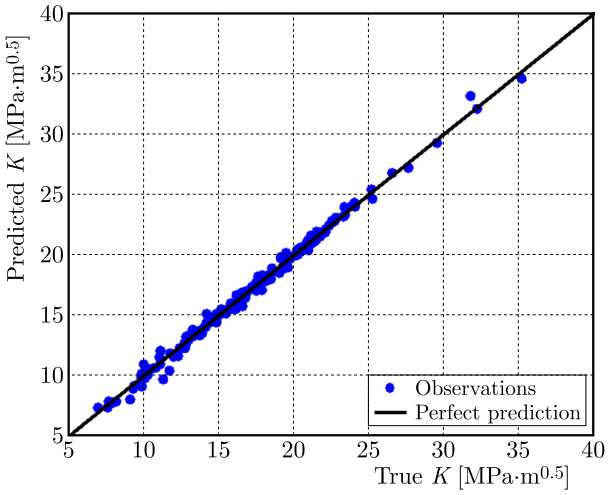

Fig. 7. Predicted K using PA-GPR vs. true K (calculated by FRANC3D) for a semi-elliptical surface crack in a turbine disk firtree groove

When the convergence is reached, the numbers of required samples of PA-GPR and the traditional ML method are shown in Table 1. That means, the proposed PA-GPR is two orders of magnitude more efficient than the traditional ML method.

It should be noted that the proposed PA-GPR adds time for sample selection. However, compared to the time to get the label of the reduced samples (calculating K by the finite element method or other K-solution method), the time for sample selection is negligible.

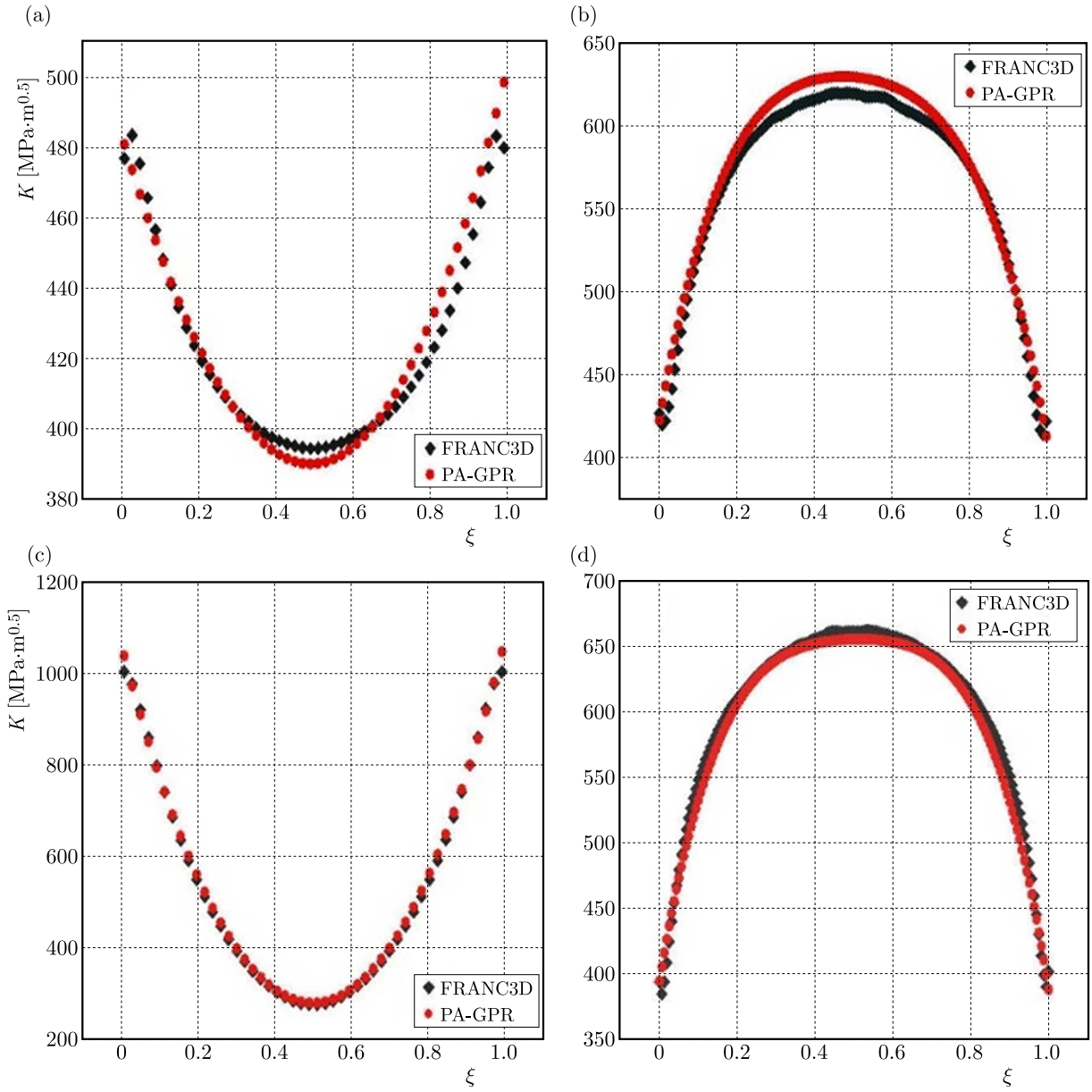

Fig. 8. K results with different dimensional parameters: (a) $a = 0.53\,\text{mm}$, $c = 0.58\,\text{mm}$, (b) $a = 0.65\,\text{mm}$, $c = 2.49\,\text{mm}$, (c) $a = 3.42\,\text{mm}$, $c = 3.47\,\text{mm}$ and (d) $a = 0.65\,\text{mm}$, $c = 3.31\,\text{mm}$

Table 1. The sample size required for PA-GPR and the supervised ML method

	Traditional ML method	PA-GPR
The number of required samples	5E4	1135 (including initial 100 samples)

5. Discussion

The ML-based method becomes an effective stress intensity factor solution in the recent linear elastic fracture mechanics studies. However, for traditional ML regression problems, a good regression performance always means a lot of labeled training samples. That causes a time--consuming issue.

In traditional machine learning for regression, there are often spatial overlaps or approximate overlaps between the sample points in the training data set. For example, there are two sample points, $(a, c, \xi, K) = (3.3738, 1.5372, 0.1961, 21.1314)$ and $(3.4334, 1.3629, 0.8013, 21.1316)$ in the training data set for the traditional ML model in Section 4. These two sample points approximately overlap in Euclidean space, which makes the contribution of these two sample points to training of the model equal to the contribution of only one sample point. This phenomenon results in waste of sample points. Further, spatial overlaps or approximate overlaps of many sample points make the training of the regression model time-consuming.

As mentioned in this paper, the pool-based active learning strategy could solve this time--consuming problem by selecting specific samples using the learning function. The purpose of GS is to achieve diversity of sample space (inputs space or outputs space). Whether to choose GS on the inputs or outputs space depends on a specific application situation.

Diversity of the sample space could avoid the waste of sample points. This is also the main idea of the learning function based on GS. Specifically, the learning function based on GS could pick only one sample point among samples with spatial overlaps or approximate overlaps situations into the training data set. When the action of picking is done, sample points (picked by the learning function) of the training data set could cover the range of the independent (or dependent) variables. That achieves diversity of the sample space using a few sample points. Further, the regression model would have a great regression performance using a few sample points.

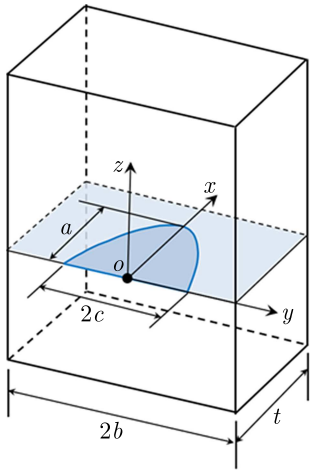

Fig. 9. The geometry configuration of a semi-elliptical surface crack in a finite plate

A calculation case is evaluated to visualize the diversity of the inputs space and the mechanism of the learning function based on GS. In this case, the calculation of K for a semi-elliptical surface crack in a finite plate is evaluated. The data for this validation case were obtained from the literature (Newman and Raju, 1981). The geometry configuration of a semi-elliptical surface crack in a finite plate is shown in Fig. 9, where the plate width is $2b = 50\,\text{mm}$, and the plate thickness is $t = 10\,\text{mm}$. The depth and half-length of the surface crack are represented by a and c, respectively. The plate is subjected to a remote uniform tension load with the stress ratio $R = 0$. This uniform tension load could be characterized by $\sigma = 800\,\text{MPa}$. The input variables are $\mathbf{X} = (a, c)$, and the output variable is the stress intensity factor K. Each of the input variables is defined as

$$\ln a \simeq N(-1.346, 0.49) \qquad \frac{a}{c} \in [0.2, 1] \tag{5.1}$$

where the depth of the surface crack a is assumed to fit lognormal distribution (Liu and Mahadevan, 2009), and its mean value and standard deviation are 0.33 mm and 0.26 mm, respectively. 10^5 samples are randomly sampled to make up the candidate sample pool $\mathbf{S}$ based on the distri-

bution or range of input variables. as shown in Eq. (5.1). In detail, for a sample $\mathbf{X}_0 = (a_0, c_0)$, a_0 is sampled based on the lognormal distribution in Eq. (5.1) using the Box Muller method. Then, values of a_0/c_0 could be sampled by a uniform sampling method based on the distribution in Eq. (5.1).

100 samples are selected by the learning function based on GS on the inputs and randomly sampled, as shown in Fig. 10a and 10b, respectively. Meanwhile, a candidate sample pool including 10^4 samples is given in Fig. 10c, which shows the range of inputs space as a control.

As Fig. 10b shows, there are many sample points with spatial overlaps or approximate overlaps situations clustered in the dashed red line ellipse, while there are a few sample points in the dashed blue line circle. If the regression model is trained using these 100 samples, the imbalance situation will inevitably cause a bad regression performance.

Compared with Fig. 10b, Fig. 10a shows a good distribution of sample points in the sample space. Sample points, selected by the learning function, are evenly distributed in the sample space. That means the diversity of the sample space is achieved. If the regression model is trained using these 100 samples selected by the learning function, the diversity of the sample space would lead to a great regression performance using much fewer samples.

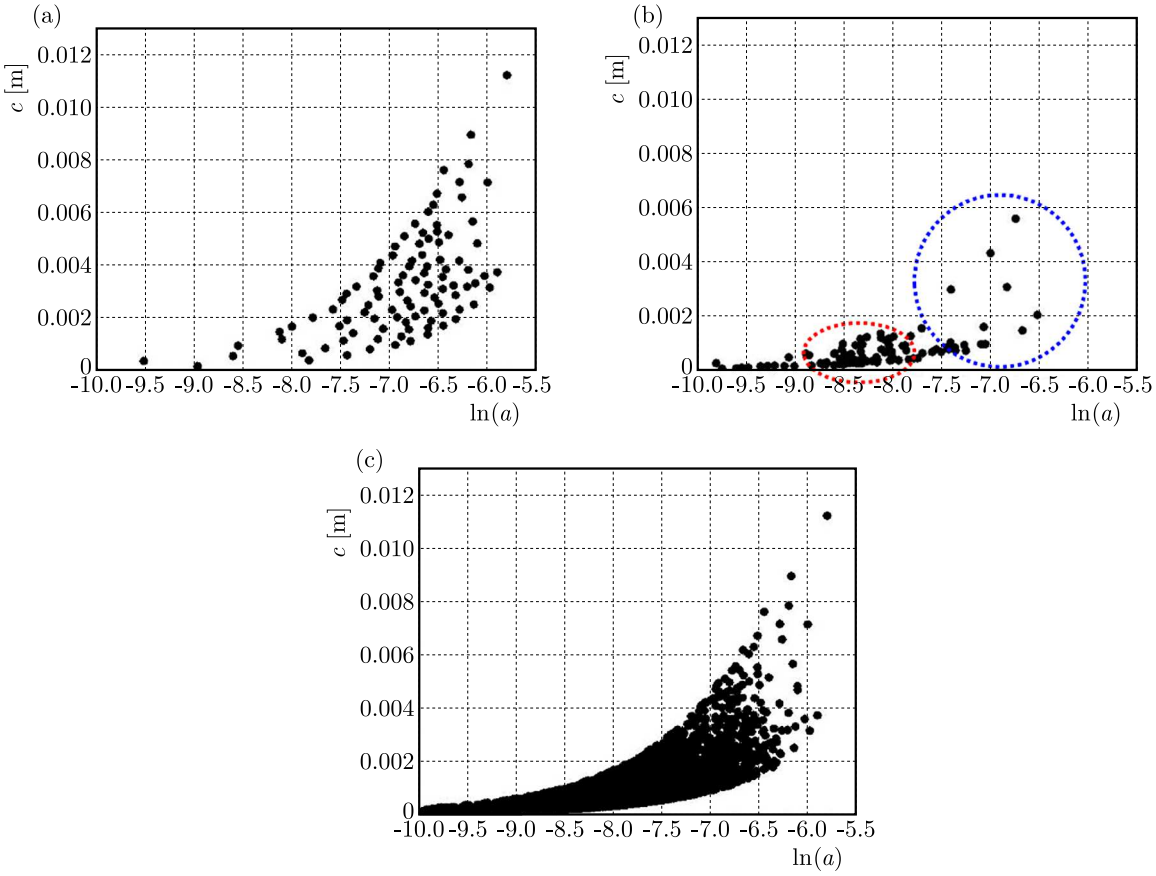

Fig. 10. Distribution of sample points in the inputs space: (a) samples selected by the learning function based on GS, (b) samples selected by randomly sampling and (c) range of the inputs space

6. Conclusion

Based on this study, three conclusions can be drawn:

- A novel K-solution method for surface cracks in the firtree groove structure of a turbine disk called PA-GPR (Pool-based Active learning with Gaussian Process Regression) is pro-

posed in this paper. Combining active learning strategy and Gaussian Process Regression (GPR), this novel method is accurate, time-saving and effective.

- Using the active learning strategy, the trained GPR model could have a great computational accuracy with only a few training samples required. For K calculation problems of surface cracks in the firtree groove structure of a turbine disk, the proposed PA-GPR is two orders of magnitude more efficient than the traditional ML method with almost identical K results.
- The learning function based on GS, the core of the proposed method, could select samples with a high contribution to the training of the GPR model by the achievement of diversity of the sample space. Focusing on spatial overlaps or approximate overlaps situations, the learning function picks only one sample point among samples with spatial overlaps or approximate overlaps situations into the training data set. That makes the GPR model have a great computational accuracy using a few samples only.

Acknowledgments

This study was supported by the National Major Science and Technology Project (Grant No. J2019-IV-0007-0075) and the Fundamental Research Funds for the Central Universities (grant No. YWF-23-L-1134).

References

1. Basista M., Węglewski W., 2006, Modelling of damage and fracture in ceramic matrix composites – an overview, *Journal of Theoretical and Applied Mechanics*, **44**, 3, 455-484
2. Boulenouar A., Benseddiq N., Mazari M., Benamara N., 2014, FE model for linear-elastic mixed mode loading: estimation of SIFs and crack propagation, *Journal of Theoretical and Applied Mechanics*, **52**, 2, 373-383
3. Cui W., Wang J., 2011, Probabilistic analysis of gas turbine disk multi-crack propagation, *Turbo Expo: Power for Land, Sea, and Air*, DOI: 10.1115/GT2011-45439
4. Huang D., Yan X., Li P., Qin X., Zhang X., Qi M., Liu Z., 2018, Modeling of temperature influence on the fatigue crack growth behavior of superalloys, *International Journal of Fatigue*, **110**, 22-30
5. Huang D., Yan X., Qin X., Zhang X., Qi M., Liu Z., Tao Z., 2019, Scatter in fatigue crack growth behavior of a Ni-base superalloy at high temperature, *International Journal of Fatigue*, **118**, 1-7
6. Huang X., Chen C., Xuan H., 2021, Experimental and analytical investigation for fatigue crack growth characteristics of an aero-engine fan disc, *International Journal of Fatigue*, **148**
7. Keprate A., Chandima Ratnayake R.M., Sankararaman S., 2017, Comparison of various surrogate models to predict stress intensity factor of a crack propagating in offshore piping, *Journal of Offshore Mechanics and Arctic Engineering*, **139**, 6
8. Li P., Cheng L., Yan X., Huang D., Qin X., Zhang X., 2018, A temperature-dependent model for predicting the fracture toughness of superalloys at elevated temperature, *Theoretical and Applied Fracture Mechanics*, **93**, 311-318
9. Li Y., Wang J., Guo W., Guo J., 2019, A modified model of residual strength prediction for metal plates with through-thickness cracks, *Journal of Theoretical and Applied Mechanics*, **57**, 3, 537-547
10. Liu X., Athanasiou C.E., Padture N.P., Sheldon B.W., Gao H., 2020, A machine learning approach to fracture mechanics problems, *Acta Materialia*, **190**, 105-112

11. Liu Y., Mahadevan S., 2009, Probabilistic fatigue life prediction using an equivalent initial flaw size distribution, *International Journal of Fatigue*, **31**, 3, 476-487

12. Meguid S.A., Kanth P.S., Czekanski A., 2000, Finite element analysis of fir-tree region in turbine discs, *Finite Elements in Analysis and Design*, **35**, 4, 305-317

13. Moustabchir H., Alaoui M.A.H., Babaoui A., Dearn K.D., Pruncu C.I., Azari Z., 2017, The influence of variations of geometrical parameters on the notching stress intensity factors of cylindrical shells, *Journal of Theoretical and Applied Mechanics*, **55**, 2, 559-569

14. Moustabchir H., Arbaoui J., Zitouni A., Hariri S., Dmytrakh I., 2015, Numerical analysis of stress intensity factor and T-stress in pipeline of steel P264GH submitted to loading conditions, *Journal of Theoretical and Applied Mechanics*, **53**, 3, 665-672

15. Muñoz-Abella B., Rubio L., Rubio P., 2015, Stress intensity factor estimation for unbalanced rotating cracked shafts by artificial neural networks, *Fatigue and Fracture of Engineering Materials and Structures*, **38**, 3, 352-367

16. Newman Jr J., Raju I., 1981, Stress-intensity factor equations for cracks in three-dimensional finite bodies, *ASTM National Symposium on Fracture Mechanics*, DOI: 10.1520/stp37074s

17. Rasmussen C.E., 2003, Gaussian processes in machine learning, *Summer School on Machine Learning*, 63-71, Springer, DOI: 10.1007/978-3-540-28650-9_4

18. Rinaldi A., Krajcinovic D., Mastilovic S., 2006, Statistical damage mechanics-constitutive relations, *Journal of Theoretical and Applied Mechanics*, **44**, 3, 585-602

19. Shlyannikov V., Zakharov A., Yarullin R., 2016, Structural integrity assessment of turbine disk on a plastic stress intensity factor basis, *International Journal of Fatigue*, **92**, 234-245

20. Witek L., 2012, Numerical simulation of fatigue fracture of the turbine disc, *Fatigue of Aircraft Structures*, **1**, 4, 114-122

21. Wu D., Lin C.-T., Huang J., 2019, Active learning for regression using greedy sampling, *Information Sciences*, **474**, 90-105

22. Xu T., Ding S., Zhou H., Li G., 2021, Machine learning-based efficient stress intensity factor calculation for aeroengine disk probabilistic risk assessment under polynomial stress fields, *Fatigue and Fracture of Engineering Materials and Structures*, **45**, 2, 451-465

23. Yang F., Pan C., Zhang D., Tang J, Yan J., 2017, Stress distribution and deformation analysis of gas turbine blades and disk with FEM method, *ASME Power Conference*, DOI: 10.1115/POWER-ICOPE2017-3409

24. Yu H., Kim S., 2010, Passive sampling for regression, *2010 IEEE International Conference on Data Mining*, DOI: 10.1109/icdm.2010.9

25. Yuan R., Liao D., Zhu S.P., Yu Z.Y., Correia J., De Jesus A., 2021, Contact stress analysis and fatigue life prediction of turbine disc-blade attachment with fir-tree tenon structure, *Fatigue and Fracture of Engineering Materials and Structures*, **44**, 4, 1014-1026

Manuscript received August 8, 2023; accepted for print September 14, 2023

JOURNAL OF THEORETICAL AND APPLIED MECHANICS
62, 1, pp. 103-115, Warsaw 2024
https://doi.org/10.15632/jtam-pl/174733

COMPARATIVE ANALYSIS OF STRUCTURE PERFORMANCE OF PDC CUTTER TOOTH SURFACE AND INTERFACE MATCHING PAIR

Fuxiao Zhang, Yanjun Lu

School of Mechanical and Precision Instrument Engineering, Xi'an University of Technology, Xi'an, China

Corresponding author Fuxiao Zhang, e-mail: zhangfuxiaoswpu@163.com

Hai Zhu, Jutong Ding

Electromechanical Engineering College, Southwest Petroleum University, Chengdu, China

With the improvement of research on the tooth surface and interface, the rock breaking technology of a polycrystalline diamond compact (PDC) bit has witnessed significant advancements and widespread applications in various domains. However, the current research on the tooth surface and interface is largely independent of each other, lacking integration between the two. This study aims to explore the influence of the connection between the tooth surface and interface on cutting efficiency and failure mechanisms during PDC bit cutting operations. Six different mating structures are selected for analysis, and the cutting process is simulated using Abaqus software in a consistent environment. The study examined the crushing specific energy, stress distribution, cutting force and temperature rise effect of different mating structures. Comparative analysis revealed that the efficiency and failure mechanism of the cutter are influenced by the interface shape, both within the same tooth shape and across different tooth shapes. Among the selected mating structures, the saddle-tooth surface with a radial interface exhibited superior performance in all aspects and demonstrated significant improvements. The findings provide a theoretical foundation for the study of the mechanism behind PDC cutter mating structures.

Keywords: Abaqus, PDC cutter, interface structure, matching pair

1. Introduction

The polycrystalline diamond compact (PDC) cutter plays a crucial role in the cutting process of PDC bits, with its performance significantly influencing the drilling effectiveness. In recent years, the drilling industry has witnessed the emergence of numerous specialised tooth profiles, owing to continuous advancements in PDC tooth profile research and development. Alongside improvements in cutter profile and interface optimisation, the drilling technology has made a remarkable progress, leading to enhanced drilling efficiency. With its extensive adaptability to various formations and cost-effectiveness, PDC bits have captured more than 70% of the market share (Zhang *et al.*, 2022). The global trend of ultra-deep drilling has further solidified the use of PDC bits as the mainstream approach for efficient and rational resource extraction (Zhu *et al.*, 2021).

To comprehensively understand the action mechanisms of PDC cutters, researchers worldwide have conducted studies on the rock breaking mechanism of PDC bits, predominantly employing empirical models and finite element simulations. Liu *et al.* (2018) analysed the rock breaking process of cutting tools using discrete elements. Fu *et al.* (2022) employed discrete element analysis to analyse PDC cutting forces, studying the force response of rock in conjunction with microscopic failure mechanisms and elucidating the influence of tool geometry. Wu *et al.* (2020) utilised the finite element method to simulate rock breaking and proposed a novel simulation method for optimising PDC rock breaking research. Hang *et al.* (2013) deserved recognition

for their ability to simultaneously reproduce elastoplastic strain, damage and brittle fracture, which they employed in the study of tool-rock interaction, among other applications. With the maturation of finite element simulation technology and improvement in analysis methods, the use of finite element simulation software for analysis purposes has become a prevailing trend in PDC rock breaking analysis.

To investigate potential connections between different tooth surfaces and interfaces of PDC cutters, a comparative study is conducted on the structural performance of three distinct tooth surfaces and their corresponding interfaces and interface matching pairs. Interfaces with favourable performance are selected for analysis. A PDC cutter linear cutting rock model is constructed using Abaqus to simulate PDC cutter cutting tests, and the influence of accessory structure on the cutting action is examined from four perspectives: the crushing specific energy, cutting force, cutter stress and temperature rise effect.

2. Interface structure optimisation

The interface plays a crucial role in determining the overall cutting performance of a PDC bit. Thermal residual stress in PDC is widely considered the primary cause of abnormal failures. Different forms of interface structures and variations in material thickness within the same material can significantly influence the size and distribution of thermal stress (Xu, 2009). This study focuses on optimising the four interface structures depicted in Fig. 1.

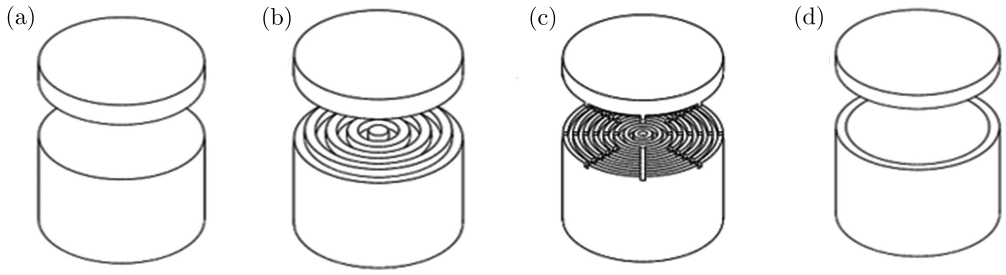

Fig. 1. Four different interface structures: (a) flat interface, (b) circular ring interface, (c) radial interface, (d) circular and concave interface

Abaqus/Standard is used to simulate the cooling process of a synthetic cavity, reducing the residual stress generated inside the cutter from 1000°C to 25°C. The materials used are listed in Table 1, and the mesh is created using the transition mesh drawing method and an adaptive mesh algorithm.

Table 1. Parameters of the cutter and rock material

Material	Modulus of elasticity [GPa]	Density [Kg/m^3]	Thermal conductivity [J/(ms°C)]	Specific heat capacity [J/(Kg°C)]	Coefficient of thermal expansion [10^{-6}/°C]	Poisson's ratio [–]
PCD	890	3510	543	790	2.5	0.07
Hard alloy	579	15000	100	230	5.2	0.22
Rock	40	2650	3.5	800	52	0.25

Figure 2 displays the resulting equivalent residual stress nephogram for the output interface.

The analysis results shown in Fig. 2 reveal that the flat interface (a) exhibits the most regular stress distribution with the smallest equivalent stress value. The equivalent stress gradually increases from the centre to the circumference of the cemented carbide layer interface, resulting in stress concentration at the outer circumference of the matrix interface of the flat interface teeth.

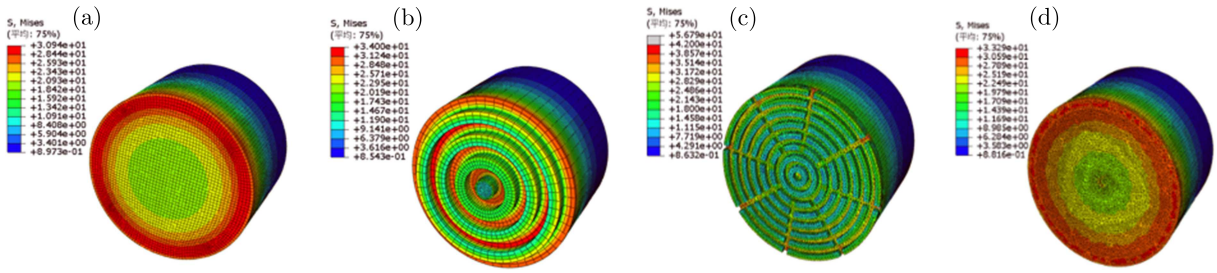

Fig. 2. Equivalent stress nephogram of four interfaces: (a) flat interface, (b) circular ring interface, (c) radial interface, (d) circular and concave interface

The circular concave interface (d) shares similarities with the flat interface, but the equivalent stress of the cemented carbide layer interface is slightly higher, leading to more severe stress concentration at the matrix interface. The circular interface (b) demonstrates significant stress concentration at the interface, particularly in the areas that match its geometric characteristics. On the other hand, the radial interfacial tooth (c) exhibits a more balanced distribution of the equivalent stress on its surface due to its interface joint being divided into multiple surfaces by multiple rings and transverse stiffening bars, thereby avoiding significant stress concentration.

To further evaluate the special-shaped interface, the circumscribed equivalent residual stress on the working surface of the PCD layer is extracted (Fig. 3), and its distribution along the circumferential path is plotted (Fig. 4).

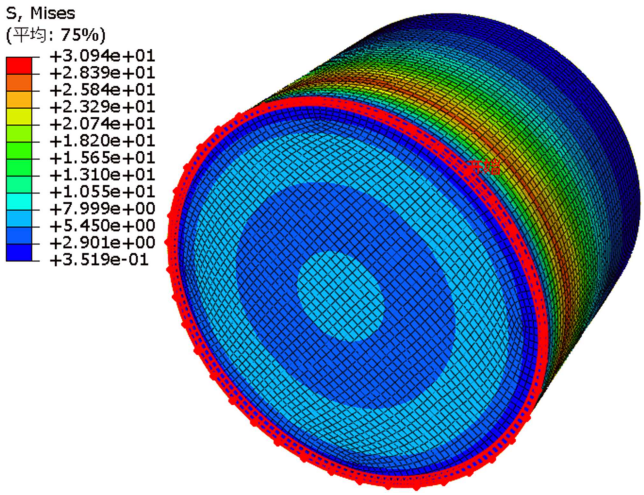

Fig. 3. Stress extraction of the working surface

The distribution of the equivalent residual stress along the circumference of the working surface of the cutter corresponds to geometric characteristics of the interface. The plane interface, radial interface, concave interface and circular interface exhibit a uniform stress distribution. The circular interface experiences a notably higher stress value, whereas the flat interface demonstrates lower stress. Overall, the plane, radial, round and concave interfaces exhibit better performance.

From Fig. 5 one can see that the plane interface, circular interface and radial interface still perform the best, with values of 1.42 MPa, 1.53 MPa and 1.52 MPa, respectively. These values are significantly reduced compared with the circular interface. In summary, among the examined samples, the radial interface exhibits the most favourable effect. The equivalent residual stress distribution and surface stress at the interface joint are relatively uniform, avoiding significant stress concentration, and resulting in a low average equivalent residual stress. Therefore, the

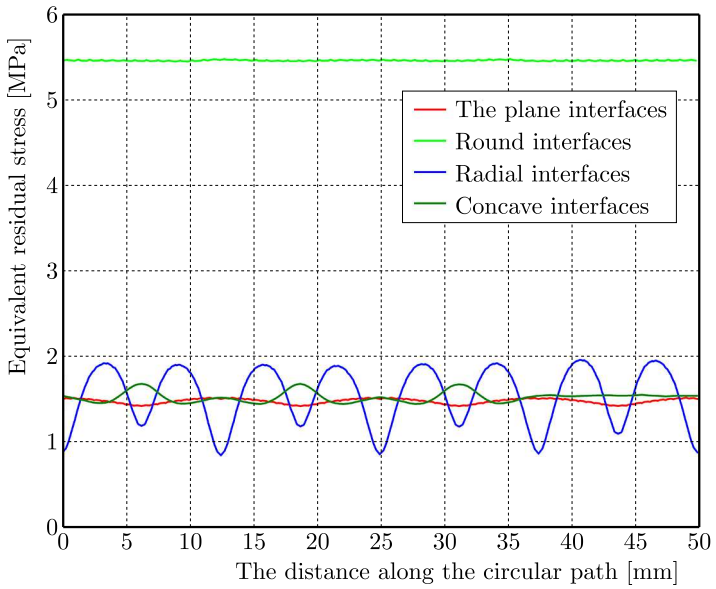

Fig. 4. Circumferential equivalent residual stress on the working surface

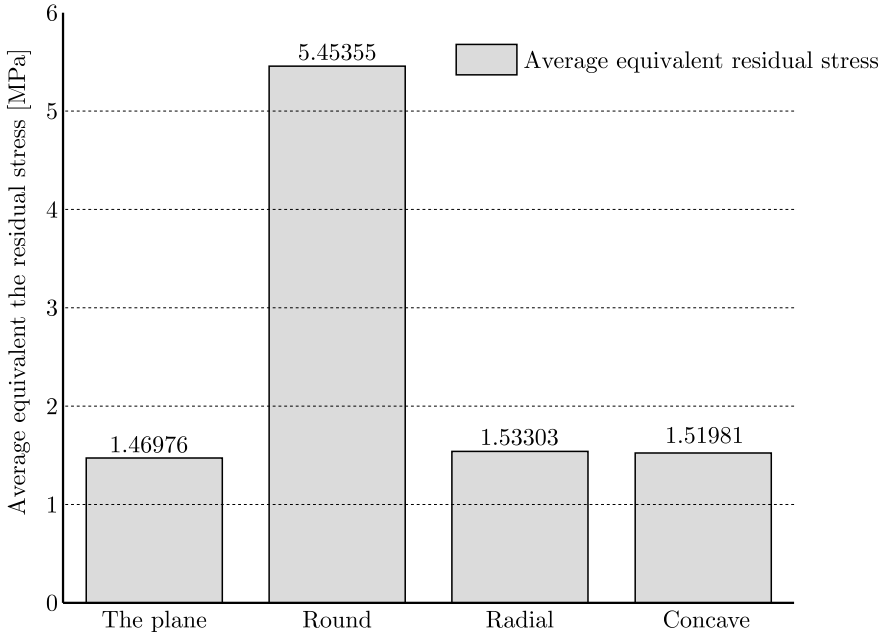

Fig. 5. Average residual stress at the four interfaces

radial interface is selected as the mating structure interface, with the flat interface serving as a comparison object for a comprehensive study on the performance of the mating structure.

3. Establishment of the finite element model of auxiliary structures

Six different tooth surfaces and interface auxiliary structures have been established, as depicted in Fig. 6. The size of the rock model is $50 \times 30 \times 15$, whereas the PDC cutter size is 15.88×13.2 (unit: mm).

The rock employs the Drucker-Prager model with a fracture displacement set at 0.001. The material parameters of the rock and cutter are listed in Table 1 (Yang *et al.*, 2007; Lu *et al.*, 2004; Liang, 2005). The dynamic process of the PDC teeth cutting rock is solved using

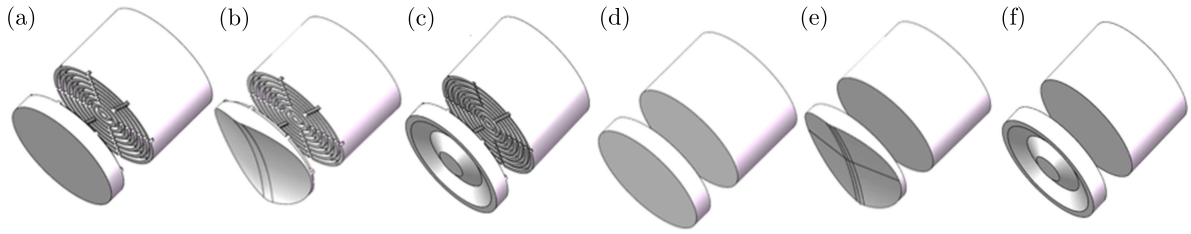

Fig. 6. Schematic of six different auxiliary structures: (a) plane tooth-radial interface, (b) saddle tooth-radial interface, (c) multidimensional cutter tooth-radial interface, (d) plane-tooth interface, (e) saddle tooth-flat interface, (f) multidimensional cutter tooth-planel interface

Abaqus/Explicit. The analysis step time is 0.01 s, and the analysis step follows the "power, temperature-displacement, display" sequence (Zhu, 2015).

4. Comparative analysis of simulation results

4.1. Evaluation index

The evaluation of different auxiliary structures in this comparative analysis is based on several key factors that influence the performance of the cutter. These factors include stress fluctuation, which serves as an objective indicator for cutter lifespan, quantitative measurement of rock breaking efficiency through crushing specific work, measurement of the tooth impact degree through cutting force fluctuation and analysis of the temperature rise curve and tooth profile contact surface stress fluctuation. To account for any deviation resulting from the simulation model, several groups of grids with different quantities were added and re-run to verify grid independence. The following results confirmed the grid independence, with errors kept within 5%.

In summary, the performance evaluation criteria for each tooth profile are as follows: crushing specific work, cutting force fluctuation, temperature rise curve and tooth profile contact surface stress fluctuation.

4.2. Influence of the auxiliary structure on specific work of crushing

In the oil drilling industry, the evaluation of rock breaking efficiency is based on the energy required for toothed rock breakage, known as the specific energy of crushing. Zhou *et al.* (2017) indicated that the specific energy of crushing, which represents the energy consumed per unit volume of rock, could quantitatively reflect the rock breaking efficiency. It can be approximated as

$$MSE_n \approx \frac{A}{V_c} \tag{4.1}$$

Among them, MSE_n stands for the crushing specific work, A is the energy consumed by breaking a certain volume of rock, V_c is the volume of broken rock (Teale, 1965).

The shape of the tooth surface determines the cutting path of the rock. When comparing tooth shapes with the same relative contact area, the volume of rock cut per unit time is approximately the same. However, the contact area of the saddle-shaped tooth is smaller relative to the projection plane, resulting in a different cutting trajectory compared with the other two tooth shapes (Figs. 7b and 7e).

Taking the crushing power as a priority for cutting performance allows for an objective reflection of the rock breaking efficiency of the bit. The final cutting diagrams in Fig. 7 show that the volume difference of toothed rocks with the same relative contact area is small, with

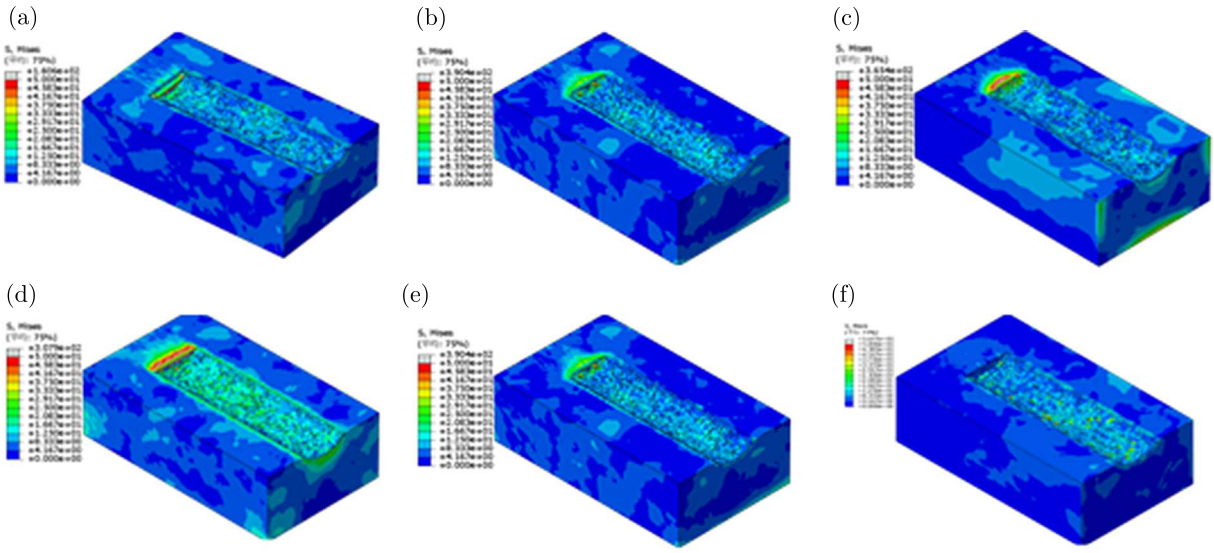

Fig. 7. Cut marks of rock: (a) plane tooth-radial interface, (b) saddle tooth-radial interface, (c) multidimensional cutter tooth-radial interface, (d) plane-tooth interface, (e) saddle tooth-flat interface, (f) multidimensional cutter tooth-plane interface

any differences falling within the error range due to mesh failure during different simulation processes. The initial unstable trend observed in the front section of each model necessitates the removal of data from that region to ensure data accuracy. Despite differences in the correction points among different auxiliary structures, their impact on the overall specific energy of crushing can be ignored.

As shown in Table 2, when using a flat interface, the specific energy of crushing shows a small difference among various tooth shapes. The maximum specific energy of crushing is 11.86 for planar teeth, whereas the minimum is 11.2 for multidimensional cutters. When the same tooth shape is used, the difference in specific energy of crushing is noticeable with changes in the interface. The most significant difference is observed with the saddle structure, which reduces the specific energy of crushing by 14%. When the tooth surface and interface are combined to form a mating structure, the saddle-shaped pairing structure (saddle-tooth interface) demonstrates an obvious improvement compared with the flat tooth-flat interface effect.

Table 2. Work done by external forces, volume variation of rock and crushing specific work of cutting pairs

Auxiliary structure		Work done by external forces [mJ]	Volume change of rock [mm^3]	Specific work of crushing [mJ/mm^3]
Flat interface	Planar tooth	8725.655	735.5	11.86357
	Saddle tooth	7246.007	628.0	11.53823
	Multidimensional cutter	7850.786	701.5	11.19143
Radial interface	Planar tooth	7446.651	717.8	10.37427
	Saddle tooth	6196.092	623.0	9.945572
	Multidimensional cutter	7748.145	694.6	11.15483

4.3. Influence on tooth stress during cutting of the mating structure

The maximum stress fluctuation on the main contact surface of different teeth reflects stress fluctuations at the contact point between the cutter and rock to a certain extent, indicating

periodic changes in the stress (Beak *et al.*, 2017). The average stress can provide insight into the stress of the contact surface, but it has a low impact on the tooth life. Therefore, the maximum stress fluctuation is used as the basis for assessing quality of the tooth.

During the simulation of cutting actions for each mating structure, the stress fluctuation on the cutter exhibits a pulsating distribution and instability due to dynamic calculation in Abaqus. To facilitate a more intuitive comparison, the maximum stress is limited to a range of 100 MPa in the displayed maps. It is observed that the stress is mainly concentrated on the contact surface between the tooth and rock, with the stress distributed in a specific area of the tooth. Figure 8 illustrates a comparison of stress regions and stress fluctuations on the main contact surface of the (a) plane tooth-radial interface tooth shapes.

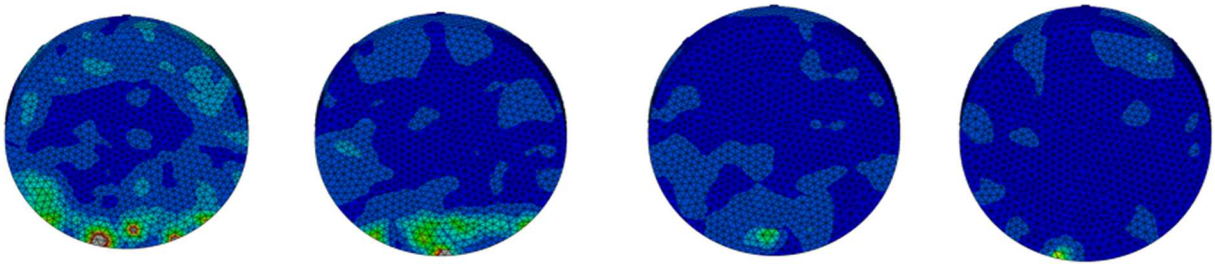

Fig. 8. Tooth surface stress fluctuation diagram of the mating structure

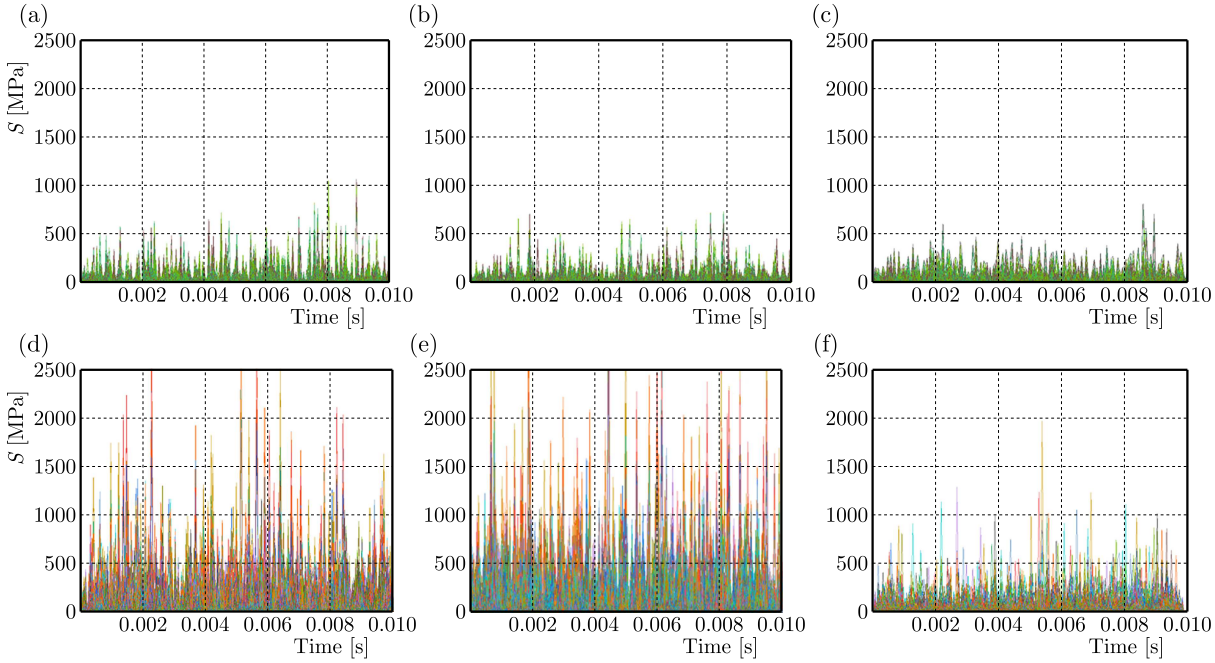

Fig. 9. Comparison diagram of the main contact stress of each pair: (a) planar tooth-radial interface, (b) flat interface-tangential force, (c) multidimensional-radial interface, (d) planar tooth-flat interface, (e) saddle tooth-flat interface, (f) multidimensional-flat interface

As shown in Fig. 8, optimisation of the interface structure significantly improves the stress distribution and magnitude on the tooth surface. To analyse the stress data, a clear standard for measuring the stress fluctuation during dynamic calculation is currently lacking. Zhang *et al.* (2019) sampled 8 points to observe stress, but it is not applicable when there is a significant stress fluctuation. To address this, a new comparison method is introduced here. It involves sampling of the main contact area, dividing it into 1500 sampling points and exporting the sampling point data for analysis. As each sampling point has 200 time segments, the stress fluctuation

on the tooth surface can be analysed more intuitively. Although this method requires a large amount of data and slower derivation, it provides more accurate analysis results. In this study, the main stress distribution points in the main contact area of each auxiliary structure model were selected, and the corresponding equivalent stress values for each distribution point in each time period were derived and analysed (Fig. 9).

To better illustrate the data, separate analyses of the maximum values in each segment were conducted for the above mating structures to represent the volatility (Fig. 10).

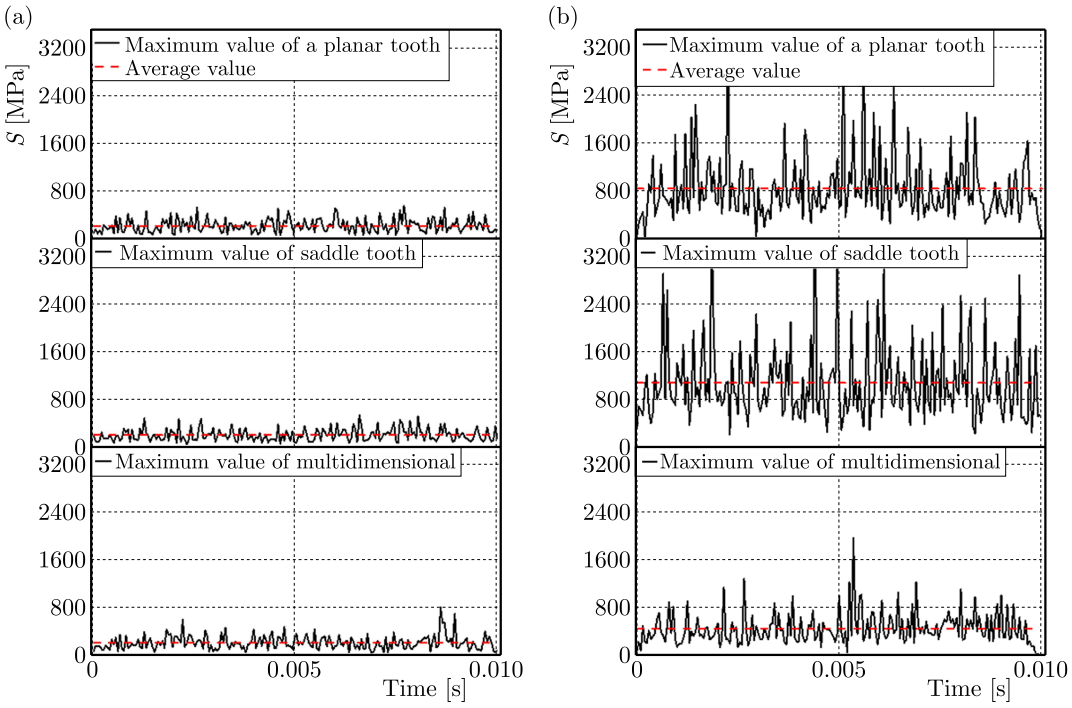

Fig. 10. Maximum value and average value of each auxiliary structure in each period

By comparing the mating structures between the flat interface (a) and the radial interface (b), it is evident that the use of the radial structure can significantly reduce the maximum stress and average stress on the three tooth surfaces (Baker, 2021).

As shown in Fig. 11, when the radial interface is used, the stress reduction on saddle teeth is most pronounced. The average stress value for saddle teeth with a flat interface is 1076.79 MPa, whereas it decreases to 191.35 MPa with the radial interface, which is 5.6 times lower. Additionally, when the plane interface is used, the stress on multidimensional teeth is significantly reduced compared with planar and saddle teeth. These results indicate that the radial interface effectively enhances the resistance of the tooth surface to macroscopic fracturing. When a flat interface is used, the multidimensional cutter demonstrates a distinct advantage, which is consistent with the actual performance of the multidimensional cutter.

4.4. Influence of the coupling structure on the cutting force

In addition to the specific work and stress factors, the instantaneous reaction cutting force and its fluctuation greatly affect the life of the cutter. Therefore, the impact load on the tooth in the rock breaking process can be measured by the size and fluctuation of the cutting force (Lin., 2019; Zhang *et al.*, 2021). Theoretically, a smaller fluctuation of the cutting force is better as it helps extending the life of the cutter.

The instantaneous tangential and axial forces at the radial interface and interface are compared and analysed. For the tangential force, as shown in Fig. 12, the instantaneous tangential

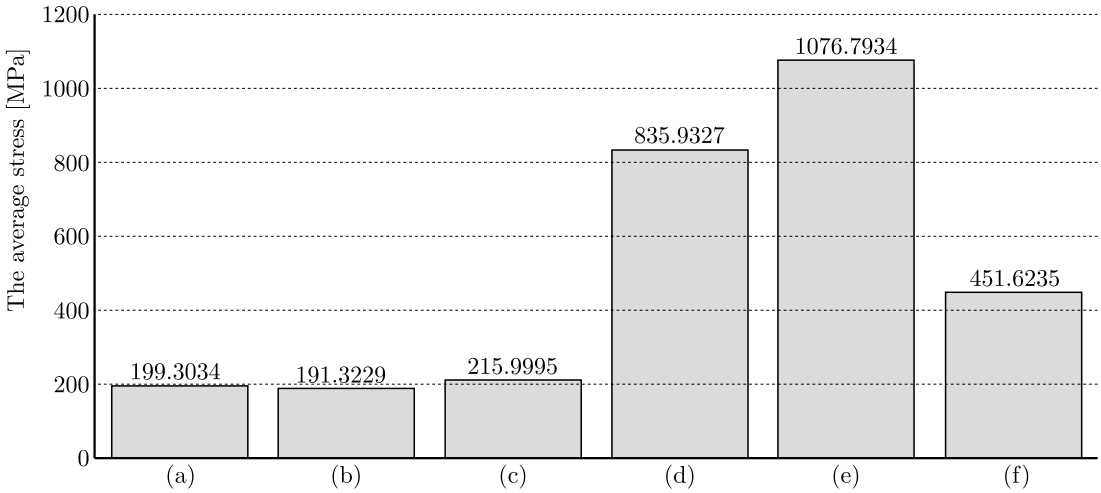

Fig. 11. Average stress of the auxiliary structure: (a) planar tooth-radial interface, (b) flat interface-tangential force, (c) multidimensional-radial interface, (d) planar tooth-flat interface, (e) saddle tooth-flat interface, (f) multidimensional-flat interface

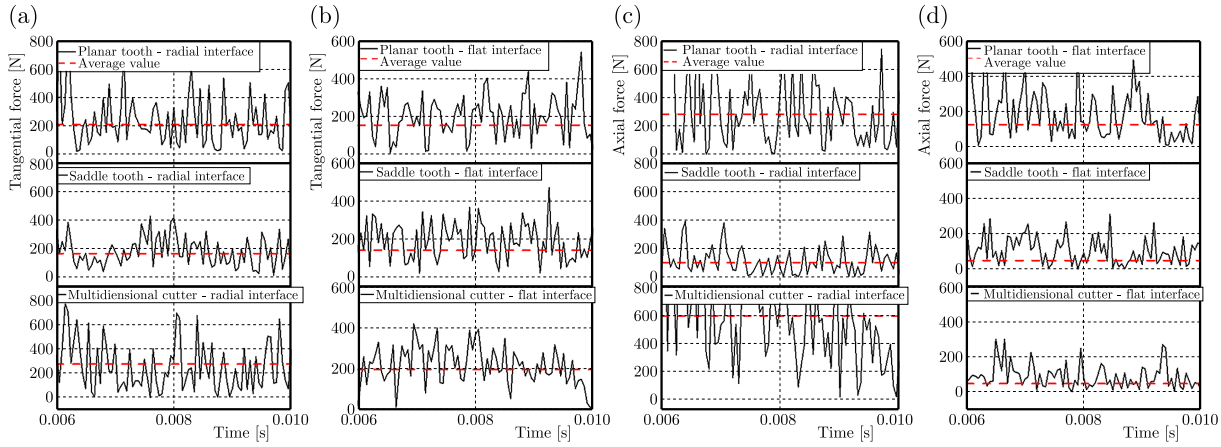

Fig. 12. Instantaneous tangential force and axial force comparison: (a) radial interface-tangential force, (b) flat interface-tangential force, (c) radial interface-axial force, (d) flat interface-axial force

force fluctuation does not change significantly due to the interface, except for the saddle-toothed radial interface. However, the tangential force magnitude and fluctuation increased. The tangential force represents the ease of rock breaking for cutters, where a smaller tangential force indicates easier rock destruction. Whether the radial interface (a) or the flat interface (b) is used, the tangential force of the saddle structure is smaller and more stable than that of other auxiliary structures.

The axial force represents the weight on the bit required by a single tooth. As shown in Fig. 12, compared with the flat interface (d), both multidimensional cutters and planar teeth using the radial interface (a) will increase the axial cutting force and fluctuation. This effect is most significant on multidimensional cutters. The instantaneous axial cutting force and fluctuation of saddle teeth exhibit little change. From the average level of the tangential and axial force, as shown in Table 3, when the radial interface is used, the average tangential force of plane teeth remains almost unchanged, whereas for saddle-shaped teeth decrease and for multidimensional cutters increase significantly. Additionally, the radial interface significantly increases the axial force level of the tooth shape, with the multidimensional cutter showing the most significant increase (6.8 times), followed by the plane teeth (1.6 times). The influence on saddle teeth is low.

Table 3. Anisotropic values of the average cutting force of each pair structure

Interface shape	Tooth surface shape	Mean value of tangential force [N]	Mean value of axial force [N]
Radial	Planar tooth	206	285
	Saddle tooth	166	101
	Multidimensional cutter tooth	248	594
Plane	Planar tooth	203	181
	Saddle tooth	188	89
	Multidimensional cutter tooth	195	88

In sum, the radial interface structure significantly decreases the tangential force of saddle teeth, but the axial force changes little. Planar and multidimensional cutters show improvements, with multidimensional cutters exhibiting the most noticeable changes. The saddle-radial interface coupling structure demonstrates excellent performance in both the axial and tangential forces, with a lower degree of cutting force fluctuation. This indicates that PDC bits using a saddle-shaped coupling structure not only require less torque but also have stronger axial intrusion ability, smoother cutting ability and are less prone to tooth damage caused by alternating loads. Therefore, when evaluating the cutting force, the radial interface is used for lifting saddle teeth, whereas the multidimensional cutters will be subjected to the radial interface reaction.

4.5. Influence of the accessory structure on the temperature rise effect

During downhole operations, the diamond mesa experiences high tensile stress after the temperature rises. Simultaneously, the cooling effect of the drilling fluid results in different contraction between the diamond layer and carbide matrix, accelerating crack propagation (Gao *et al.*, 2019). Hence, the temperature rise curve is considered a standard to measure the quality of teeth.

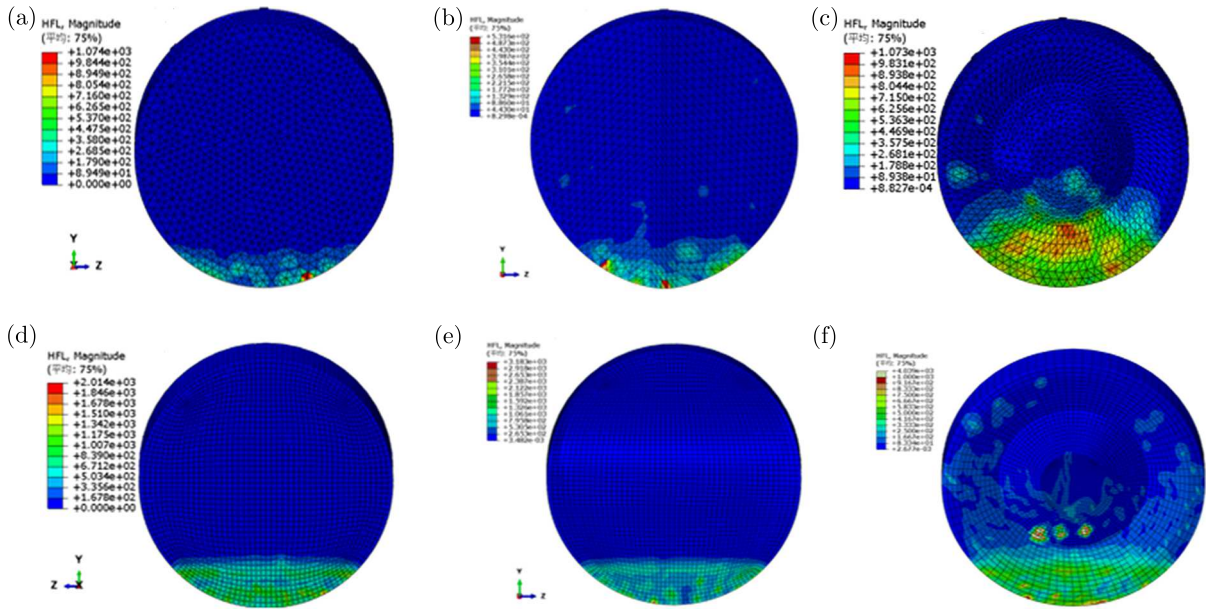

Fig. 13. Heat flow vector of each auxiliary structure: (a) plane tooth-radial interface, (b) saddle tooth-radial interface, (c) multidimensional tooth-radial interface, (d) plane tooth-plane interface, (e) saddle tooth-plane interface, (f) multidimensional tooth-plane interface

The heat generated on the tooth surface varies with different accessory structures. In this paper, the heat flow vector is introduced to simulate heat conduction. As shown in Fig. 13b and 13e, the magnitude of the radial vector heat flow is significantly reduced compared with the flat interface. Among the auxiliary structures, the saddle-toothed interface auxiliary structure exhibits the lowest heat generation, indicating better performance in heat conduction and reduced heat generation.

Owing to the differences in the heat flow vector of each coupling structure, it will certainly affect the surface temperature of PDC cutters (Grimmert *et al.*, 2019). During the initial cutting stage, when the front face of the cutter comes into contact with the rock, high-speed friction and extrusion between the teeth and the rock surface lead to rapid heat accumulation. After reaching a certain stability, the temperature remains within a certain range. On the other hand, a low temperature fluctuation also reduces the likelihood of PDC delamination caused by an uneven coefficient of thermal expansion inside the diamond (Hareland *et al.*, 2009). As seen in the derived chart from Abaqus, the temperature changes of the selected unit nodes in each model are too intensive, and the change trend is minimal. Therefore, the temperature rise curve is introduced, taking the average value of each unit node in each time period, which allows for a more intuitive comparison of temperature differences between the results of each coupling structure. Figure 14a displays the temperature rise curve of each model, where all auxiliary structures, except for the saddle-tooth interface, are influenced by the high-speed heat accumulation during the early stage.

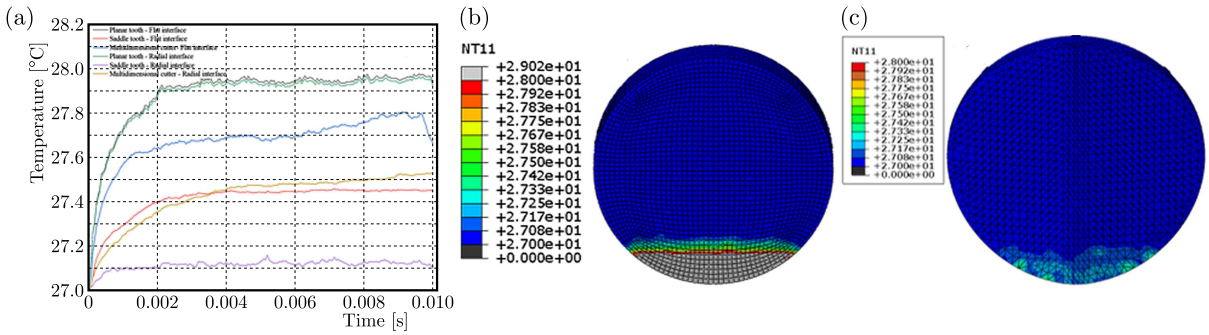

Fig. 14. Tooth surface temperature contrast: (a) temperature rise curve of each auxiliary tooth profile, (b) plane tooth-plane interface, (c) saddle tooth-radial interface

From the temperature rise curve of the auxiliary structures, the temperature rise tends to decrease when the radial interface structure is used, especially in the case of the saddle-tooth and the radial interface auxiliary structure (Fig. 14b and 14c). Furthermore, when the interface is the same, the tooth shape is also a contributing factor to the noticeable difference in the temperature rise curve, with saddle-shaped teeth exhibiting the lowest temperature rise effect.

5. Conclusion

In this paper, the optimization of the cutting tooth interface and the tooth surface and interface matching structure were studied. The main conclusions are summarized as follows.

- The comparative analysis of different interfaces with the same tooth shape reveals that different interfaces have a significant influence on the overall performance of the cutter. The radial interface needs to be paired with a specific tooth shape to achieve optimal performance, with the strongest reaction observed in multidimensional cutting teeth when using the radial interface.

- The comparison of different tooth shapes at the same interface demonstrates that different tooth shapes have varying influences on the crushing specific work, cutting force, stress distribution and temperature rise effect of PDC teeth. When using flat tooth shapes, PDC teeth should be selected based on the specific application. In the case of the flat interface, multidimensional cutters exhibit lower stress fluctuations and crushing specific work compared with other tooth shapes, making them a better choice for overall cutting performance.
- The comparative analysis of each coupling structure highlights the saddle-tooth radial interface as a suitable choice for evaluating the crushing specific work, cutting force, stress distribution and temperature rise effect.

Acknowledgements

This work was supported by the National Natural Science Foundation of China (Grant No. 52075438), the Key Research and Development Program of Shaanxi Province of China (Grant No. 2020GY-106), and the Open Research Fund of Key Laboratory of Oil & Gas Equipment of Ministry of Education (Grant No. OGE201702-110).

References

1. Baek M.-S., Park H.S., Lee J.-I., Lee K.-A., 2017, Effect of diamond particle size on the microstructure and wear property of high pressure high temperature (HPHT) sintered polycrystalline diamond compact (PDC), *The Korean Institute of Metals and Materials*, **55**, 790-797
2. Baker H., 2021, *StayCool 2.0 Multidimensional Cutter Technology [EB/OL]*, https://dam.bakerhughes.com/m/7edd5c3a7cb78480/original/StayCool-2-0-Multidimensional-Cutter-Technology-Overview-PDF
3. Fu Z., Tergeist M., Kueck A., Ostermeyer G.P., 2022, Investigation of the cutting force response to a PDC cutter in rock using the discrete element method, *Journal of Petroleum Science and Engineering*, **213**
4. Gao M.Y., Zhang K., Zhou Q., *et al.*, 2019, Research on PDC high speed rock cutting mechanism based on Abaqus, *China Petroleum Machinery*, **47**, 1-7
5. Grimmert A., Pachnek F., Wiederkehr P., 2023, Temperature modeling of creep-feed grinding processes for nickel-based superalloys with variable heat flux distribution, *CIRP Journal of Manufacturing Science and Technology*, **41**, 477-489
6. Hareland G., Nygaard R., Yan W., Wise J.L., 2009, Cutting efficiency of a single PDC cutter on hard rock, *Journal of Canadian Petroleum Technology*, **48**, 6, 60-65
7. Huang H., Lecampion B., Detournay E., 2013, Discrete element modeling of tool-rock interaction I: rock cutting, *International Journal for Numerical and Analytical Methods in Geomechanics*, **37**, 1913-1929
8. Liang Z., 2005, *Analysis of Rock Failure Process in Three-Dimensional Condition and Study on its Numerical Test Method*, Northeast University
9. Lin Z., 2019, *Research and Design of New Non-Planar PDC Cutting Gear*, Southwest Petroleum University
10. Liu W.J., Zhu X.H., LI B., 2018, The rock breaking mechanism analysis of rotary percussive cutting by single PDC cutter, *Arabian Journal of Geosciences*, **11**, 192
11. Lu Y., Ge X., Jiang Y., *et al.*, 2004, Full-process tests and constitutive equations of conventional triaxial compression in marble, *Journal of Rock Mechanics and Engineering*, **23**, 2489-2493
12. Teale R., 1965, The concept of specific energy in rock drilling, *International Journal of Rock Mechanics and Mining Sciences and Geomechanics Abstracts*, **2**, 57-73

13. Wu Z.B., Zhang S., Wang Y.Y., *et al.*, 2020, Parameterized tooth distribution and rock breaking simulation of PDC bit based on Abaqus, *Petroleum Machinery*, **483**, 30-36

14. Xu G., 2009, *Study on Thermal Residual Stress and Interface Structure Optimization of PDC for Oil Field Drilling*, Central South University

15. Yang T., Xu C., Wang B., *et al.*, 2007, Cohesion and internal friction angle in triaxial tests of rock and soil, *China Mining*, **12**, 104-107

16. Zhang F., Lu Y., Xie D., Luo H., Shi R., Zhang P., 2022, Experimental study on the impact resistance of interface structure to PDC cutting tooth, *Engineering Failure Analysis*, **140**

17. Zhang Z., Zhao D., Zhau Y., Xhou Y., Tang Q., Han J., 2019, Simulation and experimental study on temperature and stress field of full-sized PDC bits in rock breaking process, *Journal of Petroleum Science and Engineering*, **186**, 1, 106679

18. Zhang Z., Zhao D., Zhao Y., Gao K., Zhang C., Lü X., 2021, 3D numerical simulation study of rock breaking of the wavy PDC cutter and field verification, *Journal of Petroleum Science and Engineering*, **203**, 108578

19. Zhou Y., Zhang W., Gamwo I., Lin J.-S., 2017, Mechanical specific energy versus depth of cut in rock cutting and drilling, *International Journal of Rock Mechanics and Mining Sciences*, **100**, 287-297

20. Zhu X., Luo Y., Liu W., Yang F., Li Z., Lu D., 2021, Rock cutting mechanism of special-shaped PDC cutter in heterogeneous granite formation, *Journal of Petroleum Science and Engineering*, **210**, 3, 110020

21. Zhu Y., 2015, Research on explicit dynamical analysis method based on Abaqus, *Mechanical Design and Manufacturing*, **4**, 107-109

Manuscript received July 18, 2023; accepted for print September 17, 2023

JOURNAL OF THEORETICAL AND APPLIED MECHANICS
62, 1, pp. 117-128, Warsaw 2024
https://doi.org/10.15632/jtam-pl/177321

HIGH ACCURACY RECOGNITION OF MUSCLE FATIGUE BASED ON SEMG MULTIFRACTAL AND LSTM

Xia Zhang, Zhongli Gu

College of Mechatronics and Automobile Engineering, Chongqing Jiaotong University, Nanan District, Chongqing, China
corresponding author Xia Zhang, w-mail: zhangx82@cqjtu.edu.cn

A muscle fatigue identification method that integrates the multifractal of sEMG with LSTM is proposed. The MFDMA method was introduced to analyze and extract non-linear properties of sEMG. The significance of differences between the fatigue and non-fatigue states in terms of spectral width, Hurst index variation difference, and peak singularity index was determined using the t-test. A LSTM networks under the combined feature set comprising multiple fractals was built, and its recognition accuracy was 98.91%. The LSTM network model was found to be more accurate than other classification methods in identifying muscle fatigue under the same feature set.

Keywords: multifractal, muscle fatigue, LSTM, sEMG, MFDMA

1. Introduction

Dynamic muscular fatigue is a physiological condition in which engaging in physical activity temporarily lowers the maximum force or power output that can be generated by the participating muscles (cao *et al.*, 2018). Continuous and repeated muscle contractions during exercise or rehabilitation training can easily cause muscle fatigue and a rapid loss of muscle strength, which can seriously cause muscle damage. A prompt adjustment of rehabilitation training modalities can effectively stop muscle damage and prevent secondary injury. Therefore, accurate measurement of the level of muscle tiredness is crucial in the fields of neuromuscular research and rehabilitation medicine.

In recent years, there has been a lot of interest (Zhang *et al.*, 2021a) in a method for measuring muscle fatigue that combines the surface electromyography (sEMG) signal denoising technology with the artificial intelligence. However, muscle fatigue estimation using sEMG frequently heavily relies on preprocessing techniques like signal filtering, noise reduction, and feature extraction because of the highly nonstationary, nonlinear, and complex nature of sEMG signals caused by irregular muscle contractions during the exercise (Na and Kim, 2016). Both time-domain and frequency-domain analysis approaches are now employed to extract features (Liu etal, 2021a,b; Boyer *et al.*, 2021). There are restrictions when analyzing complicated transient nonlinear dynamic characteristics in sEMG signals since this method of linear analysis makes the assumption that sEMG signals are smooth.

Because of this, some researchers have created a technique for examining nonlinear dynamical properties of sEMG signals that revolves around self-similarity, inhomogeneity, complexity, and other nonlinear dynamic properties of sEMG signals (Xiong *et al.*, 2013). For instance, Katz's technique was applied in the literature (Xu *et al.*, 2022; Biancardi *et al.*, 2021; Beretta-Piccoli *et al.*, 2023) to extract the multiscale entropy, which has a fractal dimension of sEMG signals. However, the complicated nonlinear dynamic development that takes place during dynamic muscle exhaustion cannot be adequately described using a single fractal dimension. As a result,

more research into changes in the local features of various levels of sEMG signals is necessary using the multifractal technology.

A spectrum that depicts a subset and the appropriate fractal dimension is typically used to define multifractals (Wang and Zhou, 2000). The major algorithms are multifractal detrended fluctuation analysis (MFDFA) (Kantelhaedt *et al.*, 20o2) and a multifractal detrended moving average (MFDMA) (Gu and Zhou, 2010). The program using the MFDMA technique is faster than that using the MFDFA method when there are fewer data points in a one-dimensional signal sequence, the computational cost is smaller, and the algorithm performs better (Xi *et al.*, 2015). Several researchers, including França, have examined the nonlinear properties of ECG and EEG signals based on multiple fractals. Electroencephalography (EEG) and simulated data were used by França*et al.* (2018) to examine the sensitivity of monofractal and multifractal approaches to signal variance. In order to quantitatively compare the complexity of rhythm sequences in healthy and congestive heart failure, Li (2020) and Mahananto *et al.* (2019) used the MFDFA method to extract multiple fractal features. Mahananto *et al.* (2019) also used the MFDFA method to find out how well heart rate variability parameters could predict a short--term prognosis in sepsis patients. However, research on the use of various fractal approaches to characterize dynamic muscle exhaustion is scarce.

Regarding muscle fatigue recognition models, Zhang *et al.* (2021b) proposed a dual-sensor fusion of sEMG signals and *A*-type ultrasound and investigated the efficacy of the dual-sensor mode for static muscle fatigue detection. Liu *et al.* (2021a) conducted a study on static muscle fatigue recognition using a combination of kernel principle component analysis (KPCA) and support vector machines (SVM). Using high-resolution time-frequency approaches, Karthick and Ramakrishnan (2016) suggested a method for analyzing muscular tiredness by comparing classification abilities of simple Bayesian, SVM, and random forest classifiers. Long short-term memory networks (LSTM) and enhanced threshold wavelet denoising were used in Wang *et al.* (2022) who suggested a muscular fatigue identification model, and the findings showed that the denoising helped one to increase recognition rates. In 1997, Hochreiter and Schmidhuber introduced the concept of gated units in standard Recurrent Neural Networks (RNNs), addressing the issue of gradient vanishing that was present in standard RNNs (Hochreiter and Schmidhuber, 1997). Due to the design of LSTM, which allows the network to selectively retain or forget information, it has achieved a significant success in tasks involving long-term dependency (Skrobek *et al.*, 2022). LSTM methods are widely used in various applications, including energy and medicine (Skrobek *et al.*, 2020). In conclusion, the problem of low accuracy of muscle fatigue recognition models that utilize the time and frequency domain features results from the difficulty of describing the nonlinear and complex characteristics of sEMG signals in detail and comprehensively using the time and frequency domain analysis techniques based on the assumption of a linear muscle system.

This work intends to introduce a nonlinear signals analysis technique and conduct research on the nonlinear feature analysis and extraction method of sEMG signals in light of the aforementioned issues. An accurate evaluation of muscle fatigue in physical training, rehabilitation medicine, and other domains is made possible by a novel approach and research idea based on merging of multifractal data and conventional features.

2. Acquisition and pre-processing of the sEMG signal

2.1. Acquisition equipment and subjects

A wearable wireless sEMG signal collection device from OT Bioeletronica s.n.c., Italy, was used in this investigation to collect sEMG signals. This device can simultaneously collect sEMG signals from 14 muscles at a sample frequency of 2048 Hz. Ten subjects were chosen for the

examination. Ten young male participants were recruited, with an age range of 23 ± 2 years, height of 171 ± 10 cm, and weight of 60 ± 8 kg. To ensure the scientific rigor of the experiment, necessary health information was provided to the participants prior to the experiment, including guidance, training, and risk warnings. The participants were instructed to rest adequately and refrain from vigorous exercise in the 24 hours leading up to the experiment. Myoelectric data gear included an AMD Ryzen 7 4800H 2.90 GHz CPU, 16 GB of memory, and the MATLAB R2022b software for doing numerical calculations.

2.2. Signal collecting technique

The vastus medialis, vastus lateralis, and rectus femoris sEMG signals were recorded while the patients were seated and performing reciprocal knee flexion and extension motions. A 3-kg sandbag was linked to the subject's ankle joint in order to hasten the development of muscular exhaustion. The experimental scenario is schematically depicted in Fig, 1. The range of motion of the knee joint was 5° to 80°. After 20 minutes of rest, the experiment was restarted when the individual felt subjectively exhausted or had significant leg muscular tremors. Data from the minutes before the start and end of the measurement were utilized for the data analysis of fatigue and non-fatigue comparison groups. A maximum of five sets of data were collected per individual each day. Additionally, before the experiment, sEMG signals were collected for each subject's muscle during maximal voluntary contraction (MVC) for normalization reasons (Tomohiro *et al.*, 2006).

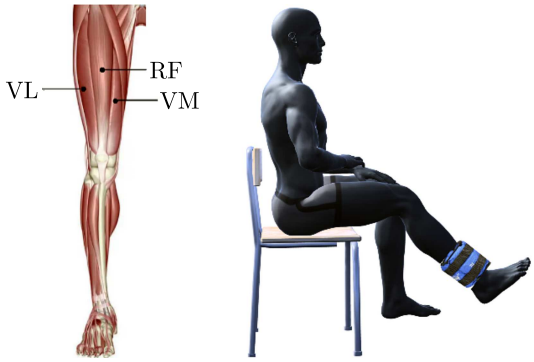

Fig. 1. A diagram of the distribution of the muscles and experimental scenarios

2.3. Data preprocessing

The effective signal range of sEMG signals is 0 Hz to 500 Hz, and the main energy concentration occurs between 20 Hz and 350 Hz. A 50 Hz trap is used to remove industrial frequency interference from the collected data before a fourth-order Butterworth band-pass filter is used to filter the data between 20 Hz and 350 Hz. Empirical mode decomposition (EMD) (Ye *et al.*, 2023) is also used to reduce the impact of baseline drift on the signal. In order to decrease computational redundancy and maintain motor physiological information, which is useful for further feature extraction and analysis, the envelope thresholding (Chen *et al.*, 2023) approach was employed to determine the active segments that indicate the aim of human action execution. Figure 2 illustrates the continuous sEMG signals of a particular subject's rectus femoris muscle throughout the transition from non-fatigue to fatigue states, along with their corresponding envelopes and segmented activity segments. In this study, the first activity segment is labeled as the non-fatigue state, and the last activity segment is labeled as the fatigue state. This paper sets the muscle state in the experimental dataset to 1 for rows corresponding to the feature data extracted from the sEMG data based on muscle fatigue status, and sets the muscle state to 0 for other rows.

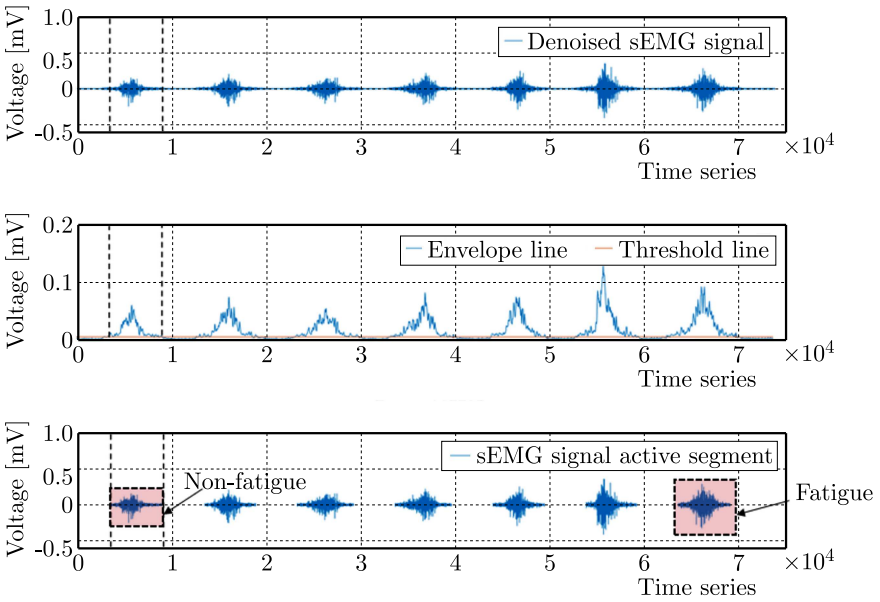

Fig. 2. The continuous sEMG signals of a subject's rectus femoris muscle throughout the transition from non-fatigue to fatigue states, along with their corresponding envelopes and segmented activity segments

3. Extraction of multifractal features from sEMG signals

3.1. MFDMA method

One of the most popular techniques for estimating multifractal measures is the MFDMA algorithm. The steps of computation are as follows:

Step 1: Create a new sequence from the specified time series $x(t)$, $t = 1, 2, \ldots, N$

$$y(t) = \sum_{t=1}^{N} x(t) \qquad t = 1, 2, \ldots, N \tag{3.1}$$

Step2: Calculate the moving average over a time window with a scale value of s

$$\widetilde{y}(t) = \frac{1}{s} \sum_{k=\lfloor (s-1)\theta \rfloor}^{\lceil (s-1)(1-\theta) \rceil} y(t-k) \tag{3.2}$$

The greatest non-negative integer less than or equal to x is represented by $\lfloor x \rfloor$, while the smallest non-negative integer larger than or equal to x is represented by $\lceil x \rceil$, $\theta \in [0, 1]$ denotes the location of the moving average. When $\theta = 0$, the moving average function is defined as

$$\widetilde{y}(t) = \frac{1}{s} \sum_{k=0}^{s-1} y(t-k) \tag{3.3}$$

Step 3: Calculate the residual time series of the signal

$$e(i) = y(t) - \widetilde{y}(t) \tag{3.4}$$

Take n data points from each interval segment by dividing the residual sequence $e(i)$ into N_n disjoint interval segments of equal size, namely: $N_n = [(N - n + 1)/n]$, $3 \leqslant n \leqslant (N + 1)/11$.

Step 4: Determine the value of the local root mean square

$$F(s) = \sqrt{\frac{1}{s} \sum_{i=1}^{s} e^2[(v-1)s + i]} \qquad v = 1, 2, 3, \ldots, N_m \tag{3.5}$$

Step 5: Determine the global order q root mean square value. The wave function is defined as

$$F_q(s) = \begin{cases} \left(\dfrac{1}{2N_n}\displaystyle\sum_{v=1}^{2N_n}[F_v(s)]^q\right)^{\frac{1}{q}} & \text{for} \quad q \neq 0 \\ \exp\left(\dfrac{1}{2N_n}\displaystyle\sum_{v=1}^{2N_n}\ln[F_v(s)]\right) & \text{for} \quad q = 0 \end{cases} \tag{3.6}$$

Step 6: By altering the scale s, the following techniques may be used to determine the power-law connection between $F_q(s)$ and the scale s

$$F_q(s) \sim s^{H(q)} \tag{3.7}$$

where $H(q)$ stands for the Hurst index of the order q, and the multifractal mass exponent $\tau(q)$ is characterized by

$$\tau(q) = qH(q) - D_f \tag{3.8}$$

The surface EMG signal examined in this study is a one-dimensional time series signal, hence $D_f = 1$. D_f is the topological dimension of the multifractal signal. The Legendre transformation may be used to produce the multifractal spectrum $f(\alpha)$ and the singularity strength $\alpha(q)$, as shown below

$$\alpha(q) = \frac{d\tau(q)}{dq} \qquad f(\alpha) = q\alpha(q) - \tau(q) \tag{3.9}$$

The span of the multifractal singularity intensity function may be used to determine the strength of multifractality (SOM)

$$\text{SOM} = \alpha_{max} - \alpha_{min} \tag{3.10}$$

H_{max} and H_{min} differ in terms of the degree of multifractality (DOM)

$$\text{DOM} = H_{max} - H_{min} \tag{3.11}$$

The subsequent nonlinear characterization also attempted to incorporate two nonlinear indicators, the difference of the multifractal spectrum and the peak singularity index, in order to more thoroughly define the muscular fatigue condition (Ye *et al.*, 2023; Marri and Swaminathan, 2016). The multifractal spectrum difference (DFS) can be represented as

$$\text{DFS} = |f(\alpha_{max}) - f(\alpha_{min})| \tag{3.12}$$

The PSE, or peak singularity exponents, can be written as

$$\text{PSE} = \alpha(q = -5) \tag{3.13}$$

3.2. Non-fatigue and fatigue comparison group multifractal feature extraction study

This Section employs the aforementioned multifractal algorithm for feature extraction of the labeled segments and a statistical approach to investigate the differences in multifractal features between non-fatigued and fatigued controls in order to examine the changes in multifractal properties of the surface EMG signals during muscle fatigue. The initial and last active segments of the signal, which were labeled as non-tired and fatigued phases, respectively, should be noted.

Figures 3a and 3b, which were generated using equations (3.7) and $(3.9)_1$, respectively, display the Hurst index and multiple fractal spectra, where the multifractal features of the

fatigue state and non-fatigue state are represented by the red and blue curves, respectively. Figure 3 demonstrates that the multifractal breadth of the spectrum is about SOM. For non-exhausted and fatigued muscles, respectively, the peak singularity index PSE is roughly 0.405 and 0.727. The difference in change of the Hurst curve DOM is approximately 0.402 and 0.621, and the measure DFS difference is approximately 0.082 and 0.421. According to the aforementioned findings, the SOM, DOM, DFS and PSE widths of the multifractal spectra were wider during fatigue than when they were during non-fatigue. The multifractal spectra are symmetrical along the approximate axis in the non-fatigued condition, but with muscular fatigue, this symmetry tendency is greatly diminished. The motor unit discharge rate fluctuates more during dynamic contraction of the muscle as tiredness rises, leading to an increase in the DOM feature parameter, which is one of the factors affecting the change in features. A higher level of multifractality and enhanced chaos are also caused by the increased recruitment of motor units and the intricacy of their spatio-temporal nonlinear connection with muscle exhaustion.

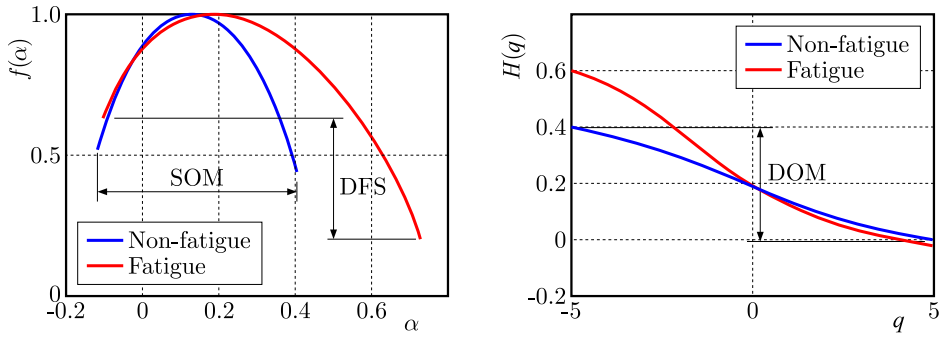

Fig. 3. Extraction of multifractal features from the comparison group of subjects with and without muscle fatigue

The scatter plots for the four multiple fractal characteristics of SOM, DOM, DFS and PSE are shown in Figs. 4a,b,c and 4d, respectively. The SOM, DOM and PSE features that correspond to Figs. 4a,b and 4d have clear feature distinctions between the non-fatigue and fatigue states, and the feature overlap rate of the two states is low, whereas the DFS features that correspond to Fig. 4c have a greater overlap, and the distinction is less clear. This can be seen more intuitively.

The difference between the aforementioned mean values of the properties of the myoelectric signals of 10 subjects under the fatigue and non-fatigue scenarios was observed using the t-test method in order to further determine whether the SOM, DOM, DFS and PSE extracted by the MFDMA algorithm have statistically significant differences under such scenarios. Table 1 displays the mean of each feature and P-value in the control condition. According to the findings, the three characteristics (SOM, DOM and PSE) that were derived from the multiple fractal spectrum using the MFDMA method were statistically significant (P-value 0.01) in determining whether or not the muscles were exhausted. Comparatively, the difference in DFS variability is relatively small. The findings could offer a fresh feature reference for deep learning and machine learning models that recognize muscle exhaustion.

Table 1. Statistical variations of attributes in the comparative groups

Features	Non-fatigue mean	Fatigue mean	P-value
SOM	0.9034	1.2414	0.0000
DOM	0.5343	0.8741	0.0000
DFS	−0.4172	−0.4960	0.0647
PSE	0.3393	0.5714	0.0000

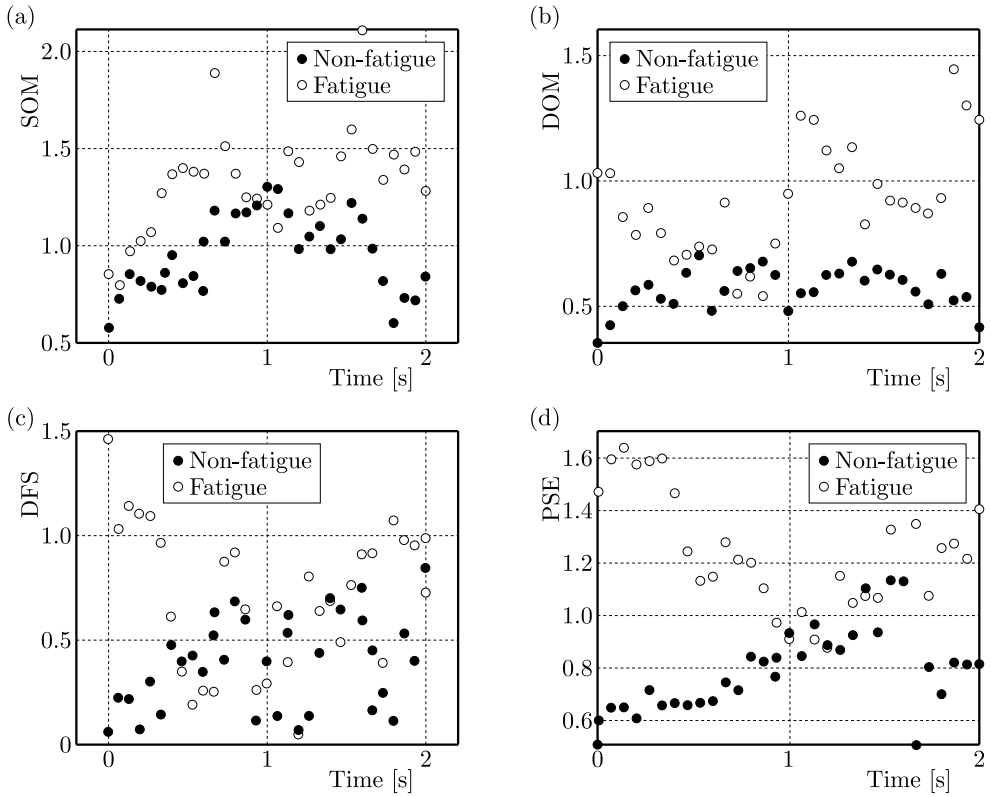

Fig. 4. Comparison of the fatigue group with the non-fatigue group using multifractal features

4. Model for recognizing muscle tiredness

Long Short Term Memory (LSTM) is a widely used recurrent neural network that effectively alleviates the problems of gradient disappearance, gradient explosion, and long-term dependence in sequence data by adding cell states and updating them through forgetting gates and memory gates (Ghislieri *et al.*, 2021). LSTM units consist of input gates, output gates, and forgetting gates. The LSTM model was used to build a muscle fatigue recognition model in dynamic muscle contraction based on the multiple fractal features of sEMG signals extracted in the preceding section; its structure and hyperparameter settings are shown in Table 2, and its workflow is shown in Fig. 5. First, a feature vector is created by extracting the multiple fractal feature data from the pre-processed data using the sliding time window method. Next, the experimental feature dataset is combined to produce a total of 14,400 items, 80% of which are used for the training set, and the rest 20% are used for the test set. Finally, a stochastic gradient descent algorithm is used to optimize learning.

Table 2. Configuration of LSTM parameters

Hyperparameter	Value
Number of layers	3
LSTM unit	120
Optimizer	Adam
Loss function	RTRL
Activation function	Relu
Batch size	100
Initial learning rate	0.001

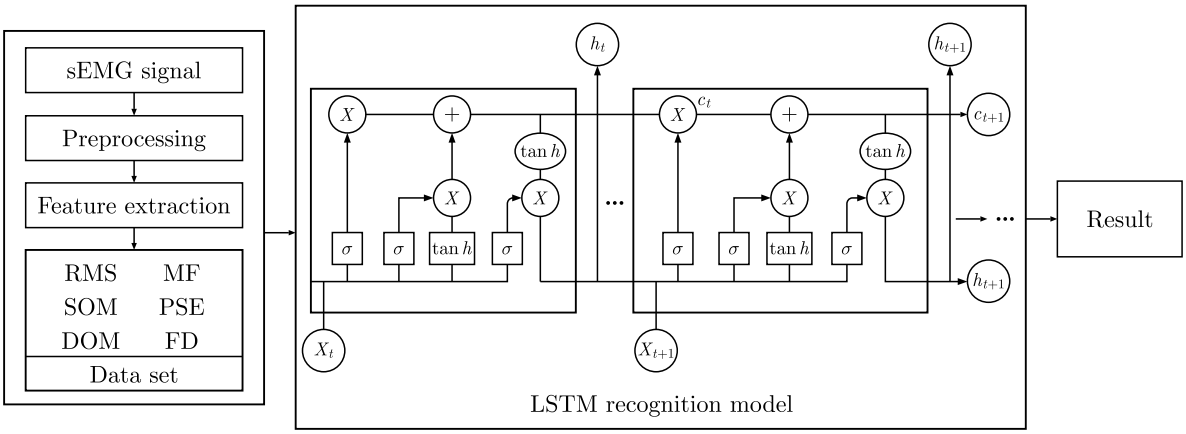

Fig. 5. LSTM model for identifying muscle fatigue

5. Experimental results of muscle fatigue recognition

5.1. The LSTM model performance for recognition using a single feature

The identification accuracy of the LSTM model was examined for each individual feature of SOM, DOM, PSE, root mean square (RMS), median frequency (MF), and fractal dimension (FD) (Xu *et al.*, 2022) in order to investigate the performance of each feature in describing muscle tiredness. The accuracy of model recognition is shown for each feature test set, as depicted in Fig. 6. The red line within the box in the image indicates the median of the experimental findings,

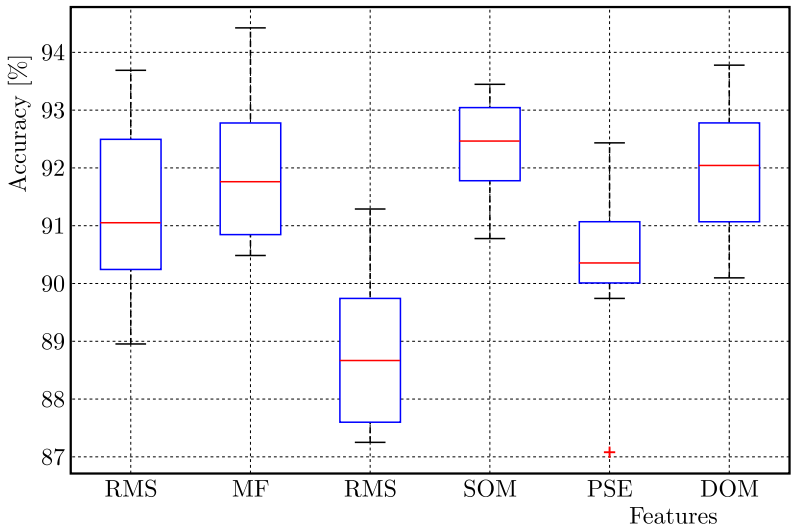

Fig. 6. Feature recognition accuracy for various characteristics

and the top and lower bounds of the box in the figure reflect the upper and lower quartiles of the 10 times recognition accuracy. In terms of the recognition accuracy, the single fractal dimension feature FD has the worst performance in the fatigue recognition model. The reason can be considered that the single fractal dimension is not sufficient to portray subtle changes of the motor unit recruitment. The highest recognition accuracy of the frequency domain feature MF and the time domain feature RMS reach 94.32% and 93.82%, respectively, but the main range of recognition accuracy of both is concentrated in 90.24% to 92.56% and 90.89% to 92.91%, with a relatively scattered distribution and low stability. The reasons for this can be considered as a large number of different types of motor units with an irregular discharge order and discharge frequency during dynamic muscle contraction due to fatigue, resulting in the time domain and frequency domain features of sEMG not changing significantly. The highest recognition accuracy

of multifractal features SOM, DOM and PSE are 93.23%, 93.92% and 92.67%, respectively, and the recognition accuracy of SOM performs the best. The highest recognition accuracy of SOM is slightly lower than that of MF and RMS, but the main range of recognition accuracy is concentrated in 91.61% 92.57%, and the distribution is more concentrated compared with MF and RMS. In addition, the main ranges of recognition accuracy of DOM and PSE are concentrated in 89.92% 91.03% and 91.04% 92.67%, with a more concentrated distribution and higher reliability. The results demonstrate that the MFDMA feature extraction method can characterize the nonlinear dynamics of EMG signals during dynamic muscle contraction. These multifractal features vary slightly with a change in the collected local motion units, so the recognition accuracy distribution is stable. This establishes a theoretical foundation for the feature fusion of the following fatigue recognition model.

5.2. Results of the LSTM model for different feature set combinations in recognizing muscle fatigue

To further optimize the feature set and achieve a muscle fatigue recognition model with high accuracy, the evaluation metrics of the LSTM model were investigated under different combinations of feature sets. The confusion matrix was utilized to calculate the accuracy, precision, recall, and F1_score of the LSTM model for different feature set combinations. Each metric parameter was calculated 10 times, and the average was taken as the final reference result. The features, combinations, and their evaluation metric parameters are presented in Table 3. The findings demonstrate that: 1) combining feature sets generally enhances muscle fatigue recognition performance compared to using single features; 2) the recognition accuracy rises as the number of features increases; and 3) combining multifractal features on conventional EMG time- and frequency-domain features can achieve 98.91% recognition accuracy, which is an increase by 4.73% over conventional feature combinations. This outcome shows how combining numerous fractal characteristics with conventional time-frequency domain features can increase the precision of muscle fatigue detection.

Table 3. The evaluation metric parameters for different combinations of feature sets

Feature combination	Accuracy	Precision	Recall	F1_score
RMS+MF	94.18	95.89	93.95	94.57
SOM+DOM	95.93	97.01	95.04	96.14
RMS+MF+SOM+DOM	97.84	98.93	96.88	98.06
RMS+MF+SOM+DOM+PSE	98.91	99.27	98.68	99.19

5.3. Recognition outcomes for various models using the ideal feature set

The recognition accuracy of the LSTM model was compared with that of K nearest neighbors (KNN) (Zhang *et al.*, 2018), support vector machines (SVM) (Burges, 1998), and back propagation (BP) neural network (LeCun *et al.*, 1989) under the ideal set of characteristics in order to investigate the superiority of the models. SVM apply a non-linear transformation of the kernel function to map the solution of a non-linear problem to a high-dimensional feature space; KNN uses distance measurements between different feature values to classify; BP neural networks consist of two processes: forward propagation and backward propagation of the error, i.e., calculating the error output in the direction from the input to output while adjusting the weights.

The numerical values of evaluation metric parameters for each model are shown in Table 4. The accuracy of LSTM is as high as 98.91%, which is 3.02% higher than that of KNN, 2.08% higher than that of BP neural network, and 1.89% higher than that of SVM, as can be seen

from the figure. Since the sEMG signal features before and after a specific time segment in the process of muscle fatigue are correlated, the LSTM network can deeply capture the important details of the EMG features and preserve a specific time interval while forgetting some redundant information, so the model has better accuracy in identifying muscle fatigue.

Table 4. The evaluation metric parameters for several categorization models

Recognition models	Accuracy	Precision	Recall	F1_score
LSTM	98.91%	99.27%	98.68%	99.19%
BP	96.83%	94.97%	93.63%	94.26%
KNN	95.89%	93.84%	92.42%	93.09%
SVM	97.02%	92.62%	94.55%	93.95%

The experimental results confirm that our idea of using multifractal analysis to improve the recognition rate of muscle fatigue is effective. To begin with, unlike static contraction, the discharge sequence and frequency of a large number of different types of motor units are irregular when the muscle is dynamically contracted to fatigue, which has a high degree of non-stationarity, nonlinearity, complexity, and is a typical multifractal system. The complicated nonlinear dynamic evolution process formed during dynamic muscle exhaustion is challenging to define using the time-domain, frequency-domain, and single fractal analysis approaches. Contrarily, multifractal analysis is used to analyze datasets. The technique entails distorting datasets extracted from patterns to generate multifractal spectra that illustrate how scaling varies over the dataset. According to the experimental results, the multifractal feature can characterize complex characteristics of the muscle discharge rate, motor unit recruitment, and degree of nonlinear coupling of motion of the unit in space-time, making it an effective method for analyzing muscle dynamic fatigue.

6. Conclusion

- A muscle fatigue identification approach based on a combination of sEMG multifractal technology and LSTM was presented in order to address the issue of inaccurate assessment of muscle fatigue caused by complex properties of the sEMG signal, such as non-stationarity, nonlinearity and self-similarity.
- A new reference feature for the muscle fatigue recognition model based on deep learning is provided by the introduction of the MFDMA method to analyze and extract nonlinear properties of sEMG signals. Additionally, the t-test method is used to assess the significance of differences between the multifractal characteristics under fatigue and non-fatigue conditions.
- A methodology for recognizing muscle fatigue based on LSTM networks was created. The recognition accuracy of the model was as high as 98.91% by fusing the combined feature set of multifractals, which was 4.73% higher than that of the conventional EMG feature set. In addition, the recognition accuracy of the LSTM network model was 2.08%, 3.02%, and 1.89% higher than that of BP neural networks, K-nearest neighbors, and SVM, respectively, for the same feature set. The findings of the study might lead to the development of a novel technique for precisely identifying muscle exhaustion during physical activity and rehabilitation therapy.

Acknowledgement

This work was supported by the Science and Technology Project of the Chongqing Municipal Education Commission (grant: KJZD-K201900702).

References

1. Beretta-Piccoli M., Cescon C., Vistarini A., Pisegna C., Vannini B., Zampella C., Calanni L., Soldini E., Barbero M., D'Antona G., 2023, Motor unit synchronization and firing rate correlate with the fractal dimension of the surface EMG: A validation study, *Chaos, Solitons and Fractals: the Interdisciplinary Journal of Nonlinear Science, and Nonequilibrium and Complex Phenomena*, **167**

2. Biancardi C.M., Chumino R., Gianneechini G., 2021, Linear correlation between the fractal dimension of surface EMG signals and the peak power of vertical jumps, *IEEE URUCON*, 223-226

3. Boyer M., Bouyer L., Roy J.S., Campeau-Lecours A., 2021, A real-time algorithm to estimate shoulder muscle fatigue based on surface EMG signal for static and dynamic upper limb tasks., *Annual International Conference of the IEEE Engineering in Medicine and Biology Society*, 100-106

4. Burges C.J.C., 1998, A tutorial on support vector machines for pattern recognition, *Data Mining and Knowledge Discovery*, **2**, 2, 121-167

5. Cao A., Zhang S., Liu R., Zou L., Fan C., 2018, A muscle fatigue state classification system based on surface electromyographic signals, *Computer Applications*, **38**, 6, 1801-1808

6. Chen X., Pan X., Ji T., Yu S., Sun Y., 2023, Fusion classification of stroke patients' biosignals by weighted cross-validation-based feature selection (W-CVFS) method, *Biomedical Signal Processing and Control*, **80**, 104282

7. França L.G.S., Miranda J.G.V., Leite M., Sharma N.K., Walker M.C., Lemieux L., Wang Y., 2018, Fractal and multifractal properties of electrographic recordings of human brain activity: toward its use as a signal feature for machine learning in clinical applications, *Frontiers in Physiology*, **9**, 1767

8. Ghislieri M., Cerone G.L., Knaflitz M., Agostini V., 2021, Long short-term memory (LSTM) recurrent neural network for muscle activity detection, *Journal of NeuroEngineering and Rehabilitation*, **18**, 1-15

9. Gu G.F., Zhou W.X., 2010, Detrending moving average algorithm for multifractals, *Physical Review*, **82**, 1, 011136

10. Hochreiter S., Schmidhuber J., 1997, Long short-term memory, *Neural Computation*, **9**, 8, 1735-1780

11. Kantelhardt J.W., Zschiegner S.A., Koscielny-Bunde E., Havlin S., Bunde A., Stanley H.E., 2002, Multifractal detrended fluctuation analysis of nonstationary time series, *Physica A: Statistical Mechanics and its Applications*, **316**, 1-4, 87-114

12. Karthick P.A., Ramakrishnan S., 2016, Surface electromyography based muscle fatigue progression analysis using modified B distribution time-frequency features, *Biomedical Signal Processing and Control*, **26**, 42-51

13. LeCun Y., Boser B., Denker J., Henderson D., Howard R.E., Hubbard W., Jackel L.D., 1989, Backpropagation applied to handwritten zip code recognition, *Neural Computation*, **1**, 4, 541-551

14. Li S., 2020, Multifractal detrended fluctuation analysis of congestive heart failure disease based on constructed heartbeat sequence, *IEEE Access*, **8**, 205244-205249

15. Liu G., Dong M., Zhang S., Xu L., Zhou G., Cai J., 2021a, Study on fatigue classification of surface EMG signals based on KPCA-SVM, *Journal of Electronic Measurement and Instrumentation*, **35**, 10, 1-8

16. Liu Q., Liu Y., Zhang C., Ruan Z., Meng W., Cai Y., Ai Q., 2021b, sEMG-based dynamic muscle fatigue classification using SVM with improved whale optimization algorithm, *IEEE Internet of Things Journal*, **8**, 23, 16835-16844

17. Mahananto F., Riksakomara E., Aditya R.Z., 2019, Multifractal detrended fluctuation analysis of heart rate variability predicts short-term outcomes of patients with sepsis, *2019 International Biomedical Instrumentation and Technology Conference (IBITeC)*

18. Marri K., Swaminathan R., 2016, Analysis of concentric and eccentric contractions in biceps brachii muscles using surface electromyography signals and multifractal analysis, *Proceedings of the Institution of Mechanical Engineers, Part H: Journal of Engineering in Medicine*, **230**, 9, 829-839

19. Na Y., Kim J., 2016, Dynamic elbow flexion force estimation through a muscle twitch model and sEMG in a fatigue condition, *IEEE Transactions on Neural Systems and Rehabilitation Engineering*, **PP**, 99, 1-1

20. Skrobek D., Krzywanski J., Sosnowski M., Kulakowska A., Zylka A., Grabowska K., Ciesielska K., Nowak W., 2020, Prediction of sorption processes using the deep learning methods (long short-term memory), *Energies*, **13**, 24, 6601

21. Skrobek D., Krzywanski J., Sosnowski M., Kulakowska A., Zylka A., Grabowska K., Ciesielska K., Nowak W., 2022, Implementation of deep learning methods in prediction of adsorption processes, *Advances in Engineering Software*, **173**, 103190

22. Tomohiro K., Tadashi M., Tohru K., Tsugutake S., 2006, *Biomechanism Library Practical Usage of Surface Electromyogram* (in Japanese), Japan Society of Biomechanisms

23. Tuncer S.A., Alkan A., 2022, Classification of EMG signals taken from arm with hybrid CNN-SVM architecture, *Concurrency and Computation: Practice and Experience*, **34**, 5, e6746

24. Wang J.-H., Sun S.-M., Sun Y.-N., Chen J., Peng W., Li L., 2022, Research on muscle fatigue recognition model based on improved wavelet denoising and long and short term memory network, *Journal of Biomedical Engineering*, **39**, 3, 9

25. Wang Z.L., Zhou Y.Q., 2000, Multifractal spectrum and its calculation, *Journal of Beijing University of Aeronautics and Astronautics*, **2000**, 3, 256-258

26. Xi C.-P., Zhang S.-N., Xiong G., *et al.*, 2015, Comparative analysis of fractal spectrum algorithms by multifractal descending fluctuation analysis and moving average method, *Journal of Physics*, **13**, 14

27. Xiong A.-B., Zhao X.-G., Han J.-D., Liu G.-J., 2013, Chaotic analysis of EMG on the patients of facial paralysis, *Science Bulletin*, **58**, S2, 152-165

28. Xu Q.S., Bai R., Li S., 2022, Dual regulation of surface EMG nonlinear parameters by strength training load and muscle fatigue, *Chinese Sports Science and Technology*, **58**, 8, 8

29. Ye L.-H., Li Q.-S., Lu Q., 2023, Feature extraction and classification of electrocardiogram signals based on ensemble empirical mode decomposition and multifractal analysis, *Journal of Signal Processing*, **39**, 1, 143-153

30. Zhang S., Li X., Zong M., Zhu X., Wang R., 2018, Efficient kNN classification with different numbers of nearest neighbors, *IEEE Transactions on Neural Networks and Learning Systems*, **29**, 5, 1774-1785

31. Zhang Y., Chen S., Cao W., Guo P., Gao D., Wang M., Zhou J., Wang T., 2021a, MFFNet: Multi-dimensional Feature Fusion Network based on attention mechanism for sEMG analysis to detect muscle fatigue, *Expert Systems with Applications*, **185**, 115639

32. Zhang Y.A.L., Zhang S.W., Sun S.H., *et al.*, 2021b, A novel method for muscle fatigue detection by fusing EMG signals with A-type ultrasound, *Journal of Electronic Measurement and Instrumentation*, **2022**, 6, 036

Manuscript received June 6, 2023; accepted for print November 6, 2023

JOURNAL OF THEORETICAL AND APPLIED MECHANICS
62, 1, pp. 129-142, Warsaw 2024
https://doi.org/10.15632/jtam-pl/177259

ANALYTICAL MODELLING AND SHAPE OPTIMIZATION OF COMPOSITE GIRDER WITH ADHESIVE BONDLINE

Paweł Szeptyński, Dorota Jasińska, Leszek Mikulski

Cracow University of Technology, Faculty of Civil Engineering Division of Structural Mechanics and Material Mechanics, Cracow, Poland

corresponding author Paweł Szeptyński: e-mail: pawel.szeptynski@pk.edu.pl

The paper presents a beam theory for composite girders consisting of two beams joined together with an adhesive layer. The height of the bottom beam is considered variable. The governing equations are suitable for formulation of a shape optimization problem in terms of control theory. The use of Pontryagin's maximum principle enables finding an optimal solution satisfying necessary optimality conditions. The presented optimization approach allows for including issues which cannot be accounted for by commercial topology optimization software. The introduced theory provides an estimated solution, which is then validated by an analysis of a 3D finite element model.

Keywords: composite beam theory, anisotropic limit state condition, structural optimization

1. Introduction

In recent decades, the use of composite structures has emerged as one of the most efficient solutions in structural engineering. Among a wide variety of distinct types of structures, those made of glue laminated timber (GLT) are especially suitable for structural optimization. Research devoted to this problem concerns shape optimization of load bearing elements (Mayencourt and Mueller, 2020; de Vito *et al.*, 2023), optimization of the structural layout (Hua *et al.*, 2020), combined shape and layout optimization (Šilih *et al.*, 2010; Kravanja and Žula, 2021) and also multiple aspects of optimal material usage (Mayencourt and Mueller, 2019; Pech *et al.*, 2019). With regard to composite structures exploiting advantageous mechanical properties of wood, a common solution is to combine solid wood or GLT girders with top reinforced concrete (RC) slabs – reviews on the topic of Timber-Concrete Composites (TCC) can be found in (Clouston and Schreyer, 2018; Dias *et al.*, 2018). The use of adhesive connections is still not a wide-spread approach in civil engineering, especially regarding the most heavily loaded bearing elements, as sufficiently precise modelling and technological issues are still a challenge. Various methods have been used to perform optimization tasks regarding timber structures, e.g. particle swarm optimization (Decker *et al.*, 2014), topology optimization (de Vito *et al.*, 2023) or genetic algorithms (Villar-García *et al.*, 2019). The making use of these methods does not guarantee that the obtained solutions satisfy necessary conditions of optimality. On the other hand, the use of Pontryagin's maximum principle (PMP) provides a solution that indeed satisfies the necessary conditions. The PMP is commonly used for solving one-dimensional control theory (CT) problems with a temporal independent variable. Its application to problems of structural optimization is thus restricted to one-dimensional problems of structural optimization, such as, e.g. optimization of rods and beams. Indeed, the PMP has been successfully applied to the problems

of optimization of cross-section of bar structures (Jasińska and Kropiowska, 2018; Jasińska and Mikulski 2019; Mikulski *et al.*, 2022; Szeptyński and Mikulski, 2023). Combining the simplified one-dimensional analytical model of a deformable solid with the general form of equilibrium equations in two dimensions enables an approximate description of a plane stress state. This is the approach used in the presented research. We shall consider a composite beam consisting of a top RC slab and a bottom GLT girder, which are connected by of an adhesive layer. The problem of shape optimization of the wooden girder is solved by means of the PMP, taking into account both serviceability and load carrying capacity constraints. The goal of this paper is to present a beam theory for composite girders and propose a useful method for determining nearly optimal shapes of such structures, which could not be found by of standard topology optimization techniques, due to specific problem conditions. Detailed engineering design is not the subject of this research as, in fact, there are still no regulations on the design of glued TCC structures, which is beyond the scope of the CEN/TS 19103. For these reasons and for the sake of simplicity of the presented numerical examples, the RC slab dimensioning, reinforcement specification, and cracking of the concrete are not taken into consideration – these issues might be, however, accounted for in a similar manner as other Eurocode regulations (Szeptyński and Mikulski, 2023). Among the novel contributions of the presented research to the current state-of-art, the following may be named:

- **Application an anisotropic limit state condition in optimization** – standard tools in topology optimization cannot take the anisotropic limit state condition into account, being restricted to the use of von Mises equivalent stress, which is applicable to isotropic solids only (Abaqus Tosca Structure, Ansys Structural Optimization). In both programs, it is also not possible to create such constraints with the user-defined responses. The PMP--based optimization does not suffer from these restrictions as it may take into consideration arbitrary nonlinear equality or inequality constraints.
- **Optimization within the regions with prescribed boundary conditions** – the topology optimization encounters problems when boundary conditions are prescribed in the design zone, since these conditions must propagate in some way to other nodes if some of them are removed. It is common to exclude the loaded and supported areas from the design zone (e.g. both in Tosca and Ansys). This approach usually leads to considerable overdimensioning of the structure in the supported zone. Contrary to this, the use of a simplified one-dimensional model enables optimization of the beam height along the whole length.
- **Numerical validation of results obtained via PMP-based optimization** – since the optimization by means of control theory requires a simplified one-dimensional model, validation of the obtained results has been performed with the use of a three-dimensional finite element model.

1.1. Scope of research

Three problems will be considered. The first one is derivation of governing equations and boundary conditions for the problem of bending of a composite beam with the bottom girder having variable height. These equations will then be transformed into a system of 1st order ODE, which suits the formalism of the PMP. The second task is solving the optimization problem for the considered single-span and double-span beams within the framework of the PMP. The problem is solved numerically by Dircol software which utilizes the direct collocation method. The third task is the validation of the obtained optimization results through a more detailed 3D Finite Element Method (FEM) numerical model. Finite element analysis (FEA) is performed with the use of Abaqus software.

2. Theoretical description

In the following Section, the theoretical background of the considered optimization problem will be presented. This includes an analytical model of a multilayer composite beam and an energy--based limit state condition for anisotropic materials exhibiting different strengths in tension and in compression. These equations will then be transformed in order to derive a system suitable for the application of Pontryagin's maximum principle.

2.1. Analytical model of a multilayer composite beam

The general theory of linear elastic multilayer composite beams, considered in this research, is derived and discussed in detail in (Szeptyński, 2020). A beam considered in this analytical model consists of a finite number of bent panels (beams) and sheared adhesive layers, placed in an alternating way. Deformation of the adhesive layers is assumed to be governed primarily by a simple shear state, while the bent panels are described within the Bernoulli-Euler beam theory. In the present research, the original statement of the problem is specified for the case of a three-layer beam (top slab + adhesive layer + bottom girder) and generalised in order to make it capable of taking into account variable height of the bottom panel.

2.1.1. Governing equations

We are considering a composite timber-concrete beam, the cross-section of which is shown in Fig. 1a. RC slab thickness is h_1 and width b_{pl} (which may be considered as the distance between neighbouring girders), as well as thickness of the adhesive layer is t and GLT girder width b. All parameters are fixed. The height of the bottom timber girder h_2 is the design variable.

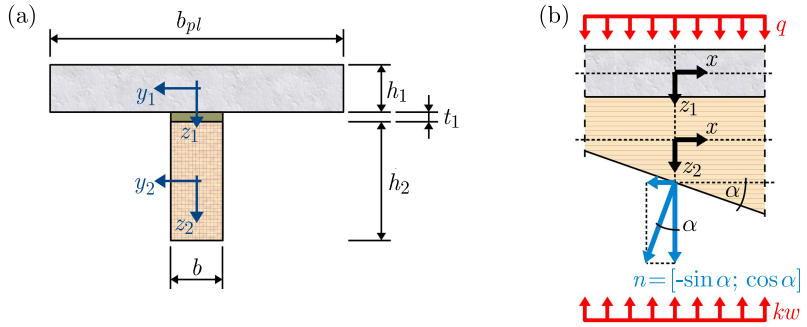

Fig. 1. a) Cross-section of the considered composite timber – concrete beam; b) Static boundary condition on the bottom face of the bottom beam

The derivation of a general form of governing equations from equilibrium equations, presented in (Szeptyński, 2020) is generalized here in a way enabling accounting for the variable height h_2 as well as bottom surface tractions representing contact stresses over the beam bearings, modelled by Winkler's subgrade, see Eq. (2.1). Besides, the method for including the static boundary conditions on the sloped bottom face of the beam is presented in the following Section. Linear elastic constitutive relations of Bernoulli-Euler beam theory are assumed for description of both the RC slab and the GLT girder. The kinematics of a pure shear state is used for description of deformation of the adhesive layer, in the same way as it is done in classical shear lag theories (Volkersen, 1938; Goland and Reissner, 1944). Due to relatively small thickness of the adhesive layer and slenderness of the layers in bending, transverse linear strain may be considered to be negligibly small. This justifies the assumption that the transverse displacement (deflection) is the same for both beam components. As a result, the following system of governing equations is obtained

$$
\begin{aligned}
&\frac{d}{dx}\Big(E_1A_1\frac{du_1}{dx}\Big)+G_1\frac{b}{t_1}\Big[(u_2-u_1)+\Big(\frac{h_1}{2}+\frac{h_2}{2}\Big)\frac{dw}{dx}\Big]=0\\
&\frac{d}{dx}\Big(E_2A_2\frac{du_2}{dx}\Big)-G_1\frac{b}{t_1}\Big[(u_2-u_1)+\Big(\frac{h_1}{2}+\frac{h_2}{2}\Big)\frac{dw}{dx}\Big]=0\\
&\frac{d^2}{dx^2}\Big[(E_1I_1+E_2I_2)\frac{d^2w}{dx^2}\Big]=\widehat{q}-kbw\\
&\quad+G_1\frac{b}{t_1}\left\{\Big[\Big(\frac{du_2}{dx}-\frac{du_1}{dx}\Big)+\Big(\frac{h_1}{2}+\frac{h_2}{2}\Big)\frac{d^2w}{dx^2}+\frac{1}{2}\Big(\frac{dh_1}{dx}+\frac{dh_2}{dx}\Big)\frac{dw}{dx}\Big]\Big(\frac{h_1}{2}+\frac{h_2}{2}+t_1\Big)\right\}\\
&\quad+G_1\frac{b}{2t_1}\left\{\Big[(u_2-u_1)+\Big(\frac{h_1}{2}+\frac{h_2}{2}\Big)\frac{dw}{dx}\Big]\Big(\frac{dh_1}{dx}+\frac{dh_2}{dx}\Big)\right\}
\end{aligned}
\tag{2.1}
$$

In formula (2.1), A_i and I_i stand for the area and 2nd moment of area of the cross-section of the i-th layer in bending ($i=1$ – RC slab; $i=2$ – GLT girder), respectively; E_i stands for Young's modulus of the material of the i-th bent layer and G_1 is Kirchhoff's modulus of the adhesive; k is the subgrade reaction coefficient describing stiffness of the bearing (outside the support area $k=0$); w, u_1 and u_2 are the common deflection of all layers and longitudinal displacements of the RC slab and GLT girder, respectively. Please note, that the governing equations depend only on one elastic constant of an anisotropic material, which makes an impression that the anisotropy is disregarded. This is an apparent inconsistency, since the beams under consideration are assumed to be slender enough so that the Bernoulli-Euler beam theory may be applied. As a result, both transverse shear deformation and transverse contraction are disregarded. As a consequence, the deflection of the beam is determined with just a single elastic constant. Such an approach is consistent with the use of the anisotropic limit state condition. The equivalent transverse load $\widehat{q}$ is defined as follows

$$\widehat{q}=q+(h_1g_1b_{pl}+h_2g_2b+t_1f_1b) \tag{2.2}$$

where q is the acting load, g_1, g_2 and f_1 are the specific weights of RC, GLT and adhesive, respectively.

2.1.2. Cross-sectional forces

The axial forces in the layers under bending are equal

$$N_1=E_1A_1\frac{du_1}{dx}\qquad N_2=E_2A_2\frac{du_2}{dx}\qquad N=N_1+N_2 \tag{2.3}$$

where N is the total axial force applied to the composite cross-section. The bending moment about the point P, placed in the distance Z_P from the top surface of the RC slab may be expressed as follows

$$
\begin{aligned}
M_P=&-\frac{b_{pl}E_1h_1^3+bE_2h_2^3}{12}\frac{d^2w}{dx^2}+E_1b_{pl}h_1\Big(\frac{h_1}{2}-Z_P\Big)\frac{du_1}{dx}\\
&+E_2bh_2\Big(h_1+t_1+\frac{h_2}{2}-Z_P\Big)\frac{du_2}{dx}
\end{aligned}
\tag{2.4}
$$

The formula for the transverse shear force – according to Schwedler's formula – after considering the equilibrium of axial forces, may be expressed in the following form

$$
\begin{aligned}
Q_P=&-\frac{1}{4}\Big(E_1b_{pl}h_1^2\frac{dh_1}{dx}+E_2bh_2^2\frac{dh_2}{dx}\Big)\frac{d^2w}{dx^2}-\frac{E_1b_{pl}h_1^3+E_2bh_2^3}{12}\frac{d^3w}{dx^3}\\
&+\frac{d}{dx}\Big(E_1A_1\frac{du_1}{dx}\Big)\frac{h_1}{2}+E_1b_{pl}h_1\frac{du_1}{dx}\frac{1}{2}\frac{dh_1}{dx}\\
&+\frac{d}{dx}\Big(E_2A_2\frac{du_2}{dx}\Big)\Big(h_1+t_1+\frac{h_2}{2}\Big)+E_2bh_2\frac{du_2}{dx}\Big(\frac{dh_1}{dx}+\frac{1}{2}\frac{dh_2}{dx}\Big)
\end{aligned}
\tag{2.5}
$$

2.1.3. Distribution of stress

Distribution of normal stress in bent layers is given by the following formulae

$$\sigma_{xx,i}(x,z_i) = E_i\Big(\frac{du_i}{dx} - \frac{d^2w}{dx^2}z_i\Big) \qquad i=1,2 \tag{2.6}$$

where $z_i \in (-h_i/2; h_i/2)$ is the distance from the centroid of the cross-section of the i-th layer in bending (Fig. 1a). The shear stress distribution in the adhesive layer is given by the following formula

$$\tau_a = \frac{G_a}{t}\Big[(u_2-u_1) + \Big(\frac{h_1}{2}+\frac{h_2}{2}\Big)\frac{dw}{dx}\Big] \tag{2.7}$$

The shear stress distribution in bent layers may be approximated with the use of Zhuravsky's formula, by integration of local equilibrium equations

$$\begin{aligned}
\sigma_{xz,1}(x,z_1) &= -\int\limits_{-\frac{h_1}{2}}^{z} \frac{\partial\sigma_{xx,1}}{\partial x}\,d\zeta = -E_1\Big[\frac{d^2u_1}{dx^2}\Big(z_1+\frac{h_1}{2}\Big) - \frac{1}{2}\frac{d^3w}{dx^3}\Big(z_1^2 - \Big(\frac{h_1}{2}\Big)^2\Big)\Big] \\
\sigma_{xz,2}(x,z_2) &= \tau_n - \int\limits_{\frac{-h_2}{2}}^{z} \frac{\partial\sigma_{xx,2}}{\partial x}\,d\zeta = \tau_n + E_2\Big[\frac{d^2u_2}{dx^2}\Big(\frac{h_2}{2}-z_2\Big) - \frac{1}{2}\frac{d^3w}{dx^3}\Big(\Big(\frac{h_2}{2}\Big)^2 - z_2^2\Big)\Big]
\end{aligned} \tag{2.8}$$

where τ_n is the shear stress at the bottom face of the GLT beam resulting from its slope. Let us denote the transverse normal stress at the bottom face of the GLT beam with p_n. The general static boundary condition for the bottom surface of the bottom layer, Eq. (2.9), enables finding the boundary shear stress (Fig. 1b)

$$\begin{bmatrix} \sigma_{xx,2}\Big(\frac{h_2}{2}\Big) & \tau_n \\ \tau_n & p_n \end{bmatrix}\begin{bmatrix} -\sin\alpha \\ \cos\alpha \end{bmatrix} = \begin{bmatrix} 0 \\ -kw \end{bmatrix} \quad \Rightarrow \quad \tau_n = \tan(\alpha)E_2\Big(\frac{du_2}{dx} - \frac{d^2w}{dx^2}\frac{h_2}{2}\Big) \tag{2.9}$$

Transverse normal stress in the layers in bending may be found by integration of local equilibrium equations

$$\frac{\partial\sigma_{xz,i}}{\partial x} + \frac{\partial\sigma_{zz,i}}{\partial z_i} + g_i = 0 \quad \Rightarrow \quad \sigma_{zz,i} = -\int\Big(\frac{\partial\sigma_{xz,i}}{\partial x} + g_i\Big)\,d\zeta + C_i \qquad i=1,2 \tag{2.10}$$

Since the through-the-thickness distribution of shear stress is quadratic, the transverse normal stress will be a cubic function of the z-coordinate

$$\sigma_{zz,1} = A_0 + A_1z_1 + A_2z_1^2 + A_3z_1^3 \qquad \sigma_{zz,2} = B_0 + B_1z_2 + B_2z_2^2 + B_3z_3^3 \tag{2.11}$$

Coefficients A_j, B_j $(j=0,1,2,3)$ are in fact functions of x, which are determined from the static boundary conditions and interface equilibrium conditions. The first four conditions are

$$\begin{aligned}
&\sigma_{zz,1}\Big(-\frac{h_1}{2}\Big) = -\frac{q}{b_{pl}} \qquad &&\sigma_{zz,1}\Big(\frac{h_1}{2}\Big) = p_{1,B} \\
&\sigma_{zz,2}\Big(-\frac{h_2}{2}\Big) = p_{2,T} \qquad &&\sigma_{zz,2}\Big(\frac{h_2}{2}\Big) = p_n
\end{aligned} \tag{2.12}$$

where $p_{1,B}$ and $p_{2,T}$ are the peel stresses at the bottom of the top layer (RC slab) and at the top of the bottom layer (GLT beam), respectively. They may be found from the equilibrium equation for transverse forces applied to the sheared layer

$$\begin{aligned}
p_{1,B} &= \frac{1}{b}\Big[\frac{d^2}{dx^2}\Big(E_1I_1\frac{d^2w}{dx^2}\Big) - \frac{d\tau_1}{dx}\frac{bh_1}{2} - \tau_1\frac{b}{2}\frac{dh_1}{dx} - q - h_1g_1b_{pl}\Big] \\
p_{2,T} &= p_{1,B} - G_1\Big[\Big(\frac{du_2}{dx} - \frac{du_1}{dx}\Big) + \frac{1}{2}\Big(\frac{dh_1}{dx} + \frac{dh_2}{dx}\Big)\frac{dw}{dx} + \Big(\frac{h_1}{2}+\frac{h_2}{2}\Big)\frac{d^2w}{dx^2}\Big] - t_1f_1
\end{aligned} \tag{2.13}$$

The normal stress p_n is determined according to (2.9)

$$p_n = \tan(\alpha)\tau_n - kw\sqrt{1+\tan^2(\alpha)} = \tan^2(\alpha)E_2\Big(\frac{du_2}{dx} - \frac{d^2w}{dx^2}\frac{h_2}{2}\Big) - kw\sqrt{1+\tan^2(\alpha)} \quad (2.14)$$

The remaining four conditions are derived from equilibrium equations, which determine the boundary values of derivatives of these distributions

$$\left.\frac{\partial\sigma_{zz,i}}{\partial z_i}\right|_{\pm\frac{h_i}{2}} = -\left.\frac{\partial\sigma_{xz,i}}{\partial x}\right|_{\pm\frac{h_i}{2}} - g_i \qquad i = 1,2 \quad (2.15)$$

2.1.4. Boundary conditions

In order to determine the solution to equations (2.1) unambiguously, it is necessary to prescribe appropriate boundary conditions. The static boundary conditions on the top face of the RC slab and on the bottom face of the GLT girder are taken into consideration both in the governing equations and in the formulae for transverse normal stress. The sidewalls are assumed to be traction-free boundaries. The static boundary conditions are prescribed in an analogous way to classical beam theory as the conditions for end-values of cross-sectional forces.

2.2. Energy-based limit state condition for anisotropic materials with an asymmetric elastic range

A crucial aspect of the design of timber structures is the anisotropy of mechanical and strength properties of the material. It has been noted that in the case of slender beams, the anisotropy of elastic properties is of minor importance – it is not so regarding the strength properties of wood. An important feature is also the asymmetry of the elastic range, namely the difference between the limit values of tensile and compressive stress. Material properties corresponding with appropriate strength classes of structural timber can be found in the EN 338:2016 standard. However, standards regulating the structural design of timber structures may not specify any general approach to determine the ULS condition in the case of an arbitrary complex stress state. Only certain specific combinations of simple mechanical states are considered in the EN 1995-1-1:2010. In the considered optimization process, a general plane stress state is considered. For this reason, the energy-based limit state condition for orthotropic material exhibiting asymmetry of elastic range is used (Szeptyński, 2017)

$$F(\sigma) = A_I\sigma_I^2 + B_I\sigma_I + A_{II}\sigma_{II}^2 + B_{II}\sigma_{II} + A_{III}\sigma_{III}^2 \leqslant 1 \quad (2.16)$$

where projections of the current stress state on elastic eigensubspaces are equal

$$\sigma_I = \sigma_{11}\cos\kappa + \sigma_{22}\sin\kappa \qquad \sigma_{II} = -\sigma_{11}\sin\kappa + \sigma_{22}\cos\kappa \qquad \sigma_{III} = \sigma_{12} \quad (2.17)$$

The parameter κ is a function of the stiffness distributor. In (Szeptyński, 2017), one may find formulas for the parameter κ as well as coefficients A_I, A_{II}, A_{III}, B_I, B_{II}, expressed in terms of elastic constants and strength values. All these parameters can be found e.g. in the EN 338:2016, except for Poisson's ratio, however in the EN 1995-2:2004 it is allowed to take $\nu = 0$.

2.3. Formulation of the control theory problem

The optimization problem considered in this article may be stated as follows:
— minimize the total amount of GLT

$$V = \int_0^L A_2\,dx = b\int_0^L h_2\,dx \quad (2.18)$$

— subject to the following constraints

– Ultimate Limit State (ULS) condition

$$F(\sigma) - 1 \leqslant 0 \tag{2.19}$$

– Serviceability Limit State (SLS) condition

$$w_{max} - w_{adm} \leqslant 0 \tag{2.20}$$

where w_{max} is the maximum deflection, while w_{adm} is the maximum admissible deflection. The problem is meant to be solved with the use of Pontryagin's maximum principle. For this reason, the problem must be formulated in the form of a system of the 1st order ordinary differential equations (ODE). Let us introduce the following state variables

$$\begin{aligned}
&X_1 = u_1 \qquad X_2 = E_1 A_1 \frac{du_1}{dx} \qquad X_3 = u_2 \qquad X_4 = E_2 A_2 \frac{du_2}{dx} \\
&X_5 = w \qquad X_6 = \frac{dw}{dx} \qquad X_7 = (E_1 I_1 + E_2 I_2) \frac{d^2 w}{dx^2} \\
&X_8 = \frac{d}{dx}\Big[(E_1 I_1 + E_2 I_2) \frac{d^2 w}{dx^2}\Big] \qquad X_9 = h_2 \qquad X_{10} = \frac{dh_2}{dx} = \tan\alpha
\end{aligned} \tag{2.21}$$

We introduce a single control variable, namely

$$U_1 = \frac{d^2 h_2}{dx^2} \tag{2.22}$$

According to (2.18), the objective function is given by the integral functional stating the Lagrange optimization problem. It may be transformed into the Meyer optimization problem by introduction of an additional state variable and defining a new objective function J

$$X_{11}(x) = V(x) = b \int_0^x X_9(\xi)\, d\xi \quad \Rightarrow \quad J = X_{11}(L) \tag{2.23}$$

The new initial condition $X_{11}(0) = 0$ must be also prescribed. After this transformation, the governing equations take the following form

$$\begin{aligned}
&X_1' = \frac{1}{E_1 b_{pl} h_1} X_2 \qquad X_2' = -b \frac{G_1}{t_1}\Big[X_3 - X_1 + \Big(\frac{h_1}{2} + \frac{X_9}{2}\Big) X_6\Big] \\
&X_3' = \frac{1}{E_2 b X_9} X_4 \qquad X_4' = b \frac{G_1}{t_1}\Big[X_3 - X_1 + \Big(\frac{h_1}{2} + \frac{X_9}{2}\Big) X_6\Big] \\
&X_5' = X_6 \qquad X_6' = \frac{12 X_7}{E_1 b_{pl} h_1^3 + E_2 b X_9^3} \qquad X_7' = X_8 \\
&X_8' = q + h_1 g_1 b_{pl} + X_9 g_2 b + t_1 f_1 b - k b X_5 \\
&\quad + G_1 b\Big(\frac{h_1 + X_9}{2t_1} + 1\Big)\Big[\Big(\frac{1}{E_2 b X_9} X_4 - \frac{1}{E_1 b_{pl} h_1} X_2\Big) + \frac{6(h_1 + X_9)}{E_1 b_{pl} h_1^3 + E_2 b X_9^3} X_7 + \frac{1}{2} X_{10} X_6\Big] \\
&\quad + G_1 b \frac{X_{10}}{2t_1}\Big[X_3 - X_1 + \Big(\frac{h_1}{2} + \frac{X_9}{2}\Big) X_6\Big] \\
&X_9' = X_{10} \qquad X_{10}' = U_1 \qquad X_{11}' = b X_9
\end{aligned} \tag{2.24}$$

Cross-sectional forces and stresses may then be calculated according to equations (2.3)-(2.8) and (2.11) after expressing the derivatives of displacement functions in terms of the introduced state variables. The set of admissible values of the control variable is also defined. The final formal statement of the control theory problem is complex as the form of necessary optimality criteria depends on whether the constraints are active or not. The mathematical structure of a formulation of control theory problem subjected to PMP-based optimization may be found in (Mikulski *et al.*, 2022).

3. Numerical results

The single-span beam is assumed to be 15 m long with 40 cm at both ends resting on elastic supports. The double-span beam is assumed to be symmetrical, 28 m long, with two identical 14 m long spans, resting at both ends on 40 cm long elastic supports 40. The middle support is 60 cm long. The girder cross-sectional dimensions are assumed as follows: RC slab thickness $h_1 = 32$ cm, its width (distance between neighbouring GLT girders) $b_{pl} = 100$ cm, and the GLT beam width $b = 30$ cm. The adhesive layer is $t = 2$ cm thick. The elastic and strength properties of wood are adopted as for GL 26h, while mechanical properties of concrete are chosen as for C30/37 concrete class. The adhesive layer is assumed to be made of the SikaPSM flexible, virtually incompressible polyurethane adhesive, with Kirchhoff's modulus $G = 1.4$ MPa (Kwiecień, 2012; Śliwa-Wieczorek *et al.*, 2020). The total load applied to the beam includes the dead load of RC slab $g_1 = 25\,\mathrm{kN/m^3}$ and GLT girder $g_2 = 4.37\,\mathrm{kN/m^3}$ as well as the dead load of non-structural elements and live load, which together sum up to $q = 35\,\mathrm{kN/m^2}$. The subgrade reaction modulus is assumed to be equal to $k = 380\,\mathrm{MPa/m}$, as for an elastomeric support according to EN 1337-3:2005. In the supported section of the beam, the coefficients in the anisotropic limit state condition (2.16) are modified, namely, the compressive strength perpendicular to grain is increased by 75% according to Eurocode 5 recommendations 6.1.5 (2) and (3) of EN 1995-2:2007. Only a single load combination is considered, namely the one corresponding to uniform distribution of q, however the formulation of the problem and its solution may easily be expanded in order to account for multiple load combinations. The maximum admissible deflection is assumed to be $w_{adm} = L/250$. The range of admissible values of the control variable is $U_1 \in (-0.1; 0.1)$, while the height of the GLT beam itself may vary within the range $h_2 \in (0.3\,\mathrm{m}; 1.15\,\mathrm{m})$.

3.1. Results of the PMP-based optimization

The optimization problem stated in the previous Section is solved with the use of Dircol software. The results of completed optimization tasks for both analysed beams are presented in Figs. 2-4. Figures 2 and 3 illustrate the distributions of the GLT girders heights and deflections of optimal beams, respectively. The distribution of the magnitude of the left-hand side of the ultimate limit state criterion (material effort – see Eq. (2.17)) presented in Fig. 4, is plotted for five values of the z-coordinate, corresponding with the top, middle and bottom material fibres, as well as two additional intermediate coordinates.

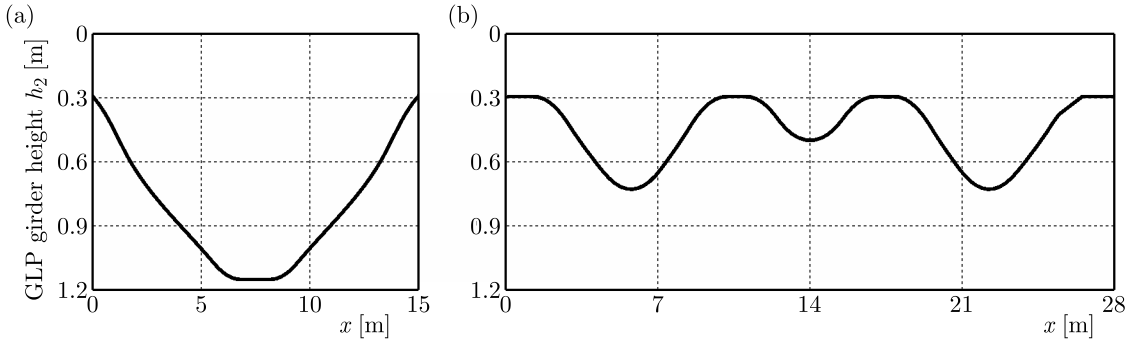

Fig. 2. Optimal distribution of the GLT girder height $h_2(x)$: (a) single-span beam, (b) double-span beam

An important feature of the obtained results is that in both analysed cases (the single and double-span beams) both SLS and ULS constraints are active. The highest material effort, activating the ULS constraints, appears at the bottom fibres ($z = 0,5h_2$) for both girders. It

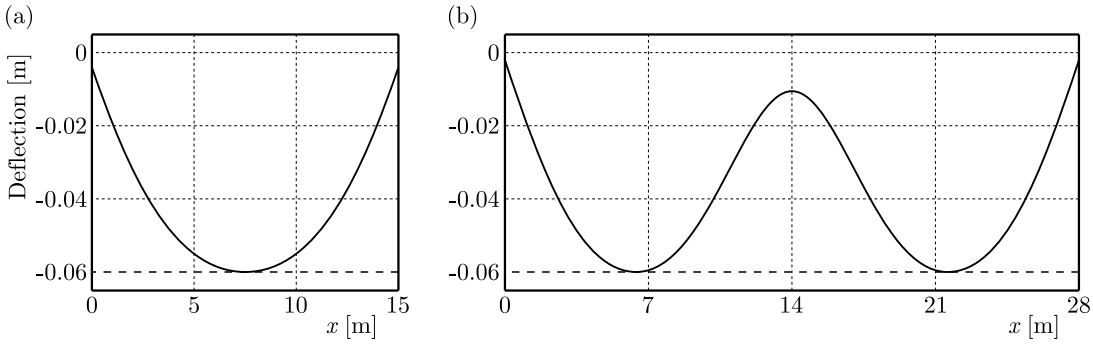

Fig. 3. Beam deflections with SLS: (a) single-span beam, (b) double-span beam

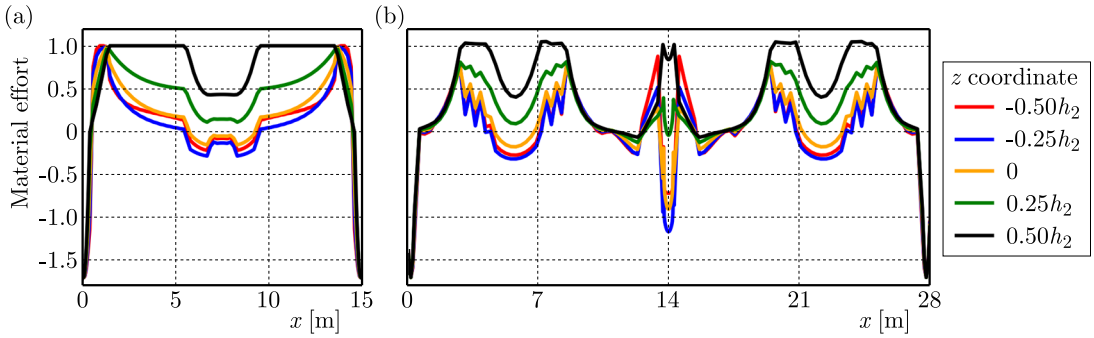

Fig. 4. Material effort: (a) single-span beam, (b) double-span beam

was observed that the acquired optimal control is singular, which means that the Hamiltonian of the system is piecewise constant. See Büskens *et al.* (2001) for a more detailed discussion.

3.2. Comparison with the 3D FE model

The optimal solutions obtained based on beam theory are compared with the results of a three-dimensional (3D) finite element analysis (FEA) performed with the use of Abaqus software.

3.2.1. Description of the FEM numerical model

The geometries of the 3D FEM girders models are assumed as follows: all cross-sectional and longitudinal beam dimensions, as well as material properties (span and support zone lengths) are the same as adopted for the above discussed 1D model (see the first paragraph of Section 3). The distributions of heights of the GLT girders (h_2) are taken from the results of the PMP based optimization (see Fig. 2). Both the concrete slab and GLT girder materials are assumed to be isotropic and linearly elastic. Since a pure shear elastic material model is not available in Abaqus, the adhesive is also assumed to be linearly elastic with $E_a = 4.14\,\text{MPa}$ and $\nu_a = 0.48$. The FEM mesh consists of linear hexahedral 8 node elements. The large number of used elements (over 100000) results from the necessity of precise modelling of the variable beam shapes, while keeping regular meshes, to obtain smooth stress maps along curved surfaces representing GLT fibres. The bearing supports are realized by applying linear vertical springs (with stiffnesses summing up to $k = 380\,\text{MPa/m}$) to nodes at the bottom girder surfaces in the support zones.

3.2.2. Comparison of results obtained with 1D beam and 3D FEA models

The distributions of displacements and stress tensor components found with the use of Dircol and Abaqus for both beams are compared in Figs. 5-9.

Since the bottom fibres of the GLT girder experience the highest stress levels (see Fig. 4), only these distributions are presented. The comparison of deflections of the single-span beam obtained by Dircol and Abaqus is presented in Fig. 5, whereas stress tensor components and measures of the material effort are compared in Fig. 6.

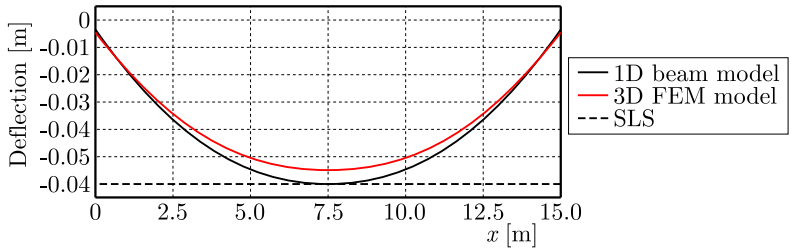

Fig. 5. Comparison of deflection of a single-span beam obtained from the 1D beam and 3D FEA models

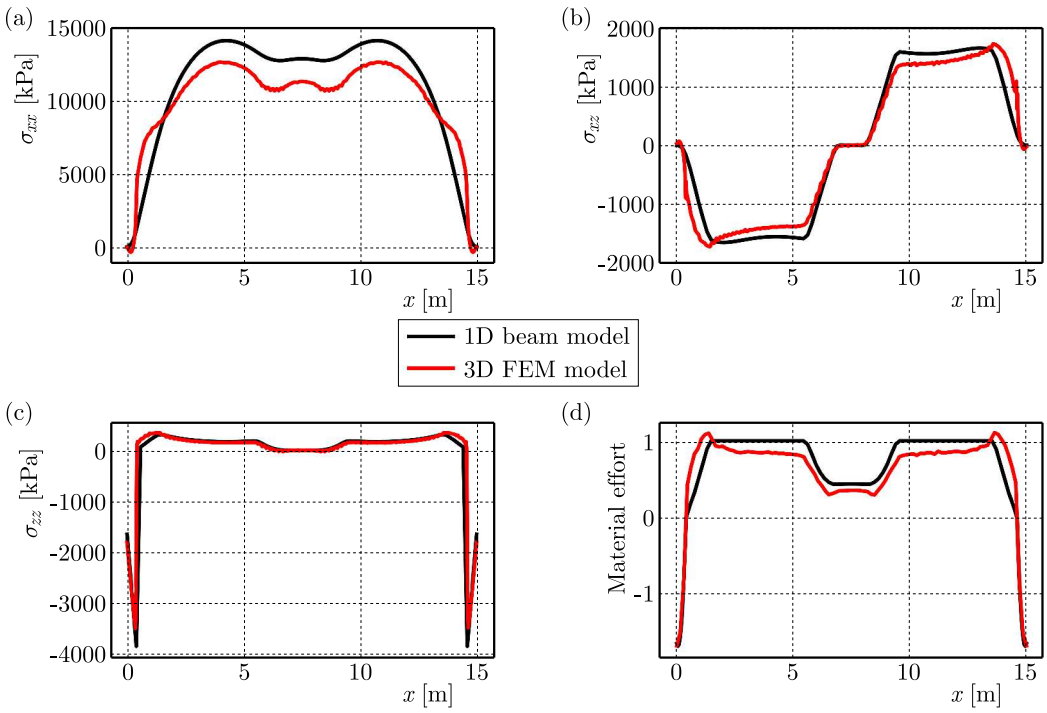

Fig. 6. Comparison of stress measures obtained from the 1D beam model and 3D FEA for bottom fibres of the GLT single-span beam: (a) axial normal stress, (b) shear stress, (c) transverse normal stress, (d) material effort

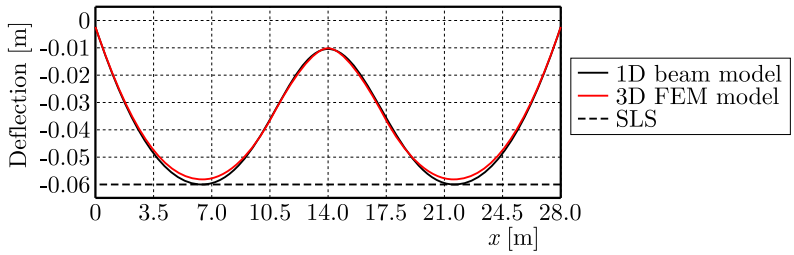

Fig. 7. Comparison of deflection of a double-span beam obtained from the 1D beam and 3D FEA models

Analogous comparisons of deflections and stresses obtained by Dircol and Abaqus for the double-span beam are collated in Figs. 7 and 8, respectively. Additionally, the distributions of shear stresses in the adhesive layers are compared in Fig. 9.

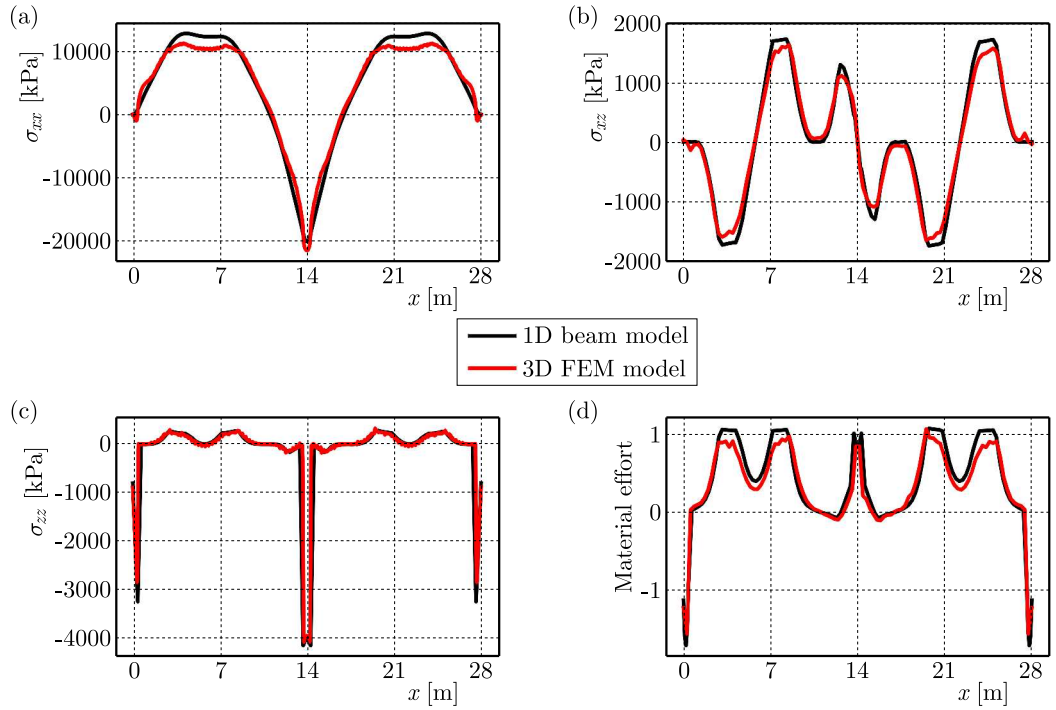

Fig. 8. Comparison of stress measures obtained from the 1D beam and 3D FEA models for the bottom fibers of the GLT double-span beam: (a) axial normal stress, (b) shear stress, (c) transverse normal stress, (d) material effort

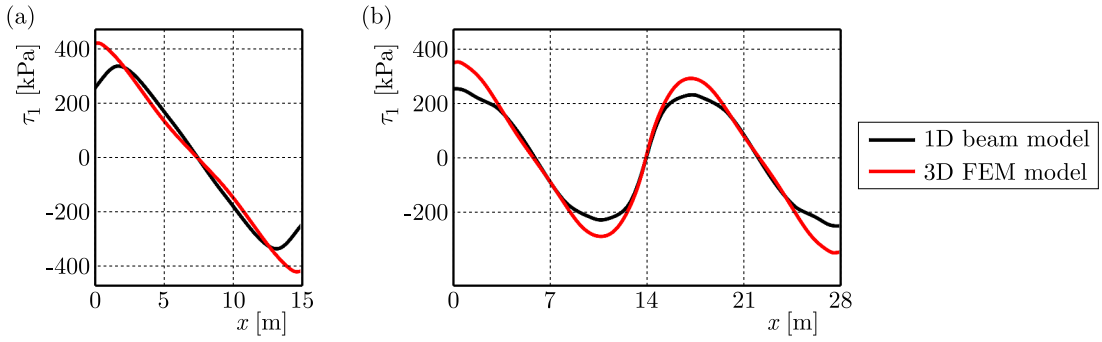

Fig. 9. Distribution of shear stress in the adhesive layer in (a) single-span beam, (b) double-span beam

4. Discussion

Analysing the comparison of stresses and deflections of optimal beams acquired with the 1D composite beam and 3D FEA models, under the same material assumptions (linear elasticity of all materials, isotropy of elastic constants of timber with the anisotropic limit state condition), presented in Section 3.2, one can note that:

- The 3D FEM model gives slightly smaller displacements (Figs. 5 and 7). Relative differences amount to 8% for the single-span beam and 4% in the case of the double-span beam.
- There is good agreement between the two models in stress distributions for both beams (Figs. 6 and 8). The ULS is active in these traction-free areas of the bottom fibres in both girders (Figs. 6d and 8d). Analysing the material effort in the 3D FEM model, one can notice that for the single-span beam the ULS is violated only pointwise by 2% (Fig. 6d) and is not exceeded in the case of the double-span beam (Fig. 8d).

- The greatest discrepancies between these two models concern the shear stresses in the adhesive layer (Fig. 9). This can be attributed to the simplifying assumption made in the 1D model according to which the adhesive layer undergoes simple shear deformation only, whereas in the FE analysis a general three-dimensional stress state is considered.
- One worrying result is the maximal deflection, which was greater for the 1D beam model than for the one obtained from the 3D FEA. One should expect that the 1D model, which is more severely constrained due to Bernoulli's hypothesis, should exhibit greater flexural rigidity. This result may be explained by the fact that in the simplified 1D model the longitudinal stiffness of the adhesive was completely disregarded as the adhesive was assumed to undergo simple shear only – in this sense this model is more compliant than the FEA model in which the three-dimensional stress and strain state is fully accounted for.

5. Summary and conclusions

The problem of shape optimization of a TCC beam with an adhesive layer has been stated. Governing equations have been derived, as well as expressions for cross-sectional forces and stresses. The problem has been reformulated in order to make it suitable for the application of Pontryagin's maximum principle. The optimization task has been carried out with the use of Dircol software for two composite beams – single and double span. Two constraint types have been considered: SLS condition restricting the maximum deflection and the ULS, which is formulated as a single inequality constraint making use of the energy-based estimate of the material effort for orthotropic materials exhibiting asymmetry in the elastic range. Both the ULS and SLS conditions are active in the obtained solutions. The observed discrepancies between the 1D beam theory solution and the results of 3D FEA indicate that the results obtained from the PMP-based optimization cannot be used without additional elaboration, however, the final shape may be easily found even by manual adjustment of the optimal solution obtained from the 1D beam model, according to the maps of the material effort.

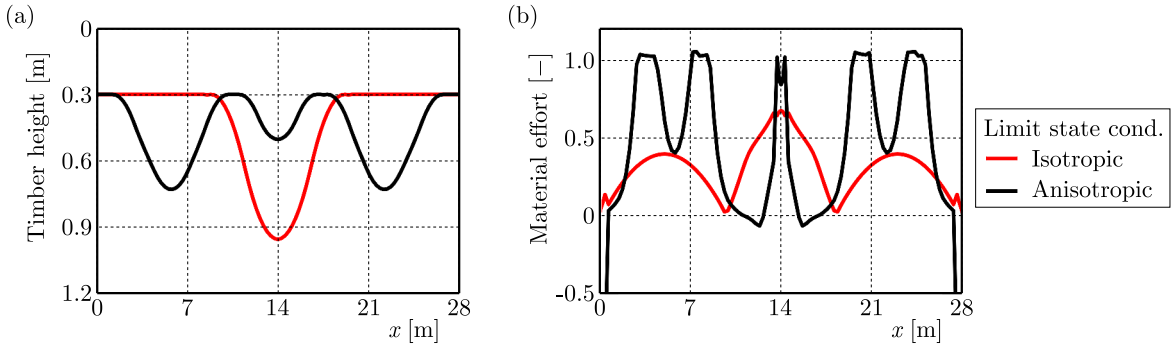

Fig. 10. Comparison of optimal double-span GLT girders obtained under isotropic and anisotropic limit state conditions: (a) height distribution, (b) material effort along bottom beam fibers

To estimate material savings achieved by shape optimization of the girders, the volumes of optimal beams have been compared with the volumes of composite beams with the same span lengths, loads and supports, but a constant GLT girder height. Minimal heights for which the SLS and ULS were not exceeded, and were adopted for this comparison. The relative material savings for the single-span beam are approximately 8%, while for the double-span beam 30%. An important conclusion arises when the anisotropy of the GLT is totally neglected in the task formulation, namely, when the timber is considered as an isotropic solid. Such an approach might be the first approximation in an optimization procedure. It can be shown that considerable errors

may occur when the anisotropy is not involved. In Fig. 10a, the optimal shape of the double-span beam obtained for the beam with the anisotropic limit state condition is compared with the one corresponding with the HMH condition (isotropic limit state condition).

In the case of the beam with the isotropic yield condition only the SLS constraint is active, wheteas if anisotropy is taken into account both SLS and ULS conditions are active (Fig. 10b). This is especially important when considering the fact that commercially available optimization programs offering topology or shape optimization often do not support anisotropy of strength properties (e.g. Tosca Structure). Even if anisotropy of elastic properties is taken into account, the fully stressed body optimization procedures can be governed only by isotropic limit state conditions such as the Huber-Mises-Hencky yield condition.

The performed analyses enable formulation of the following conclusions:

- The one-dimensional analytical model of a composite beam is suitable for application in the formalism of an optimization task of a control theory problem solved with the use of Pontryagin's maximum principle.
- A singular optimal solution may be found, for which both SLS and ULS constraints are active.
- Simplifications due to reduction of the dimension of the problem in the Bernoulli-Euler beam theory do not introduce significant errors neither in deformation nor in measure of the material effort.
- The results of the optimization of the 1D model need validation with the use of more accurate numerical models.
- The performed analyses prove that accounting for anisotropy of strength properties of the material and asymmetry of the elastic range play an important role in the optimization of timber beam structures. Failure to take into account for material anisotropy may lead to significant errors.

The proposed approach may readily be applied for shape optimization of composite beams with adhesive layers with any other support and load layout with multiple load cases taken into account.

References

1. Büskens C., Pesch H.J., Winderl S., 2001, Real-time solutions of bang-bang and singular optimal control problems, [In:] *Online Optimization of Large Scale Systems*, Springer-Verlag Berlin Heidelberg GmbH, 129-142
2. Clouston P., Schreyer A.C., 2018, Wood-concrete composites: a structurally efficient material option, *Civil Engineering Practice*, **21**, 1, 5-22
3. de Vito A.F., Vicente W.M., Xie Y.M., 2023, Topology optimization applied to the core of structural engineered wood product, *Structures*, **48**, 1567-1575
4. Decker S.A., Ndiaye A., Brangeon B., Sempey A., Galimard Ph., Pauly M., Lagiere Ph., Bos F., 2014, Design of multi-story timber building using mutli-objective particle swarm optimization, *Proceedings of the WCTE 2014 – World Conference on Timber Engineering*, **2**, 10-15
5. Dias A., Schänzlin J., Dietsch P., 2018, *Design of Timber-Concrete Composite Structures*, A state-of-the-art report by COST Action FP1402/WG4
6. Goland M., Reissner E., 1944, The stresses in cemented joints, *Journal of Applied Mechanics*, **11**, A17-A27
7. Hua H., Hovestadt L., Tang P., 2020, Optimization and prefabrication of timber Voronoi shells, *Structural and Multidisciplinary Optimization*, **61**, 1897-1911

8. Jasińska D., Kropiowska D., 2018, The optimal design of an arch girder of variable curvature and stiffness by means of control theory, *Mathematical Problems in Engineering*, **2018**, 1-13
9. Jasińska D., Mikulski L., 2019, Strength optimization of structural elements by means of optimal control, *MATEC Web of Conferences*, **262**, 10006
10. Kravanja S., Žula T., 2021, Optimization of a single-storey timber building structure, *International Journal of Computational Methods and Experimental Measurements*, **9**, 2, 126-140
11. Kwiecień A., 2012, Stiff and flexible adhesives bonding CFRP to masonry substrates – Investigated in pull-off test and Single-Lap test, *Archives of Civil and Mechanical Engineering*, **12**, 2, 228-239
12. Mayencourt P., Mueller C., 2019, Structural optimization of cross-laminated timber panels in one-way bending, *Structures*, **18**, 48-59
13. Mayencourt P., Mueller C., 2020, Hybrid analytical and computational optimization methodology for structural shaping: Material-efficient mass timber beams, *Engineering Structures*, **215**, 110532
14. Mikulski L., Jasińska D., Dąbrowska O., 2022, Structure of optimal control in optimal shaping of the steel arch, *Civil and Environmental Engineering Reports*, **32**, 3, 143-165
15. Pech S., Kandler G., Lukacevic M., Füssl J., 2019, Metamodel assisted optimization of glued laminated timber beams by using metaheuristic algorithms, *Engineering Applications of Artificial Intelligence*, **79**, 129-141
16. Šilih S., Kravanja S., Premrov M., 2010, Shape and discrete sizing optimization of timber trusses by considering of joint flexibility, *Advances in Engineering Software*, **41**, 2, 286-294
17. Śliwa-Wieczorek K., Zając B., Kozik T., 2020, Tests on the mechanical properties of polymers in the aspect of an attempt to determine the parameters of the Mooney-Rivlin hyperelastic model, *Civil and Environmental Engineering Reports*, **30**, 2, 1-14
18. Szeptyński P., 2017, Energy-based yield criteria for orthotropic materials, exhibiting strength--differential effect. Specification for sheets under plane stress state, *Archives of Metallurgy and Materials*, **62**, 2, 729-736
19. Szeptyński P., 2020, Comparison and experimental verification of simplified one-dimensional linear elastic models of multilayer sandwich beams, *Composite Structures*, **241**, 112088
20. Szeptyński P., Mikulski L., 2023, Preliminary optimization technique in the design of steel girders according to Eurocode 3, *Archives of Civil Engineering*, **69**, 1, 71-89
21. Villar-García J.R., Vidal-López P., Rodríguez-Robles D., Guaita M., 2019, Cost optimisation of glued laminated timber roof structures using genetic algorithms, *Biosystems Engineering*, **187**, 258-277
22. Volkersen O., 1938, Die Nietkraftverteilung in zugbeanspruchten Nietverbindungen mit konstanten Laschenquerschnitten, *Luftfahrtforschung*, **15**, 41-47

Manuscript received October 26, 2023; accepted for print November 30, 2023

JOURNAL OF THEORETICAL AND APPLIED MECHANICS
62, 1, pp. 143-156, Warsaw 2024
https://doi.org/10.15632/jtam-pl/176309

STUDY ON DUCTILE FRACTURE CRITERION APPLIED TO SHEAR FRACTURE PREDICTION OF DP780 SHEET

Jiaxiong Wu, Xuguang Sun, Xiaoce Sun, Fu Chang
China North Vehicle Research Institute, Beijing, China
corresponding author Xuguang Sun, e-mail: sun_xuguang@163.com
Shudi Yang, Senqi Tan
China North Artificial Intelligence and Innovation Research Institute, Beijing, China

With the development of automotive lightweight technology, the improvement of the design of body sheet metal forming processes has gradually become a research focus. Advanced high--strength dual-phase steel is the main material for lightweight vehicle bodies, and exploring its accurate ductile fracture criteria plays an important role in predicting the forming fracture behavior of the sheet metal. The characterizations of the plastic behavior of the DP780 sheet before fracture were performed by the Swift hardening model. Three sets of tests from pure shear to tensile-shear stress states are designed to calibrate the ductile fracture parameters of Lou-Huh, Cockcroft-Latham, and Rice-Tracey criteria. The calibrated parameters are used to predict tensile shear test fractures and punching fractures at small bend fillets of molds. The results show the Lou-Huh criterion can accurately predict the shear fracture behavior of the DP780 sheet in the low-stress triaxiality (0.08-0.33).

Keywords: ductile fracture criterion, DP780, fracture prediction, shear fracture, sheet forming

1. Introduction

Based on the consideration of automobile lightweight, advanced high-strength steel DP780 has become the preferred material for body lightweight due to its high specific strength and good energy absorption (Zhou *et al.*, 2021). It is widely used in key parts such as the threshold beam, B column, anti-collision beam, and ceiling beam. In 2002, the international iron and steel federation's "Advanced Automotive Concept for Ultra Light Steel Bodies (ULSAB-AVC)" project showed a high usage rate of 74% for DP steel in the body structure design. However, advanced high-strength steel also has a defect of poor room temperature formability. Therefore, to improve the formability of the sheet, a larger blank holder force or a smaller die-bending fillet is often used in the design of the stamping process, which results in shear fracture behavior of the DP780 sheet with no obvious necking before failure at the die bending fillet (Luo and Wierzbicki, 2010; Banabic *et al.*, 2020). The shear fracture of high-strength steel in the forming process is one of the main problems that hinder its application in automobile bodies. Traditional FLC curves and various criteria based on necking instability theory (Silva *et al.*, 2008) such as Swift dispersive instability theory (Swift, 1952), Hill concentrated instability theory (Hill, 1952), and the Marciniak-Kuczynski instability theory (Marciniak and Kuczynski, 1967), cannot accurately predict this type of shear fracture. In addition, the lack of accurate shear fracture criteria greatly limits the application of the sheet metal and forming process design. Therefore, from the perspective of industrial application, it is of great significance to explore the shear fracture criterion with an accurate prediction and a simple form to foresee the forming fracture of sheet metal.

The fracture of metal sheets evolved from micro-defects such as micro-dimples and micro--shear bands, and the evolution of the two types of micro-defects is controlled by the stress state (Li *et al.*, 2011b). The necking dominant fracture in a high-stress triaxiality region is related to continuous nucleation, growth and convergence of micro dimples, while the shear dominant fracture in the low-stress triaxiality region is caused by a continuous extension of micro cracks and micro holes into shear bands under shear action (Hu *et al.*, 2009). The researchers analyzed mechanical factors affecting the nucleation, growth, polymerization, and fracture of micro-voids in the material from the microscopic mechanism of ductile fracture (McClintock *et al.*, 1966; Puttick, 1959) and proposed many uncoupled ductile fracture criteria for predicting sheet-forming fracture (Rice and Tracey, 1969; Cockcroft and Latham, 1968; Oh *et al.*, 1979; Clift *et al.*, 1990). The above criteria mainly consider mechanical variables such as maximum normal stress, maximum shear stress and stress triaxiality, as well as combinations of mechanical variables. Nevertheless, due to the lack of research on a specific influence mechanism of mechanical variables selected in the criteria on the evolution of micro-defects, the stress state interval and fracture type applicable to the above criteria are different.

Based on the micro-mechanism theory, the criterion considering both the stress triaxiality and the Lode parameter has received extensive attention due to the wider range of applicable stress states. With a broad application of DP780 high-strength steel in the industry, it is of great research value to explore a more flexible and accurate ductile fracture criterion in forming simulation. In this paper, the advanced high-strength steel DP780 sheet is used as the research object. The stress and strain state parameters of the material in the low-stress triaxiality range are obtained by designing four kinds of unidirectional loading samples combined with numerical simulation. The parameters of Lou-Huh, Cockcroft-Latham, and Rice-Tracey ductile fracture criteria are calibrated, and then applied to fracture prediction of a tensile-shear test and shear fracture in stretch-bending forming of grooved parts in order to study their applicability and accuracy.

2. The test design and process

2.1. Sample design for different stress states

In this paper, the thickness of the advanced high-strength steel DP780 sheet sample is 1mm, and its chemical composition is shown in Table 1.

Table 1. Material chemical composition of the sample

C	Si	Mn	P	S	Alt
0.1	0.16	2.02	0.008	0.003	0.039

In order to analyze plasticity and fracture behavior of the DP780 sheet under low-stress triaxiality, four unidirectional loading specimens with different shapes and sizes are designed as shown in Fig. 1. The figure shows the uniaxial tensile specimen, pure shear specimen, 45° tensile shear specimen, and 60° tensile shear specimen, respectively.

2.2. The anisotropic test process

Three sets of uniaxial tensile specimens with different orientations are prepared by laser wire cutting to determine plastic anisotropy of DP78 sheets. The preparation orientations of laser wire cutting are 0°, 45° and 90° with the rolling direction, respectively. For the test method, the RDL50 universal testing machine is used to load the specimen with an elongation rate of 0.2 mm/min at room temperature. The loading process is quasi-static, and nominal stress-strain curve of the specimen gauge section can be obtained by an extensometer.

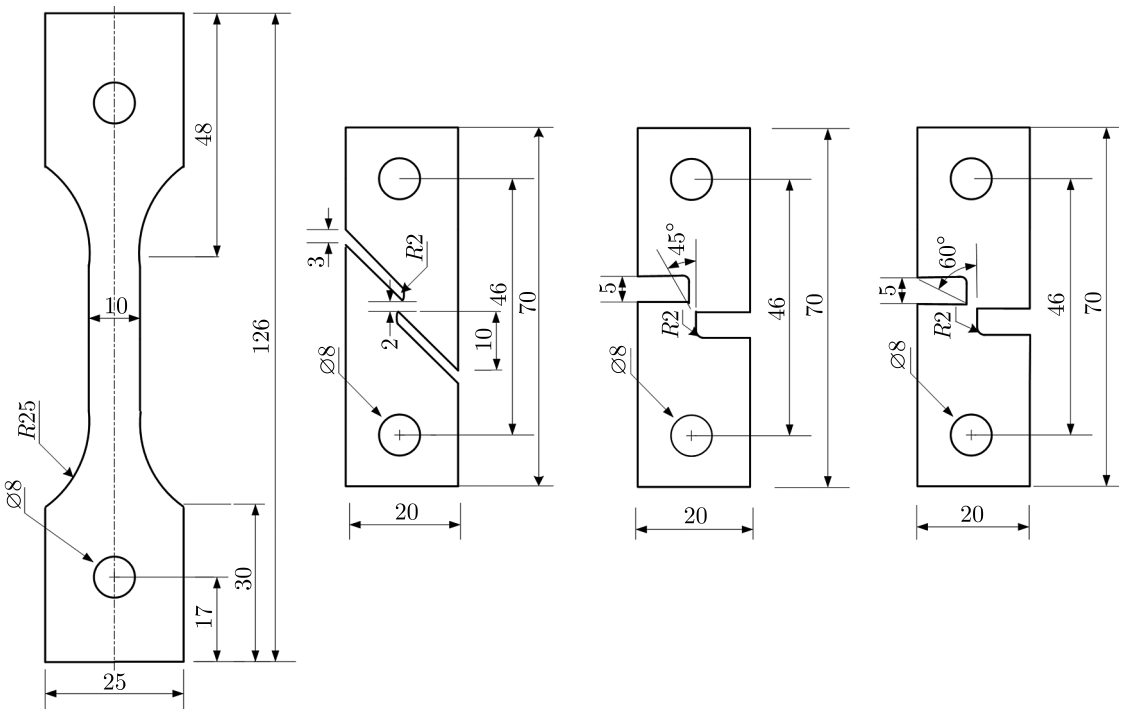

Fig. 1. Shape and size of the unidirectional loading sample

The equations for converting the nominal stress-strain curve into a real stress-strain curve are shown as follows

$$\varepsilon = \ln(1+\varepsilon_e) \qquad \sigma = \sigma_e(1+\varepsilon_e) \tag{2.1}$$

where σ is the real stress, ε is the real strain, ε_e is the nominal strain, σ_e is the nominal stress.

The real stress-true strain curves of the three orientations of the uniaxial tensile specimen can be obtained by the experimental results and Eqs. (2.1). The real stress-true strain curves are shown in Fig. 2. It can be seen from Fig. 2 that the true stress-strain curves of 0° and 45° orientations are consistent, and the real stress-true strain of 90° orientation is slightly higher by about 2%. The anisotropy characteristics of the DP780 sheet were not very obvious, and it could be assumed that the DP780 sheet had plane isotropy (Luo and Wierzbicki, 2010), so the von Mises yield criterion was used to describe its yield behavior.

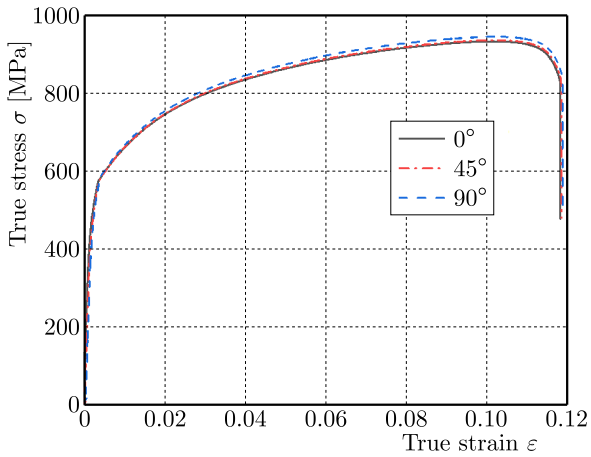

Fig. 2. The true stress-true strain curves of samples with different orientations

2.3. Comparison of DP780 hardening models

An accurate description of the hardening behavior of materials before fracture is the key to calibrating the parameters of the ductile fracture criterion. During the deformation of the specimen, the fracture strain is often higher than the maximum uniform strain, so it is necessary to establish a suitable hardening model to accurately predict the flow stress of the material in a large plastic strain range. In this paper, the classical Swift unsaturated hardening model (Swift, 1952) and the Voce saturated hardening model (Voce, 1948) are selected to characterize the hardening behavior of the DP780 sheet. The von Mises criterion based on constitutive relation matrix representation can be referred to in the literature (Ortiz and Simo, 1986). The hardening models are shown in Eq. (2.2) and (2.3), respectively

$$\sigma = K(\varepsilon_0 + \overline{\varepsilon}_p)^n \tag{2.2}$$

where K is the hardening coefficient, n is the hardening exponent, ε_0 is the initial yield strain and $\overline{\varepsilon}_p$ is the equivalent plastic strain.

Compared with the Swift model, the Voce model fully considers the effect of the initial yield point on the flow stress, and the stress will constantly approach the saturation state under large strain conditions, which means that the stress-strain curve will exhibit horizontal asymptotes, which can prove the constitutive relationship of metal materials under large strain conditions

$$\sigma = \sigma_0 + A(1 - exp(-c\overline{\varepsilon}_p)) \tag{2.3}$$

where A and c are material constants and σ_0 is the saturation stress.

The transformation equation of the true stress-true strain curve and true stress-plastic strain curve is given by

$$\overline{\varepsilon}_o = \varepsilon - \frac{\sigma}{E} \tag{2.4}$$

where E is the elastic modulus.

The real stress-plastic strain test curve of the tensile specimen at 0° with the rolling direction in the uniform deformation section is shown in Fig. 3.

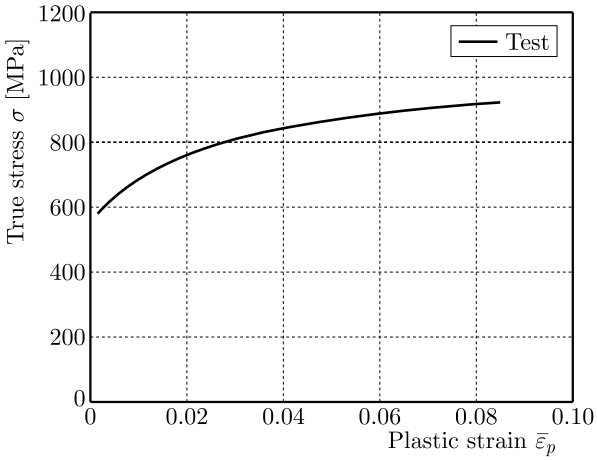

Fig. 3. True stress-plastic strain curve

Through the least square method, the Swift and Voce model parameters can be obtained from the true stress-plastic strain curve, as shown in Table 2.

Table 2. Hardening model parameters

Parameter	K [MPa]	ε_0	n	σ_0 [MPa]	σ_s [MPa]	A [MPa]	c
Value	1388	0.004	0.157	570	584.59	357.1	34.8

To verify the accuracy of the two hardening models for the characterization of the plastic behavior of the DP780 sheet, the von Mises yield criterion and the VUMAT subroutine of the two hardening models are compiled by the Fortran language. The compiled subroutine is embedded in Abaqus to simulate the tension process of uniaxial tensile specimens through the finite element method (FEM). A comparison of the simulation and experiment is shown in Fig. 4. It can be seen from Fig. 4a, both Swift and Voce hardening models can accurately describe the hardening behavior of DP780 specimens in the uniform plastic zone. From Figs. 4a and 4b, the Voce model underestimates the flow stress of DP780 in a large strain range, however, the Voce model cannot accurately predict the stress in a large strain range. While the Swift model slightly overestimates the flow stress in a large strain range, but still accurately describes the stress of DP780 in that range. Therefore, the Swift hardening model is selected to describe the hardening behavior of the DP780 specimen in a uniform plastic zone.

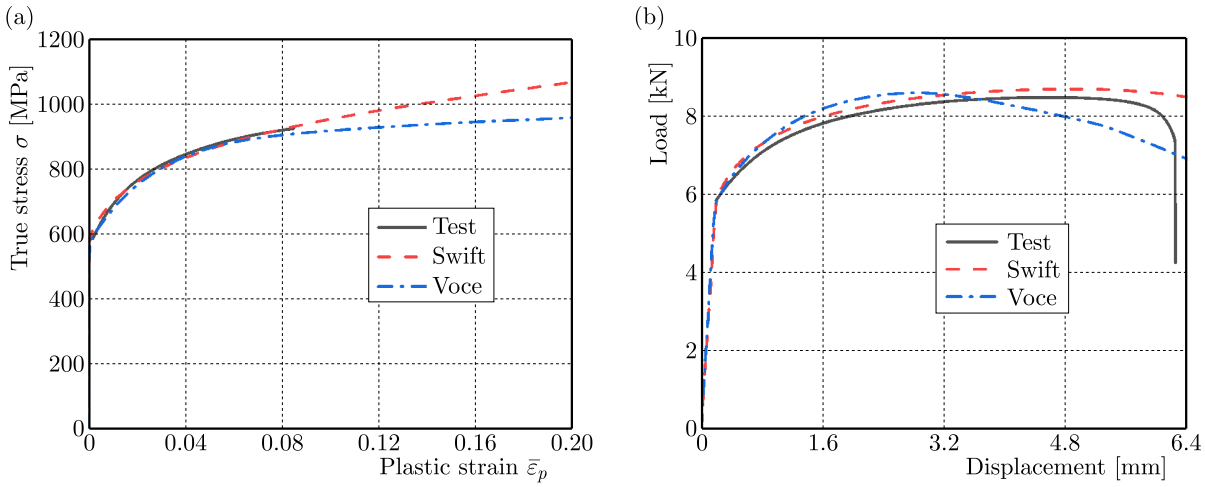

Fig. 4. Comparison of the simulation and test curves obtained by using two hardening models: (a) comparison of true strain-plastic strain curves, (b) comparison of load-displacement curves

Unidirectional loading tests of pure shear and tensile shear specimens with different notch angles can only find load-displacement curves in order to obtain stress parameters and fracture strain at the notch. Hence, corresponding simulations are performed to further verify the accuracy of the von Mises yield criterion and the Swift hardening model for predicting the plastic behavior of DP780 sheets before fracture. When the load-displacement curve of the FEM simulation is in good agreement with the test, the stress parameters and fracture strain at the moment of fracture of each sample can be obtained.

The S4R shell element is used in the finite element model of the tension-shear specimen to ensure simulation accuracy and computational efficiency. The S4R element has high simulation accuracy in large strain simulation and a wider scope of application (Luo and Wierzbicki, 2010). The grids of the central ligament area of the sample with large plastic deformation are refined, and the refined grid size is 0.08 mm. A comparison of FEM simulated and test load-displacement curves are shown in Fig. 5. The von Mises yield criterion and Swift hardening model well characterize the plastic behavior of DP780 tensile-shear specimens before fracture, which can be used to calibrate the ductile fracture criterion.

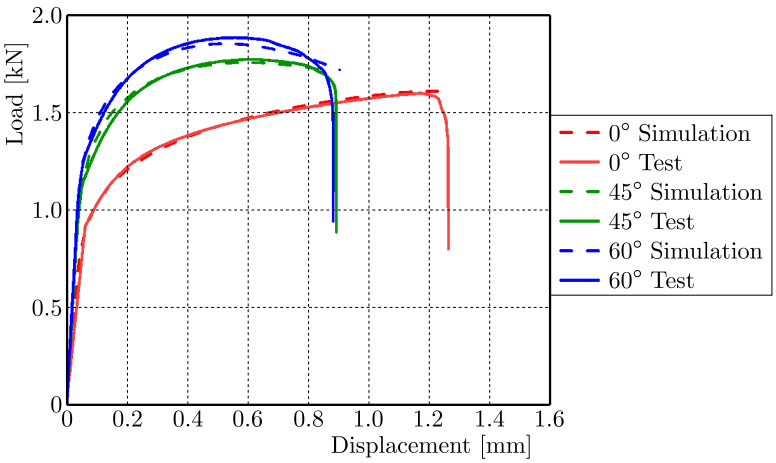

Fig. 5. Comparison of simulation and test load-displacement curves of tensile-shear specimens with different notch angles

3. Parameter calibration of the ductile fracture criterion and prediction of the tensile-shear test of DP780 sheet

3.1. Ductile fracture criterion including stress triaxiality and the Lode parameter

The stress triaxiality and Lode parameter are the determining factors affecting fracture initiation of the sheet. Therefore, the three criteria of Lou-Huh (Lou *et al.*, 2012), Cockcroft--Latham (Cockcroft and Latham, 1968), and Rice-Tracey (Rice and Tracey, 1969) are applied to the shear fracture prediction of the DP780 sheet. The expressions of the three criteria are shown in Table 3.

Table 3. Expressions of relevant ductile fracture criteria

Ductile fracture criterion	Expressions
Lou-Huh	$\int_0^{\overline{\varepsilon}_f} \left(\frac{2}{\sqrt{L^2+3}}\right)^{a_1} \left(\frac{\langle 1+3\eta\rangle}{2}\right)^{a_2} d\overline{\varepsilon}_p = a_3$
Cockcroft-Latham	$\int_0^{\overline{\varepsilon}_f} \sigma(\overline{\varepsilon})^* \left(\eta + \frac{3-L}{3\sqrt{L^2+3}}\right) d\overline{\varepsilon}_p = b$
Rice-Tracey	$\int_0^{\overline{\varepsilon}_f} 0.283 \exp\left(\frac{3\eta}{2}\right) d\overline{\varepsilon}_p = c$

3.2. Parameter calibration of three ductile fracture criteria

In this paper, pure shear specimens, 45° and 60° tensile shear specimens are selected to calibrate the fracture criterion parameters. It is difficult to directly obtain the state parameters such as stress triaxiality η, Lode parameters L, and fracture strain $\overline{\varepsilon}_f$. Consequently, based on the hardening model selected in Table 3, the ductile fracture criterion is calibrated by a combination of the test method and FEM simulation. Since the initial fracture time of the specimen cannot be accurately determined during the test, the moment when the load-displacement curve drops sharply is equivalent to the initial fracture time, and the displacement d corresponding to the fracture time is taken as the fracture displacement. The elements with the maximum equivalent plastic strain in the ligament region at the fracture time are selected as the initial fracture elements. The equivalent plastic strain value of these initial fracture elements at the initial

fracture time is taken as the fracture strain. The variation curves of the stress triaxiality and Lode parameter with the equivalent plastic strain $\bar{\varepsilon}_p$ of initial fracture elements are shown in Fig. 6.

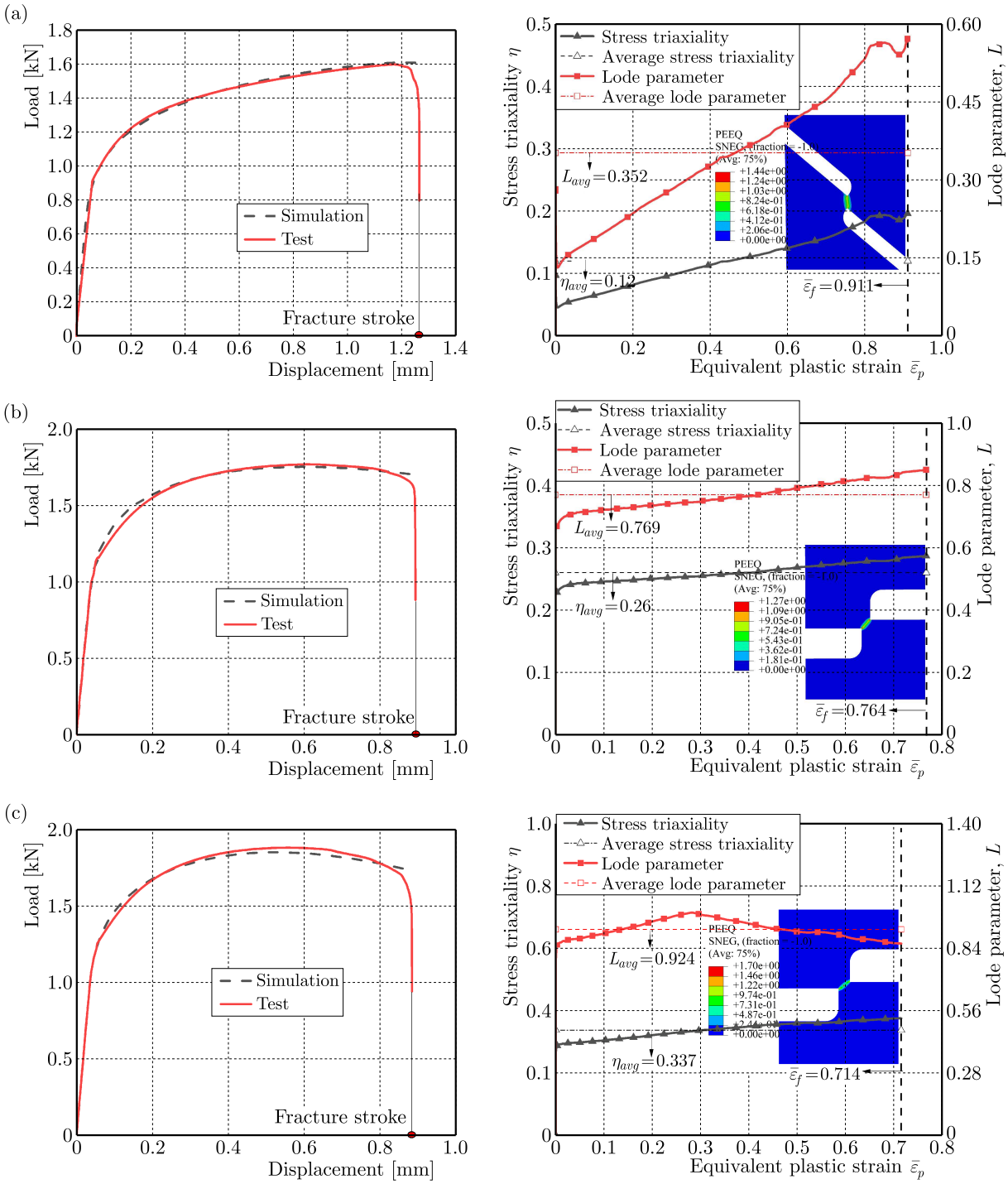

Fig. 6. The stress triaxiality and Lode parameter change curve of tensile-shear specimens with different notch angles: (a) pure shear specimen, (b) 45° tensile-shear specimen, (c) 60° tensile-shear specimen

The stress triaxiality and Lode parameters vary with the equivalent plastic strain $\bar{\varepsilon}_p$, which cannot be directly substituted into the fracture criterion to solve the fracture parameters. According to Eqs. (3.1), the stress triaxiality η and lode parameters L in the whole process of

stress change are averaged to obtain the average stress triaxiality η_{avg} and average Lode parameters L_{avg} (Qian *et al.*, 2020)

$$\eta_{avg} = \frac{1}{\overline{\varepsilon}_f}\int_0^{\overline{\varepsilon}_f} \eta(\overline{\varepsilon})\, d\overline{\varepsilon}_p \qquad L_{avg} = \frac{1}{\overline{\varepsilon}_f}\int_0^{\overline{\varepsilon}_f} \theta(\overline{\varepsilon})\, d\overline{\varepsilon}_p \tag{3.1}$$

where η_{avg} is the average stress triaxiality, L_{avg} is the average Lode parameter, and $\overline{\varepsilon}_f$ is the fracture strain. The calculated fracture state parameters are shown in Table 4.

Table 4. Parameters of the fracture state

Specimen type	Fracture displacement	Fracture strain	Stress triaxiality	Lode parameter
Pure shear	1.25 mm	0.911	0.08	0.352
45° tensile-shear	0.88 mm	0.764	0.26	0.764
60° tensile-shear	0.85 mm	0.714	0.337	0.714

The stress and strain state parameters in Table 4 are respectively substituted into the expression for the fracture criterion in Table 3 to obtain equations with undetermined fracture criterion parameters. The fracture criterion parameters are calculated by solving the equations, as shown in Table 5.

Table 5. Calibrated fracture criterion parameters

Ductile fracture criterion	Parameter 1	Parameter 2	Parameter 3
Lou-Huh	3.32	1.5128	0.7658
Cockcroft-Latham	0.3067	–	–
Rice-Tracey	1312	–	–

3.3. Tension-shear fracture prediction by three criteria

The tensile-shear test is simulated by using the three calibrated fracture criteria, and the fracture morphologies of the experimental and simulated samples are consistent. It can be seen from Fig. 7 that the fracture section of the sample is relatively flat with obvious shear slip bands. The fracture surface is gray and suede, and the fracture is full of dimples. The large notch angle of the fracture indicates that the shear part generates large plastic deformation under dislocation tension on both sides during loading, so the rotation effect occurs.

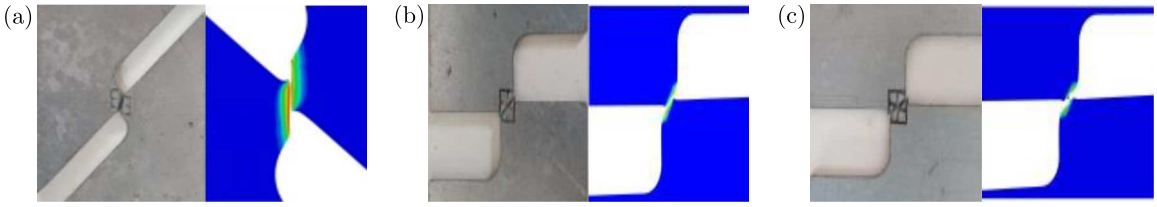

Fig. 7. Comparison of sample fracture morphology between the simulation and experiment: (a) pure shear specimen, (b) 45° tensile-shear specimen, (c) 60° tensile-shear specimen

In order to further verify the prediction accuracy of the ductile fracture criterion for fracture displacement of the tensile-shear specimen, the load-displacement curves of the test and FEM simulated tensile-shear fracture are compared as shown in Fig. 8. When the element fracture threshold of the finite element model of the specimens reaches 1, the corresponding elements are deleted to determine that the sheet begins to fracture.

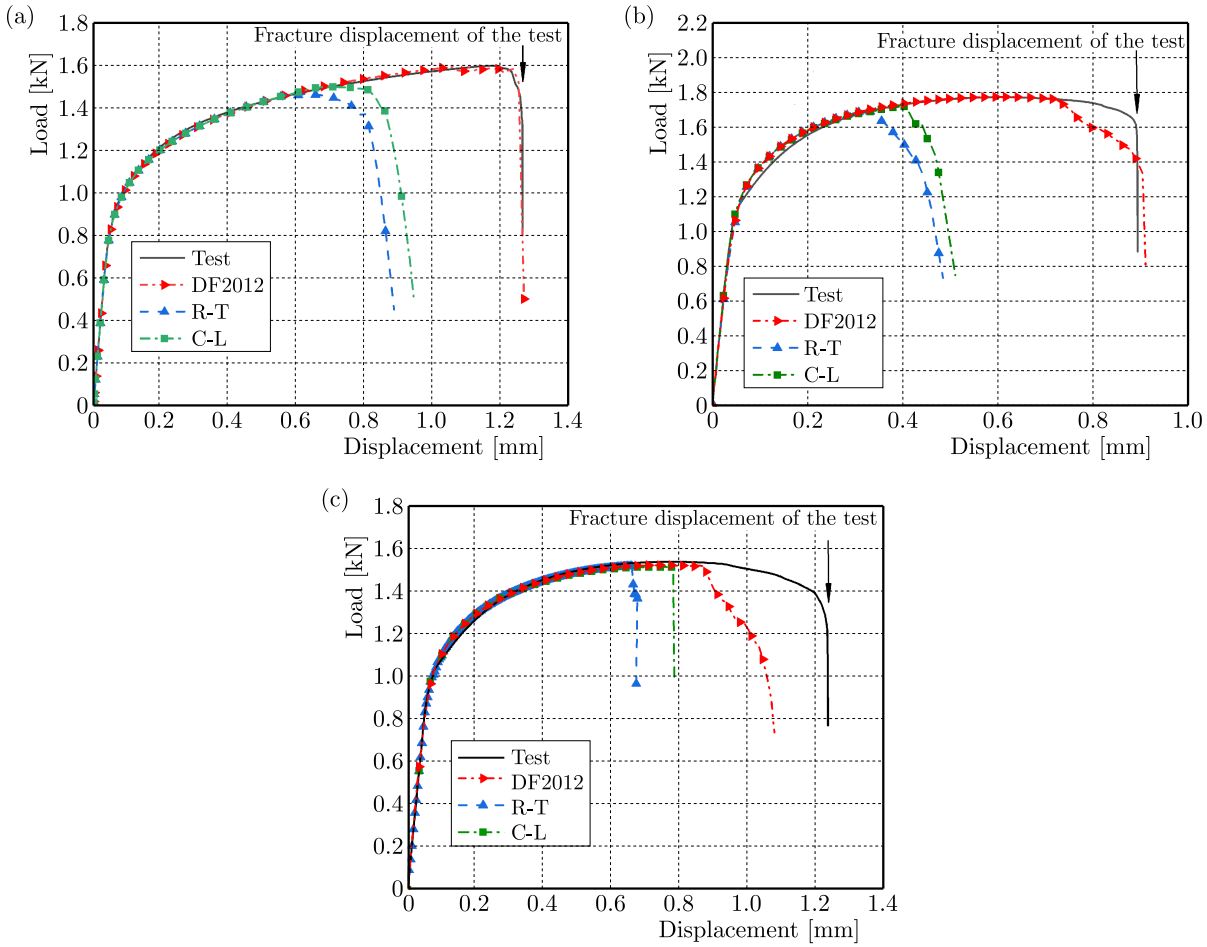

Fig. 8. Fracture displacement and test displacement of specimens with different notch angles: (a) pure shear specimen, (b) 45° tensile-shear specimen, (c) 60° tensile-shear specimen

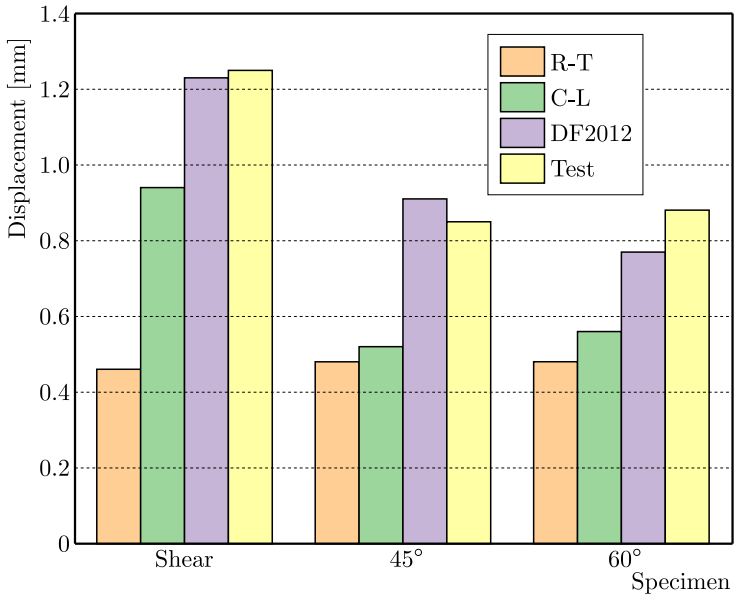

Fig. 9. Comparison of fracture displacement simulation values of various criteria

The fracture displacement values and test values of the specimens are summarized in Fig. 9. The Lou-Huh ductile fracture criterion can more accurately predict the fracture displacement of the specimens than the other two criteria, which indicates that the Lou-Huh ductile fracture criterion can be used to predict the tensile-shear fracture of the DP780 sheet in the low-stress triaxiality range (0.08-0.33). The reason for the accurate prediction of the Lou-Huh ductile fracture criterion is that both the stress triaxiality and the Lode parameter on material fracture are considered, and a more reasonable relationship between the fracture strain, stress triaxiality, and Lode parameter are constructed.

4. Application of the Lou-Huh criterion to shear fracture prediction in stretch bending of DP780 sheet

4.1. DP780 trough forming test

Relevant studies have shown that the blank holder force and the ratio of fillet radius to sheet thickness t are the main technological factors affecting fracture behavior. The sheet is prone to shear fracture under a larger blank holder force or a smaller ratio of fillet radius to sheet thickness. The shear-dominated fracture in the low-stress triaxiality region is caused by continuous development of micro-cracks and micro-voids into shear bands under shearing action (Li *et al.*, 2011b).

Based on the precise prediction effect of the Lou-Huh ductile fracture criterion on the fracture behavior of tensile-shear specimens, a pull-bending forming shear fracture test of the DP780 sheet under the condition of a small ratio of fillet radius to sheet thickness and large blank holder force is designed. In addition, the Lou-Huh ductile fracture criterion is also applied to the forming FEM simulation to verify the fracture prediction accuracy of the Lou-Huh ductile fracture criterion by comparing the FEM simulation results with test results.

Figure 10 shows the trough mold for the pull-bending forming shear fracture test. The fillet radius at the entrance of the die is $R_{d1} = 2.5\,\text{mm}$, and the gap between the die and the punch is $G = 1.1\,\text{mm}$. During the test, the blank holder force remained unchanged, and the shear fracture behavior of the DP780 sheet under different bending fillet radii R_p is observed by adjusting the bending fillet radius.

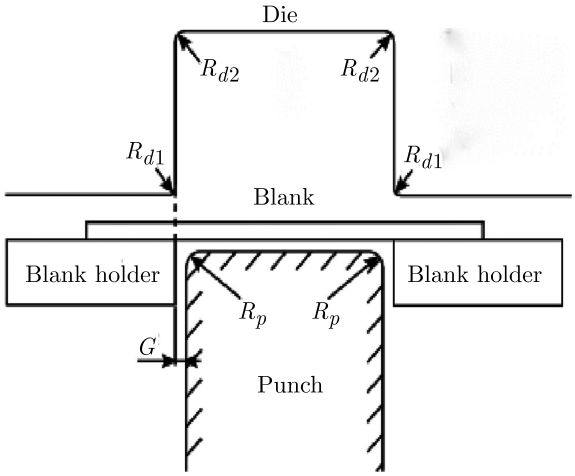

Fig. 10. Drawing and bending forming die size

The model of the test press is YZ32-160S, which is mainly composed of a die, punch, draw bead, and blank holder, as shown in Fig. 11a. The size of the trough sheet sample is 250 mm×30 mm×1 mm. The test process is as follows.

The sample is placed flat in the middle of the blank holder, and the die moves downward at a speed of 10 mm/s and contacts the sheet. At this time, the sheet is fixed between the die and the blank holder due to the blank holder force. Then the punch moves upward at a speed of 1 mm/s to push the sheet out and press the sheet into its concave die. When the sheet breaks, the punch stops moving. During the test, the test blank holder force is set to 185 kN, and the bending fillet radius of the die is adjusted by replacing the punch (1 mm, 3 mm, 5 mm) so that the DP780 sheet stamping exhibits shear fracture behavior at different small bending fillets of the punch.

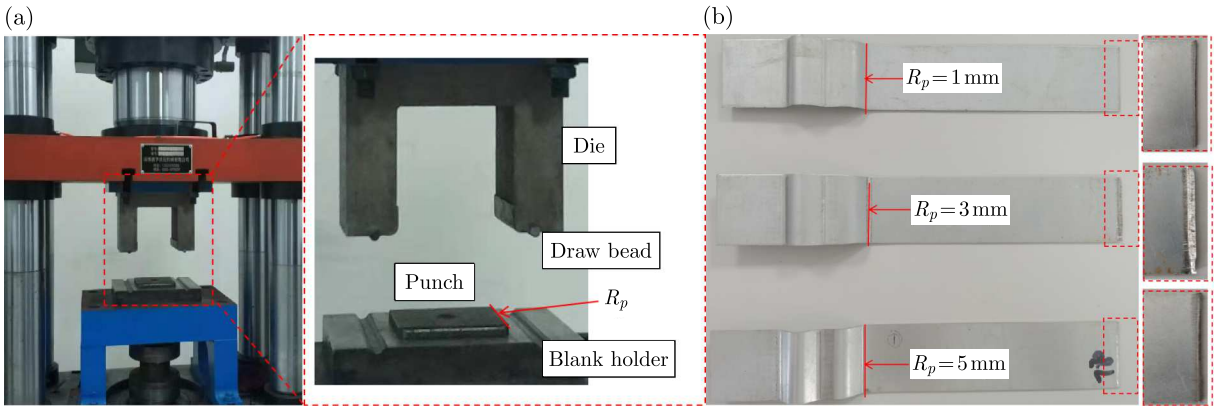

Fig. 11. Tension-bending fracture specimen

The DP780 sheet after stamping fracture is shown in Fig. 11b. A shear fracture of the DP780 sheet is generated at the bending fillet of the punch, the fracture is relatively flat without obvious necking, and the fracture is full of dimples of uniform size, which is similar to a brittle fracture. The reason for the brittle fracture is owing to the strength difference between martensite and ferrite in the dual-phase steel and a large number of micro-voids nucleated during the deformation process under the coupled action of tension and bending. However, the nucleation fails to grow sufficiently, so the material undergoes a cleavage fracture, and the fracture failure type of the sheet is basically the brittle failure (Luo and Wierzbicki, 2010).

Test data under different punch fillet radii are shown in Table 6. Under the condition that the blank holder force remains approximately constant, the forming depth before fracture gradually increases with an increase of the R_p/t value, which indicates that the R_p/t value is one of the technological factors affecting the fracture.

Table 6. Results of the stamping test

R_p/t	Forming depth	Stamping force	Fracture type
1	7.5 mm	185 kN	shear fracture
3	8 mm	179 kN	shear fracture
5	11.4 mm	184 kN	shear fracture

4.2. Simulation of the stretch-bending forming test for DP780 trough samples

According to the actual size of the stamping die, a finite element model is established in Abaqus, in which the punch, die and the blank holder are both analytical rigid bodies, while the sheet sample is a deformable body calculated by the S4R shell element. The shell element size of the DP780 sheet is 0.8 mm, and the element size of other components is 2 mm. The friction coefficient of the contact surface between the DP780 sheet and the blank holder is set to 0.125. The compiled Lou-Huh criterion VUMAT subroutine is called during stamping simulation, and the specific material parameters are shown in Table 2. The forming depth results at the moment

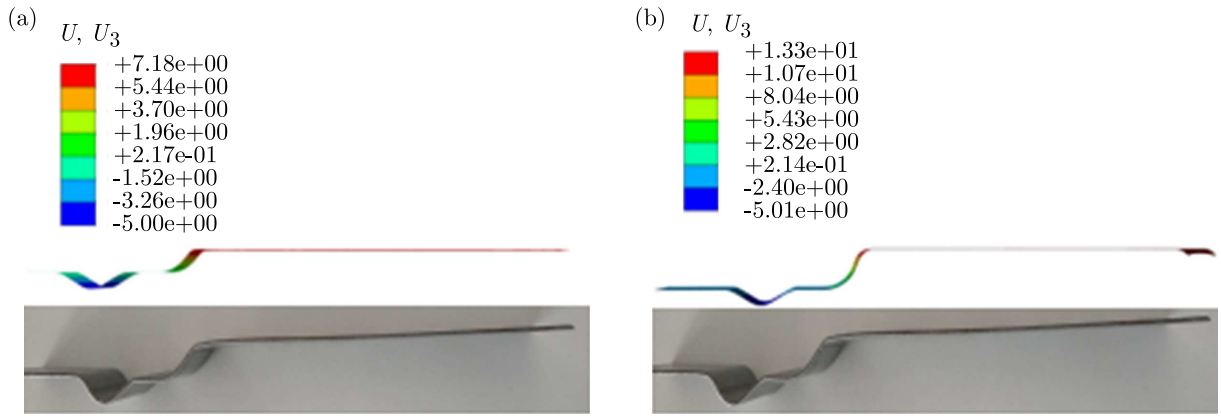

Fig. 12. Simulation and experimental values of forming depth under different punch fillets, the punch fillet radius is: (a) 1 mm, (b) 5 mm

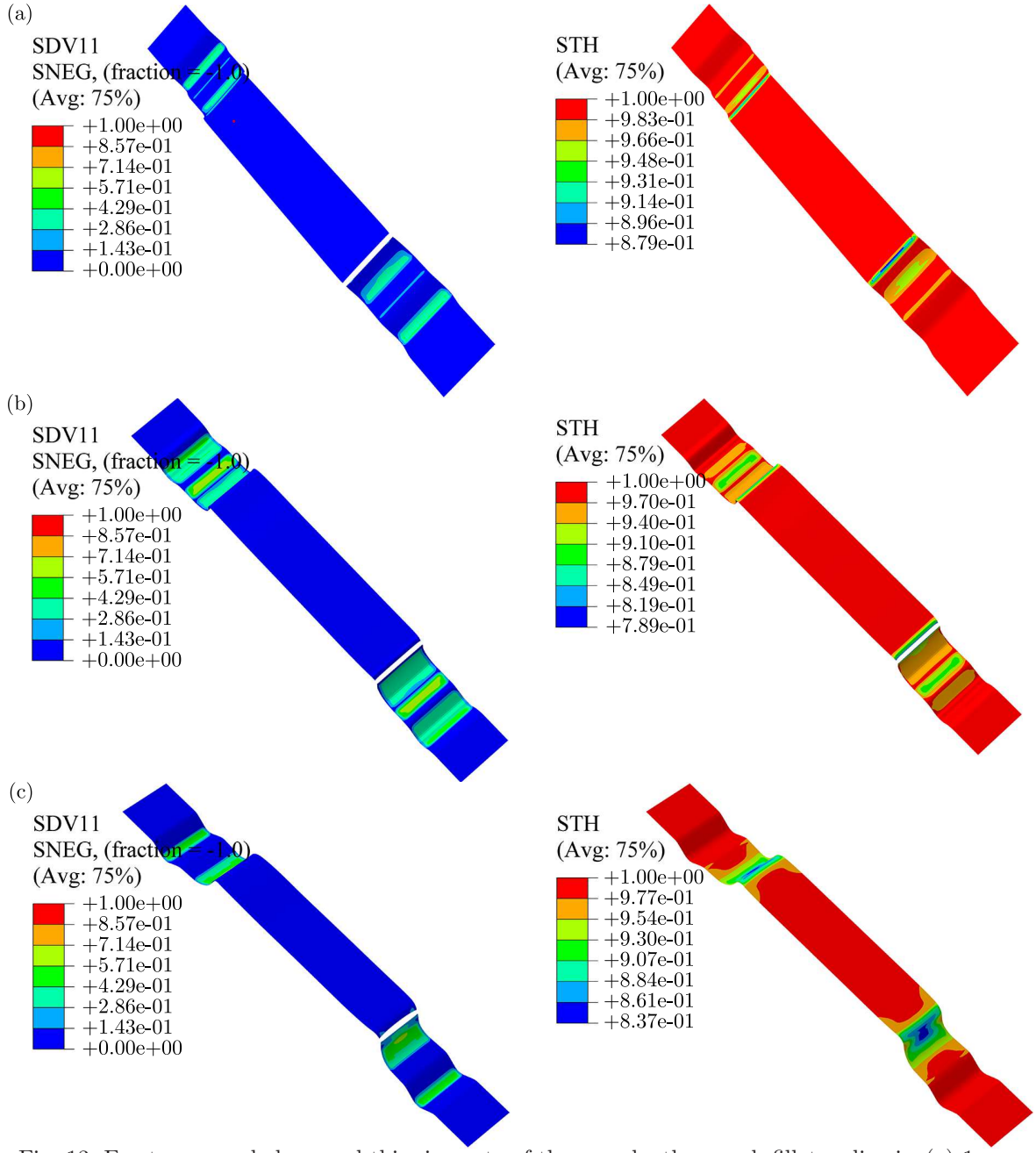

Fig. 13. Fracture morphology and thinning rate of the sample, the punch fillet radius is: (a) 1 mm, (b) 3 mm, (c) 5 mm

of sheet fracture during stamping simulation are extracted, and the simulated forming depth is compared with the test results, as shown in Fig. 12.

Different punch fillet radius values (1 mm, 3 mm, 5 mm) are used for stamping simulation to obtain the sheet fracture morphology and thinning rate data, as shown in Fig. 13. The fracture position of the simulated sheet is concentrated at the punch fillet, and the fracture section is flat without obvious necking. The maximum thinning rate at the moment of sheet fracture is only 10.4%, so the fracture type is a shear one.

The simulation results are compared with the test results as shown in Table 7. When $R_p = 1$ mm, the error between the test forming depth and the simulated forming depth is only 4.2%. When $R_p = 3$ mm, the corresponding error is a maximum of 9.5%. The results show that the Lou-Huh ductile fracture criterion can relatively accurately predict the shear fracture behavior at a small bending fillet of the die during the stamping process of the DP780 sheet.

Table 7. Comparison of simulation and experimental forming results

R_p/t	Simulated forming depth	Test forming depth	Thinning rate	Fracture type	Error
1	7.5 mm	7.18 mm	10.4%	shear fracture	4.2%
3	8 mm	8.76 mm	9.3%	shear fracture	9.5%
5	11.4 mm	10.7 mm	9.4%	shear fracture	6.2%

5. Conclusion

Based on the uniaxial loading tests of four different specimens of advanced high-strength steel DP780, the hardening model of DP780 is studied first. The Lou-Huh, Cockcroft-Latham, and Rice-Tracey criteria for the ductile fracture are calibrated by the method of combining the test and FEM simulation, and the Lou-Huh criterion is used to predict the shear fracture of the DP780 sheet at a small bending fillet of the punch in the stretch-bending test. The specific conclusions are as follows:

- The Swift hardening criterion can accurately characterize the hardening behavior of the DP780 sheet before fracture. The Voce model can accurately predict the hardening behavior of DP780 sheets in uniform plastic sections, but it overestimates the flow stress of DP780 sheets under large strain conditions where the maximum error of the flow stress before fracture is more than 20%.
- Compared with the Cockcroft-Latham and Rice-Tracey criteria, the Lou-Huh ductile fracture criterion can more accurately predict the fracture behavior of DP780 tensile-shear specimens, and can more accurately predict the shear fracture of the DP780 sheet in the range of low-stress triaxiality (0.08-0.34). The results show that the combination of the Swift hardening law and Lou-Huh fracture criterion can provide accurate shear fracture prediction for the DP780 sheet metal.

Fundings

This work is supported by the National Natural Science Foundation of China under Grant (52302509, 52202512).

References

1. Banabic D., Barlat F., Cazacu O., Kuwabara T., 2020, Advances in anisotropy of plastic behaviour and formability of sheet metals, *International Journal of Material Forming*, **13**, 749-787

2. Clift S.E., Hartley P., Sturgess C.E.N., Rowe G.W., 1990, Fracture prediction in plastic deformation processes, *International Journal of Mechanical Sciences*, **32**, 1, 1-17

3. Cockcroft M.G., Latham D.J., 1968, Ductility and the workability of metals, *Journal Institute of Metals*, **96**, 33-39

4. Hill R.T., 1952, On discontinuous plastic states, with special reference to localized necking in thin sheets, *Journal of the Mechanics and Physics of Solids*, **1**, 1, 19-30

5. Hu X., Wilkinson D.S., Jain M., Mishra R.K., 2009, The influence of particle shape, volume fraction and distribution on post-necking deformation and fracture in uniaxial tension of AA5754 sheet materials, *International Journal of Solids and Structures*, **46**, 13, 2650-2658

6. Li H., Fu M.W., Lu J., Yang H., 2011a, Ductile fracture: Experiments and computations, *International Journal of Plasticity*, **27**, 2, 147-180

7. Li M., Zhao Y.X., Hu X., Huang S., 2011, Experimental study of shear fracture on advanced high strength dual-phase steels, *Journal of Shanghai Jiaotong University*, **45**, 11, 1695-1699

8. Lou Y., Huh H., Lim S., Pack, K., 2012, New ductile fracture criterion for prediction of fracture forming limit diagrams of sheet metals, *International Journal of Solids and Structures*, **49**, 25, 3605-3615

9. Luo M., Wierzbicki T., 2010, Numerical failure analysis of a stretch-bending test on dual-phase steel sheets using a phenomenological fracture model, *International Journal of Solids and Structures*, **47**, 22-23, 3084-3102

10. Marciniak Z., Kuczynski K., 1967, Limit strain in the process of stretch-forming sheet metals, *International Journal of Mechanical Sciences*, **9**, 9, 609-620

11. McClintock F.A., Kaplan S.M., Berg C.A., 1966, Ductile fracture by hole growth in shear bands, *International Journal of Fracture Mechanics*, **2**, 614-627

12. Oh S.I., Chen C.C., Kobayashi S., 1979, Ductile fracture in axisymmetric extrusion and drawing – Part 2: Workability in extrusion and drawing, *Journal of Engineering for Industry*, **101**, 1, 36-44

13. Ortiz M., Simo J.C., 1986, An analysis of a new class of integration algorithms for elastoplastic constitutive relations, *International Journal for Numerical Methods in Engineering*, **23**, 3, 353-366

14. Puttick K.E., 1959, Ductile fracture in metals, *Philosophical Magazine*, **4**, 44, 964-969

15. Qian L., Ji W., Wang X., Sun C., Ma T., 2020, Research on fracture mechanism and prediction of high-strength steel sheet under different stress states, *Chinese Journal of Mechanical Engineering*, **56**, 24, 72-80

16. Rice J.R., Tracey D.M., 1969, On the ductile enlargement of voids in triaxial stress fields, *Journal of the Mechanics and Physics of Solids*, **17**, 3, 201-217

17. Silva M.B., Skjødt M., Atkins A.G., Bay N., Martins P.A.F., 2008, Single-point incremental forming and formability-failure diagrams, *The Journal of Strain Analysis for Engineering Design*, **43**, 1, 15-35

18. Swift H., 1952, Plastic instability under plane stress, *Journal of the Mechanics and Physics of Solids*, **1**, 1, 1-18

19. Voce E., 1948, The relationship between stress and strain for homogeneous deformation, *Journal of the Institute of Metals*, **74**, 537-562

20. Zhou X., Wang L., Fan Q., Liu S., 2021, Research on prediction method of rolling force for high strength steel in tandem cold rolling mill, [In:] *2021 China Automation Congress (CAC)*, 2398-2403

Manuscript received July 2, 2023; accepted for print November 15, 2023

JOURNAL OF THEORETICAL AND APPLIED MECHANICS
62, 1, pp. 157-169, Warsaw 2024
https://doi.org/10.15632/jtam-pl/177173

ANALYSIS AND CALCULATION OF STRESS INTENSITY FACTORS FOR TYPE I CRACKS ON THE EDGE OF ELLIPTICAL HOLES UNDER INTERNAL PRESSURE

Shiwei Chen
College of Energy and Mining Engineering, Shandong University of Science and Technology, Qingdao, China
Minglu Xing
State Key Laboratory of Mining Disaster Prevention and Control Co-founded by Shandong Province and the Ministry of Science and Technology, Shandong University of Science and Technology, Qingdao, China, and
College of Energy and Mining Engineering, Shandong University of Science and Technology, Qingdao, China
Yaxin Liu
College of Energy and Mining Engineering, Shandong University of Science and Technology, Qingdao, China
e-mail: liuyaxinlyx0309@163.com
Yanchun Yin, Yurong Li
State Key Laboratory of Mining Disaster Prevention and Control Co-founded by Shandong Province and the Ministry of Science and Technology, Shandong University of Science and Technology, Qingdao, China, and
College of Energy and Mining Engineering, Shandong University of Science and Technology, Qingdao, China
Longfei Li
College of Energy and Mining Engineering, Shandong University of Science and Technology, Qingdao, China

The stress intensity factor and stress field expression for long cracks near an infinite-length plate bore are calculated using the Muskhelishvili Complex Function Approach. It applies to engineered bore edge cracks, especially under the condition in which the elliptical bore is subjected to internal pressure or only the surface of the crack is subjected to internal pressure. The formula is validated by numerical simulation and applies both to elliptical and circular holes. The variation of stress intensity factor with crack length is analyzed when the special round hole is only subjected to internal pressure. It has practical application value in fracture engineering.

Keywords: Muskhelishvili complex function, stress intensity factor, single elliptical fissure hole, numerical simulation

1. Introduction

In recent years, rock fragmentation by expansion is a common method of rock fragmentation in tunnel engineering (Guo *et al.*, 2017). It does not only cause rock fragmentation in a short period of time, but also allows secondary rock disintegration. Its economic advantages of environmental protection, efficiency and applicability have been widely recognized in engineering. During the formation period and excavation disturbance, a large number of cracks is generated in the rock mass, and the existence of cracks reduces mechanical strength and deformation resistance of the rock mass (Zhang *et al.*, 2022, 2023a). Hole-edge cracks are a commonly observed type of cracks in engineering structures. However, due to their discontinuous nature at the interface, analytical solutions are difficult to obtain directly. Fracture mechanics has made significant progress in both theoretical and numerical approaches over the years (Zhang *et al.*, 2023b; Alderliesten, 2007; Fett, 1992; Aliabadi *et al.*, 1987; Parker and Andrasic, 1983; Andrasic and Parker, 1984;

Bakuckas, 2001; Brennan and Ten, 2004; Chen *et al.*, 2001; Deng and Matsumoto, 2017). Bowie (1956, 1964) employed numerical techniques to compute the stress intensity factors of single--hole single-crack or single-hole double-crack configurations in an infinite flat plate subjected to uniaxial or biaxial loading.

Xu *et al.* (2018) employed a weight function closure method to address the opening displacement of a symmetrical double crack with a circular hole in an infinite flat plate under partial stress on the crack surface. They provided a crack surface displacement equation for partial cracks under uniform stress through fitting calculation results from the weight function method. Hasebe and Chen (1996) investigated the analytical solution of a single crack defect on the edge of a circular hole, assuming that the crack surface receives uniform internal pressure and the edge of the hole is free, using complex variable function methods and function theory methods. They provided an expression for the stress intensity factor. Zhao *et al.* (2012) utilized a complex function method, constructing a transcendental function to map a single crack on the edge of an elliptical hole onto a complex plane, and provided an expression for the stress intensity factor. Gao *et al.* (2003a,b) were the first to apply the Stroh formula to solve the exact problem of elliptical holes containing a single and two collinear permeable cracks in magnetoelectric elastomers, and their research results could serve as a benchmark for testing the effectiveness of analytical methods for solving more complex crack problems. Xu and Yang (2022) solved the anti-plane fracture problem of regular hexagonal hole edge cracks in composite materials using complex variable function methods and studied their crack propagation laws. Zhu *et al.* (2016) and Yan (2007) investigated the stress intensity factor and opening displacement of double cracks at the edge of an infinite flat plate under stress.

The above research results are all aimed at geometric forms of single or collinear cracks along the edge of the hole. Zhou *et al.* (2020) also used the finite-cut weight function method to solve the crack problem at the edge of the hole. However, for a single crack on the edge of an elliptical hole, there are two types of weight functions: analytical and numerical. Nonetheless, the accuracy of the horizontal weight functions derived from diverse analytical techniques considerably varies, necessitating stringent verification. As of now, there is currently limited literature on the exact analytical solution of a single crack problem on the edge of an elliptical hole.

This paper employs the Muskhelishvili Complex Function method and Cauchy integral theory along with the superposition principle of elasticity to calculate the stress intensity factor. Specifically, the stress intensity factor is calculated under the condition that only the circular hole is subject to a uniform force and the crack surface is not under stress. The Abaqus cloud image fusion method is used to solve and verify the stress intensity factor, which serves as a basis for predicting the fatigue growth life of the crack near the elliptical hole on an infinite plate.

2. Muskhelishvili complex function method

Assuming the presence of an ellipse in an isotropic infinite plane with a crack located on the edge of its hole, the surface of the hole is subjected to uniform internal pressure, while there is no force at infinity, as shown in Fig. 1.

The governing equation for this problem is

$$\nabla^2\nabla^2 U = 0 \tag{2.1}$$

where $\nabla^2 = \partial^2/\partial x^2 + \partial^2/\partial y^2$, U represents the Airy stress function, and

$$\sigma_{yy} = \frac{\partial^2 U}{\partial x^2} \qquad \sigma_{xx} = \frac{\partial^2 U}{\partial y^2} \qquad \sigma_{xy} = -\frac{\partial^2 U}{\partial x \partial y} \tag{2.2}$$

where σ_{ij} is the stress component.

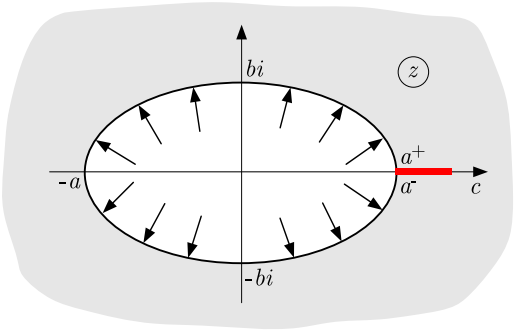

Fig. 1. Force diagram of an elliptical hole

According to literature (Bowie, 1964)

$$U(x,y) = \operatorname{Re}\left[\overline{z}\varphi_1(z) + \int \psi_1(z)\,dz\right] \tag{2.3}$$

where $\varphi_1(z)$ and $\psi_1(z)$ are two analytical functions representing the complex variable $z = x + \mathrm{i}y$, $\overline{z}$ is the conjugate of z; Re represents the real part of a complex number.

From the basic relationship of static elasticity and Eq. (2.3), the expressions for stress and displacement can be obtained as

$$\begin{aligned}
&\sigma_{xx} + \sigma_{yy} = 2[\varphi_1' + \overline{\varphi_1'(z)}] = 4\operatorname{Re}\varphi_1'(z)\\
&\sigma_{yy} - \sigma_{xx} + \mathrm{i}\sigma_{xy} = 2[\overline{z\varphi_1''(z)} + \psi_1'(z)]\\
&2\mu(u_x + \mathrm{i}u_y) = \kappa\varphi_1(z) - \overline{z\varphi(z)} - \overline{z\varphi_1'(z)} - \overline{\psi_1(z)}
\end{aligned} \tag{2.4}$$

where $\kappa = (3-v)/(1+v)$ represents the plane stress state, $\kappa = 3 - 4v$ represents the plane strain state.

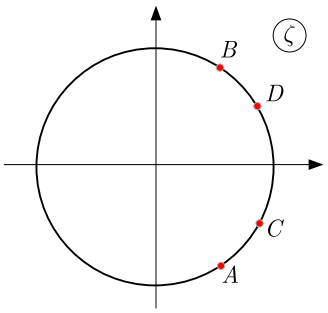

Fig. 2. Mapping from the elliptical to circular hole

If a suitable conformal mapping $z = \omega(\zeta)$ can be mapped, i.e. mapping the region on the physical plane z to the interior of the unit circle on the ζ plane (as shown in Fig. 2, then equations (2.1), (2.2) and (2.3) become

$$\begin{aligned}
&\sigma_\theta + \sigma_\rho = 4\operatorname{Re}\varphi(z)\\
&\sigma_\theta - \sigma_\rho - 2\mathrm{i}\tau_{\rho\theta} = \frac{2\zeta^2}{\rho^2\overline{\omega}'(\zeta)}[\overline{\omega}(\zeta)\phi'(\zeta) + \omega'(\zeta)\psi(\zeta)]\\
&\frac{E}{1+\mu}(u_\rho + \mathrm{i}u_\theta) = \frac{\overline{\zeta}}{\rho}\frac{\overline{\omega}'(\zeta)}{|\omega'(\zeta)|}\Big[\frac{3-\mu}{1+\mu}\varphi(\zeta) - \frac{\omega(\zeta)}{\overline{\omega}(\zeta)}\overline{\varphi}'(\zeta) - \overline{\psi}'(\zeta)\Big]
\end{aligned} \tag{2.5}$$

Among them, (ρ,θ) is ζ the polar coordinate of a plane, with

$$\begin{aligned}&\varphi_1(z)=\varphi_1[\omega(\zeta)]=\varphi(\zeta) \qquad \psi_1(z)=\psi_1[\omega(\zeta)]=\psi(z)\\&\varphi_1'(z)=\frac{\varphi'(\zeta)}{\omega'(\zeta)}=\phi(\zeta) \qquad \psi_1'(z)=\frac{\psi'(\zeta)}{\omega'(\zeta)}=\psi(\zeta)\end{aligned} \tag{2.6}$$

For the unknown functions $\varphi(\zeta)$ and $\psi(\zeta)$, the following functional equations (Fett, 1992) are satisfied

$$\begin{aligned}&\varphi(\zeta)=\frac{1+\mu}{8\pi}(f_x+\mathrm{i}f_y)\ln\zeta+B\omega(\zeta)+\varphi_0(\zeta)\\&\psi(\zeta)=-\frac{3-\mu}{8\pi}(f_x-\mathrm{i}f_y)\ln\zeta+(B'+\mathrm{i}C')\omega(\zeta)+\psi_0(\zeta)\end{aligned} \tag{2.7}$$

where f_x and f_y represent boundary conditions within the plane region, and B and $B'+\mathrm{i}C'$ represent boundary conditions at infinity, which are

$$B=\frac{1}{4}(\sigma_1+\sigma_2) \qquad B'+\mathrm{i}C'=-\frac{1}{2}(\sigma_1-\sigma_2)\mathrm{e}^{-2\mathrm{i}\alpha} \tag{2.8}$$

where α denotes the angle between the principal stress σ_1 at infinity and the Ox axis.

In equations (2.7), $\varphi_0(\zeta)$ and $\psi_0(\zeta)$, respectively

$$\begin{aligned}&\varphi_0(\zeta)+\frac{1}{2\pi\mathrm{i}}\int\limits_\sigma\frac{\overline{\omega(\sigma)}}{\omega'(\sigma)}\frac{\overline{\varphi_0'(\sigma)}}{\sigma-\zeta}\,d\sigma=\frac{1}{2\pi\mathrm{i}}\int\limits_\sigma\frac{f_0}{sigma-\zeta}\,d\sigma\\&\psi_0(\zeta)+\frac{1}{2\pi\mathrm{i}}\int\limits_\sigma\frac{\overline{\omega(\sigma)}}{\omega'(\sigma)}\frac{\overline{\varphi_0'(\sigma)}}{\sigma-\zeta}\,d\sigma=\frac{1}{2\pi\mathrm{i}}\int\limits_\sigma\frac{\overline{f}_0}{\sigma-\zeta}\,d\sigma\end{aligned} \tag{2.9}$$

where

$$f_0=\mathrm{i}\int(\overline{f}_x+\mathrm{i}\overline{f}_y)\,ds-\frac{f_x+\mathrm{i}f_y}{2\pi}\ln\sigma-\frac{1+\mu}{8\pi}(f_x-\mathrm{i}f_y)\frac{\omega(\sigma)}{\overline{\omega'(\sigma)}}-2B\omega(\sigma)-(B'-\mathrm{i}C')\overline{\omega}(\sigma) \tag{2.10}$$

Perform conformal mapping as follows (Deng and Matsumoto, 2017)

$$z=\omega(\zeta)=\frac{a+b}{2}\frac{1+\sqrt{\left(\frac{1+\zeta}{1-\zeta}\right)^2+k^2}}{1-\sqrt{\left(\frac{1+\zeta}{1-\zeta}\right)^2+k^2}}+\frac{a-b}{2}\frac{1-\sqrt{\left(\frac{1+\zeta}{1-\zeta}\right)^2+k^2}}{1+\sqrt{\left(\frac{1+\zeta}{1-\zeta}\right)^2+k^2}} \tag{2.11}$$

where

$$c+a=\alpha \qquad c-a=\beta \qquad k=\frac{\beta-b+\sqrt{\alpha\beta+b^2}}{\alpha+b+\sqrt{\alpha\beta+b^2}}$$

This mapping maps an infinite flat plate with a single cracked elliptical hole on the physical plane shown in Fig. 1 to the interior of the unit circle on the mathematical plane shown in Fig. 2, and has

$$\begin{aligned}&\omega^{-1}(-a)\to-1 \qquad \omega^{-1}(c)\to 1\\&\omega^{-1}(-bi)\to A \qquad \omega^{-1}(bi)\to B\end{aligned} \tag{2.12}$$

Thus, equations (2.9) can be solved under various boundary conditions.

After determining the function $\varphi(\zeta)$, one can obtain a very important physical quantity in fracture theory – the stress intensity factor.

The introduction of the complex stress intensity factor (Alderliesten, 2007) is

$$K_I^{(c,0)} - \mathrm{i}K_{II}^{(c,0)} = 2\sqrt{\pi}\lim_{\zeta\to 1}\sqrt{|\omega(\zeta)-c|}\frac{\varphi'(\zeta)}{\sqrt{\omega'(1)}} = 2\sqrt{\pi}\lim_{\zeta\to 1}\frac{\varphi'(\zeta)}{\sqrt{\omega''(1)}} \tag{2.13}$$

From here, it can be seen that as long as $\varphi'(\zeta)$ is determined, K_I and K_{II} can be obtained.

The following calculations are based on the specific boundary conditions of the problem. From equation (2.11), when $|\sigma| = 1$, $\omega(1/\sigma) = \omega(\sigma)$ can be obtained, where

$$H(\infty) = \frac{1}{2\pi\mathrm{i}}\int\limits_{\gamma}\frac{\omega(\sigma)}{\omega\left(\frac{1}{\sigma}\right)'}\varphi_0'\Big(\frac{1}{\sigma}\Big) \tag{2.14}$$

Then $H(\zeta)$ is analyzed outside the unit circle and can be extended to a continuous function on the circumference. It can be concluded that

$$\frac{1}{2\pi\mathrm{i}}\int\limits_{\gamma}\frac{\omega(\sigma)}{\omega\left(\frac{1}{\sigma}\right)'}\varphi_0'\Big(\frac{1}{\sigma}\Big) = H(\infty) = 0 \tag{2.15}$$

As shown in Fig. 3, first consider an infinite plate under uniform pressure at both elliptical and crack edges, with a pressure of q. In this case

$$f_0(\sigma) = -qz = -q\omega(\sigma) \qquad \varphi(\zeta) = \frac{q}{2\pi\mathrm{i}}\int\limits_{\gamma}\omega(\sigma)\frac{1}{\sigma-\zeta}\,d\sigma \tag{2.16}$$

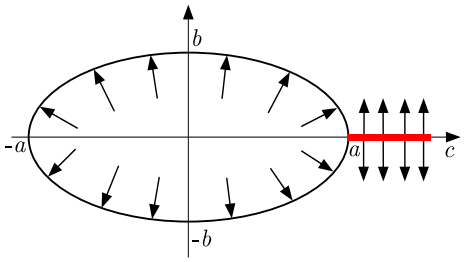

Fig. 3. Stress diagram of the ellipse with cracks

Due to the fact that there is no force on the boundary of the flat plate at infinity, and the forces on the elliptical hole and crack are balanced, the following holds

$$f_x = f_y = B = B' = C' = 0 \tag{2.17}$$

From equations $(2.7)_1$ and (2.11), it can be concluded that from equations $(2.7)_1$ and (2.11), one arrives at

$$\begin{aligned}\varphi_0'(\zeta) = \varphi'(\zeta) &= -\frac{p}{2\pi\mathrm{i}}\int\limits_{\gamma}\frac{\omega'(\sigma)}{\sigma-\zeta}\,d\sigma = \frac{a+b}{4}(g+1)\\ \lim_{\zeta\to 1}\frac{1}{\sqrt{\omega''(1)}} &= \frac{\sqrt{2(g^2-1)}}{\sqrt{(g+1)\Big[a(g^2-1)+bg\sqrt{g^2-1}\Big]}}\end{aligned} \tag{2.18}$$

where

$$g = \frac{(a+b)^2 + \Big(c+\sqrt{\alpha\beta+b^2}\Big)^2}{2(a+b)\Big(c+\sqrt{\alpha\beta+b^2}\Big)}$$

Replace Eqs. (2.9) with Eq. (2.14), and note that when both the hole and crack are subjected to uniform internal pressure, $K_{II}(c,0)=0$, there is

$$K_I'(c,0)=2\sqrt{\pi}\lim_{\zeta\to 1}\frac{\varphi_0'}{\sqrt{\omega''(1)}}=\frac{(a+b)p\sqrt{\pi(g+1)(g^2-1)}}{\sqrt{2\Big[a(g^2-1)+bg\sqrt{g^2-1}\Big]}} \tag{2.19}$$

for the case where only the crack surface is under pressure and the pore surface is not under force, as shown in Fig. 4. Their the elliptical hole edge crack is mapped to the mathematical plane through equation $(2.5)_3$. ζ is inside the unit circle above, and the lower bank a^- of the crack initiation point a is mapped to point C, and the upper bank a^+ of a is mapped to point D.

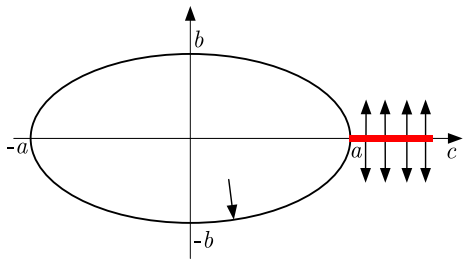

Fig. 4. Crack stress diagram only

On the arc segment of a^+ from the lower bank z_1 of a to the upper bank a^- counterclockwise, $f_1=-qz=-q\omega(\zeta)$, and on the arc segment of a^+ from the upper bank z_2 of a to the lower bank z_1 counterclockwise, $f_1=-qz_2$. The combined surface force acting on the crack at the edge of the hole is 0, and there is no force at infinity. According to equation $(2.18)_1$, it can be obtained

$$\varphi_{oL}(\zeta)=\frac{q}{2\pi \mathrm{i}}\int\limits_{AB}\omega(\sigma)\frac{1}{\sigma-\zeta}\,d\sigma+\frac{qz_2}{2\pi \mathrm{i}}\int\limits_{BA}\frac{1}{\sigma-\zeta}\,d\sigma \tag{2.20}$$

Similarly, according to Eq. (2.14), the stress intensity factor under uniform internal pressure can only be obtained on the crack surface

$$K_{I(OL)}^{(c,0)}=2\sqrt{\pi}\lim_{\zeta\to 1}\frac{\sqrt{2(g^2-1)}\frac{q}{2\pi \mathrm{i}}\int\limits_{AB}\frac{\omega(\sigma)'}{\sigma-\zeta}\,d\sigma}{\sqrt{(g+1)\Big[a(g^2-1)+bg\sqrt{g^2-1}\Big]}} \tag{2.21}$$

Using the superposition principle of elastic fracture mechanics (Alderliesten, 2007), subtract the crack stress intensity factor in Fig. 3 and the crack stress intensity factor in Fig. 4 to obtain the expression of the stress intensity factor in Fig. 1

$$K_{I(O)}^{(c,0)}=K_I^{(c,0)}-K_{I(OL)}^{(c,0)} \tag{2.22}$$

Substitute Eqs. (2.19) and (2.21) into Eq. (2.22) to obtain the stress intensity factor of the crack at the edge of an elliptical hole in an infinite flat plate under stress

$$K_{I(O)}^{(c,0)}=\frac{q\sqrt{\pi(g^2-1)}\Big[\alpha\sqrt{g+1}-\frac{q}{2\pi \mathrm{i}}\int\limits_{\gamma 12}\frac{\omega(\sigma)}{\sigma-\zeta}\,d\sigma\Big]}{\sqrt{2\Big[a(g^2-1)+bg\sqrt{g^2-1}\Big]}} \tag{2.23}$$

It is worth noting that when ζ is on the integration path, equation (2.14) is a singular integral equation, and the approximate calculation of the Cauchy principal value integral needs to be

considered. In this paper, singular point separation and a finite difference numerical method are used for calculation.

In order to clearly express the stress distribution near the crack tip, a polar coordinate system with the crack endpoint as the origin (commonly referred to as the crack leading edge coordinate system) $\zeta = re^{i\theta} = c + \zeta$ is introduced, so $z^2 - a^2 = (z+a)(z-a) = (2a+\zeta)\zeta$.

In the region near the crack end, $|\zeta| = r \ll 2a$, using the binomial theorem, expand the complex variable function of stress at the crack end within the convergence range of $|\zeta| < a$, to obtain

$$\begin{aligned}
\sigma_x &= \frac{K_I}{\sqrt{2\pi r}} \cos\frac{\theta}{2}\Big(1 - \sin\frac{\theta}{2}\sin\frac{3\theta}{2}\Big) + o(r^{-1/2}) \\
\sigma_y &= \frac{K_I}{\sqrt{2\pi r}} \cos\frac{\theta}{2}\Big(1 + \sin\frac{\theta}{2}\sin\frac{3\theta}{2}\Big) + o(r^{-1/2}) \\
\tau_{xy} &= \frac{K_I}{\sqrt{2\pi r}} \sin\frac{\theta}{2}\cos\frac{\theta}{2}\cos\frac{3\theta}{2}
\end{aligned} \tag{2.24}$$

3. Numerical calculation analysis

3.1. Calculation model

In order to verify the correctness of the analytical solution for the I stress intensity factor at the crack tip, a planar model was established using Abaqus to simulate and calculate the elliptical hole model with a single crack.

Considering that the plane model is an infinitely large flat plate, the size of the flat plate model differs significantly from the proportion of circular holes contained in the modeling process, far exceeding 100 times. Figure 5 shows the calculation model when $a = 4$, $b = 2$ and $c = 1$, with thick red lines indicating pre-fabricated cracks. The mesh type consists of tetrahedral elements, which is densely divided in the vicinity of circular holes and cracks. The boundary conditions of the model are completely fixed around the edges, while the edges of the elliptical hole are subjected to uniform internal pressure, and the cracks are not subjected to pressure. The concentric circle at the crack tip is the integral region of the cloud image.

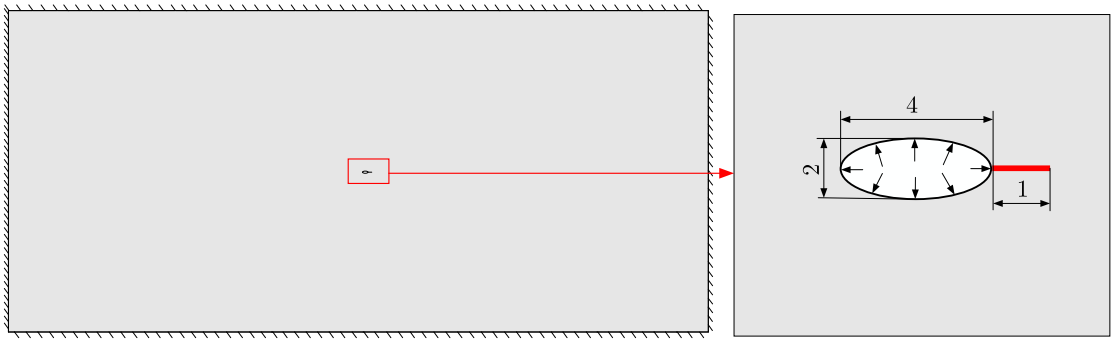

Fig. 5. Crack model, boundary conditions and a stress diagram

In order to reduce the influence of elliptical hole deformation on the calculation of stress intensity factors at the crack tip after loading, the material model of the flat plate is an elastic model, with an elastic modulus of 200 GPa and a Poisson's ratio of 0.25.

3.2. Analysis of the stress field at the crack tip of an elliptical hole

When $a = 4$, $b = 2$, $\beta = 1$, Fig. 6 shows the von Mises stress cloud map and an enlarged grid map of the crack tip finite element model calculated by the Abaqus numerical model.

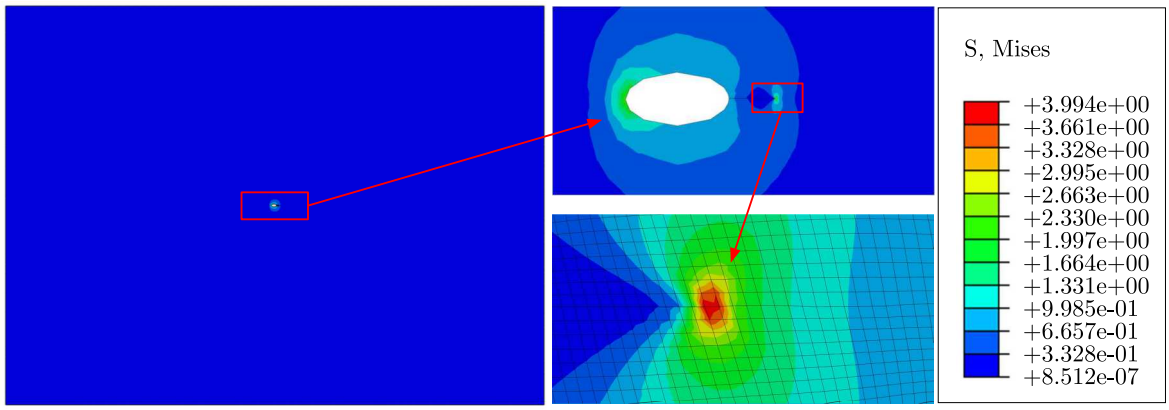

Fig. 6. Crack model and an enlarged stress cloud map of the endpoints

To more intuitively display the distribution law of the stress field at the crack tip of an elliptical hole, adjust the maximum stress values in each direction to be consistent with the von Mises stress, and then draw them separately σ_{xx}, σ_{yy} and τ_{xy}. The stress cloud diagram of τ_{xy} is shown in Figs. 7-9. From the figure, it can be seen that after the elliptical hole is loaded, the stress concentration area appears near the crack tip, and the stress cloud contour lines shown in Figs. 7-9 are consistent with equation (2.24), which is in agreement with the crack tip stress field shown in reference (Li *et al.*, 2010).

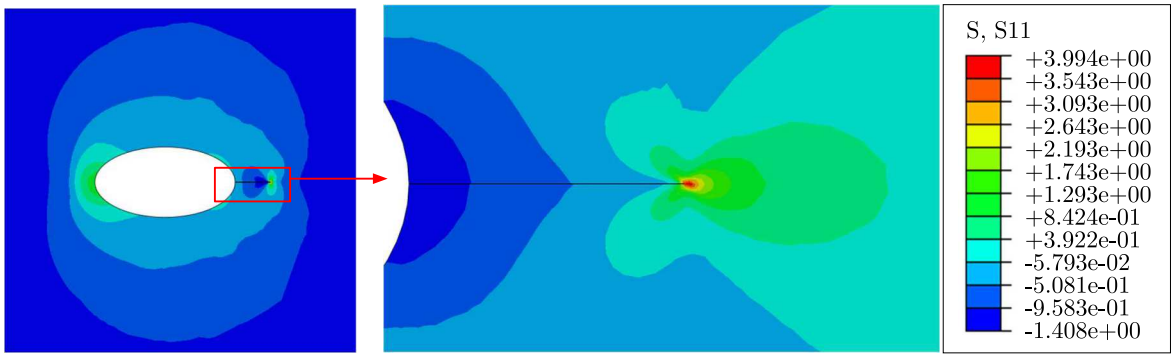

Fig. 7. σ_{xx} force cloud diagram

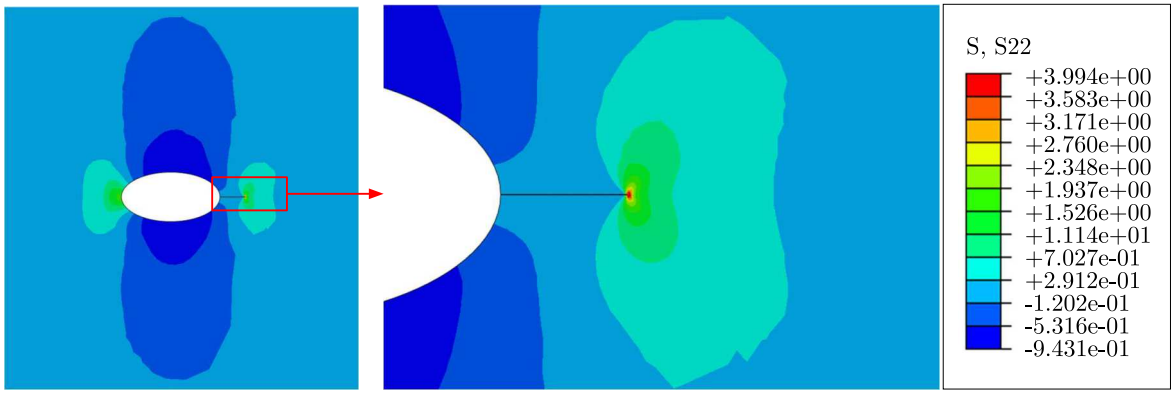

Fig. 8. σ_{yy} force cloud diagram

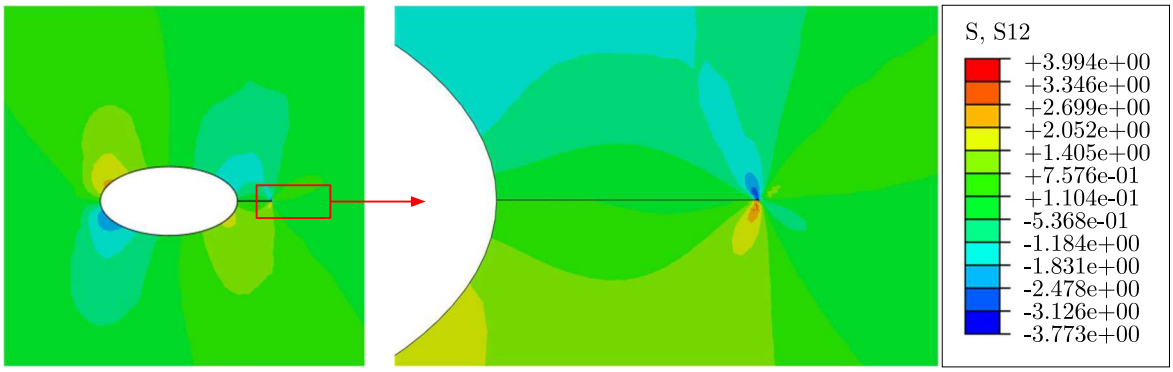

Fig. 9. τ_{xy} force cloud diagram

3.3. Analysis of factors influencing the crack tip intensity factor

To further explore the variation law of the stress intensity factor at the crack tip, it is calculated based on different lengths of elliptical hole edge cracks and elliptical hole flatness. For ease of calculation, the crack length and elliptical hole parameters are taken as dimensionless values. Figure 10 shows a comparison between the analytical and simulated solution of the stress intensity factor at the crack tip in function of crack length for elliptical holes $a = 2$, $b = 1$ and $q = 1$. As shown in the figure, as the crack length increases and the stress intensity factor error gradually decreases. The maximum error of the stress intensity factor shall not exceed 3%. This proves the correctness of the stress intensity factor for a single hole stress in this paper.

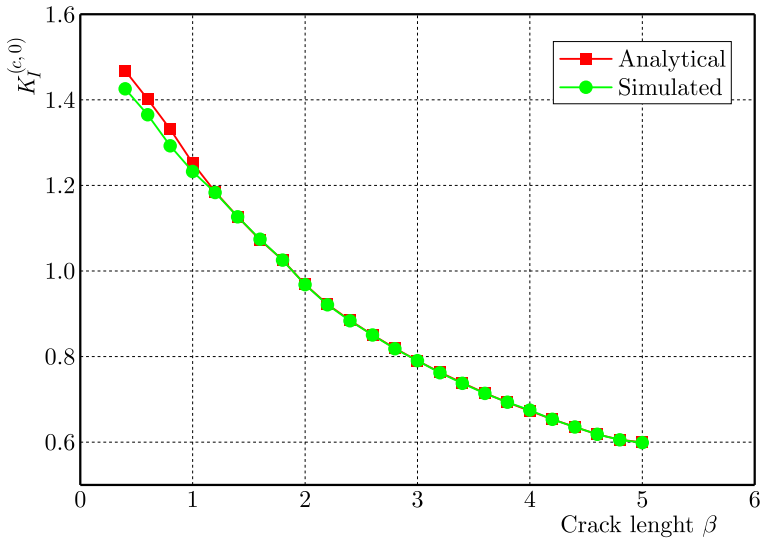

Fig. 10. Comparison of analytical and simulated solutions for stress intensity factor changes with crack length at $a = 2$ and $b = 1$

As illustrated in Fig. 11, by controlling the parameter b of the elliptical hole, while maintaining $c = 1$, $a = 1$ and $q = 1$, the calculated analytical solution is compared with the simulated solution. As shown in the figure, when the value of b increases, the stress intensity factor first increases slowly and does not change much. It reaches its maximum value when the value of b reaches about 0.55, and then rapidly decreases to a parabolic shape. Furthermore, when b approaches 0, the problem of elliptical holes with cracks degenerates into a classical problem of partial stress inside the crack. After calculation, the stress intensity factor at the tip is 0.677, which is consistent with the classical results in reference (Li *et al.*, 2010). The same conclusion can be drawn when the internal part of the crack is subjected to force.

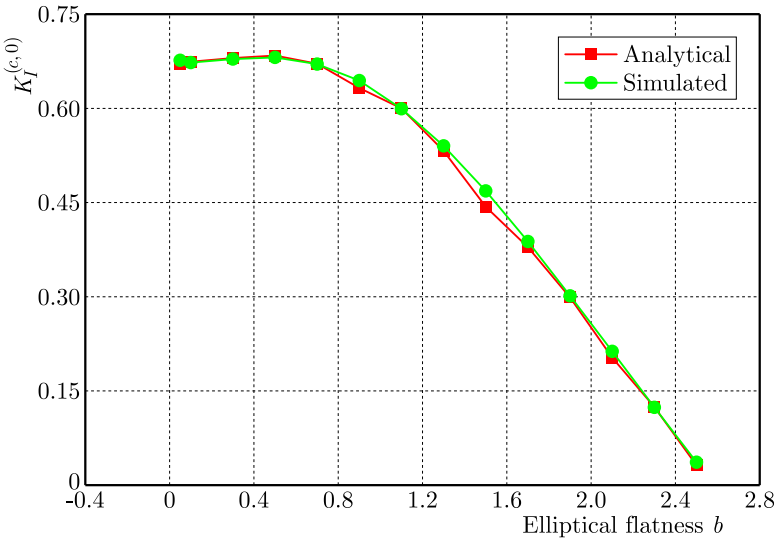

Fig. 11. Comparison of analytical and simulated solutions for a change in the crack tip intensity factor with elliptical flatness at $a = 1$, $\beta = 1$

When $a = b$, the problem of elliptical holes with cracks degenerates into a problem where a single circular hole is subjected to a force while the crack surface is not subjected to the force. A more extensive analysis of this issue is provided in this article. Figure 12 shows a comparison between the analytical and simulated solution of the stress intensity factor at the crack tip in function of the radius of the circular hole when the crack length $\beta = 1$ and $q = 1$. As shown in Fig. 12, when the radius of the circular hole increases, the rate of change of the stress intensity factor at the crack tip increases first and then decreases.

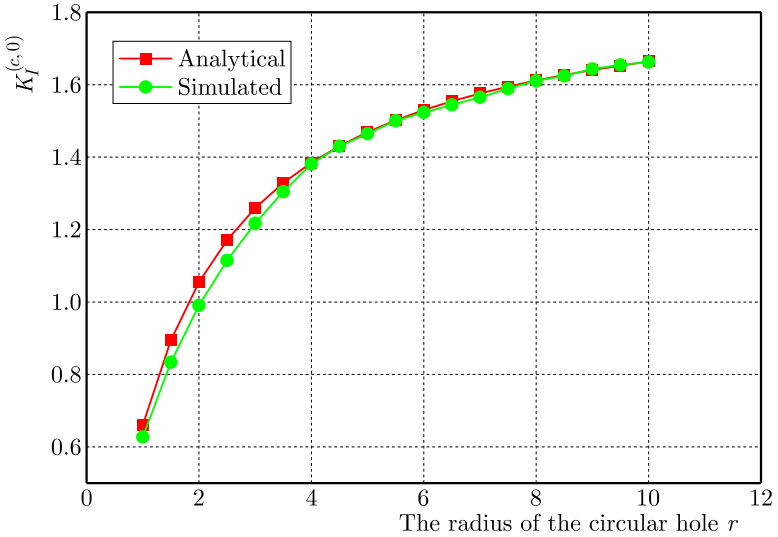

Fig. 12. Change of the stress intensity factor at the crack tips for different lengths with r at $\beta = 1$

Figure 13 shows a comparison between analytical and simulated solutions for variation patterns of the stress intensity factors under different conditions calculated using the method presented in this paper. As can be seen from Fig. 13, when the crack length changes, the stress intensity factor first increases rapidly to the peak and then slowly decreases. When a/β is about 0.5, the stress intensity factor reaches its peak.

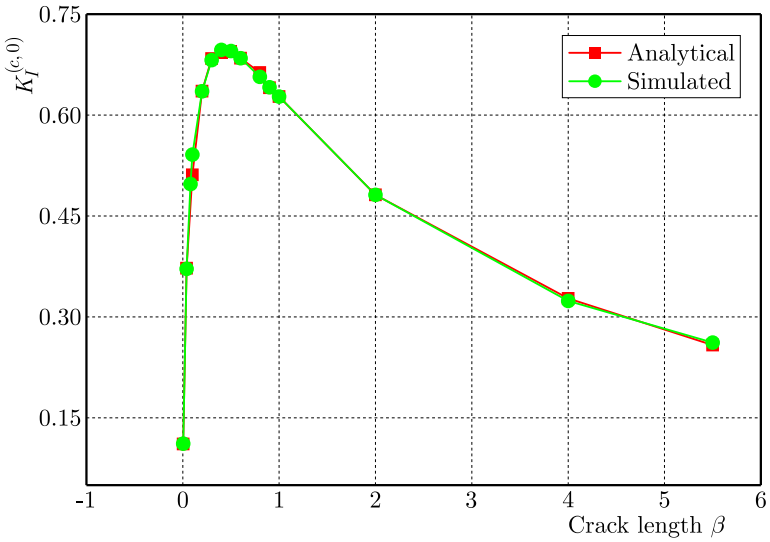

Fig. 13. Comparison of the analytical and simulated solutions for the stress intensity factor at the crack endpoint and crack length change at $a = 1$ and $b = 1$

4. Conclusion

- A transcendental function has been constructed using the Muskhelishvili method and number theory to solve the complex problem of elliptical holes with cracks. The analytical solution to the stress intensity factor at the crack tip has been obtained, which is a further extension of the Muskhelishvili complex function method and expands its application range.
- Verification based on an Abaqus numerical simulation method has been made, and the results showed that after the elliptical hole was loaded, the stress concentration area appeared near the crack tip. By comparing the analytical solution of the stress intensity factor at the crack tip with the corresponding simulated solution, the correctness of the analytical solution for a single hole under stress was confirmed.
- Further analysis was carried out on the influencing factors of the crack tip strength factor (elliptical hole edge crack length, elliptical hole flatness, circular hole radius): (1) when $a \neq b$, with the increase of short radius b, the stress intensity factor first slowly increases and does not change much, reaching its maximum value when b reaches around 0.55, and then rapidly decreases in a parabolic shape; (2) when $a = b$, as the radius of the circular hole increases, the rate of change of the stress intensity factor at the crack tip first increases and then decreases. When $a = b = 1$, the crack length changes, and the stress intensity factor first rapidly increases to the peak, then slowly decreases.

Acknowledgements

This research was supported by the National Natural Science Foundation of China (Grant No. 52074167) and the Natural Science Foundation of Shandong Province (Grant No. ZR2020QE135). The authors of this article are very grateful for the support provided.

References

1. Alderliesten R.C., 2007, On the available relevant approaches for fatigue crack propagation prediction in GLARE, *International Journal of Fatigue*, **29**, 2, 289-304

2. Aliabadi M.H., Rooke D.P., Cartwright D.J., 1987, An improved boundary element formulation for calculating stress intensity factors: Application to aerospace structures, *The Journal of Strain Analysis for Engineering Design*, **22**, 4, 203-207

3. Andrasic C.P., Parker A.P., 1984, Dimensionless stress intensity factors for cracked thick cylinders under polynomial crack face loadings, *Engineering Fracture Mechanics*, **19**, 1, 187-193

4. Bakuckas J.G., 2001, Comparison of boundary correction factor solutions for two symmetric cracks in a straight-shank hole, *Engineering Fracture Mechanics*, **68**, 9, 1095-1106

5. Bowie O.L., 1956, Analysis of an infinite plate containing radial cracks originating at the boundary of an internal cirular hole, *Journal of Mathematics and Physics*, **35**, 60

6. Bowie O.L., 1964, Rectangular tensile sheet with symmetric edge cracks, *Journal of Applied Mechanics*, **31**, 2, 208-212

7. Brennan F.P., Teh L.S., 2004, Determination of crack-tip stress intensity factors in complex geometries by the composition of constituent weight function solutions, *Fatigue and Fracture of Engineering Materials and Structures*, **27**, 1

8. Chen F., Sun Z., Xu J., 2001, Mode I fracture analysis of the double edge cracked Brazilian disk using a weight function method, *International Journal of Rock Mechanics and Mining Sciences*, **38**, 3, 475-479

9. Deng P., Matsumoto T., 2017, Weight function determinations for shear cracks in reinforced concrete beams based on finite element method, *Engineering Fracture Mechanics*, **177**, 61-78

10. Fett T., 1992, Direct determination of weight functions from reference loading cases and geometrical conditions, *Engineering Fracture Mechanics*, **42**, 3, 435-444

11. Gao C.F., Kessler H., Balke H., 2003a, Crack problems in magnetoelectroelastic solids. Part I: Exact solution of a crack, *International Journal of Engineering Science*, **41**, 9, 969-981

12. Gao C.F., Kessler H., Balke H., 2003b, Crack problems in magnetoelectroelastic solids. Part II: General solution of collinear cracks, *International Journal of Engineering Science*, **41**, 9, 983-994

13. Guo T., Qu Z., Gong F., Wang X., 2017, Numerical simulation of hydraulic fracture propagation guided by single radial boreholes, *Energies*, **10**, 10, 1680-1692

14. Hasebe N., Chen Y.Z., 1996, Stress intensity solutions for the interaction between a hole edge crack and a line crack, *International Journal of Fracture*, **77**, 351-366

15. Li S., He T., Yin X., *et al.*, 2010, *The Introduction of Rock Fracture Mechanics* (in Chinese), Hefei: University of Science and Technology of China Press

16. Parker A.P., Andrasic C.P., 1983, On the determination of stress intensity factors for cracked thick cylinders, *MRS Online Proceedings Library (OPL)*, **22**, 1, 227

17. Xu W., Wu X.R., Yu Y., Li Z.H., 2018, A weight function method for mixed modes hole-edge cracks, *Fatigue and Fracture of Engineering Materials and Structures*, **41**, 1, 223-234

18. Xu Y., Yang J., 2022, Anti-plane fracture problem of a regular hexagonal hole with radial edge cracks in piezoelectric/piezomagnetic composites (in Chinese), *Chinese Quarterly Of Mechanics*, **43**, 1, 149-158

19. Yan X., 2007, Rectangular tensile sheet with single edge crack or edge half-circular-hole crack, *Engineering Failure Analysis*, **14**, 7, 1406-1410

20. Zhang W., Guo W.Y., Wang Z.Q., 2022, Influence of lateral pressure on mechanical behavior of different rock types under biaxial compression, *Journal of Central South University*, **29**, 11, 3695-3705

21. Zhang W., Zhang B.L., Zhao T.B., 2023a, Study on the law of failure acoustic-thermal signal of weakly cemented fractured rock with diferent dip angles, *Rock Mechanics and Rock Engineering*, **56**, 6, 4557-4568

22. Zhang W., Zhao T.B., Zhang X.T., 2023b, Stability analysis and deformation control method of swelling soft rock roadway adjacent to chambers, *Geomechanics and Geophysics for Geo-Energy and Geo-Resources*, **9**, 1, 91

23. Zhao J., Xie L., Liu J., Zhao Q., 2012, A method for stress intensity factor calculation of infinite plate containing multiple hole-edge cracks, *International Journal of Fatigue*, **35**, 1, 2-9

24. Zhou J., Wang G., Li L., *et al.*, 2020, Truncated conformal mapping approach for four cracks with unequal length emanating from elliptical hole-edge in infinite plates (in Chinese), *Journal of Inner Mongolia Normal University (Natural Science Edition)*, **49**, 1, 35-38

25. Zhu Q., Han F., Sui M., 2016, Stress intensity factors and crack-surface opening displacements for two cracks emanating from a circular hole in an infinite plate, *Acta Aeronautica et Astronautica Sinica*, **37**, 3, 883-893

Manuscript received July 11, 2023; accepted for print December 1, 2023

JOURNAL OF THEORETICAL AND APPLIED MECHANICS
62, 1, pp. 171-185, Warsaw 2024
https://doi.org/10.15632/jtam-pl/178521

ELASTIC BUCKLING OF A RECTANGULAR SANDWICH PLATE WITH AN INDIVIDUAL FUNCTIONALLY GRADED CORE

Krzysztof Magnucki
Łukasiewicz Research Network – Poznan Institute of Technology, Poznan, Poland
Ewa Magnucka-Blandzi
Poznan University of Technology, Institute of Mathematics, Poznan, Poland
Krzysztof Sowiński
Poznan University of Technology, Institute of Applied Mechanics, Poznan, Poland
e-mail: krzysztof.sowinski@put.poznan.pl

This paper is devoted to a thin-walled sandwich plate with an individual functionally graded core. The nonlinear shear deformation theory of a straight normal line is applied. A system of three differential equations of equilibrium of this plate is obtained, based on the principle of stationary potential energy, which is reduced to two differential equations and solved analytically. The critical load of the rectangular sandwich plate is determined. A detailed analytical study is carried out for selected exemplary plates. Moreover, a numerical FEM model of this plate is developed. The results of these calculations are compared with each other.

Keywords: buckling, sandwich structures, shear deformation theory, functionally graded core

1. Introduction

Composite materials have attracted considerable interest in recent decades. Their properties, including a high strength-to-mass ratio and exceptional stiffness providing significant buckling resistance, allow designing of more effective structures. Unlike homogeneous materials, they are characterised by variable properties toward one or more specific directions, which, to some extent, can be controlled by manufacturing processes. It gives an opportunity to control their mechanical behaviour such as deformation or the dynamic response. These advantages make them highly desired structures in numerous branches of the industry, including the aerospace industry, biomedical engineering, civil and marine engineering.

The application of composites, including thin-walled sandwich structures and functionally graded materials (FGMs), requires appropriate tools to study and predict their behaviour. As classical beam, plate, and shell theories cannot capture their variable properties, it is necessary to formulate new theories and assess their accuracy. This topic gained significant attention; thus, many researchers are striving to provide more unified and general analytical formulations. In the last two decades, a significant advancement has been achieved in this field.

Yang and Qiao (2005) developed a higher-order impact model aiming to simulate the free--vibration response of a soft-core sandwich beam subjected to a foreign object impact. Carrera and Brischetto (2009) described a large variety of plate theories including higher-order, zig-zag, layerwise, and mixed theories to evaluate bending and vibration of sandwich structures. By performing an asymptotic analysis of three-dimensional linear elasticity, Berdichevsky (2010) developed a two-dimensional theory of sandwich plates. Bouazza *et al.* (2010) presented a numerical study on bending of symmetrically laminated plates, where attention was paid to the shear effect.

Meiche *et al.* (2011) proposed an enhanced theory of hyperbolic shear deformation that takes into account transverse shear deformation effects and may be used to analyse free vibration problems in thick, functionally graded sandwich panels. Mantari *et al.* (2012) proposed an innovative shear deformation theory for sandwich and composite plates that parameterized the displacement field. The authors demonstrated that their theory and three-dimensional elasticity-bending solutions were in good agreement.

Grover *et al.* (2013) presented a new inverse hyperbolic shear deformation theory and validated it for a variety of numerical examples of laminated composite and sandwich plates considering static and buckling responses. Lopatin and Morozov (2013) focused on solving the buckling problem of a uniformly compressed rectangular composite sandwich plate with varying boundary conditions. The authors referred to the Lagrange principle and the first-order shear deformation theory to formulate the variational buckling equation.

For the static analysis of laminated composite and sandwich panels, Sahoo and Singh (2014) introduced a novel inverse trigonometric zigzag theory that was elaborated in their paper. The theory assumed a higher-order displacement field that satisfied the continuity requirements at the layer interfaces across the thickness of the plate. Kołakowski and Mania (2015) investigated the dynamic interactive response of square FGM plates subjected to an in-plane pulse loading using the modified classical laminate plate theory. Marczak and Jędrysiak (2015) studied free vibration of periodic three-layered sandwich structures referring to the Kirchhoff thin plate theory and the tolerance averaging technique. Sobhy (2016) introduced a novel shear deformation plate theory to study hygrothermal vibration and buckling of FGM sandwich plates supported by an elastic foundation.

Bouzza and Benseddiq (2015) focused on analytical modelling of thermoelastic buckling behaviour of functionally graded rectangular plates using a hyperbolic shear deformation theory. Ellali *et al.* (2015) derived an exact analytical solution for mechanical buckling analysis of a megnetoelectroelastic plate resting on the Pasternak foundation referring to the third-order shear deformation plate theory. The use of sandwich structures and the current state of mathematical modelling were explored by Birman and Kardomateas (2018). The authors focused on various core types, development of nanotubes, intelligent materials, and functionally graded properties of sandwich structures.

Magnucki *et al.* (2019) studied buckling and vibration of a rectangular plate with symmetrically variable mechanical properties across its thickness. The proposed nonlinear deformation hypothesis was assumed, while the derivation was based on the Hamilton principle. Bouazza *et al.* (2019) investigated bending behaviour of laminated composite plates. They studied a multilayer plate by the shear deformation theory and finite element method. Adhikari *et al.* (2020) focused on modelling the effect of porosity-type defects and analysing their effect on buckling behaviour of various types of FGM sandwich combinations, including multiple arrangements of layers. Foroutan *et al.* (2021) developed a unified formulation of a fully geometrically nonlinear refined plate theory in a total Lagrangian approach. The study aimed to analyse the post-buckling and large deflection behaviour of a sandwich FGM plate with a porous core. Magnucka-Blandzi *et al.* (2021) studied bending and buckling problems for simply supported circular plates with mechanical properties that varied symmetrically in the thickness direction.

Magnucki and Magnucka-Blandzi (2021) devoted their work to generalisation of the analytical model of sandwich structures. A continuous variation of mechanical properties across the thickness was assumed, whereas the problem was formulated referring to the principle of stationary potential energy.

Aguib *et al.* (2021) studied buckling of a plate made of steel and a magnetorheological elastomer subject to a compressive load. Analytical models of sandwich beams, homogeneous beams with bisymmetric cross sections, and beams with symmetrically variable mechanical characteristics were presented by Magnucki (2022). They were developed utilising a novel shear deformation

theory that was inspired by the Zhuravsky shear stress formula. Katili *et al.* (2023) described the problem of buckling of FGM sandwich plates in the numerical FEM analysis. Magnucki *et al.* (2023) using the generalised theory of deformation studied the buckling problem of an axially compressed generalised cylindrical sandwich panel and a rectangular sandwich plate.

Many studies in the field of composite structures investigate the problem of buckling using a specific shear deformation theory, where the form of shear deformation function is assumed in advance, e.g. trigonometric, inverse trigonometric, hyperbolic, or inverse hyperbolic. In the presented paper, the buckling of a simply supported rectangular thin-walled plate of length a, width b, and total thickness h is resolved using the nonlinear shear deformation theory, where the shear deformation function is obtained analytically with consideration of the classical shear stress formula. In contrast to other shear deformation theories, in the presented formulation, the accuracy of the solution does not depend on the pre-defined shear deformation functions. Instead of predicting these functions here, the classical shear stress formula recalled by Magnucki (2022) is applied to analytically solve the shear deformation function. Moreover, the proposed formulation enables studying the composite structures with variable mechanical properties described by complex functions.

The plate is compressed in the middle plane with a uniformly distributed load of the intensities N_x and N_y (Fig. 1). Young's modulus of the core is assumed to be described by a parametric function that allows one to describe homogeneous, three-layer, and five-layer structures. This approach constitutes a generalisation of sandwich structures, which is possible by introducing an individual functionally graded core. The stiffness ratio between yjr layers can be optional, whereas transition of Young's modulus between them is smooth. The main objective of this paper is to develop analytical and numerical models and the determine the critical load of the plates.

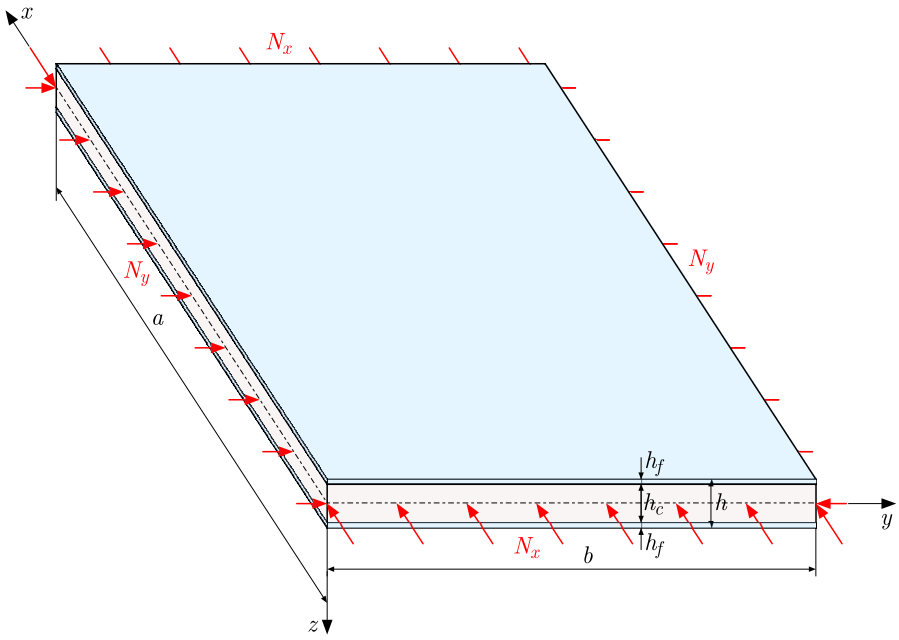

Fig. 1. Scheme of the rectangular sandwich plate compressed in the middle plane

The total thickness of the plate is the sum of the following layers

$$h = 2h_f + h_c \tag{1.1}$$

where: h_f – thicknesses of the faces, h_c – thickness of the core.

2. Analytical model of the rectangular sandwich plate

Young's modulus varies in the direction of thickness of the plate as follows:
— the upper face $(-1/2 \leqslant \zeta \leqslant -\chi_c/2)$ and the lower face $(\chi_c/2 \leqslant \zeta \leqslant 1/2)$

$$E_f(\zeta) = E_f = \text{const} \tag{2.1}$$

— the core $(-\chi_c/2 \leqslant \zeta \leqslant \chi_c/2)$

$$E_c(\zeta) = E_f f_c(\zeta) \tag{2.2}$$

where the dimensionless function is

$$f_c(\zeta) = e_c + (1 - e_c)\Big[\frac{1}{2} + \frac{1}{2}\cos\Big(4\pi\frac{\zeta}{\chi_c}\Big)\Big]^{n_e} - k\Big[\cos\Big(\pi\frac{\zeta}{\chi_c}\Big)\Big]^{10n_e} \tag{2.3}$$

and $\zeta = z/h$ denotes the dimensionless coordinate, $\chi_c = h_c/h$ – relative thickness of the core, e_c – coefficient of Young's modulus $(0 < e_c \ll 1)$, n_e – exponent-natural number, k – coefficient $(0 \leqslant k \leqslant 1 - e_c)$. An exemplary variation of Young's modulus in the direction of plate thickness is shown graphically in Fig. 2, assuming $e_c = 0.2$, $k = 0.1$, $n = 7$.

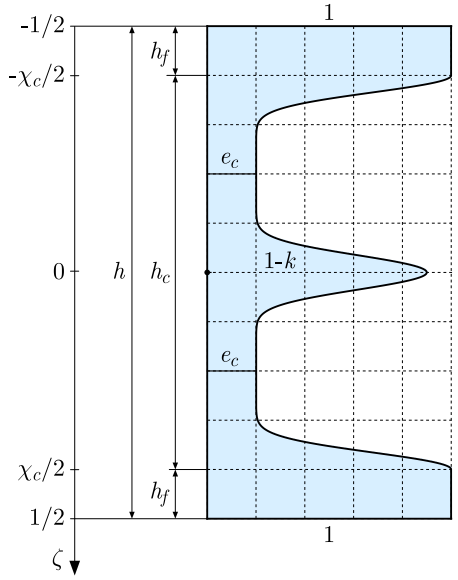

Fig. 2. Variation of Young's modulus in the direction of plate thickness

The deformation of the straight normal line to the neutral surface after buckling of this rectangular plate is shown in Fig. 3.

The longitudinal displacements according to Fig. 3 are as follows:
— the upper face $(-1/2 \leqslant \zeta \leqslant -\chi_c/2)$

$$\begin{aligned} u^{(uf)}(x,y,\zeta) &= -h\Big[\zeta\frac{\partial w}{\partial x} - f_d^{(uf)}(\zeta)\psi_f(x,y)\Big] \\ v^{(uf)}(x,y,\zeta) &= -h\Big[\zeta\frac{\partial w}{\partial y} - f_d^{(uf)}(\zeta)\varphi_f(x,y)\Big] \end{aligned} \tag{2.4}$$

— the core $(-\chi_c/2 \leqslant \zeta \leqslant \chi_c/2)$

$$\begin{aligned} u^{(c)}(x,y,\zeta) &= -h\Big[\zeta\frac{\partial w}{\partial x} - f_d^{(c)}(\zeta)\psi_f(x,y)\Big] \\ v^{(c)}(x,y,\zeta) &= -h\Big[\zeta\frac{\partial w}{\partial y} - f_d^{(c)}(\zeta)\varphi_f(x,y)\Big] \end{aligned} \tag{2.5}$$

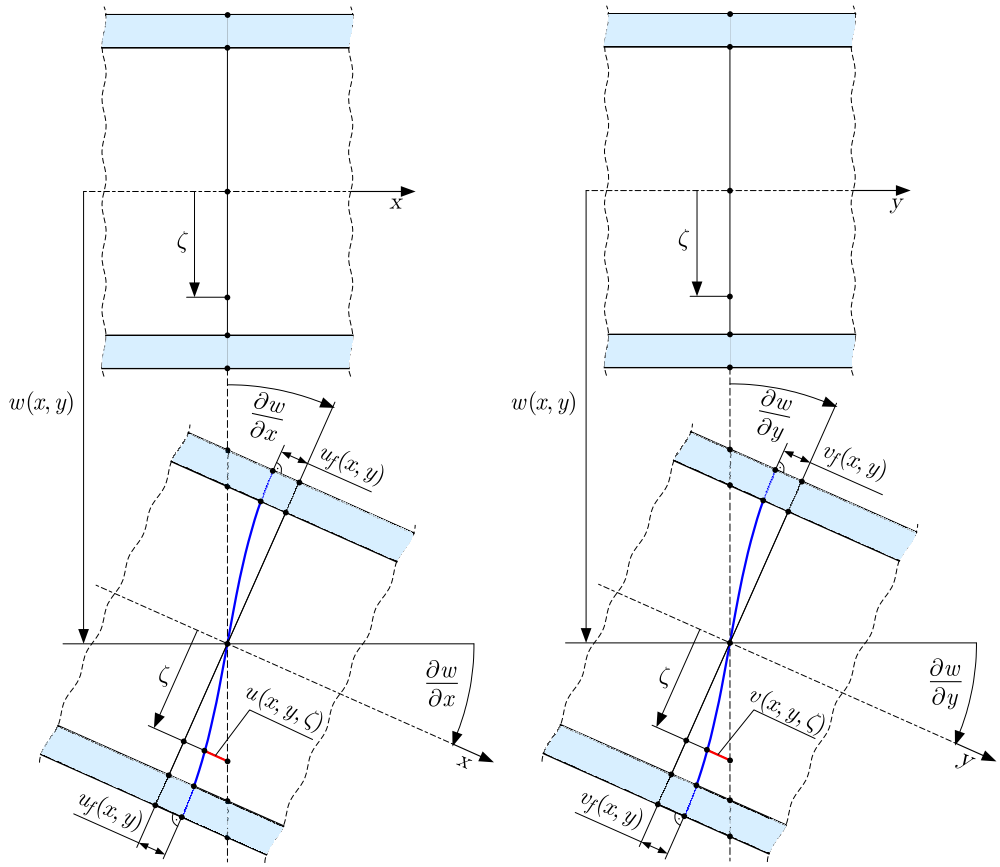

Fig. 3. The deformation scheme of the straight normal line of the plate

— the lower face ($\chi_c/2 \leqslant \zeta \leqslant 1/2$)

$$u^{(lf)}(x,y,\zeta) = -h\Big[\zeta\frac{\partial w}{\partial x} - f_d^{(lf)}(\zeta)\psi_f(x,y)\Big]$$
$$v^{(lf)}(x,y,\zeta) = -h\Big[\zeta\frac{\partial w}{\partial y} - f_d^{(lf)}(\zeta)\varphi_f(x,y)\Big] \tag{2.6}$$

where: $w(x,y)$ – deflection, $\psi_f(x,y) = u_f(x,y)/h$ and $\varphi_f(x,y) = v_f(x,y)/h$ – dimensionless displacement functions of the faces. Moreover, taking into account the papers by Magnucki (2022) and Magnucki *et al.* (2023), the dimensionless deformation functions of the straight normal line in the successive layers are of the form

$$f_d^{(uf)}(\zeta) = -C_f + \frac{1}{24}(3-4\zeta^2)\zeta \qquad f_d^{(c)}(\zeta) = \int \frac{\overline{Q}_z^{(c)}(\zeta)}{f_c(\zeta)}\,d\zeta$$
$$f_d^{(lf)}(\zeta) = C_f + \frac{1}{24}(3-4\zeta^2)\zeta \tag{2.7}$$

where

$$\overline{Q}_z^{(c)}(\zeta) = \frac{1}{8}[1-\chi_c^2 + e_c(\chi_c^2 - 4\zeta^2)] - (1-e_c)J_1(\zeta) + kJ_2(\zeta)$$
$$J_1(\zeta) = \int_{-\chi_c/2}^{\zeta}\Big[\frac{1}{2} + \frac{1}{2}\cos\Big(4\frac{\pi}{\chi_c}\zeta_1\Big)\Big]^{n_e}\zeta_1\,d\zeta_1$$

$$J_2(\zeta) = \int\limits_{-\chi_c/2}^{\zeta} \Big[\cos\Big(\frac{\pi}{\chi_c}\zeta_1\Big)\Big]^{10n_e} \zeta_1 \, d\zeta_1$$

$$C_f = -\frac{1}{48}(3-\chi_c^2)\chi_c + \int\limits_0^{\chi_c/2} \frac{\overline{Q}_z^{(c)}(\zeta)}{f_c(\zeta)} \, d\zeta$$

Thus, the strains can be described in the following manner.
— the upper face $(-1/2 \leqslant \zeta \leqslant -\chi_c/2)$

$$\begin{aligned}
&\varepsilon_x^{(uf)}(x,y,\zeta) = -h\Big[\zeta\frac{\partial^2 w}{\partial x^2} - f_d^{(uf)}(\zeta)\frac{\partial \psi_f}{\partial x}\Big] \\
&\varepsilon_y^{(uf)}(x,y,\zeta) = -h\Big[\zeta\frac{\partial^2 w}{\partial y^2} - f_d^{(uf)}(\zeta)\frac{\partial \varphi_f}{\partial y}\Big] \\
&\gamma_{xy}^{(uf)}(x,y,\zeta) = -h\Big[2\zeta\frac{\partial^2 w}{\partial x \partial y} - f_d^{(uf)}(\zeta)\Big(\frac{\partial \psi_f}{\partial y} + \frac{\partial \varphi_f}{\partial x}\Big)\Big] \\
&\gamma_{xz}^{(uf)}(x,y,\zeta) = \frac{df_d^{(uf)}}{d\zeta}\psi_f(x,y) \qquad \gamma_{yz}^{(uf)}(x,y,\zeta) = \frac{df_d^{(uf)}}{d\zeta}\varphi_f(x,y)
\end{aligned} \tag{2.8}$$

— the core $(-\chi_c/2 \leqslant \zeta \leqslant \chi_c/2)$

$$\begin{aligned}
&\varepsilon_x^{(c)}(x,y,\zeta) = -h\Big[\zeta\frac{\partial^2 w}{\partial x^2} - f_d^{(c)}(\zeta)\frac{\partial \psi_f}{\partial x}\Big] \qquad \varepsilon_y^{(c)}(x,y,\zeta) = -h\Big[\zeta\frac{\partial^2 w}{\partial y^2} - f_d^{(c)}(\zeta)\frac{\partial \varphi_f}{\partial y}\Big] \\
&\gamma_{xy}^{(c)}(x,y,\zeta) = -h\Big[2\zeta\frac{\partial^2 w}{\partial x \partial y} - f_d^{(c)}(\zeta)\Big(\frac{\partial \psi_f}{\partial y} + \frac{\partial \varphi_f}{\partial x}\Big)\Big] \\
&\gamma_{xz}^{(c)}(x,y,\zeta) = \frac{df_d^{(c)}}{d\zeta}\psi_f(x,y) \qquad \gamma_{yz}^{(c)}(x,y,\zeta) = \frac{df_d^{(c)}}{d\zeta}\varphi_f(x,y)
\end{aligned} \tag{2.9}$$

— the lower face $(\chi_c/2 \leqslant \zeta \leqslant 1/2)$

$$\begin{aligned}
&\varepsilon_x^{(lf)}(x,y,\zeta) = -h\Big[\zeta\frac{\partial^2 w}{\partial x^2} - f_d^{(lf)}(\zeta)\frac{\partial \psi_f}{\partial x}\Big] \\
&\varepsilon_y^{(lf)}(x,y,\zeta) = -h\Big[\zeta\frac{\partial^2 w}{\partial y^2} - f_d^{(lf)}(\zeta)\frac{\partial \varphi_f}{\partial y}\Big] \\
&\gamma_{xy}^{(lf)}(x,y,\zeta) = -h\Big[2\zeta\frac{\partial^2 w}{\partial x \partial y} - f_d^{(lf)}(\zeta)\Big(\frac{\partial \psi_f}{\partial y} + \frac{\partial \varphi_f}{\partial x}\Big)\Big] \\
&\gamma_{xz}^{(lf)}(x,y,\zeta) = \frac{df_d^{(lf)}}{d\zeta}\psi_f(x,y) \qquad \gamma_{yz}^{(lf)}(x,y,\zeta) = \frac{df_d^{(lf)}}{d\zeta}\varphi_f(x,y)
\end{aligned} \tag{2.10}$$

Consequently, the stresses are derived:
— the upper face $(-1/2 \leqslant \zeta \leqslant -\chi_c/2)$

$$\begin{aligned}
&\sigma_x^{(uf)}(x,y,\zeta) = \frac{E_f}{1-\nu^2}[\varepsilon_x^{(uf)}(x,y,\zeta) + \nu\varepsilon_y^{(uf)}(x,y,\zeta)] \\
&\sigma_y^{(uf)}(x,y,\zeta) = \frac{E_f}{1-\nu^2}[\varepsilon_y^{(uf)}(x,y,\zeta) + \nu\varepsilon_x^{(uf)}(x,y,\zeta)] \\
&\tau_{xy}^{(uf)}(x,y,\zeta) = \frac{E_f}{2(1+\nu)}\gamma_{xy}^{(uf)}(x,y,\zeta) \qquad \tau_{xz}^{(uf)}(x,y,\zeta) = \frac{E_f}{2(1+\nu)}\gamma_{xz}^{(uf)}(x,y,\zeta) \\
&\tau_{yz}^{(uf)}(x,y,\zeta) = \frac{E_f}{2(1+\nu)}\gamma_{yz}^{(uf)}(x,y,\zeta)
\end{aligned} \tag{2.11}$$

— the core $(-\chi_c/2 \leqslant \zeta \leqslant \chi_c/2)$

$$\begin{aligned}
\sigma_x^{(c)}(x,y,\zeta) &= \frac{E_f}{1-\nu^2}[\varepsilon_x^{(c)}(x,y,\zeta) + \nu\varepsilon_y^{(c)}(x,y,\zeta)]f_c(\zeta)\\
\sigma_y^{(c)}(x,y,\zeta) &= \frac{E_f}{1-\nu^2}[\varepsilon_y^{(c)}(x,y,\zeta) + \nu\varepsilon_x^{(c)}(x,y,\zeta)]f_c(\zeta)\\
\tau_{xy}^{(c)}(x,y,\zeta) &= \frac{E_f}{2(1+\nu)}\gamma_{xy}^{(c)}(x,y,\zeta)f_c(\zeta)\\
\tau_{xz}^{(c)}(x,y,\zeta) &= \frac{E_f}{2(1+\nu)}\gamma_{xz}^{(c)}(x,y,\zeta)f_c(\zeta)\\
\tau_{yz}^{(c)}(x,y,\zeta) &= \frac{E_f}{2(1+\nu)}\gamma_{yz}^{(c)}(x,y,\zeta)f_c(\zeta)
\end{aligned} \tag{2.12}$$

— the lower face $(\chi_c/2 \leqslant \zeta \leqslant 1/2)$

$$\begin{aligned}
\sigma_x^{(lf)}(x,y,\zeta) &= \frac{E_f}{1-\nu^2}[\varepsilon_x^{(lf)}(x,y,\zeta) + \nu\varepsilon_y^{(lf)}(x,y,\zeta)]\\
\sigma_y^{(lf)}(x,y,\zeta) &= \frac{E_f}{1-\nu^2}[\varepsilon_y^{(lf)}(x,y,\zeta) + \nu\varepsilon_x^{(lf)}(x,y,\zeta)]\\
\tau_{xy}^{(lf)}(x,y,\zeta) &= \frac{E_f}{2(1+\nu)}\gamma_{xy}^{(lf)}(x,y,\zeta) \qquad \tau_{xz}^{(lf)}(x,y,\zeta) = \frac{E_f}{2(1+\nu)}\gamma_{xz}^{(lf)}(x,y,\zeta)\\
\tau_{yz}^{(lf)}(x,y,\zeta) &= \frac{E_f}{2(1+\nu)}\gamma_{yz}^{(lf)}(x,y,\zeta)
\end{aligned} \tag{2.13}$$

where Poisson's ν ratio is constant for this plate.

3. The analytical study of the elastic buckling of the plate

The elastic strain energy of the plate

$$U_{\varepsilon,\gamma} = \frac{E_f h}{2(1-\nu^2)}\int_0^a\int_0^b [\Phi_{\varepsilon,\gamma}^{(uf)}(x,y) + \Phi_{\varepsilon,\gamma}^{(c)}(x,y) + \Phi_{\varepsilon,\gamma}^{(lf)}(x,y)]\,dx\,dy \tag{3.1}$$

where

$$\begin{aligned}
\Phi_{\varepsilon,\gamma}^{(uf)}(x,y) &= \Phi_{\varepsilon}^{(uf)}(x,y) + \Phi_{\gamma}^{(uf)}(x,y)\\
\Phi_{\varepsilon}^{(uf)}(x,y) &= \int_{-1/2}^{-\chi_c/2}\left\{[\varepsilon_x^{(uf)}(x,y,\zeta)]^2 + 2\nu\varepsilon_x^{(uf)}(x,y,\zeta)\varepsilon_y^{(uf)}(x,y,\zeta) + [\varepsilon_y^{(uf)}(x,y,\zeta)]^2\right\}d\zeta\\
\Phi_{\gamma}^{(uf)}(x,y) &= \frac{1-\nu}{2}\int_{-1/2}^{-\chi_c/2}\left\{[\gamma_{xy}^{(uf)}(x,y,\zeta)]^2 + [\gamma_{xz}^{(uf)}(x,y,\zeta)]^2 + [\gamma_{yz}^{(uf)}(x,y,\zeta)]^2\right\}d\zeta\\
\Phi_{\varepsilon,\gamma}^{(c)}(x,y) &= \Phi_{\varepsilon}^{(c)}(x,y) + \Phi_{\gamma}^{(c)}(x,y) \qquad \Phi_{\varepsilon,\gamma}^{(lf)}(x,y) = \Phi_{\varepsilon}^{(lf)}(x,y) + \Phi_{\gamma}^{(lf)}(x,y)\\
\Phi_{\varepsilon}^{(c)}(x,y) &= \int_{-1/2}^{-\chi_c/2}\left\{[\varepsilon_x^{(c)}(x,y,\zeta)]^2 + 2\nu\varepsilon_x^{(c)}(x,y,\zeta)\varepsilon_y^{(c)}(x,y,\zeta) + [\varepsilon_y^{(c)}(x,y,\zeta)]^2\right\}f_c(\zeta)\,d\zeta
\end{aligned}$$

$$\Phi_{\gamma}^{(c)}(x,y) = \frac{1-\nu}{2}\int\limits_{-1/2}^{-\chi_c/2}\Big\{[\gamma_{xy}^{(c)}(x,y,\zeta)]^2 + [\gamma_{xz}^{(c)}(x,y,\zeta)]^2 + [\gamma_{yz}^{(c)}(x,y,\zeta)]^2\Big\}f_c(\zeta)\,d\zeta$$

$$\Phi_{\varepsilon}^{(lf)}(x,y) = \int\limits_{-1/2}^{-\chi_c/2}\Big\{[\varepsilon_x^{(lf)}(x,y,\zeta)]^2 + 2\nu\varepsilon_x^{(lf)}(x,y,\zeta)\varepsilon_y^{(lf)}(x,y,\zeta) + [\varepsilon_y^{(lf)}(x,y,\zeta)]^2\Big\}\,d\zeta$$

$$\Phi_{\gamma}^{(lf)}(x,y) = \frac{1-\nu}{2}\int\limits_{-1/2}^{-\chi_c/2}\Big\{[\gamma_{xy}^{(lf)}(x,y,\zeta)]^2 + [\gamma_{xz}^{(lf)}(x,y,\zeta)]^2 + [\gamma_{yz}^{(lf)}(x,y,\zeta)]^2\Big\}\,d\zeta$$

The work of the load is

$$W = \frac{1}{2}\int\limits_0^a\int\limits_0^b\Big[N_x\Big(\frac{\partial w}{\partial x}\Big)^2 + N_y\Big(\frac{\partial w}{\partial y}\Big)^2\Big]\,dx\,dy \tag{3.2}$$

Based on the principle of stationary total potential energy $\delta(U_{\varepsilon,\gamma} - W) = 0$ with consideration of the expressions in Eqs. (3.1) and (3.2), after integration and simple transformation, three differential equations of equilibrium of this rectangular sandwich plate are obtained in the following form

$$\begin{aligned}
&D_o\Big\{C_{ww}\nabla^4 w(x,y) - C_{w\theta}\Big[\frac{\partial}{\partial x}\nabla^2\psi_f(x,y) + \frac{\partial}{\partial y}\nabla^2\varphi_f(x,y)\Big]\Big\} + N_x\frac{\partial^2 w}{\partial x^2} + N_y\frac{\partial^2 w}{\partial y^2} = 0\\
&C_{w\theta}\frac{\partial}{\partial x}\nabla^2 w(x,y) - C_{\theta\theta}\Big[\frac{\partial^2\psi_f}{\partial x^2} + \frac{1-\nu}{2}\frac{\partial^2\psi_f}{\partial y^2} + \frac{1+\nu}{2}\frac{\partial^2\varphi_f}{\partial x\partial y}\Big] + C_\theta\frac{\psi_f(x,y)}{h^2} = 0\\
&C_{w\theta}\frac{\partial}{\partial y}\nabla^2 w(x,y) - C_{\theta\theta}\Big[\frac{1+\nu}{2}\frac{\partial^2\psi_f}{\partial x\partial y} + \frac{1-\nu}{2}\frac{\partial^2\varphi_f}{\partial x^2} + \frac{\partial^2\varphi_f}{\partial y^2}\Big] + C_\theta\frac{\varphi_f(x,y)}{h^2} = 0
\end{aligned} \tag{3.3}$$

where the dimensionless coefficients are

$$C_{ww} = 1 - \chi_c^3 + 12\int\limits_{-\chi_c/2}^{\chi_c/2}\zeta^2 f_c(\zeta)\,d\zeta$$

$$C_{\theta\theta} = 12\Bigg(2\int\limits_{-\chi_c/2}^{1/2}[f_d^{(lf)}(\zeta)]^2\,d\zeta + \int\limits_{-\chi_c/2}^{\chi_c/2}[f_d^{(c)}(\zeta)]^2 f_c(\zeta)\,d\zeta\Bigg)$$

$$C_{w\theta} = 3(1-\chi_c^2)C_f + \frac{1}{40}(4 - 5\chi_c^3 + \chi_c^5) + 12\int\limits_{-\chi_c/2}^{\chi_c/2}\zeta f_d^{(c)}(\zeta)f_c(\zeta)\,d\zeta$$

$$C_\theta = \frac{1-\nu}{2}\Bigg(\frac{1}{80}(8 - 15\chi_c + 10\chi_c^3 - 3\chi_c^5) + 12\int\limits_{-\chi_c/2}^{\chi_c/2}\frac{[\overline{Q}_z^{(c)}(\zeta)]^2}{f_c(\zeta)}\,d\zeta\Bigg)$$

and

$$D_o = \frac{E_f h^3}{12(1-\nu^2)}\ [\mathrm{Nmm}]$$

Taking into account the papers by Magnucki *et al.* (2019) as well as Magnucki and Magnucka-Blandzi (2021), two unknown dimensionless displacement functions of the faces are assumed as follows

$$\psi_f(x,y) = \frac{\partial\theta}{\partial x} \qquad \varphi_f(x,y) = \frac{\partial\theta}{\partial y} \tag{3.4}$$

where $\theta(x,y)$ [mm] is the generalised displacement. Thus, the three differential equations of equilibrium convert into the following two equations

$$\begin{aligned} &D_o[C_{ww}\nabla^4 w(x,y) - C_{w\theta}\nabla^4\theta(x,y)] + N_x\frac{\partial^2 w}{\partial x^2} + N_y\frac{\partial^2 w}{\partial y^2} = 0 \\ &C_{w\theta}\nabla^2 w(x,y) - C_{\theta\theta}\nabla^2\theta(x,y) + C_\theta\frac{\theta(x,y)}{h^2} = 0 \end{aligned} \tag{3.5}$$

These equations are approximately solved, and so two typical unknown functions describing the shape of the deformed structure are assumed in a general form as follows

$$w(x,y) = w_a \sin\Big(m\pi\frac{x}{a}\Big)\sin\Big(n\pi\frac{y}{b}\Big) \qquad \theta(x,y) = \theta_a \sin\Big(m\pi\frac{x}{a}\Big)\sin\Big(n\pi\frac{y}{b}\Big) \tag{3.6}$$

where: w_a [mm], θ_a [mm] – coefficients of these functions, m, n – natural numbers.

Substituting these functions into Eqs. (3.5), after simple transformations, one obtains

$$\theta_a = \frac{C_{w\theta}}{C_{\theta\theta} + \frac{ab}{\pi^2 h^2 a_{mn}} C_\theta} w_a \qquad m^2\frac{b}{a}N_x + n^2\frac{a}{b}N_y = \frac{\pi^2}{ab}(1 - C_{se})\alpha_{mn}^2 D_p \tag{3.7}$$

where the dimensionless coefficient is expressed as

$$\alpha_{mn} = m^2\frac{b}{a} + n^2\frac{a}{b}$$

and $D_p = C_{ww}C_o$ [Nmm] is the flexural rigidity of this plate, while the coefficient of the shear effect is

$$C_{se} = \frac{\pi^2\alpha_{mn}}{\pi^2\alpha_{mn}C_{\theta\theta} + \frac{ab}{h^2}C_\theta}\frac{C_{w\theta}^2}{C_{ww}} \tag{3.8}$$

Moreover, for further study, the plate load is assumed in the following form

$$N_x = c_x N_o \qquad N_y = c_y N_o \tag{3.9}$$

where: c_x and c_y are positive dimensionless coefficients. Thus, the critical load is as follows

$$N_{0,CR} = \min_{m,n}\Big[(1 - C_{se})\frac{\alpha_{mn}^2}{\alpha_N}\Big]\frac{\pi^2 D_p}{ab} \tag{3.10}$$

where another dimensionless coefficient is introduced

$$\alpha_N = m^2\frac{b}{a}c_x + n^2\frac{a}{b}c_y$$

Consequently, the critical load of the square plate ($b = a$, $m = n = 1$, $\alpha_{mn} = 2$) is in the form

$$N_{0,CR} = 4\pi^2\frac{1 - C_{se}}{c_x + c_y}\frac{D_p}{a^2} \tag{3.11}$$

For the particular case of the homogeneous square plate without the shear effect ($C_{ww} = 1$, $D_p = C_o$, $C_{se} = 0$, $c_x = 1$, $c_y = 0$), one obtains the classical critical stress

$$\sigma_{x,CR} = \frac{\pi^2}{3(1 - \nu^2)}E\Big(\frac{h}{a}\Big)^2 \tag{3.12}$$

Examplary calculations are carried out for square sandwich plates with the selected following data: $E_f = 72000\,\mathrm{MPa}$, $a = b = 2000\,\mathrm{mm}$, $h = 30\,\mathrm{mm}$, $h_f = 1.5\,\mathrm{mm}$, $h_c = 27\,\mathrm{mm}$, $\chi_c = 9/10$,

Table 1. The results of analytical calculations for $n_e = 2$

k	0	0.5	$1 - e_c$
C_{se}	0.00637523	0.00716652	0.0102967
$N_{0,CR}^{(lc-1)}$ [N/mm]	1081.99	1074.65	1065.34
$N_{0,CR}^{(lc-2)}$ [N/mm]	721.33	716.43	710.26
$N_{0,CR}^{(lc-3)}$ [N/mm]	541.00	537.32	532.67

Table 2. The results of analytical calculations for $n_e = 10$

k	0	0.5	$1 - e_c$
C_{se}	0.00860048	0.00878646	0.00961103
$N_{0,CR}^{(lc-1)}$ [N/mm]	813.91	813.15	811.92
$N_{0,CR}^{(lc-2)}$ [N/mm]	542.61	542.10	541.28
$N_{0,CR}^{(lc-3)}$ [N/mm]	406.96	406.58	405.96

$e_c = 1/24$, $\nu = 0.3$, $k = (0, 0.5, 1 - e_c)$ and for three load cases: $lc - 1$ ($c_x = 1.0$, $c_y = 0$), $lc - 2$ ($c_x = 1.0$, $c_y = 0.5$), $lc-3$ ($c_x = 1.0$, $c_y = 1.0$). The assumed parameters are exemplary, however, the mechanical properties of the faces are typical for aluminium alloys, while the core can be considered to be a densly graded aluminium foam. The results of the analytical calculations of the shear coefficient C_{se} (3.8) and critical load values $N_{0,CR}^{(lc-i)}$ (3.11) for three load cases ($lc - i$, $i = 1, 2, 3$) and for two values of the exponent-natural number $n_e = 2$, 10 are specified in Tables 1 and 2.

Analysing the results of the above calculations, it can be noted that an increase in the stiffness near the neutral plane has negligible influence on the critical load. Such an observation is consistent with the literature provided. This confirms that five-layer plates with symmetrically varying mechanical properties are insignificantly more resistant to buckling than three-layer structures. Assuming that Young's modulus is connected with density of the material, the three--layer plates can be characterised by a smaller mass while maintaining the same buckling load. As expected, an increase of n_e leads to a decrease in the critical load, since this parameter refers to the transition rate of Young's modulus (Fig. 1) between the faces and the core of the plate. The faster Young's modulus of the face reaches the value of e_c in the core, the smaller the overall stiffness of the plate, thus one may notice a decrease in buckling performance.

4. The numerical FEM study of the elastic buckling of the plate

To provide more insight into the study, numerical finite element method (FEM) analyses are carried out in Ansys 2021 R2 system. The problem is solved using linear static structural analysis. The parameters describing geometry as well as the material are consistent with the analytical study.

Typically, the buckling behaviour of a structure should be studied without symmetry boundary conditions since one cannot predict whether the first buckling mode is symmetric. As an accurate representation of Young's modulus distribution (Fig. 2) requires a relatively large number of finite elements across the thickness, this problem becomes computationally demanding. To address this issue, preliminary analyses with a reduced number of elements are performed using the full plate model. Those confirm that the first buckling mode is symmetric just like in the case of homogeneous square plates, and thus a quarter of the plate can be considered in the numerical analysis.

The geometry of the quarter thin-walled plate is shown in Fig. 4. The applied boundary conditions assume simply supported edges and symmetry boundary conditions in the faces coincident with symmetry planes. The first of them is introduced by restraining translations w towards z axis on two edges highlighted in blue in Fig. 4. The symmetric behaviour is included by blocking the translations u and v, i.e. towards x and y axes. These components refer to normal directions to the faces highlighted in green in Fig. 4. The compressive loads N_x and N_y acting on the faces are shown in red in Fig. 4. Following the introduced loads and boundary conditions, those are consistent with the analytical study.

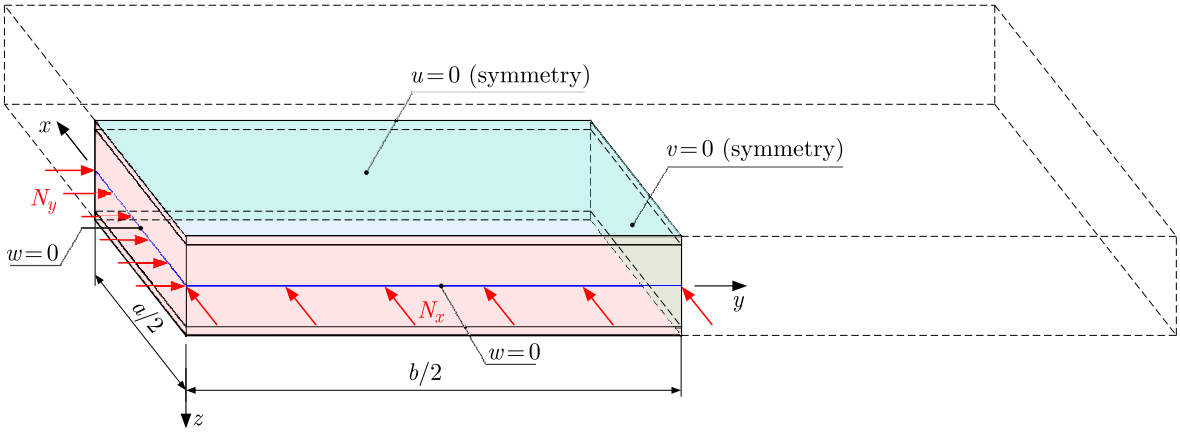

Fig. 4. The geometry of a quarter of the plate and the applied boundary conditions

The geometry of the structure is divided into first-order hexahedral finite elements SOLID185. The value of Young's modulus from Fig. 2 is mapped to the centres of finite elements. The choice of the first order elements provides a more detailed Young's modulus distribution (Fig. 2) than second-order elements for the same number of nodes. The resulting finite element model is shown in Fig. 5, where Fig. 5a shows the model with the reduced number of finite elements for better readability, while Fig. 5b refers to the actual mesh. The latter is the result of a mesh convergence study and consists of 48 elements across the thickness and 91 elements along the sides of the square plate. The total number of nodes and elements is 414736 and 397488, respectively. The aspect ratio of the elements is approximately 18. It has been found that a further increase in the aspect ratio can cause the inability to achieve the convergence of results. In addition, a numerical analysis is performed for a homogeneous plate with consistent parameters applied in the analytical study. Using the well-known expression for the critical stress described in the literature (Eq. (3.12)) for comparison, the relative difference between the results is 1.38%, showing an adequate numerical modelling.

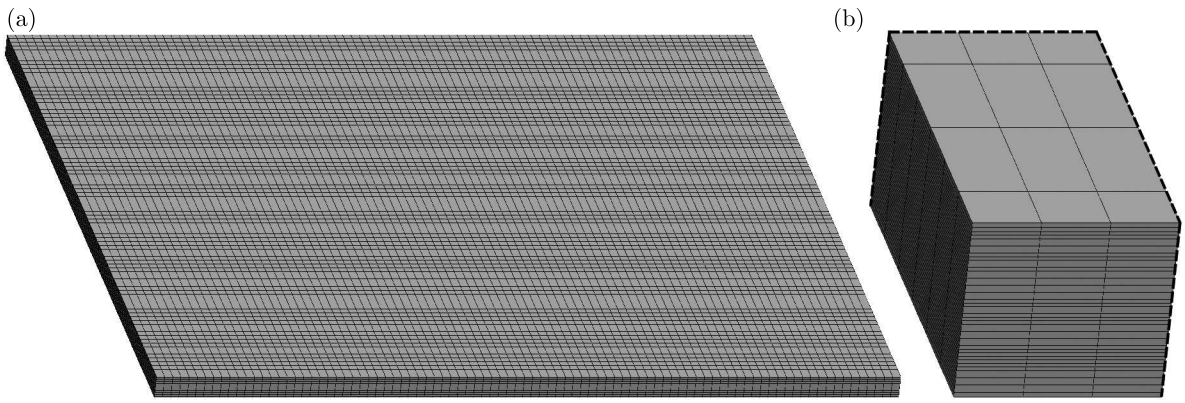

Fig. 5. Model divided into finite elements

Following Young's modulus function in Eqs. (2.2), (2.3) shown in Fig. 2, its distribution depends on the parameters k and n_e. The first of them refers to the relationship between Young's modulus on the external faces and the middle of the plate. The latter describes the pace of its transition. Exemplary Young's modulus distributions are shown in Fig. 6 for two sets of parameters. The effect of non-uniform mechanical property in Ansys software is achieved by linking the so-called "field variable" to the elastic properties of the material. This variable can be described by an external text file, which in this case consists of numerous coordinates in a three-dimensional coordinate system within the plate volume and consistent values of Young's modulus in a dimensionless form. The software interpolates the values provided to calculate Young's modulus in the centre of each finite element. The more points are provided in the text file, the more accurate the representation of the selected mechanical parameter becomes.

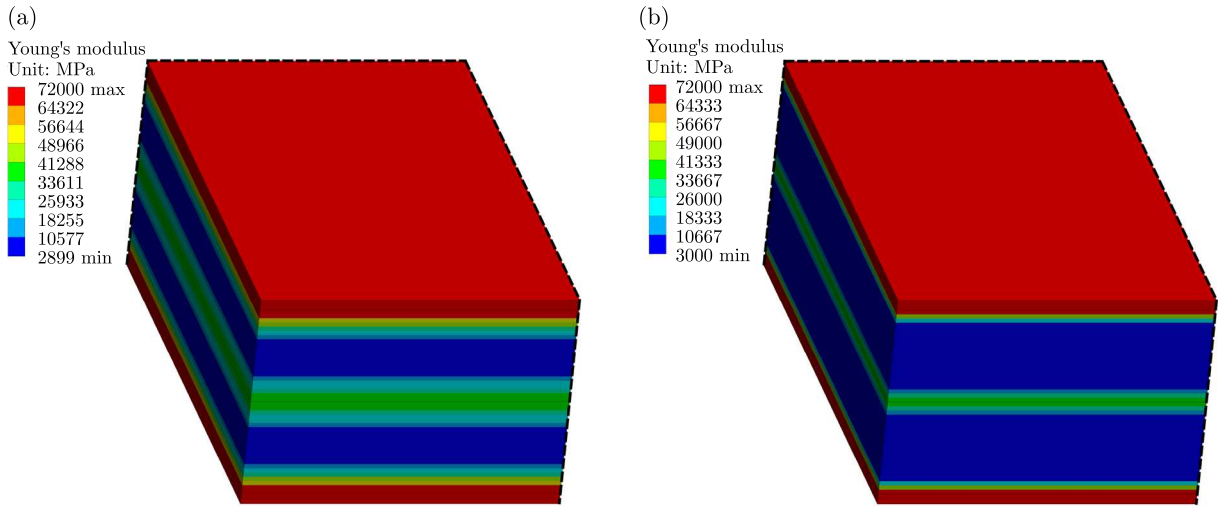

Fig. 6. Exemplary Young's modulus distribution for different material parameters

As expected, the first buckling mode (Fig. 7) is similar to the case of homogeneous and sandwich plates. Despite the fact that its symmetry is enforced by the applied boundary conditions, such behaviour was confirmed in the FEM study for the model with its complete geometry considered.

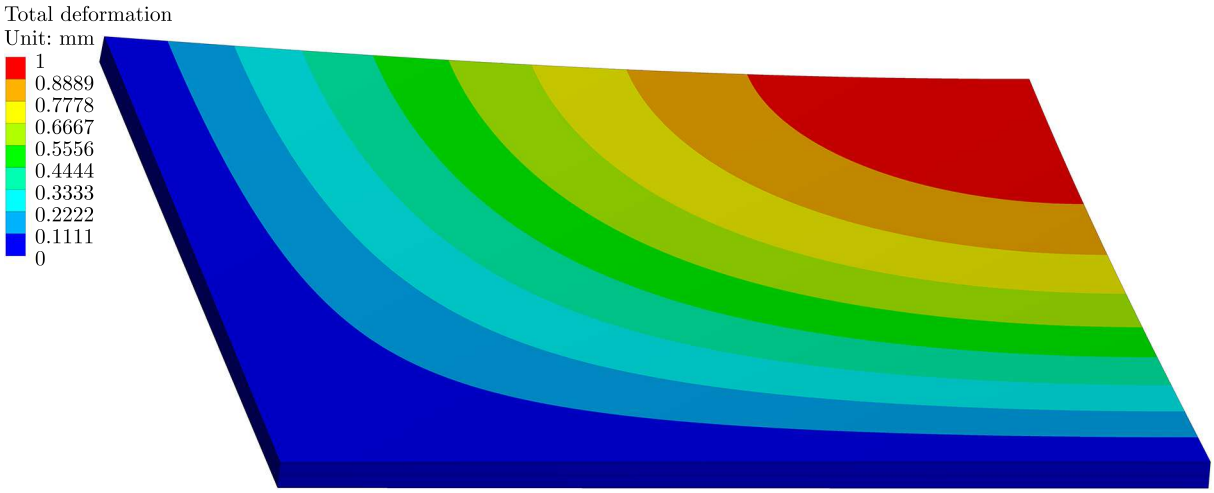

Fig. 7. First buckling mode for $k = 0.5$, $n_e = 10$

To provide more insight into the results, they are summarised in Tables 3 and 5 for $n_e = 2$ and $n_e = 10$, respectively. These are compared to the analytical solution by calculating the

relative difference shown in Tables 4 and 6, while the analytical solution is referred to as the reference value.

Table 3. Results of numerical FEM calculations for $n_e = 2$

k	0	0.5	$1 - e_c$
$N_{0,CR}^{(lc-1)}$ [N/mm]	1051.62	1042.21	1027.89
$N_{0,CR}^{(lc-2)}$ [N/mm]	701.11	694.87	685.39
$N_{0,CR}^{(lc-3)}$ [N/mm]	525.83	521.15	514.05

Table 4. Relative differences in analytical and numerical FEM calculations for $n_e = 2$

k	0	0.5	$1 - e_c$
$\delta N_{0,CR}^{(lc-1)}$ [%]	2.89	3.11	3.64
$\delta N_{0,CR}^{(lc-2)}$ [%]	2.88	3.10	3.63
$\delta N_{0,CR}^{(lc-3)}$ [%]	2.88	3.10	3.62

Table 5. Results of numerical FEM calculations for $n_e = 10$

k	0	0.5	$1 - e_c$
$N_{0,CR}^{(lc-1)}$ [N/mm]	786.60	785.63	783.26
$N_{0,CR}^{(lc-2)}$ [N/mm]	524.44	523.80	522.24
$N_{0,CR}^{(lc-3)}$ [N/mm]	393.33	392.85	391.68

Table 6. Relative differences in analytical and numerical FEM calculations for $n_e = 10$

k	0	0.5	$1 - e_c$
$\delta N_{0,CR}^{(lc-1)}$ [%]	3.47	3.50	3.66
$\delta N_{0,CR}^{(lc-2)}$ [%]	3.46	3.49	3.65
$\delta N_{0,CR}^{(lc-3)}$ [%]	3.47	3.49	3.65

5. Conclusions

The advancement in manufacturing methods allows for the designing of structures characterised by variable mechanical parameters in a controlled manner. This property can be used to achieve more efficient structural behaviour of load-carrying members. The proposed symmetric variation in Young's modulus allows the description of different structures, including homogeneous structures, three-layer and five-layer structures, with a smooth and controlled transition rate between layers.

Many studies in the field of composites refer to numerous shear deformation theories that are based on general predefined shear deformation functions that are usually suitable for specific FGMs. To solve the problem given in the presented paper, a novel nonlinear shear deformation theory of a straight normal line was applied. Unlike other theories, the derivation of the shear deformation function can be achieved analytically without assuming its form in advance; thus, it allows the study of FGMs and sandwich structures with various properties.

The influence of the studied parameters that affect Young's modulus distributions can be considered to be predictable. Both analyses have shown that an increase in Young's modulus transition rate from the faces to the core results in a reduced value of the critical load, as the overall stiffness of this structure is lower. Similarly, an increase of Young's modulus in the

neutral plane area of the plate has quite a limited effect on buckling resistance. Considering the consistency of the results in analytical and numerical applications, one may notice that there is a limited relationship between Young's modulus distribution and the results in both methods.

In general, the numerical study shows good agreement with the analytical results, where the maximum relative difference in critical loads reaches 3.7%. Having in mind the approximate nature of the obtained solution and numerical errors, such a difference can be considered satisfactory.

Acknowledgement

The paper is developed based on the scientific activity of the Łukasiewicz Research Network – Poznan Institute of Technology, Rail Vehicles Center, and the statutory activity of the Institute of Mathematics and Institute of Applied Mechanics, Poznan University of Technology, funded by the Ministry of Science and Higher Education in Poland (grant No. 0612/SBAD/3605).

References

1. Adhikari B., Dash P., Singh B.N., 2020, Buckling analysis of porous FGM sandwich plates under various types nonuniform edge compression based on higher order shear deformation theory, *Composite Structures*, **251**, 112597
2. Aguib S., Chikh N., Kobzili L., Djedid T., Nour A., Meloussi M., 2021, Analysis of buckling stability behavior of hybrid plate using Ritz approach and numerical simulation, *Structures*, **34**, 3222-3237.
3. Berdichevsky V.L., 2010, An asymptotic theory of sandwich plates, *International Journal of Engineering Science*, **48**, 3, 383-404
4. Birman V., Kardomateas G.A., 2018, Review of current trends in research and applications of sandwich structures, *Composites Part B: Engineering*, **142**, 221-240
5. Bouazza M., Becheri T., Boucheta A., Benseddiq N., 2019, Bending behavior of laminated composite plates using the refined four-variable theory and the finite element method, *Earthquakes and Structures*, **17**, 3, 257-270
6. Bouazza M., Benseddiq N., 2015, Analytical modeling for the thermoelastic buckling behavior of functionally graded rectangular plates using hyperbolic shear deformation theory under thermal loadings, *Multidiscipline Modeling in Materials and Structures*, **11**, 4, 558-578
7. Bouazza M., Hammadi F., Khadir M., 2010, Bending analysis of symmetrically laminated plates, *Leonardo Journal of Sciences*, **16**, 105-116
8. Carrera E., Brischetto S., 2009, A survey with numerical assessment of classical and refined theories for the analysis of sandwich plates, *Applied Mechanics Review*, **62**, 1, 010803
9. Dhuria M., Grover N., Goyal K., 2021, Influence of porosity distribution on static and buckling responses of porous functionally graded plates, *Structures*, **34**, 1458-1474
10. Ellali M., Amara K., Bouazza M., Bourada F., 2015, The buckling of piezoelectric plates on Pasternak elastic foundation using higher-order shear deformation plate theories, *Smart Structures and Systems*, **21**, 1, 113-122
11. Foroutan K., Carrera E., Pagani A., Ahmadi H., 2021, Post-buckling and large-deflection analysis of a sandwich FG plate with FG porous core using Carrera's Unified Formulation, *Composite Structures*, **272**, 114189
12. Grover N., Maiti D.K., Singh B.N., 2013, A new inverse hyperbolic shear deformation theory for static and buckling analysis of laminated composite and sandwich plates, *Composite Structures*, **95**, 667-675

13. Katili I., Batoz J.-L., Bouabdallah S., Maknun I.J., Katili A.M., 2023, Discrete shear projection method for mechanical buckling analysis of FGM sandwich plates, *Composite Structures*, **312**, 116825

14. Kołakowski Z., Mania R.J., 2015, Dynamic response of thin FG plates with a static unsymmetrical stable postbuckling path, *Thin-Walled Structures*, **86**, 10-17

15. Lopatin A.V., Morozov E.V., 2013, Buckling of a uniformly compressed rectangular SSCF composite sandwich plate, *Composite Structures*, **105**, 108-115

16. Magnucka-Blandzi E., Magnucki K., Stawecki W., 2021, Bending and buckling of a circular plate with symmetrically varying mechanical properties, *Applied Mathematical Modelling*, **89**, 2, 1198-1205

17. Magnucki K., 2022, An individual shear deformation theory of beams with consideration of the Zhuravsky shear stress formula, *Current Perspectives and New Directions in Mechanics, Modelling and Design of Structural Systems*, 682-689

18. Magnucki K., Magnucka-Blandzi E., 2021, Generalization of a sandwich structure model: Analytical studies of bending and buckling problems of rectangular plates, *Composite Structures*, **255**, 112944.

19. Magnucki K., Magnucka-Blandzi E., Wittenbeck L., 2023, Elastic buckling of a generalized cylindrical sandwich panel under axial compression, *Bulletin of the Polish Academy of Sciences – Technical Sciences*, **71**, 2, 144623

20. Magnucki K., Witkowski D., Magnucka-Blandzi E., 2019, Buckling and free vibrations of rectangular plates with symmetrically varying mechanical properties – analytical and FEM studies, *Composite Structures*, **220**, 355-361

21. Mantari J.L., Monge J.C., 2016, Buckling, free vibration and bending analysis of functionally graded sandwich plates based on an optimized hyperbolic unified formulation, *International Journal of Mechanical Sciences*, **119**, 170-186

22. Mantari J.L., Oktem A.S., Soares C.G., 2012, A new higher order shear deformation theory for sandwich and composite laminated plates, *Composites Part B: Engineering*, **43**, 3, 1489-1499

23. Marczak J., Jędrysiak J., 2015, Tolerance modelling of vibrations of periodic three-layered plates with inert core, *Composite Structures*, **134**, 854-861

24. Meiche N.E., Tounsi A., Ziane N., Mechab I., Adda Bedia E.A., 2011, A new hyperbolic shear deformation theory for buckling and vibration of functionally graded sandwich plate, *International Journal of Mechanical Sciences*, **53**, 4, 237-247

25. Sahoo R., Singh B.N., 2013, A new shear deformation theory for the static analysis of laminated composite and sandwich plates, *International Journal of Mechanical Sciences*, **75**, 324-336

26. Sahoo R., Singh B.N., 2014, A new trigonometric zigzag theory for buckling and vibration analysis of laminated composite and sandwich plates, *Composite Structures*, **117**, 316-332

27. Sitli Y., Mhada K., Bourihane O., Rhanim H., 2021, Buckling and post-buckling analysis of a functionally graded material (FGM) plate by the Asymptotic Numerical Method, *Structures*, **31**, 1031-1040

28. Sobhy M., 2016, An accurate shear deformation theory for vibration and buckling of FGM sandwich plates in hygrothermal environment, *International Journal of Mechanical Sciences*, **110**, 62-77

29. Yang M., Qiao P., 2005, Higher-order impact modeling of sandwich structures with flexible core, *International Journal of Solids and Structures*, **42**, 20, 5460-5490

Manuscript received September 15, 2023; accepted for print November 22, 2023

INFORMATION FOR AUTHORS

Journal of Theoretical and Applied Mechanics (***JTAM***) is devoted to all aspects of solid mechanics, fluid mechanics, thermodynamics and applied problems of structural mechanics, mechatronics, biomechanics and robotics. Both theoretical and experimental papers as well as survey papers can be proposed.

JTAM accepts full-text articles (max. 12 pages) as well as the short communications with all the requirements concerning standard publications, except a volume that is limited to 4 pages.

We accept articles in English only. The text of JTAM paper should not exceed 12 pages of standard format A4 (11-point type size, standard margins – 2.5 cm, single line spacing) including abstract, figures, tables and references.

The material for publication should be sent to the Editorial Office via electronic journal system: http://www.editorialsystem.com/jtam

Papers are accepted for publication after the review process. Blind review model is applied, which means that the reviewers' names are kept confidential to the authors. Reviewer(s) declare that there is no interpersonal relation with the author(s) that would affect the opinion and recommendation of the article for publication in JTAM. The final decision on paper acceptance belongs to the Editorial Board.

Starting from January 1, 2020, the Publisher of *Journal of Theoretical and Applied Mechanics* introduces a fee for published articles.

This applies only to papers submitted after this date and accepted by the Editorial Board for publication.

A payment of 500 EUR will be a condition for commencing the editorial procedure for upcoming articles.

After qualifying your paper for publication we will require LaTeX or TeX or Word document file and figures.

The best preferred form of figures are files obtained by making use of editorial environments employing vector graphics.

Requirements for paper preparation

Contents of the manuscripts should appear in the following order:

- Title of the paper.
- Authors' full name, affiliation and e-mail.
- Short abstract (maximum 100 words) and 3-5 key words (1 line).
- Article text (equations should be numbered separately in each section; each reference should be cited in the text by the last name(s) of the author(s) and the publication year).
- References (maximum 25) in alphabetical order.
- Titles of references originally published not in English, should be translated into English.

All the data should be reported in SI units.